Government of **Western Australia**
Department of **Mines and Petroleum**

RECORD 2009/12

A KINEMATIC, METAMORPHIC, GEOCHEMICAL AND GEOCHRONOLOGICAL FRAMEWORK FOR INTRACRATONIC REWORKING IN THE WESTERN MUSGRAVE BLOCK, CENTRAL AUSTRALIA

by
Tom Raimondo

TRaX
Tectonics, Resources and Exploration

THE UNIVERSITY OF ADELAIDE
AUSTRALIA
SUB CRUCE LUMEN


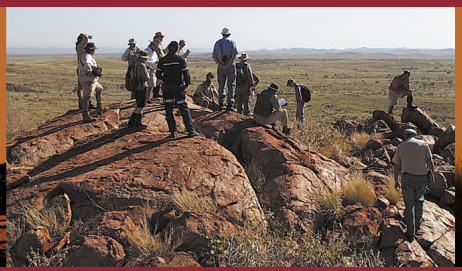

Geological Survey of
Western Australia

NGAANYATJARRA COUNCIL (Aboriginal Corporation)

A kinematic, metamorphic, geochemical and geochronological framework for intracratonic reworking in the western Musgrave Block, central Australia

Tom Raimondo

Continental Evolution Research Group
Department of Geology and Geophysics
School of Earth and Environmental Sciences
University of Adelaide, South Australia
thomas.raimondo@student.adelaide.edu.au

26 October, 2007

Notice to the reader

This Record is one of a series of BSc. Hons theses researched, written and compiled by students from the Centre of Tectonics, Resources and Exploration (TRaX), University of Adelaide, through an ongoing collaborative project between the Geological Survey of Western Australia (GSWA) and the University of Adelaide. Although GSWA has provided field and laboratory support for this project, the scientific content of each Record, and the drafting of figures, has been the responsibility of the authors. No editing has been undertaken by GSWA.

All work carried out in the west Musgrave region is done so within the framework of an ongoing collaborative project involving GSWA, the Traditional Owners of the region and the Ngaanyatjarra Council. The considerable efforts of the Traditional Owners and of the Ngaanyatjarra Council in facilitating this work is gratefully acknowledged.

Table of Contents

Abstract ... 1
1. Introduction ... 2
2. Geological setting and previous work ... 3
3. Structural setting and field relationships ... 4
4. Metamorphic petrology ... 5
4.1. General overview ... 5
4.2. Petrological groups ... 6
4.2.1. Group 1 – Felsic mylonite ... 6
4.2.2. Group 2 – Hornblende-bearing felsic mylonites ... 6
4.2.3. Group 3 – Clinopyroxene-bearing felsic mylonites ... 7
4.2.4. Group 4 – Migmatitic mylonites ... 7
5. Mineral chemistry ... 8
5.1. Garnet ... 8
5.2. Biotite ... 8
5.3. Hornblende ... 8
5.4. Clinopyroxene ... 9
5.5. Feldspar ... 9
5.6. Iron oxides ... 9
6. Thermobarometry ... 9
6.1. Sample selection and THERMOCALC overview ... 9
6.2. Recalculated assemblages ... 10
6.3. Selection of water activity ... 11
6.4. P-T estimates ... 11
7. LA-ICPMS and SHRIMP U-Th-Pb Geochronology ... 12
7.1. Sample preparation ... 12
7.2. SHRIMP operating procedures and data reduction ... 13
7.3. LA-ICPMS operating procedures and data reduction ... 14
7.4. Titanite descriptions ... 15
7.5. Zircon descriptions ... 15
7.6. SHRIMP titanite age data ... 16
7.6.1. Sample 184495 ... 17
7.6.2. Sample 187323 ... 17
7.6.3. Sample 187337 ... 17
7.6.4. Sample 155731 ... 18
7.7. LA-ICPMS zircon age data ... 18
7.7.1. Sample 187323 ... 18
7.7.2. Sample 187325 ... 19
7.7.3. Sample 184464 ... 19
7.7.4. Sample 184468 ... 20
8. LA-ICPMS trace element analysis ... 20
8.1. Operating procedures and data reduction ... 20
8.2. Trace element thermometry ... 21
8.3. Temperature estimates ... 22
8.3.1. Titanite temperature estimates ... 22
8.3.2. Zircon temperature estimates ... 23
8.4. REE analysis ... 23
8.4.1. Titanite REE chemistry ... 23
8.4.2. Zircon REE chemistry ... 24
9. Interpretation of results ... 24
9.1. P-T estimates ... 24
9.2. Geochronological data ... 25
9.2.1. Titanite ages ... 25
9.2.2. Zircon ages ... 26
9.3. Trace element thermometry ... 28
9.3.1. Titanite temperature estimates ... 28
9.3.2. Zircon temperature estimates ... 29
9.4. REE analysis ... 30
9.4.1. Titanite REE chemistry ... 30
9.4.2. Zircon REE chemistry ... 31
10. Discussion ... 32
10.1. Thermobarometric evolution and exhumation history of the Petermann Orogeny ... 32
10.2. Fluid partitioning and zircon recrystallisation ... 33
10.3. Strain partitioning within mylonitic shear zones ... 34
10.4. Structural and tectonic evolution of the Petermann Orogeny ... 36
11. Conclusion ... 39
12. Acknowledgements ... 40
13. Appendices ... 41
14. References ... 55
15. Figure captions ... 64
16. Tables ... 69
17. Figures ... 81

A kinematic, metamorphic, geochemical and geochronological framework for intracratonic reworking in the western Musgrave Block, central Australia

Tom Raimondo

Continental Evolution Research Group
Department of Geology and Geophysics
School of Earth and Environmental Sciences
University of Adelaide, South Australia
thomas.raimondo@student.adelaide.edu.au

Abstract

The crustal architecture of central Australia has been profoundly affected by periods of intracontinental deformation. Within the western Musgrave Block, Western Australia, the Neoproterozoic to Early Cambrian (600–520 Ma) Petermann Orogeny resulted in pervasive mylonitic reworking of Mesoproterozoic granites and granitic gneisses at deep crustal levels (P = 10–13 kbar and T = 700–780°C). SHRIMP and LA-ICPMS analysis of zircon and titanite indicate that peak metamorphic conditions were attained at *c.* 570 Ma, followed by progressive cooling to *c.* 600–660°C by *c.* 540 Ma driven by exhumation along the Woodroffe Thrust. A slight increase in average geothermal gradients moving south of this location suggests that deeper crustal sections experienced more rapid exhumation. This is supported by good correspondence between the record of thermal equilibration retained by equilibrium mineral assemblages and the crystallisation conditions of zircon and titanite identified using Ti and Zr thermometry. Shearing conditions during deep crustal mylonitisation appear to be dominantly anhydrous, although evidence of fluid influx into discrete shear zones is indicated by solid-state zircon recrystallisation and relatively hydrous mineral assemblages. This suggests a complex pattern of fluid partitioning and limited structural connectivity between mylonitised domains. At the outcrop scale, the correlation between distinctive structural expressions and strain intensity is interpreted to represent the simultaneous development of pure and simple shearing, resulting in the progressive partitioning of coaxial and non-coaxial strain components into discrete rock packages. This has implications for the genetic interpretation of lineations that plunge at oblique angles to the predominant regional orientation. At the orogenic scale, the relationship between kinematic partitioning and an anomalous lobate geometry of the Woodroffe Thrust trace suggests that north-directed emplacement of a broad thrust sheet was accompanied by southwest-directed lateral extrusion driven by gravitational collapse. This is indicated by the rotation of regional lineation patterns from orogen-parallel adjacent to the approximately linear fault trace to highly oblique at the point of greatest curvature further west, representing a change in the trajectory of material flow caused by lateral escape towards the orogen margin. Pervasive extensional deformation was thus produced in the hanging wall of the Woodroffe Thrust whose kinematic polarity is decoupled from the bulk tectonic transport of the Petermann Nappe Complex.

Key words: Musgrave Block, Petermann Orogeny, intracratonic deformation, thermobarometry, zircon, titanite.

Mineral abbreviations after Kretz (1983).

1. Introduction

Central Australia contains a remarkable record of intracontinental deformation spanning the latest Proterozoic and Phanerozoic. The Neoproterozoic to Early Cambrian (600–520 Ma; Wade et al., 2005) Petermann Orogeny and the Mid- to Late Palaeozoic (450–300 Ma; Haines et al., 2001) Alice Springs Orogeny are major intraplate events affecting the crustal architecture of this region (Shaw & Black, 1991; Lambeck & Burgess, 1992; Flöttmann & Hand, 1999; Flöttmann et al., 2004). The former resulted in the exhumation of the Musgrave Block from depths of 40–45 km along crustal-scale faults such as the Woodroffe Thrust and Mann Fault (Camacho et al., 1997; Scrimgeour & Close, 1999; Edgoose et al., 2004), while the latter exhumed the Arunta Inlier from beneath the previously contiguous Centralian Superbasin (Hand & Sandiford, 1999; Sandiford et al., 2001). Despite the good exposure of these orogenic systems, however, the precise details of their evolution remain poorly understood. This is most apparent with regard to the Petermann Orogeny, which has only recently become the subject of more focused studies (e.g. Camacho et al., 1997, 2001; White & Clarke, 1997; Scrimgeour & Close, 1999). An understanding of the metamorphic and thermobarometric response of different crustal levels during this event is hampered by relatively sparse *P-T* constraints, while precise estimates of the duration and rate of orogenesis are still subject to revision in light of fresh geochronological data (e.g. Wade et al., 2005). Furthermore, a model for its structural and kinematic development which integrates apparently anomalous tectonic transport in the western Musgraves (e.g. Walker-Hallam, 2006) has yet to be proposed. There is thus a pressing need for more detailed study into a variety of aspects relating to this orogenic event. In particular, better constraints need to be developed concerning its spatial and temporal scales, the rate and kinematics of exhumation, and the controls on cooling patterns and rock flow. This has the potential to generate new insights into the driving forces behind intracontinental orogenesis, the mechanisms by which deformation is localised, and the deep crustal architecture and rheology of central Australia.

This study uses structural mapping, thermobarometry, SHRIMP and LA-ICPMS dating of zircon and titanite, trace element thermometry and REE analysis to investigate the kinematic, metamorphic, geochronological and geochemical record of intracontinental deformation within the western Musgrave Block, a region dominantly affected by the Petermann Orogeny. It specifically addresses a series of mylonitic shear zones in the eastern domain of the Geological Survey of Western Australia (GSWA) Bates 1:100 000 Sheet (Howard et al., 2006), situated at the junction of the South Australian, Western Australian and Northern Territory borders (Figure 1). This area forms part of a deep crustal block exhumed along the Woodroffe Thrust, and is characterised by high grade metamorphism and pervasive mylonitic deformation. It has been the subject of a detailed metamorphic and thermobarometric study by White & Clarke (1997) and additional geochronological, kinematic and microstructural evaluation by Walker-Hallam (2006). It also lies directly to the west of a regional *P-T* investigation completed in the Mann Ranges by Scrimgeour & Close (1999). The products of this study thus provide a much-needed link between adjacent areas of the Musgrave Block, assisting an integrated and multi-faceted understanding of its evolution during intracontinental orogenesis. A new orogenic model is also presented which reconciles the regional kinematic partitioning documented by Walker-Hallam (2006) with the gross tectonic expression of the Petermann Orogeny. This may assist in developing a more detailed understanding of exhumation mechanisms, spatial and temporal variations in rock flow, and the behaviour of intracratonic lithosphere.

2. Geological setting and previous work

The Musgrave Block (Figure 1) is a Proterozoic mobile belt which forms a broad, east-west trending gravity high straddling the South Australian, Western Australian and Northern Territory borders (Kelly et al., 2006). It is bounded to the north by the Amadeus Basin and to the south by the Officer Basin, both of which formed part of the Centralian Superbasin that was fragmented by intracontinental deformation during the Neoproterozoic (Wade et al., 2005). Current exposures throughout this terrane are dominated by 1600–1540 Ma ortho- and paragneisses, along with widespread 1215–1120 Ma granites (Edgoose et al., 2004). They preserve evidence of a complex history of polyphase metamorphism, magmatism and deformation, beginning with the production of migmatitic layering in the western Musgraves at *c.* 1300 Ma (White et al., 1999). This was followed by regionally extensive granulite facies metamorphism during the *c.* 1200–1160 Ma Musgravian Orogeny, which reached conditions of T = 800–850°C and P = 5–6 kbar (Clarke et al., 1995; White et al., 2002). Accompanying this event was voluminous granitic magmatism between *c.* 1215–1120 Ma, resulting in the emplacement of Pitjantjatjara Supersuite lithologies that dominate outcrops in the Northern Territory and parts of Western Australia (Camacho & Fanning, 1995; Edgoose et al., 2004; Howard et al., 2006). A second phase of magmatism occurred at *c.* 1080 Ma, producing the layered mafic and ultramafic sills and dykes of the Giles Complex (Glikson et al., 1995; Kelly et al., 2006). This was closely followed by a major deformational event at *c.* 1060 Ma that affected the Champ de Mars, Mount Aloysius and Mount West areas (Figure 2), where pressures of 5–11 kbar and temperatures of 700–750°C are documented (Clarke et al., 1995; Stewart, 1995). From this period until the onset of the Petermann Orogeny, activity within the Musgrave Block was punctuated only by the emplacement of two suites of mafic dykes at *c.* 1000 and *c.* 800 Ma (Sun & Sheraton, 1992; Sun et al., 1996).

An influx of basement-derived sediments into the Officer Basin at *c.* 600 Ma is interpreted to mark the exhumation of the Musgrave Block from beneath the Centralian Superbasin, and thus the beginning of the Petermann Orogeny (Wade et al., 2005). The main locus of deformation was focused on the northern margin of this terrane, producing a series of major east-west trending fault structures which dissect the deep crust (Camacho et al., 1997; Sandiford et al., 2001). These include the Hinckley, Mann and Champ de Mars Faults and the Woodroffe Thrust (Figures 1 and 2). The latter is a shallowly south-dipping mylonite and pseudotachylite zone up to 3 km thick that offsets the Moho by *c.* 20 km (Lambeck & Burgess, 1992; Camacho et al., 1995). In the western Musgraves, its position is inferred from aeromagnetic and remote gravity data due to lack of exposure (Edgoose et al., 2004). The Woodroffe Thrust accommodated significant displacement during north-south shortening, resulting in the exhumation of granulite facies gneisses from depths of 40–45 km and their structural juxtaposition with amphibolite facies gneisses further north (Scrimgeour & Close, 1999). Mid- to upper-crustal rocks are exposed in a large scale imbricate thrust stack (the Petermann Nappe Complex) in its footwall, and contain interleaved sedimentary sequences of the Amadeus Basin (Edgoose et al., 2004). The northern margin of the Petermann Orogen thus contains a near-complete range of crustal exposure.

Sequential cross section restorations suggest that north-vergent shortening during the Petermann Orogeny exceeded 100 km, and was accommodated by substantial crustal thickening (Flöttmann et al., 2004). This is supported by thermobarometric constraints from the high grade orogenic core exposed between the Woodroffe

Thrust and Mann Fault, which indicate pressures of 12–14 kbar and temperatures of *c.* 650–750°C (Camacho et al., 1997; White & Clarke, 1997; Scrimgeour & Close, 1999). Metamorphic grade decreases towards the foreland to the north, and parallel to major structures towards the east (Edgoose et al., 2004). Estimates of the average geothermal gradient during orogenesis indicate that it was not significantly elevated from a stable cratonic geotherm, suggesting that cooling was largely controlled by uplift and denudation. Camacho et al. (1997) estimated that the average rate of exhumation was *c.* 0.2–1.5 mm per year, corresponding to a slow to moderate cooling rate of *c.* 3–23°C per million years. The latest record of exhumation is preserved by synkinematic biotite and muscovite growth within the Woodroffe Thrust in the eastern Musgrave Block at *c.* 520 Ma (Camacho & Fanning, 1995).

The Petermann Orogen is usually regarded as a crustal-scale dextral transpressive shear system. North-vergent movement was principally concentrated along the Woodroffe Thrust, while south-vergent overthrusting was accommodated along the southern margin of the Musgrave Block. Rapid burial and exhumation thus generated a divergent flower structure (Camacho & McDougall, 2000), cored by a major dextral strike-slip zone (the Mann Fault). It is likely that intracontinental orogenesis was driven by north-south compression of the Australian plate during the amalgamation of Gondwana in the Neoproterozoic (Sandiford & Hand, 1998; Collins & Pisarevsky, 2005). The stationary position of northwestern Australia relative to anti-clockwise rotation of the southern plate margin may be responsible for the generation of large-scale dextral transpression within the continental interior.

3. Structural setting and field relationships

Throughout the eastern domain of the Bates 1:100 000 Sheet, Mesoproterozoic (1215–1120 Ma; Edgoose et al., 2004; Howard et al., 2006) Pitjantjatjara Supersuite granites and pre-Musgravian Orogeny granitic gneisses have been extensively reworked by deep crustal deformation associated with the Petermann Orogeny (600–520 Ma; Camacho & Fanning, 1995; Edgoose et al., 2004; Wade et al., 2005). Deformation grades from discrete mylonitic shear bands within undeformed granite to 50–100 m wide mylonitic shear zones featuring extensive recrystallisation and grain size reduction (Figure 3a-b). Overall, however, deformation is pervasive at a regional scale, and manifests as a consistent mylonitic fabric with an associated mineral stretching lineation (Figure 4). This fabric predominantly dips shallowly to moderately southeast, and is occasionally reconfigured by south- to southeast-plunging open folds. Elongate aggregates of quartz and feldspar crystals define the associated stretching lineation, which typically plunges subhorizontally towards the southwest and northeast.

The feldspar-rich composition and fine-grained nature of mylonitic shear zones makes them extremely susceptible to weathering, often preventing the preservation of their contact relationships with the surrounding country rock, and with differently oriented shear zones on adjacent outcrops. However, truncation of gneissic layering is evident at more extensive outcrops in southern Bates (particularly Heather's Hill; see Figure 4), while in other locations it is transposed into the mylonitic fabric. Multiple anastomosing shear zones also occur at Spaghetti Hill (see Figure 4), although no definitive cross-cutting relationships are observed, implying one generation of shear activity.

Throughout Bates, mylonitic fabrics record variable strain intensity. The highest strain zones feature extensive grain size reduction and prominent southwest-plunging stretching lineations. Asymmetric sigma and delta feldspar porphyroclasts, along with S–C and C' fabrics, consistently record top to the southwest tectonic transport (Figure 3c), although grain size reduction is often too dramatic to reveal this information to the naked eye. Tight to isoclinal intrafoliar folds are also common within these high strain domains, with their hinges orthogonal to the lineation orientation (Figure 3d). In contrast, the lower strain protomylonitic zones do not record any evidence of rotational kinematics, and are instead associated with symmetrical porphyroclasts and metre-scale tight to open folds with south- to southeast-plunging stretching lineations parallel to the fold hinges.

The relationship between high and low strain mylonitic zones is best observed at Heather's Hill in southeast Bates (inset to Figure 4). This location features a sharply defined shear zone which shows progressive fluctuations in strain intensity across its approximately 60 m width. The outer edges of the shear zone record the most intense deformation, with dramatic grain size reduction and pervasive S/L–tectonite and mylonite development. They are interspersed with an approximately 25 m wide zone of protomylonite which runs through the core of the shear zone. This variation in the degree of mylonitisation is accompanied by a progressive change in structural style and orientation of the mineral stretching lineation, as illustrated in Figure 5. High strain zones are characterised by pervasive asymmetric augens and tight intrafoliar folding, with northeast/southwest-plunging stretching lineations parallel to the inferred tectonic transport direction. Conversely, symmetric porphyroclasts and broad local folding occur within the low strain zones, and are associated with south- to southeast-plunging lineations parallel to the fold hinges.

4. Metamorphic petrology

4.1. General overview

Mineral assemblages associated with mylonitic lithologies have limited variability throughout eastern Bates, and largely reflect variations in their granitic precursors. Fine- to medium-grained quartzofeldspathic assemblages are common in the northern area, immediately south of the Woodroffe Thrust, and occasionally contain minor garnet. They are also associated with blastomylonitic outcrops featuring extensive pseudotachylite veining (Figure 3e). Coarser-grained mylonites with large rotated feldspar augens appear in small rounded outcrops immediately south of this location, and contain abundant hornblende. Fine-grained aggregates rich in garnet, titanite and hornblende are predominant throughout the central and southern domains, with variable amounts of biotite and a lesser abundance of quartz and feldspar. Clinopyroxene-bearing assemblages are observed towards southern Bates, and coincide with the development of migmatitic shear zones (Figure 3f). Limited migmatisation is observed at Spaghetti Hill and Mount Gosse, while more extensive zones are observed south of these locations. Several mylonitic outcrops throughout Bates are also highly annealed.

Despite the widespread preservation of primary igneous minerals within mylonitic lithologies, distinctive petrological features and relationships allow the identification of metamorphic assemblages. Principally,

metamorphic mineral populations are distinguished on the basis of reduced grain size and the absence of abundant inclusions, consistent with their extensive recrystallisation. In addition, metamorphic aggregates of hornblende and biotite are dominantly acicular and strongly exhibit a preferred orientation, allowing them to be differentiated from their porphyroclastic igneous equivalents. Mylonitic assemblages are thus occasionally enriched in hydrous minerals relative to their undeformed granitic precursors, and commonly feature an increase in the proportion of garnet.

4.2. Petrological groups

Twelve samples from various locations throughout eastern Bates are divided into four separate groups based on variations in their mineral assemblages. Distinctions are made largely on the presence or absence of key minerals such as clinopyroxene and hornblende, along with characteristic features such as the existence of corona textures and the preservation of primary igneous porphyroclasts. The spatial distribution of all samples is shown in Figure 4, and photomicrographs of key petrological relationships are displayed in Figure 6.

4.2.1. Group 1 – Felsic mylonites

Group 1 samples are felsic mylonites sourced from porphyritic granites of the Pitjantjatjara Supersuite (187314 and 184486 B), and augen-bearing granitic gneisses derived from the Birksgate Metamorphics (185674). They feature mineral assemblages dominated by quartz, K-feldspar and plagioclase (often up to 90%), with minor garnet and biotite. Garnet is present both as small relict porphyroclasts (<2 mm) which are enveloped by the mylonitic fabric, as well as minute grain clusters within the matrix (Figure 6a). Biotite is usually in contact with garnet and forms very thin acicular needles which locally define the foliation, while quartz and feldspar and highly elongate and often strongly annealed, forming continuous ribbons. Magnetite is present in all samples, and usually occurs in contact with garnet porphyroclasts.

4.2.2. Group 2 – Hornblende-bearing felsic mylonites

Group 2 samples are mylonitic granites (187305, 187323 and 187330 A) and metamonzogranites (155733 and 155735) of the Pitjantjatjara Supersuite. This division differs from Group 1 samples by having a much more diverse mineralogy, typically characterised by the presence of garnet, hornblende, biotite, K-feldspar, plagioclase, clinozoisite and titanite. Mineral abundances (particularly garnet and hornblende) are generally controlled by variations in the precursor lithology, with extensive recrystallisation of primary igneous minerals. Garnet is usually present as relict porphyroclasts up to 5 mm in diameter, often with abundant inclusions of biotite, ilmenite and clinozoisite and separated from hornblende porphyroclasts by plagioclase moats (Figure 6b). Numerous fine-grained metamorphic aggregates also exist in most samples, while others are relatively garnet-poor (particularly 187323). Hornblende occurs both as remnant porphyroclasts which are extensively

fragmented, and as acicular needles which locally define the mylonitic foliation. Some porphyroclasts remain relatively intact and preserve linear inclusion trails defined by elongate biotite and clinozoisite (Figure 6c). Biotite exists as elongate acicular grains up to 2 mm in length, and usually occurs in contact with garnet and opaques. Large K-feldspar grains are common, and occasionally display core and mantle structures with small recrystallised grains surrounding relict porphyroclasts. Other examples display a perthitic texture. Clinozoisite occurs both as thin rims around feldspar grains and as small grains in contact with titanite, while titanite itself often exhibits a subhedral crystal habit, usually in contact with biotite and hornblende (Figure 6d). It also occasionally displays iron oxide tails. Plagioclase and quartz dominate the matrix composition, along with minor garnet, hornblende, titanite, biotite, and accessory ilmenite, magnetite and apatite. Abundant zircon is also commonly present, usually as large (up to 900 μm) elongate grains.

4.2.3. Group 3 – Clinopyroxene-bearing felsic mylonites

Group 3 samples are mylonitic granites (184468) and metamonzogranites (184464) of the Pitjantjatjara Supersuite. They display similar mineralogical diversity to Group 2 samples, with assemblages comprising garnet, hornblende, biotite, K-feldspar, plagioclase, clinozoisite and titanite. The crucial addition is that of relict igneous clinopyroxene, which usually occurs as small porphyroclasts 0.2–0.5 mm in diameter (Figure 6e). Garnet occurs both as small fine-grained aggregates interlayered with small needles of biotite, and as inclusion-rich porphyroclasts which are usually separated from clinopyroxene by a thin plagioclase moat. In contrast to Group 2 samples, metamorphic garnet aggregates within this group generally form thin coronas around magnetite and titanomagnetite, rather than being evenly distributed throughout the matrix. Hornblende is less abundant and usually exists as small oriented needles which define the mylonitic foliation, with primary porphyroclasts rarely preserved. It also defines fine compositional layering by alternating with domains rich in quartz and feldspar. In addition to their association with garnet, fine-grained iron oxides are littered throughout the matrix. Plagioclase and K-feldspar do not occur as porphyroclasts, and together with quartz form thin ribbons which dominate the completely annealed microstructure.

4.2.4. Group 4 – Migmatitic mylonites

Group 4 samples (184484 and 185679) are sourced from felsic gneisses which have undergone migmatisation. Their mineral assemblages are dominated by garnet, quartz, plagioclase, K-feldspar, biotite and accessory magnetite and titanomagnetite, with additional orthopyroxene, clinopyroxene and hornblende. Relict porphyroclastic igneous orthopyroxene is enveloped by thin coronas containing fine-grained garnet, biotite and metamorphic clinopyroxene (Figure 6f). The accessory iron oxides also display fine coronas dominated by garnet and small biotite needles. Hornblende is occasionally present as very fine-grained aggregates associated with biotite and garnet, while quartz and feldspar occur both as fine recrystallised grains throughout the matrix, and as elongate annealed ribbons.

5. Mineral chemistry

Electron microprobe analysis (EMPA) was conducted on all samples described above, in order to constrain the thermobarometric evolution and mineral relationships of a range of rock types and locations throughout eastern Bates. Mineral compositions were obtained using a Cameca SX51 Electron Microprobe with wavelength dispersive spectrometers, located at Adelaide Microscopy. Quantitative analyses were performed using an accelerating voltage of 15 kV and a beam current of 20 nA. Mineral analyses from all samples are presented in Appendix 1, with ferric iron recalculated using stoichiometric criteria (Droop, 1987). A summary of mineral chemistry from each petrological group is also provided in Table 1.

5.1. Garnet

Garnet has a relatively homogeneous composition in all samples, although no cation mapping was undertaken to reveal more subtle compositional variations than those able to be identified from core-rim analyses alone. It is usually an almandine-grossular-dominated solid solution, with X_{Fe} (Fe/Fe+Ca+Mg+Mn) generally varying between 0.52–0.60 and X_{Ca} (Ca/Fe+Ca+Mg+Mn) ranging from 0.19–0.33. X_{Mg} (Mg/Fe+Ca+Mg+Mn) is uniformly low in Group 2 samples, falling within the range 0.03–0.10, while it is greatly enriched in Group 4 samples (X_{Mg} = 0.20–0.25). Conversely, spessartine is significantly higher in Group 2 samples, with X_{Mn} (Mn/Fe+Ca+Mg+Mn) typically varying between 0.06–0.15 compared to a usual range of 0.01–0.05 for the remaining groups.

5.2. Biotite

Biotite is uniformly Ti-rich in all petrological groups, with X_{Ti} (Ti/Fe+Mg+Al^{VI}+Ti) typically ranging between 0.04–0.11 based on eleven oxygen atoms. Group 2 samples are commonly rich in Fe, with X_{Fe} (Fe/Fe+Mg+Al^{VI}+Ti) usually ranging from 0.48–0.60, while the remaining groups are highly variable, ranging from 0.16–0.51. X_{Al}^{VI} is predominantly very low (<0.02), although occasional samples have values as high as 0.12. Group 4 samples are very magnesian (X_{Mg} = 0.61–0.82), while the remaining groups are again highly variable, ranging from 0.29–0.61. X_{Na} (Na/Na+K) is very low in all groups, reaching a maximum of just 0.02.

5.3. Hornblende

All analysed hornblende is classified within the calcic amphibole group (Leake et al., 1997), having Ca_B >1.50, Na_B < 0.50 and $(Ca+Na)_B \geq 1.50$. All analyses also have $(Na+K)_A \geq 0.50$, Ti < 0.50 and Si = 5.99–6.30, and thus plot within the pargasite-ferropargasite subgroup on a plot of X_{Mg} (Mg/Mg+Fe^{2+}) vs. Si per formula unit. Group 3 and 4 samples are very magnesian, with X_{Mg} typically 0.57–0.75, while Group 2 samples show a greater compositional variation (X_{Mg} = 0.24–0.54). Group 2 samples are also slightly more aluminous, with Al^{VI} varying between 0.38–0.62, while the remaining groups fall within the range 0.24–0.40.

5.4. Clinopyroxene

All analysed clinopyroxene is classified within the Ca-Mg-Fe quadrilateral, having Ca+Mg+Fe^{2+} values ranging from 1.59–1.82 and Na varying between 0.10–0.34 (Morimoto et al., 1988). All analyses are contained within the diopside field, being uniformly calcic (X_{Ca} = 0.45–0.46, where X_{Ca} = Ca/Ca+Mg+Fe^{2+}+Fe^{3+}+Mn^{2+}). Group 3 samples are more Fe-rich (X_{Fe} = 0.20–0.30) compared to Group 4 samples (0.14–0.15), while Group 4 samples are slightly more magnesian (X_{Mg} = *c.* 0.40) relative to Group 3 samples (0.28–0.34).

5.5. Feldspar

Metamorphic plagioclase is invariably sodic in composition for all samples, with the majority of analyses falling within the range X_{Ab} (Na/Na+Ca) = 0.74–0.84, while relict igneous porphyroclasts are more calcic (X_{Ab} = 0.56–0.63). In contrast, albite content of K-feldspar is typically low, with X_{Ab} (Na/Na+K) varying between 0.05–0.17. Orthoclase content within plagioclase is never greater than 2%, while anorthite content within K-feldspar is negligible (<0.5%).

5.6. Iron oxides

Ilmenite in Group 3 samples is an ilmenite-hematite solid solution, having X_{Ilm} (Ti/Ti + ½Fe^{3+}) = *c.* 0.90. In contrast, Group 2 samples are very hematite poor, with X_{Ilm} = 0.96–1.00. Mn content of the Group 2 samples is X_{Mn} (Mn/Fe+Mg+Mn) = 0.01–0.02. Titanomagnetite is of uniform composition in both Groups 3 and 4, with X_{Ti} (Ti/Fe+Ti) = 0.14–0.16.

6. Thermobarometry

6.1. Sample selection and THERMOCALC overview

Mylonitic lithologies which outcrop throughout Bates are ideal for thermobarometry because they are commonly extensively recrystallised and contain a large number of minerals in textural equilibrium. Their wide distribution throughout the terrane also means that good constraints can be developed on the spatial variation in *P-T* conditions. All samples selected for thermobarometry were garnet bearing, and contain metamorphic minerals which either define the mylonitic fabric or exhibit strong grain size reduction relative to primary igneous phases. *P-T* estimates were performed using EMPA compositional analyses described in Section 5, with activity and composition relationships for mineral end-members calculated using the software AX (Powell et al., 1998). A representative output file from AX is provided in Appendix 2.

Pressure and temperature estimates presented in this study were obtained using the average *P*, average *T* and average *P-T* approaches of Powell & Holland (1988, 1994). These multiple equilibria techniques deploy the

software THERMOCALC v.3.26 to calculate the optimal metamorphic conditions from the thermodynamics of an independent set of reactions (Holland & Powell, 1998). Each independent set entirely specifies the thermodynamics of a given system, and includes overlapping subsets of end-members which are inherently correlated. This allows the equilibria to respond to one another in a predictable manner, resulting in an optimal *P-T* intersection which can be statistically constrained. As documented by Powell & Holland (1994), a least-squares (χ^2) method is used for assessing the statistical robustness of a given intersection. This incorporates uncertainties and correlations on the activities and enthalpies of formation of mineral end-members which are propagated throughout the calculation process. If the optimal solution passes the χ^2 test, it is consistent with the original input data and their uncertainties. If it does not, a satisfactory solution can usually be found by either omitting outlying end-members which are poorly fitted by the average result, or by increasing the uncertainty on their activities. A representative output file demonstrating an average *T*, average *P* and average *P-T* calculation produced via this method is presented in Appendix 3.

All samples processed using THERMOCALC were able to produce an independent set of reactions. Samples from Groups 2 and 3 had particularly low variance assemblages due to their large number of minerals, with up to twelve equilibria being incorporated into the independent set. Group 1 samples were less well constrained, with three to four reactions usually involved. However, all *P-T* intersections defined using these equilibria were able to pass the χ^2 test at the 95% confidence level. End-members were occasionally omitted from calculations due to their poor fit within the equilibria generated. This improved the statistical fit of the calculation but did not significantly alter the determined *P-T* estimates. The existence of end-member outliers in otherwise well constrained dataset may reflect either inadequacies in activity models for certain ranges of mineral compositions, or analytical issues relating to electron microprobe analysis (e.g. Mawby, 2000).

6.2. Recalculated assemblages

In addition to the mineral compositions detailed in this study, *P-T* calculations were also performed using mineral compositions presented by White & Clarke (1997) from samples M010, M213 and M214. These samples are sourced from the same outcrop as sample 184468, 12 km west of Mount Gosse (see Figure 4). Primarily, the usefulness of recalculating these assemblages is in assessing the parity between pressure and temperature estimates obtained via different methods. These authors present calculations based on the geothermometers of Ellis & Green (1979), Graham & Powell (1984), Powell (1985) and Krogh (1988), and the geobarometers of Newton & Perkins (1982), Moecher et al. (1988), Kohn & Spear (1990) and Eckert et al. (1991). They also utilise the average pressure and average temperature approaches of an earlier version of the software THERMOCALC. Thus, by subjecting these assemblages to the same calculation process employed in this study, comparisons can be made not only between current THERMOCALC activity models and those contained within superseded versions of the software, but also between THERMOCALC *P-T* estimates and those obtained using a variety of well established geothermometers and geobarometers. This allows the correspondence between the thermobarometric methods employed in this study and alternative methods used in additional studies (e.g. Scrimgeour & Close, 1999) to be directly evaluated.

6.3. Selection of water activity

The majority of samples in this study were modelled as fluid-absent assemblages with low water activities ($aH_2O \leq 0.25$), which reflects the generally anhydrous nature of the shear zones from which they were derived. Shear zones with higher water activities (aH_2O = 0.50–0.75) occur at Spaghetti Hill and in the regions surrounding Mount Daisy Bates, where mineral assemblages are dominated by hydrous phases such as hornblende and biotite. This distinction is made apparent by the correspondence between THERMOCALC average *P-T* estimates and temperature calculations generated using independent Fe-Mg end-member reactions, such as garnet-biotite, garnet-hornblende and garnet-clinopyroxene mineral equilibria. A comparison of these two methods for samples 184484 and 187323 is presented in Table 2 and Figure 7. Sample 184484 is very responsive to changes in water activity, such that the χ^2 fit value is outside the 95% confidence limit for aH_2O >0.50. This is reflected by the gradual widening of the error ellipses. The smallest error ellipse occurs for aH_2O = 0.25, making it a logical selection as the most appropriate water activity. However, better confirmation of this choice is achieved by assessing its correspondence to temperature estimates generated using the Fe-Mg exchange equilibria, which operate independently of water activity models. Given that these temperature estimates fall within the *P-T* error ellipse defined by aH_2O = 0.25, it is a reasonable assumption that this value represents the best estimate of water activity within the shear zone itself.

P-T calculations that exhibit less sensitivity to modelled water activity are more problematic. For example, the fit value for sample 187323 is beneath the 95% confidence limit for all possibilities ranging from total water absence to complete saturation. This makes the assessment of the actual fluid conditions within the shear zone extremely difficult using the statistical robustness of THERMOCALC alone, especially for equilibrium assemblages which contain a limited number of phases. However, some constraints can again be achieved by considering the correspondence between the various *P-T* uncertainty envelopes and additional temperature estimates based on independent Fe-Mg mineral reactions. In this case, such estimates jointly fall within only one error ellipse, making it a logical selection for modelled water activity.

6.4. P-T estimates

A summary of *P-T* estimates for each of the sample groups is presented in Table 3, along with additional calculations generated using the mineral assemblages of White & Clarke (1997). Sample locations and their associated *P-T* conditions are also shown in Figure 8. In general, the calculations show a consistent trend of increasing temperatures towards the zone of migmatisation in southeast Bates (inset to Figure 8). Conditions vary from *c.* 620°C in the immediate hanging wall to the Woodroffe Thrust, to *c.* 780°C approximately 30 km further south. Estimates are consistently 700–750°C in the central domain which comprises Spaghetti Hill, Mount Gosse and additional outcrops to the west, coinciding with evidence of limited migmatisation within these areas. In contrast, temperatures fall within the range 650–700°C in regions immediately surrounding Mount Daisy Bates, where no indication of migmatisation was observed.

The general trend towards elevated temperatures in southeast Bates is accompanied by a steady increase in pressure, although it is less well constrained (inset to Figure 8). Conditions vary from *c.* 9.5 kbar adjacent to the Woodroffe Thrust to *c.* 12 kbar at Heather's Hill. Estimates are discernibly higher in the regions west of Mount Gosse, reaching *c.* 13 kbar using the recalculated core assemblages of White & Clarke (1997). A number of variations are also evident throughout the central domain south of Spaghetti Hill, but generally these occur over a range of only ± 0.5 kbar.

7. LA-ICPMS and SHRIMP U-Th-Pb Geochronology

Samples were selected for geochronological analysis primarily on the basis of morphological features and petrological relationships viewed in thin section. The success of U-Th-Pb geochronology performed on both zircon and titanite from Spaghetti Hill in a previous study (Walker-Hallam, 2006) meant that similar accessory minerals were targeted. A primary aim of this study was to obtain a wide distribution of age data from various sections of Bates, in order to place the existing data within a broader tectonic and metamorphic context. As such, a combined evaluation of age data from this study and that of Walker-Hallam (2006) is presented in the following sections. Laser Ablation – Inductively Coupled Plasma Mass Spectrometry (LA-ICPMS) analysis was conducted on zircons extracted from samples 184464, 184468, 187320, 187323 and 187325, while Sensitive High Mass Resolution Ion Microprobe (SHRIMP) analysis was performed on titanites sourced from samples 187323, 187337 and 184495. The spatial distribution of all samples is shown in Figure 4.

7.1. Sample preparation

Zircon and titanite extraction was undertaken at the University of Adelaide. Each sample was initially crushed using a jaw crusher. Sieving was then performed using a combination of 400 and 700 μm mesh, and the 400–700 μm fraction was collected for further refinement. This involved washing with water and detergent to remove dust, and hand panning to isolate heavier mineral components. Each heavy mineral separate was then run through methylene iodide, and finally passed over with a strong hand magnet. Approximately 150 representative zircons and/or titanite grains were hand-picked from each sample and mounted in epoxy resin, with four grains of Khan standard added to the titanite mount. All grains were then sectioned to approximately half their diameter using a combination of 100, 50 and 1 μm polishing cloths.

The polished zircon mounts were imaged using a Philips XL20 SEM with attached Gatan CL detector at Adelaide Microscopy. An operating voltage of 20 keV was used and standard cathodoluminescence (CL) and backscattered electron (BSE) imaging techniques were applied to investigate internal zonation. Identical BSE imaging was also performed on the titanite mount at Adelaide Microscopy. Additional imaging of the titanites was completed by GSWA at Curtin University, Perth, where each sample was photographed in transmitted and reflected light to identify grain inclusions, morphology and topography. The mount was then evaporatively coated with about 500 nm of high purity gold for use on the SHRIMP.

7.2. SHRIMP operating procedures and data reduction

U-Th-Pb analysis of titanite was conducted using SHRIMP II (B) at the John de Laeter Centre for Mass Spectrometry at Curtin University, Perth. Samples 184495, 187323 and 187337 were analysed during one session on 30 August 2007, while sample 155731 was analysed during a previous session in 2006 (see Walker-Hallam, 2006). Detailed operating procedures for SHRIMP II are outlined by Williams (1998), while operating techniques specific to titanite are described by Kinny (1997). A beam diameter of 30 μm was used. Prior to analysis, each spot was rastered with the ion beam for 3 minutes at 160 nA, in order to remove the gold coating and reduce surficial common lead. Five scans were then run for each analysis spot with 25 nanoseconds dead time, giving a total duration of approximately 730 seconds, and the results were averaged. U-Pb fractionation was corrected using the Khan standard (Kinny, 1994, 1997), and data reduction was completed using KRILL software (Kinny, 1997).

Due to the very low radiogenic compositions of the titanites used in this study, corrections for initial lead are a major consideration. Appreciable fractions of common Pb were detected for all samples, with average *f* 204 values (i.e. the fraction of common ^{206}Pb in total ^{206}Pb, based on measured ^{204}Pb/^{206}Pb) ranging from 0.08–0.44. This is considerably higher than that contributed from the mount surface, estimated from the proportion of common Pb in the Khan standard, and is reflected by the large imprecision of the ^{207}Pb/^{206}Pb ages. Common Pb corrections were thus applied to all titanite analyses using KRILL software (Kinny, 1997), with contemporaneous common Pb compositions determined following the method of Stacey & Kramers (1975). The ^{204}Pb-corrected isotope ratios for all samples are presented in Table 4, with all errors quoted at the 1 sigma (1σ) level.

Disproportionately high background counts on SHRIMP–B were measured throughout the analytical session. This produces the strong possibility that the proportion of very low abundance isotopes (particularly ^{204}Pb) was incorrectly measured, leading to an inappropriate common Pb correction. A strong positive correlation between *f* 204 and ^{206}Pb/^{238}U corrected ages for samples 184495, 187323 and 187337 (Figure 9a) suggests that this was indeed the case, producing age estimates that are consistently too old. The reverse is evident for sample 155731 (owing to different operating conditions during a previous SHRIMP session), with a strong negative correlation between *f* 204 and ^{206}Pb/^{238}U corrected ages (Figure 9b). This results in age estimates that are consistently too young.

Given the apparent likelihood of an inaccurate common Pb correction, a viable alternative is to treat the Pb data as a simple two-component mixture of radiogenic and common leads. In this case, the true end-member compositions can be determined via linear regression through the uncorrected data (Kinny, 1997; Williams, 1998; Frost et al., 2000). A limitation of this approach is that it assumes concordant data, i.e. that no analytical point has been affected by radiogenic Pb loss subsequent to Petermann-aged geological closure. The validity of this assumption can only be assessed from the robustness of the data-defined regression, the amount of extrapolation required, and the realism of the calculated intercepts.

Following the above approach, Yorkfit regressions were applied to the uncorrected $^{238}U/^{206}Pb$ vs. $^{207}Pb/^{206}Pb$ isotope ratios for each sample (along with their associated errors) using Isoplot/Ex 3.00 (Ludwig, 2003). This method fits a least-squares regression through the data with individual data point errors taken into account (a 'Model 1' fit). The mean square of weighted deviates (MSWD) of the regression is acceptable for all samples, ranging from 1.15 to 2.15. In addition, the calculated $^{207}Pb/^{206}Pb$ intercepts (0.814–0.928) closely correspond to the Stacey-Kramers bulk Earth $^{207}Pb/^{206}Pb$ ratios applicable to Petermann times (0.874 at 560 Ma). This implies a strong likelihood that the data-defined regression represents a true two-component mixture between a single common Pb end-member (estimated from the $^{207}Pb/^{206}Pb$ intercept) and a geologically meaningful radiogenic composition. The latter is determined from the lower concordia intercept of the $^{238}U/^{206}Pb$ vs. $^{207}Pb/^{206}Pb$ array when plotted on a Tera-Wasserburg concordia diagram (Tera & Wasserburg, 1972). For each sample, the Tera-Wasserburg regression was anchored to a common Pb composition estimated from the respective Yorkfit intercept. High positive weighted residuals (>2.5) were not recorded for any sample, again reinforcing the suggestion that they had not suffered Pb loss. However, a limited number of analyses contained high negative weighted residuals, and were removed on the basis that they have probably been affected by inherited Pb.

7.3. LA-ICPMS operating procedures and data reduction

U-Th-Pb analysis of zircon was conducted using an Agilent 7500cs ICPMS coupled with a New Wave 213 nm Nd-YAG laser. Ablation was performed in a helium atmosphere, with a beam diameter of 30 μm, repetition rate of 5 Hz and laser intensity of 70%. Total acquisition time for each analysis was 110 seconds, and involved 40 seconds of background measurement, 10 seconds for beam and crystal stabilisation, and 60 seconds of sample ablation. Other operating conditions and equipment utilised are outlined by Payne et al. (2006, 2007). U-Pb fractionation was corrected using the GEMOC GJ-1 standard (Jackson et al., 2004), and data reduction was completed using GLITTER software (Van Achterbergh et al., 2001). Accuracy was also monitored by repeat analyses of the Sri Lankan in-house internal standard BJWP-1.

Given the inability of LA-ICPMS to measure common lead, unknowns from each sample were initially corrected using the 'ComPbCorr' Excel macro (Andersen, 2002). Using the 3D concordia method, negligible common Pb (<0.5% ^{206}Pb) was detected for samples 184464, 184468 and 187325. Uncorrected isotope ratios (Table 5) are thus used in age calculations for these samples, with the conventional concordia plots and discordia chords generated using Isoplot/Ex 3.00. All errors shown on the concordia diagrams and quoted in the data tables are at the 1σ level. Ages used for weighted average calculations are $^{238}U/^{206}Pb$ ages for analyses younger than 1000 Ma, and $^{207}Pb/^{206}Pb$ ages for analyses older than 1000 Ma. This distinction is employed due to the well documented reduction in precision of $^{207}Pb/^{206}Pb$ ages for younger zircons (e.g. Ireland et al., 1998; Collins et al., 2007).

Sample 187323 displayed appreciable concentrations of common Pb for analyses <1000 Ma, consistent with SHRIMP analysis of titanites from the same sample. Unfortunately, large variations in detected common Pb across spot analyses meant that an effective correction could not be applied using 'ComPbCorr'. This is most

likely due to a wide discordance in $^{208}Pb/^{232}Th$, perhaps as a result of secondary Th loss on selected grains during metamorphism as documented by Andersen (2002). The younger age data were thus modelled as a simple two-component mixture between radiogenic and common leads, as described previously. Both Yorkfit and robust regressions were fitted through the uncorrected $^{238}U/^{206}Pb$ vs. $^{207}Pb/^{206}Pb$ isotope ratios, but yielded extremely unrealistic and poorly constrained $^{207}Pb/^{206}Pb$ intercept values. Rather than resorting to modelled average terrestrial Pb, however, the composition of common Pb was assumed from the $^{207}Pb/^{206}Pb$ intercept (0.814) calculated from titanite data from the same sample. A Tera-Wasserburg regression through the uncorrected data was then anchored at this value, with the lower concordia intercept corresponding to the true radiogenic composition. One analysis recorded a high positive weighted residual (>2.5), suggesting that it had suffered Pb loss, while one other contained a high negative weighted residual, and may have been affected by inherited Pb.

7.4. Titanite descriptions

Details concerning titanite size, colour, morphology, distinguishing features and isotopic chemistry are summarised in Table 6. Samples 155731, 184495 and 187337 are derived from highly strained mylonites that display dramatic grain size reduction relative to their porphyritic granite protoliths, while sample 187323 is sourced from a moderately strained mylonite which retains numerous large (approximately 1–2 cm diameter) rotated feldspar augens. Despite these differences, most titanites share very similar appearances. They feature characteristically angular crystal habits, irregular shapes and light yellow to light orange-brown hues. They also have typically large size variations and are commonly inclusion-rich. None of the titanites showed any form of zonation when viewed under BSE.

Titanites from samples 155731, 187323 and 187337 appear as large, subhedral and approximately diamond-shaped porphyroblasts when viewed in thin section, while those from sample 184495 are usually smaller and dominantly anhedral. This distinction is reflected by the nature of fractures in each sample. While samples 155731, 187323 and 187337 are usually multiply fractured, they contain numerous examples which are predominantly intact. In addition, the fractured grains show strong evidence of abrasion. By contrast, all titanites from sample 184495 are pervasively fractured in very thin, linear arrays. This may be explained by their relatively high radiogenic enrichment (302 ppm ave.) compared to that of larger titanites from the remaining samples (27–69 ppm ave.). Like U-rich zircons, similarly enriched titanites are more likely to contain extensive microfracturing due to brittle lattice sites damaged by α radiation (Camacho et al., 1997; Corfu et al., 2003). This implies that the fracturing of the titanites relatively depleted in U is mechanical in origin, consistent with their being strongly abraded during shearing.

7.5. Zircon descriptions

Details concerning zircon size, colour, morphology, distinguishing features and Th/U ratios are summarised in Table 6. Samples 184464 and 184468 are derived from highly strained mylonites which display extensive grain

size reduction from their porphyritic Pitjantjatjara Supersuite igneous precursors, while sample 187325 has a similar protolith but is sourced from a fine-grained L–tectonite. Overall, these samples contain zircon grains with similar characteristics, being predominantly colourless, subrounded and fairly uniformly sized. Some acicular and tabular grains are preserved in samples 184468 and 187325, indicating varying degrees of morphological alteration. However, all samples show little evidence of fracturing or abrasion. In contrast, sample 187323 is sourced from a moderately strained mylonite as mentioned previously. It contains zircon grains which are extensively cracked and contain abundant opaque inclusions. They also vary significantly in size, and are predominantly lightly coloured. Numerous acicular grains are preserved, although subrounded morphologies are most common.

Zircon luminescence under CL is usually attributed to electronic transmissions of transition elements or trivalent rare earth elements when bombarded with electrons (Koschek, 1993; Corfu et al., 2003). Stronger emissions from these elements produce more intense, brighter colours, while radiation damage caused by the decay of U^{4+} may suppress CL response, resulting in darker colours. Different growth events in zircon are thus readily identified via characteristic CL responses. Samples 184464, 184468 and 187325 reveal high chaotic internal zoning when viewed under CL (Figure 10). In some cases, oscillatory zoned domains appear to be overprinted by patchy segments with variable luminescence. In others, convolutely zoned cores are mantled by thin concentric banding. Overall, however, most grains feature reasonably homogeneous or patchily zoned cores with low CL responses. They are enveloped by moderately luminescent, irregular rims, which in some cases extend deep into the core. As an exception, sample 184464 displays much darker rims with highly luminescent cores, and several grains with relatively featureless CL domains.

Sample 187323 displays much greater regularity in internal features when viewed under CL (Figure 11). Grain interiors are characterised by patchy or convolute zoning with moderate luminescence, usually mantled by distinct oscillatory zoned domains with overall low luminescence. Featureless dark cores are also occasionally present in some grains. However, all grains display highly luminescent rims of variable thickness, which are observed to either truncate concentric banding or irregularly contact homogeneous cores. A number of thick rims show ‘ghost’ textures, regions of subtle banding which appear to mimic the primary oscillatory zoning. In most cases, original zircon morphology is preserved, with numerous grains maintaining acicular habits. Several large fractures through individual grains also appear to have completely re-healed, and appear as brightly luminescent bands which intersect rim areas. The size and pervasiveness of these fractures suggests that they are mechanical in origin, although the preservation of whole zircon grains despite clean breaks through their width suggests that they formed in a low strain regime, perhaps late in the shearing history (Wayne & Sinha, 1988; Corfu et al., 2003).

7.6. SHRIMP titanite age data

Diagrammatic representations of SHRIMP titanite data for all samples are presented in Figures 12 and 13, and analytical data are provided in Table 4. The spatial distribution of all samples is also shown in Figure 14, along with their associated age estimates.

7.6.1. Sample 184495

Thirteen analyses of an equivalent number of titanite grains were conducted on sample 184495. Two analyses are excluded from a weighted average of the ^{204}Pb corrected ^{206}Pb/^{238}U ages (Figure 12a) on the basis that they are significantly discordant from the remainder of the data. This yields an age estimate of 539 ± 4 Ma, with an acceptable MSWD of 0.98. A linear regression through the uncorrected ^{238}U/^{206}Pb vs. ^{207}Pb/^{206}Pb isotope ratios produces an identical lower concordia intercept (539 ± 4 Ma) when plotted on a Tera-Wasserburg concordia diagram (Figure 12b). The MSWD (1.05) is again acceptable. Despite its much higher radiogenic composition, ^{204}Pb counts were not significantly increased in this sample relative to the remaining samples, reflecting its lower proportion of common Pb (*f* 204 = 0.08 ave.). However, it also indicates that the measurement of ^{204}Pb was still subject to large analytical (and isobaric) uncertainties, particularly given the high background counts on SHRIMP–B. Therefore, the agreement between the two age estimates probably reflects the negligible common Pb detected, greatly reducing the influence of an inaccurate ^{204}Pb correction.

7.6.2. Sample 187323

Fifteen analyses of an equivalent number of titanite grains were conducted on sample 187323. One analysis is excluded from a weighted average of the ^{204}Pb corrected ^{206}Pb/^{238}U ages (Figure 12c) on the basis that it is significantly discordant from the remainder of the data. This produces an age estimate of 575 ± 8 Ma, with a reasonable MSWD of 1.7. However, a Tera-Wasserburg plot of the uncorrected ^{238}U/^{206}Pb vs. ^{207}Pb/^{206}Pb isotope ratios (Figure 12d) yields a lower concordia intercept of 572 ± 7 Ma, with an improved MSWD of 1.19. The disagreement between these two age estimates is probably the result of a higher proportion of common Pb (*f* 204 = 0.18 ave.) relative to sample 184495. This increases the influence of the inaccurate ^{204}Pb correction, resulting in an undercorrected ^{238}U/^{206}Pb age estimate (given the strong positive correlation between *f* 204 and the corrected ^{238}U/^{206}Pb age). As a result, the lower concordia intercept is used as the best estimate of the true titanite age from this sample.

7.6.3. Sample 187337

Fourteen analyses of an equivalent number of titanite grains were conducted on sample 187337. One analysis is excluded from a weighted average of the ^{204}Pb corrected ^{206}Pb/^{238}U ages (Figure 12e) on the basis that it is significantly discordant from the remainder of the data. This generates an age estimate of 582 ± 22 Ma, with a poor MSWD of 3.9. A more tightly constrained estimate of the true titanite age is achieved by linear regression through the uncorrected ^{238}U/^{206}Pb vs. ^{207}Pb/^{206}Pb isotope ratios. When plotted on a Tera-Wasserburg concordia diagram (Figure 12f), this produces a lower concordia intercept of 573 ± 14 Ma, with a significantly improved MSWD of 1.9. The large discrepancy between the two age estimates is most likely caused by a higher proportion of common Pb in this sample (*f* 204 = 0.44 ave.), further increasing the effect of an inaccurate ^{204}Pb correction and shifting the ^{238}U/^{206}Pb corrected ages towards older values.

7.6.4. Sample 155731

Ten analyses of an equivalent number of titanite grains were conducted on sample 155731 during an alternate SHRIMP session (see Walker-Hallam, 2006). A weighted average of the ^{204}Pb corrected ^{206}Pb/^{238}U ages (Figure 13a) generates an age estimate of 523 ± 14 Ma, with an acceptable MSWD of 0.87. However, a Tera-Wasserburg plot of the uncorrected ^{238}U/^{206}Pb vs. ^{207}Pb/^{206}Pb isotope ratios (Figure 13b) yields a much older age (552 ± 12 Ma) estimated from the lower concordia intercept. Given that the MSWD (0.90) is basically indistinguishable from that of the weighted average calculation, the age discrepancy is best explained by strongly overcorrected ^{206}Pb/^{238}U ages. This is highlighted by relatively high proportion of common Pb in this sample (f 204 = 0.40 ave.), coupled with a strong negative correlation between f 204 and the corrected ^{238}U/^{206}Pb age. The lower concordia intercept age is thus the preferred age quoted in this study.

7.7. LA-ICPMS zircon age data

Diagrammatic representations of LA-ICPMS zircon data for all samples are presented in Figures 15–18, and analytical data are provided in Table 5. The spatial distribution of all samples is also shown in Figure 14, along with their associated age estimates.

7.7.1. Sample 187323

Fifty-two analyses of twenty-seven zircon grains were conducted on sample 187323, targeting both the weakly luminescent cores and highly luminescent rims. All age data are plotted on a conventional concordia and presented in a probability density distribution in Figure 15. Two distinct clusters are apparent at *c.* 553 Ma (corresponding to zircon rims) and *c.* 1161 Ma (corresponding to convolutely and oscillatory zoned cores). Rim analyses are extremely discordant, and plot on a linear array which approximates a common Pb trend. In contrast, core analyses define a linear Pb loss trend with concordant to moderately discordant components. A number of outliers (shown as grey ellipses in Figure 15a) are excluded from subsequent age calculations for one of two reasons. Firstly, several analyses showed clear mixing between different internal regions (i.e. core and rim), but with no resolvable parts of the spectrometry signal which could be isolated. This is largely the result of both the thickness of the rims (often <20 μm with a 30 μm beam diameter), and the high intensity of the laser beam (which was necessary to maintain sufficient counts, but often resulted in deeply excavated laser pits). Secondly, a small number of analyses (particularly outliers >1000 Ma) showed highly variable spectrometry signals with strong sensitivity to the selection used for isotopic measurements. In such cases, very little confidence could be assigned to the representative age, and thus these analyses are discarded.

A weighted average of the ^{206}Pb/^{238}U ages for rim analyses (Figure 15b) generates an age estimate of 553 ± 4 Ma, with an acceptable MSWD of 1.3. This is considerably older than the age estimated by linear regression through the uncorrected ^{238}U/^{206}Pb vs. ^{207}Pb/^{206}Pb isotope ratios. When plotted on a Tera-Wasserburg concordia

diagram (Figure 15c) and anchored to a common Pb composition estimated from SHRIMP titanite data from the same sample, a lower concordia intercept of 540 ± 4 Ma is produced from these data, with an identical MSWD of 1.3. This discrepancy is probably explained by the absence of an adequate ^{204}Pb correction to the ^{238}U/^{206}Pb ages, when it is clearly apparent that non-radiogenic Pb has been incorporated during the recrystallisation process. The effect of this common Pb is to give uncorrected ages that are too old. As such, the concordia intercept represents the best approximation of the true zircon rim age.

A weighted average of the ^{207}Pb/^{206}Pb ages for core analyses with >90% concordance (Figure 15d) produces an age estimate of 1161 ± 15 Ma, with an acceptable MSWD of 0.27. This is within error of a Model 1 solution for the discordia chord (Figure 15e), which yields an upper intercept age of 1170 ± 6 Ma and a lower intercept age of 204 ± 59 Ma, with an MSWD of 1.9. The upper concordia intercept age is used as the best estimate of the true zircon core age, as it takes into account a small number of concordant grains which have undergone minimal Pb loss.

7.7.2. Sample 187325

Twenty-one analyses of seventeen zircon grains were conducted on sample 187325, targeting both the homogeneous and convolutely zoned cores and moderately luminescent rims. All age data are plotted on a conventional concordia and presented in a probability density distribution in Figure 16a. Despite the wide variety in internal features revealed by CL, only a single age population is apparent at *c.* 1171 Ma. The majority of analyses define a linear Pb loss trend with concordant to moderately discordant components. One outlier (shown as a grey ellipse) is excluded from age calculations due to a highly variable spectrometry signal, as mentioned previously. A weighted average of the ^{207}Pb/^{206}Pb ages for analyses with >90% concordance (Figure 16b) produces an age estimate of 1171 ± 12 Ma, with an acceptable MSWD of 0.21. This is within error of a Model 1 solution for the discordia chord, which yields an upper intercept age of 1178 ± 13 Ma and a lower intercept age of 217 ± 160 Ma, with an MSWD of 0.71. As for the previous sample, a limited number of approximately concordant grains give the best estimate of the true zircon age, given that they have undergone minimal Pb loss. The concordia intercept age is thus the preferred age quoted for this sample.

7.7.3. Sample 184464

Fifteen analyses of an equivalent number of zircon grains were conducted on sample 184464, targeting both the highly luminescent featureless cores, patchily zoned domains and weakly luminescent rims. All age data are plotted on a conventional concordia and presented in a probability density distribution in Figure 17a. Like sample 187325, the wide variety of chaotic internal features viewed under CL did not correspond to any distinctive age brackets, with a single maxima at *c.* 1207 Ma. There is some evidence of a linear Pb loss trend, although the majority of analyses are situated on concordia. The ^{207}Pb/^{206}Pb age weighted average for analyses with >90% concordance (Figure 17b) produces an age estimate of 1207 ± 24 Ma, with an acceptable MSWD of

0.33. This is very similar to a Model 1 solution for the discordia chord, which yields an upper intercept age of 1209 ± 17 Ma and an MSWD of 0.82. However, it is evident that the majority of analyses are poorly constrained, most likely due to a low radiogenic content of the zircon grains (as indicated by the absence of strongly metamict cores). Coupled with the lack of well defined Pb loss trend, this means that the discordia intercept age is not representative of the true zircon age. Rather, there appears to be one quite distinct and another less distinct cluster of analyses on concordia, separated by approximately 60 Ma. The younger cluster contains the majority of analyses, and produces a concordant age of 1186 ± 5 Ma, with a good MSWD of 1.05 (Figure 17c). The older cluster is situated at approximately 1250 Ma, and does not appear to correspond to any distinctive CL domains.

7.7.4. Sample 184468

Twenty-eight analyses of twenty-one zircon grains were conducted on sample 184468, targeting both homogenous and convolutely zoned cores, and moderately luminescent rims. All age data are plotted on a conventional concordia and presented in a probability density distribution in Figure 18a. Like previous samples, no correspondence is found between different CL domains and resolvable age populations. A single maxima is apparent at 1177 Ma, with the majority of analyses displaying a linear Pb loss trend with concordant to moderately discordant components. Two analyses are also severely discordant. Three outliers are excluded from age calculations due to highly variable spectrometry signals and are shown as grey ellipses. A weighted average of the $^{207}Pb/^{206}Pb$ ages for analyses with >90% concordance (Figure 18b) produces an age estimate of 1175 ± 11 Ma, with an acceptable MSWD of 0.113. This agrees with a Model 1 solution for the discordia chord, which yields an upper intercept age of 1173 ± 5 Ma and a lower intercept age of -59 ± 79 Ma (effectively zero), with an MSWD of 0.41. The linear regression through the Pb loss trend well matches analyses with both severe and minimal discordance, indicating that the concordia intercept is an appropriate estimate of the zircon age. This is supported by its internal consistence with previous samples.

8. LA-ICPMS trace element analysis

Trace element data were collected from zircon and titanite samples that record evidence of Petermann-aged metamorphism for the purposes of thermometry and rare earth element (REE) chemistry. The integration of these datasets assists in placing titanite and zircon growth within a specific metamorphic context, thus providing a crucial link between U-Th-Pb age data and the conditions of paragenesis (e.g. Rubatto, 2002; Kelsey et al., 2007). Geochronology from titanite samples 184495, 187323, 187337 and 155731 is discussed Section 7, along with zircon sample 187323. Additional geochronology concerning Petermann-aged rims from zircon sample 155735 sourced from Spaghetti Hill is documented by Walker-Hallam (2006).

8.1. Operating procedures and data reduction

Trace element analysis of zircon and titanite mounts used for geochronology was performed at Adelaide Microscopy using an Agilent 7500cs ICPMS equipped with a New Wave 213 nm Nd-YAG laser. Titanite

analyses were conducted using a 55 μm beam diameter and 5 Hz repetition rate, and directly overprinted existing SHRIMP pits. Zircon analyses were performed on both core and rim domains using a 40 μm beam diameter and repetition rate of 5 Hz. For sample 155735, spot analyses overprinted existing SHRIMP pits, while for sample 187323 they were placed immediately adjacent to laser excavations. Total acquisition time for each analysis was 105 seconds, and involved 40 seconds of background measurement, 10 seconds for beam and crystal stabilisation, and 55 seconds of sample ablation. The NIST 610 glass standard was used for calibration, employing the coefficients of Pearce et al. (1997), and accuracy was monitored via repeat measurements of the NIST 612 glass standard. Data reduction was then performed using GLITTER software (Van Achterbergh et al., 2001). Internal calibration for both titanite and zircon was completed using measurements of ^{43}Ca (for titanite) and ^{178}Hf (for zircon) obtained via EMPA. Quantitative analyses were run at Adelaide Microscopy using a Cameca SX51 Microprobe with an accelerating voltage of 15 kV and beam current of 20 nA. Measurements of Ca and Hf were collected for each corresponding LA-ICPMS trace element analysis. All LA-ICPMS trace element data is provided in Tables 7 and 8, and the spatial distribution of samples is shown in Figures 4 and 14.

8.2. Trace element thermometry

In this study, temperatures estimated from trace element concentrations in accessory minerals utilise the Zr in sphene (titanite) thermometer of Hayden et al. (2006) and the Ti in zircon thermometer of Watson et al. (2006a). The application of these thermometers provides independent verification of the temperature of zircon and titanite formation, allowing comparison with additional temperature estimates obtained via alternative methods (e.g. mineral equilibria thermometry). The agreement or disagreement between such combined estimates assists in placing zircon and titanite paragenesis within a specific thermal context, and in establishing links between accessory minerals and the specific metamorphic assemblages with which they are associated.

Both trace element thermometers are based on the limited and temperature dependent exchangeability between the essential structural constituents of titanite and zircon, namely Ti and Zr. They are calibrated using the combined results of trace element analysis completed on natural and synthetic examples of these accessory minerals whose crystallisation conditions are independently constrained. The log-linear relationships between equilibrium Ti and Zr content (expressed in ppm by weight) and reciprocal absolute temperature (K) are presented below:

$$\log(\mathrm{Zr}_{\mathrm{sphene}}) = 10.59 - \frac{7857}{T} - \frac{920P}{T} \qquad (1)$$

$$\log(\mathrm{Ti}_{\mathrm{zircon}}) = (6.04 \pm 0.03) - \frac{5080 \pm 30}{T} \qquad (2)$$

As shown above, the Ti in zircon thermometer is completely independent of pressure, while Zr in sphene shows significant sensitivity to pressure, decreasing by a factor of approximately five in response to a pressure increase of 1 GPa (10 kbar). REE and F-Al substitutions also have negligible impact on Zr and Ti concentration, implying

that analytical uncertainties present the only limitation to temperature resolution (Hayden et al., 2006; Watson et al., 2006a). However, preliminary data indicate that these elements have relatively sluggish diffusivities, implying that zircon and titanite will generally record high closure temperatures and be relatively robust to later thermal disturbances (Watson et al., 2006b). Zr diffusivities in titanite appear to be slower than that of Pb but faster than that of REE, whereas Ti diffusion in zircon is predicted to be practically negligible at all crustal conditions, making it slower than both Pb and REE (Cherniak et al., 1997b; Cherniak & Watson, 2001; Cherniak, 2006; Watson et al., 2006a). This implies that temperature estimates generated using these thermometers may be decoupled from age estimates determined from U-Th-Pb geochronology, and from REE chemical signatures.

The application of the Zr in titanite thermometer in this study is based on average Zr content. However, the range in Zr concentration measured across each sample provides a maximum and minimum temperature range upon which the quoted error is largely based. Additional uncertainty is generated by the pressure dependence of the thermometer, and in each case, errors are calculated for pressure fluctuations ± 0.1 GPa for a reference pressure of 1 GPa. This contributes an error of approximately ± 11°C, and is significantly greater than the negligible influence of 1 sigma detection errors for each analysis (± 1–4°C). Overall, the combined uncertainties give a temperature resolution of ≤ 25°C.

Similarly, the application of the Ti in zircon thermometer is based on average Ti content. Again, the quoted error is largely based on the range in Ti concentration measured across each sample, which provides a maximum and minimum temperature range. However, due to the lower abundance of Ti in zircon relative to Zr in titanite, the 1 sigma detection errors for each analysis have a greater influence on the overall temperature uncertainty, generating errors of approximately 5–10°C. Uncertainties inherent in the thermometer calibration are also taken into account, and contribute errors of 11–13°C. Overall, the combined uncertainties give a temperature resolution of ≤ 34C.

8.3. Temperature estimates

8.3.1. Titanite temperature estimates

Temperature estimates for each titanite sample are presented in Table 9 and Figures 19 and 20. Overall, the calculated values are in reasonably close agreement with alternative temperature estimates produced via THERMOCALC modelling of equilibrium mineral assemblages (Figure 19). Sample 187323 records a temperature of 738 ± 10°C, which is within error of an average *T* estimate of 676 ± 70°C generated from the same sample. Similarly, the calculated temperature from sample 155731 (756 ± 21°C) is virtually indistinguishable from average *T* estimates of 739 ± 76°C and 760 ± 72°C from samples 155735 and 155733, sourced from the same outcrop. Temperature estimates from samples 184495 (759 ± 25°C) and 187337 (752 ± 12°C) also conform to the regional pattern of increasing temperatures towards the zone of migmatisation in southeast Bates.

8.3.2. Zircon temperature estimates

Temperature estimates for each zircon sample are presented in Table 9 and Figures 19 and 20. The calculated value from recrystallised rims on sample 187323 (714 ± 34°C) closely corresponds to the temperature determined from Zr content of titanite from the same sample (738 ± 14°C), and is again within error of a THERMOCALC average *T* estimate of 676 ± 70°C. However, the temperature estimated from rim regions on sample 155735 (795 ± 23°C) is significantly elevated compared to calculations based on the Zr content of titanite (756 ± 21°C) and equilibrium mineral assemblages (739 ± 76; 760 ± 72°C) from the same outcrop (Figure 19). Finally, there are minimal (≤ 9°C) differences between the calculated temperatures from core and rim domains in both samples.

8.4. REE analysis

Recent studies have demonstrated the usefulness of integrating U-Pb geochronology with REE analysis, in order to identify genetic links between zircon composition and specific metamorphic conditions, and to place both within a well constrained temporal framework (e.g. Rubatto, 2002). This is usually achieved by using distinctive REE patterns to identify equilibrium between metamorphic zircon and other major minerals, such as garnet and feldspar, thus deciphering the metamorphic conditions of zircon formation. This study employs a similar approach, but extends the usage of REE analysis to include both zircon and titanite, thereby allowing comparison between geochemical signatures which relate to two independent temporal constraints. Furthermore, it incorporates additional temperature information provided by trace element thermometry, thus providing a multi-faceted approach to establish the conditions and mechanisms behind zircon and titanite paragenesis.

8.4.1. Titanite REE chemistry

Chondrite-normalised REE patterns obtained from titanites used for geochronology (Figure 21a-d) show a number of distinguishing features. The most striking characteristic evident is the large variation in HREE slope across all samples. Samples 184495 and 187337 show dramatic HREE depletion (Lu_n/Sm_n = 0.07–1.05, ave. 0.36; 0.18–0.97, ave. 0.58) relative to sample 187323 (Lu_n/Sm_n = 1.02–3.04, ave. 1.96), while sample 155731 exhibits an approximately flat HREE pattern (Lu_n/Sm_n = 0.33– 1.58, ave. 0.83). LREE signatures are similarly variable, with marked depletion shown by samples 155731, 187323 and 187337 (Sm_n/La_n = 4.73–9.42, ave. 7.60; 6.92–25.53, ave. 11.94; 3.58–13.91, ave. 10.41) compared to sample 184495 (Sm_n/La_n = 1.30–4.94, ave. 3.04).

An additional distinguishing characteristic for all titanite samples is the magnitude of their negative Eu anomalies, calculated using $Eu/Eu^* = Eu_n /(Sm_n \times Gd_n)^{1/2}$, and positive Ce anomalies, calculated using $Ce/Ce^* = Ce_n /(La_n \times Pr_n)^{1/2}$ (Taylor & McClennan, 1985). Samples 155761, 187323 and 187337 show less pronounced Eu anomalies (Eu/Eu* = 0.56–0.94, ave. 0.74; 0.54–0.80, ave. 0.66; 0.64–0.95, ave. 0.82) relative to sample 184495

(Eu/Eu* = 0.32–0.76, ave. 0.58). In addition, single analyses in samples 187323 and 187337 display minor Ce anomalies (dashed lines) discordant with the remaining data.

8.4.2. Zircon REE chemistry

Chondrite-normalised REE patterns obtained from zircons used for geochronology (Figure 21e-f) exhibit a number of similar features to those mentioned above. In addition to distinctions between samples, however, there is also contrast between core and rim domains. The most prominent characteristic displayed by sample 187323 is the strong HREE enrichment of the core areas (Lu_n/Sm_n = 28–222, ave. 113) relative to the rims (Lu_n/Sm_n = 2–51, ave. 18). This is matched by a marked reduction of the negative Eu anomaly, such that cores show enhanced Eu depletion (Eu/Eu* = 0.14–0.34, ave. 0.21) compared to the recrystallised rims (Eu/Eu* = 0.43–0.58, ave. 0.50). A broad flattening of the LREE slope and overall depletion of the MREE is also apparent for rim areas. In contrast, positive Ce anomalies are similarly large across both domains (Ce/Ce* = 3–27, ave. 12; 4–23, ave. 11).

The strong partitioning of REE between core and rim in sample 187323 is not reflected by sample 155735. In this case, both domains exhibit a similarly strong HREE enrichment (Lu_n/Sm_n = 8–184, ave. 110; 8–305, ave. 86) and limited evidence of LREE or MREE flattening. There is, however, a marginal drop in the Eu anomaly (Eu/Eu* = 0.22–0.55, ave. 0.34; 0.23–0.83, ave. 0.52), and strong reduction of the Ce anomaly (Ce/Ce* = 1–74, ave. 31; 2–21, ave. 9) between core and rim. Nevertheless, the extent of apparent Ce depletion in recrystallised rims is heavily influenced by one analysis, and is probably much more conservative.

In contrast to the generally uniform trends exhibited by both samples, some analyses show extremely discordant signatures (dashed lines). Three analyses show dramatic LREE enrichment in sample 187323, while two analyses from the same sample and one from sample 155735 display severe LREE depletion.

9. Interpretation of results

9.1. P-T estimates

The pattern of increasing temperatures and pressures moving southwards through Bates is consistent with similar *P-T* trends documented in surrounding regions of the western Musgraves (Figure 22). Scrimgeour & Close (1999) report conditions of P = 9–10 kbar and T = 610–730°C from mylonitised granites of the Umutju Region, situated immediately south of the Woodroffe Thrust. These estimates are consistently lower than peak metamorphic conditions obtained from deep crustal granulitic mylonites in the Mann Ranges, which fall within the range P = 12–13 kbar and T = 700–750°C. Additional estimates indicate increasingly elevated conditions further south, moving into deeper crustal sections. Clarke et al. (1995) describe estimates of $P = 14 \pm 1$ kbar and $T \geq 750$°C in areas south of Bates, while Camacho et al. (1997) obtained estimates of *c.* 12 kbar and *c.* 650°C from eclogites in the Davenport Shear Zone, Musgrave Ranges.

Nevertheless, it must be noted that the above calculations employ considerably different approaches to thermobarometry, utilising a variety of mineral equilibria thermometers and barometers. Even those generated using THERMOCALC software (e.g. Scrimgeour & Close, 1999) rely on superseded activity models which may drastically affect *P-T* estimates. This suggests that the results of previous studies are not directly comparable to one another, nor to the products of this study. However, the correspondence between the calculations of White & Clarke (1997) and those generated using the updated THERMOCALC activity models employed in this study suggests that a reasonable parity exists between alternative thermobarometric methods. All except one recalculated assemblage were within error of the published results (see Table 3), and conformed to identical calculations performed on sample 184468, sourced from the same outcrop addressed by these authors. The general trend of increasing pressures and temperatures moving south of the Woodroffe Thrust can therefore be confidently purported as genuine.

9.2. Geochronological data

9.2.1. Titanite ages

Titanite grains are commonly aligned parallel to needles of biotite and hornblende which define the mylonitic foliation (see Figure 6d). This suggests that titanite formation originated during shearing, and thus the maximum age recorded by their U-Th-Pb systematics will correspond to the age of metamorphic crystallisation, rather than the diffusive resetting of protolith grains (Frost et al., 2000). However, more precise constraints on the timing of titanite growth can be achieved by considering its textural relationships to other minerals which comprise the metamorphic assemblage. The associations between titanite, ilmenite, plagioclase, garnet and clinozoisite suggest that titanite formation was controlled by reactions between these minerals. Titanite features iron oxide tails and contains abundant opaque inclusions, indicating that its Ti content is largely sourced from ilmenite replacement. It is also commonly in contact with plagioclase grains which display clinozoisite rims, suggesting that Ca is sourced from the breakdown of anorthite. This is consistent with the uniformly sodic composition of metamorphic plagioclase in all samples, compared to the more calcic composition of igneous grains. Furthermore, garnet rims feature an increase in grossular content (Walker-Hallam, 2006), and usually contain clinozoisite inclusions. This indicates that garnet production came at the expense of clinozoisite, and most likely occurred during prograde metamorphism. Titanite growth can thus be inferred from the following reaction:

$$\text{Ca-Pl} + \text{Czo} + \text{Ilm} + \text{Qtz} \rightarrow \text{Na-Pl} + \text{Ttn} + \text{Grt} \qquad (3)$$

Since this process involves the modification of prograde mineral assemblages, it appears likely that titanite formation occurred at peak metamorphic conditions. Nevertheless, it does not automatically follow that the timing of metamorphic crystallisation will be recorded by its U-Th-Pb systematics. If the closure temperature for titanite is below the peak conditions attained during metamorphism, then age estimates have the potential to reflect the cessation of Pb diffusion, rather than the timing of initial titanite growth. Frost et al. (2000) estimate a closure temperature of *c.* 660°C for grains with a diffusive radius of 100 μm and a cooling rate of 10°C/Ma,

while Cherniak & Watson (2001) calculate a temperature of *c.* 600°C using the same parameters. Given that trace element thermometry indicates temperatures in excess of 730°C for all titanite samples, it is quite plausible that their corresponding age estimates could coincide with cooling below Pb closure, rather than initial growth at peak metamorphic conditions.

The validity of the above inference depends crucially on two relationships. Firstly, diffusion radius increases with increasing grain size, allowing large grains to have higher closure temperatures relative to small grains (Frost et al., 2000; Cherniak & Watson, 2001). This raises the possibility that large grains may be impervious to Pb diffusion at temperatures approaching their crystallisation conditions, reducing the likelihood of age resetting. Secondly, effective diffusive volume decreases with increasing grain size. This is because diffusion operates most efficiently at grain boundaries. Pb transfer will thus be confined to the periphery of large grains, preserving significant internal volumes unaffected by diffusion. In contrast, Pb exchange in smaller grains will be much more extensive, allowing a volumetrically greater proportion to undergo re-equilibration. This has two important implications: (1) the core domains of large grains will be disconnected from diffusion pathways, preventing disruption to their initial U-Th-Pb systematics; (2) the core domains of small grains may be in direct communication with grain boundaries, making them vulnerable to Pb diffusion and resetting. In other words, age estimates from larger grains are more likely to coincide with crystallisation events, while those from smaller grains will usually reflect cooling below Pb closure.

Titanites from samples 187323 and 187337 are significantly larger (*c.* 500 μm ave. diameter) than those from sample 184495 (*c.* 200 μm ave.), while those from sample 155731 are intermediate between the two (*c.* 350 μm ave.). The effective diffusive radius on the largest grains (250 μm) is thus potentially 2.5 times greater than that on the smallest grains (100 μm), indicating that the former will have an appreciably elevated closure temperature relative to the latter. Furthermore, it is likely that the volumetric proportion affected by diffusion will be consistently lower for larger grains, increasing the probability of minimal disturbance to their U-Th-Pb systematics. Thus, assuming that all samples experienced similar cooling rates (and since the majority of SHRIMP analyses were positioned in core regions), it is predicted that their estimated ages should systematically reduce with decreasing grain size. This is precisely what is observed, and allows some constraints to be placed on the events recorded by their respective age determinations. Firstly, given their large grain size, age estimates from samples 187323 and 187337 (*c.* 570 Ma) are interpreted to reflect the timing of initial titanite crystallisation. This suggests that peak metamorphic temperatures were attained within 30 Ma of the onset of the Petermann Orogeny at 600 Ma (Wade et al., 2005). Secondly, geochronological data from samples 155735 (*c.* 550 Ma) and 184495 (*c.* 540 Ma) are interpreted to represent the progressively later timing of Pb closure as a function of decreasing grain size and increasingly extensive volumetric diffusion.

9.2.2. Zircon ages

The clear visual distinction between core and rim zones in sample 187323 suggests two discrete phases of zircon growth. This is borne out by the wide separation between their respective age populations. Core domains cluster at *c.* 1170 Ma, consistent with the timing of Pitjantjatjara Supersuite granite emplacement within the western

Musgraves (1215–1120 Ma; Edgoose et al., 2004; Bodorkos et al., 2006; Howard et al., 2006). Coupled with their characteristic convolute and oscillatory zoning, which is construed as a primary magmatic growth pattern, this suggests that the age determination from the core domains corresponds to the timing of igneous zircon formation within the Pitjantjatjara Supersuite granite protolith from which this mylonite sample is derived.

In contrast, rim domains return an age estimate of *c.* 540 Ma, correlating to deep crustal reworking during the Petermann Orogeny (600–520 Ma; Camacho & Fanning, 1995; Edgoose et al., 2004; Wade et al., 2005). The effect of Petermann-aged metamorphism on zircon growth appears to be limited to closed-system recrystallisation of protolith magmatic grains, rather than local dissolution and reprecipitation. This is revealed by the discrete partitioning of trace elements between core and rim domains. Th/U elemental ratios calculated from U-Th-Pb geochronology indicate a systematic decrease in Th/U between these zones. Figure 23 shows a distinct cluster of rim analyses with Th/U ratios <0.05 (grey shaded area), while their corresponding core analyses lie above 0.18. Such partitioning is commonly attributed to differential Th expulsion during metamorphism, as a result of its incompatibility within the zircon lattice relative to U (Cherniak et al., 1997a; Schaltegger et al., 1999; Hoskin & Schaltegger, 2003). Although some rim analyses have significantly higher Th/U ratios than the conventional cut-off for metamorphic zircon (*c.* 0.1), they remain systematically lower than core analyses from the same grain. This is consistent with the appearance of 'ghost' zoning on several of the zircon rims, which Hoskin & Black (2000) interpret as indicative of metamorphic recrystallisation in the solid state. They describe the diffusion of large radius atoms (including Th) away from the rim an important process by which lattice strain is reduced and zircon may be stabilised within an elevated thermal regime. In most cases, the extent of diffusion will be dependent on the relative enrichment of trace elements, and the extent of thermal modification to intra-crystalline elemental diffusivities.

All brightly luminescent rims are thus interpreted to represent closed-system solid-state metamorphic recrystallisation domains. Coupled with that fact that peak temperatures recorded in eastern Bates are well below the closure temperature for Pb volume diffusion in zircon (>900°C; Cherniak & Watson, 2001), this suggests that the age determined from zircon rims (*c.* 540 Ma) corresponds to the timing of peak metamorphism associated with the Petermann Orogeny. However, this estimate strongly disagrees with the crystallisation age recorded by titanites from the same sample (*c.* 570 Ma). It is therefore possible that zircon modification did not occur during peak metamorphism, perhaps due to strongly anhydrous conditions, and instead occurred in response to post-peak fluid infiltration (Harley & Kelly, 2007). A problem with this interpretation is that it requires zircon recrystallisation to occur without either additional titanite growth or diffusive resetting of pre-existing grains, whose chemical stability during fluid influx would be well below that of zircon. Furthermore, temperatures estimated from the zircon rims (*c*. 714°C) are drastically incompatible with the conditions inferred from Pb closure of titanite sample 184495 (*c.* 600°C) at an identical time (*c.* 540 Ma), suggesting that actual zircon recrystallisation occurred at a much later date. As such, the disparity between the two age estimates is attributed to a poorly constrained LA-ICPMS geochronological dataset, rather than a complex thermal or diffusive history. This is probably symptomatic of a spatial resolution issue, given the very thin diameter of the recrystallised domains. The titanite crystallisation age (*c.* 570 Ma) is thus retained as the best timing constraint for peak metamorphic conditions, as it precisely corresponds to the zircon age from sample 155735.

The irregular internal structures exhibited by samples 184464, 184468 and 187325 are consistent with high temperature (granulite facies) metamorphism, which has partially or completely obliterated the regular internal geometries of magmatic zircon. Chaotic textures are characteristic of late to post-magmatic crystallisation, while homogeneously dark domains are indicative of high trace element concentrations or metamictisation, which dull the CL response (Corfu et al., 2003). Given that the Petermann Orogeny did not attain granulite facies conditions, it is likely that these samples preserve features indicative of high temperature metamorphism approximately coeval with the emplacement of their Pitjantjatjara Supersuite granitic precursors. Granulite facies conditions were widespread during the Musgravian Orogeny (1225–1160 Ma; Camacho et al., 1997; Edgoose et al., 2004; Howard et al., 2006), throughout which the voluminous Pitjantjatjara Supersuite lithologies were emplaced. This is consistent with age maxima of *c.* 1186–1173 Ma obtained from these samples. An older age cluster from sample 184464 (situated at approximately 1250 Ma) does not appear to correspond to any distinctive CL domains, and may be representative of inherited xenocrystic grains.

The lower concordia intercept ages exhibited by samples 187323 and 187325 (*c.* 200 Ma) may represent a poorly constrained thermal pulse subsequent to Petermann times. However, it appears more likely that Pb loss was primarily driven by weathering processes, given the limited and progressive disruption to the U-Pb systematics. This is supported by the well constrained Pb-loss trend displayed by sample 184468, which shows no evidence of a marked thermal disturbance at any point in its history.

9.3. Trace element thermometry

9.3.1. Titanite temperature estimates

The slow diffusion of Zr in titanite implies that it should be retentive of Zr chemical signatures imprinted during crystallisation, and relatively robust to later thermal disruption (Cherniak, 2006). All temperature estimates obtained using the Zr in sphene thermometer are thus interpreted to represent the conditions of titanite growth. With this in mind, their generally good agreement with alternative temperature estimates based on the average *T* of equilibrium mineral assemblages reinforces the suggestion that titanite formation occurred at peak metamorphic conditions (*c.* 740–760°C). The large discrepancy exhibited by sample 187323 (*c.* 60°C) may indicate that thermal equilibration of the major minerals continued for a significant period of time following titanite crystallisation, allowing titanite to preserve an anomalously hot thermal signature compared to its corresponding mineral assemblage. Alternatively, the slightly lower temperature determination from this sample relative to the remaining samples may suggest that Zr was able to undergo limited diffusion following titanite crystallisation at peak metamorphic conditions. In this case, thermal equilibration of the major minerals must have occurred both simultaneously and subsequent to Zr closure, allowing the preservation of a lower temperature equilibrium assemblage. Both scenarios imply that sample 187323 experienced a slower cooling rate relative to the remaining samples, given that thermal equilibration of their mineral assemblages ceased at peak metamorphic conditions and their Zr concentrations were unaffected by diffusive re-equilibration.

9.3.2. Zircon temperature estimates

Diffusion of Ti in zircon is slower than Zr in titanite, implying a greater resistance to thermally-driven diffusive alteration and hence increased likelihood of preserving a Ti chemical signature representative of crystallisation conditions (Cherniak, 2006; Watson et al., 2006). As a result, it is unclear that the metamorphic recrystallisation of magmatic zircons will result in sufficient diffusive re-equilibration to alter its pre-existing thermal signature. This may explain the close agreement between temperature estimates obtained from core and rim domains of each zircon sample, which may both preserve Ti chemistry corresponding to the conditions of igneous crystallisation. However, it does not account for the large discrepancy (*c.* 80°C) in calculated temperatures between the two samples, given that they are sourced from similar granitic precursors. It is therefore possible that the anomalously high temperature determination from sample 155735 is due to Ti contamination. A common source of minor residual Ti is the gold coat applied to zircon mounts in preparation for ion microprobe analysis (Watson et al., 2006a). However, this is typically of very low concentration (*c.* 1 ppm), and thus unlikely to affect temperature estimates by more than ± 15°C. More significant concentrations of Ti are also present in reddish-brown oxide coatings on zircons extracted from weathered rock samples. Such coatings have the potential to penetrate into zircon fractures and contaminate Ti analyses (Watson et al., 2006a). Although sample 155731 was not strongly weathered, its extracted zircons were typically light tan in colour, suggesting that they may have contained a thin oxide film. Nevertheless, sectioning to half the original zircon width was performed to remove the outermost (potentially weathered) surface, and care was taken to avoid cracks when positioning trace element analyses.

The lack of probable Ti contaminants suggests that the inexplicably high temperature determination from sample 155735 genuinely represents an inherited thermal signature. If this is the case, then a reasonable constraint of *c.* 800°C can be placed on the temperature of granite crystallisation. Nevertheless, a similar interpretation is untenable for sample 187323, given that it would require crystallisation of an approximately equivalent lithology to have occurred at *c.* 710°C. This leaves the possibility that zircons extracted from this sample may have undergone extensive re-equilibration during Petermann-aged shearing, eradicating the previous thermal imprint. The 'ghost' zoning preserved in several of the recrystallised rims suggests that this may indeed be true, because at a bare minimum such texturing requires that the sluggish REE have undergone diffusion (Cherniak, 1997b). Furthermore, there is strong agreement between the temperature recorded by the rim domains and that estimated from the Zr content of titanites from the same sample. The problem of temperature inheritance is not as significant in this case, given that ample petrological and geochronological evidence confirms that the titanites have grown during shearing.

If the above interpretation is accepted, it lends further weight to the inference that the zircon and titanite samples experienced variable cooling rates. Samples 155735, 155731, 184495 and 187337 underwent rapid exhumation, preventing extensive re-equilibration of slowly diffusing elements such as Ti and Zr and preserving a thermal signature of crystallisation. Conversely, sample 187323 endured a much more gradual cooling history, allowing Ti and Zr diffusion to gain pace and eradicate a pre-existing thermal memory, and sustaining thermal equilibration of its corresponding mineral assemblage subsequent to the attainment of peak metamorphic conditions.

9.4. REE analysis

9.4.1. Titanite REE chemistry

The extent of HREE depletion exhibited by each titanite sample is correlated with the degree of garnet saturation in their respective equilibrium mineral assemblages. Garnet has a strong affinity for the small atomic radii HREE cations, and thus will scavenge these elements from other coexisting minerals (Schaltegger et al., 1999; Rubatto, 2002; Storkey et al., 2005). Samples 184495 and 187337 are heavily enriched in small (<1 mm) garnets, indicating their relative ease of growth during mylonitisation. In contrast, sample 187323 is relatively garnet-poor, with larger (1–2 mm) porphyroblasts being preserved in rare occurrences. This suggests that the primary mechanism for HREE partitioning was the concurrent growth of garnet. The relatively flat HREE signal exhibited by titanites from sample 155731, despite the absence of garnet from its mineral assemblage, may be explained by the presence of abundant garnet porphyroblasts in proximal areas of the shear zone from which it is sourced. This suggests that HREE scavenging is able to operate over considerable length scales, especially in relatively hydrous shear zones.

The characteristic LREE depletion pattern shown by all titanite samples is most likely indicative of the concurrent growth of clinozoisite. Unlike garnet, clinozoisite has a strong affinity for the large atomic radii LREE cations. It is also intimately associated with the formation of titanite, often occurring in contact with titanite grains (see Figure 6d) and as thin rims enveloping adjacent feldspars. The strong LREE depletion shown by samples 155731, 187323 and 187337 compared to sample 184495 may be explained by the lack of clinozoisite enrichment in the latter. This may indicate more extensive clinozoisite replacement by garnet, increasing LREE availability to the equilibrium chemical pool. Other potential LREE scavengers include allanite, a constituent of the mineral assemblage of sample 187337.

The existence of a negative Eu anomaly is typically interpreted to represent either the coexistence of feldspar phases, known sinks for Eu, or the relative depletion of Eu in the rock as a whole (Schaltegger et al., 1999; Rubatto, 2002). However, given that all samples had very similar granitic protoliths, the observed differences in Eu concentration are not attributed to inherited chemical signatures. Rather, the small anomalies exhibited by sample 155731, 187323 and 187337 may indicate that titanite did not form in equilibrium with feldspar. This is consistent with its paragenesis at peak metamorphic conditions in response to the breakdown of anorthite. The slightly larger anomaly shown by sample 184495 may therefore indicate that feldspar breakdown was not as extensive, resulting in reduced Eu release. This explains the relatively low proportion of titanite in this sample, given that reduced Ca availability would fundamentally restrict titanite growth. It also accounts for its dramatically enriched radiogenic composition (300 ppm U ave.) relative to the remaining samples (27–69 ppm U ave.), because U would be more strongly partitioned into individual grains within a small titanite population. Finally, the minor Ce anomalies exhibited by single analyses in sample 187323 and 187337 (dashed lines) may indicate small microinclusions of zircon within titanites, given that the remaining elements conform to the general REE pattern.

9.4.2. Zircon REE chemistry

The strong HREE enrichment exhibited by magmatically zoned core domains in sample 187323 suggests that they grew in the absence of garnet. This is consistent with the overall garnet-poor composition of their granitic protolith. Strong HREE depletion in the rim domains can thus be explained by zircon recrystallisation occurring at peak metamorphic conditions, after the growth of garnet during prograde metamorphism. This is supported by the flattening of the Sm anomaly between core and rim, which is indicative of increased Sm scavenging by garnet formation during mylonitisation. Given that zircon-garnet REE distribution coefficients favour the incorporation of HREE into zircon, it is likely that limited equilibration was achieved between these two phases, and furthermore, that zircon and garnet coexisted within a 'closed' system with a finite trace element reservoir (Schaltegger et al., 1999; Rubatto, 2002; Harley & Kelly, 2007). This may indicate either restricted chemical communication between zircon and garnet, or a relatively short duration of peak metamorphism, given that REE closure in zircon would rapidly occur following the onset of retrograde cooling (Cherniak, 1997b; Cherniak & Watson, 2001).

Further evidence of peak metamorphic recrystallisation of sample 187323 is indicated by the reduction of the negative Eu anomaly between core and rim. The enhanced Eu depletion of the core domains is consistent with primary magmatic zircon growth occurring in equilibrium with feldspar (Rubatto, 2002; Kelsey, 2007). However, it is likely that the replacement of anorthite during peak metamorphism (leading to titanite formation) triggered the release of Eu, allowing its subsequent incorporation into the recrystallised rim domains. This is consistent with the Eu enriched signature of titanites from the same sample.

The change in mineral equilibria between core and rim domains is matched by the overall flattening of the LREE slope, which is indicative of the expulsion of unstable large ionic radius cations from the recrystallised zircon lattice (Hoskin & Black, 2000). This is accompanied by overall depletion in the MREE, most likely related to the concurrent growth of MREE-rich titanite (Rubatto, 2002). However, the existence of a similar positive Ce anomaly across core and rim suggests that Ce-rich minerals such as apatite and clinozoisite were not extensively replaced during peak metamorphism, allowing the preservation of an inherited Ce signature. The extreme discrepancy and LREE enrichment shown by three analyses (dotted lines) is interpreted to represent small microinclusions of apatite in the zircon, while the strong LREE depletion shown by an additional two analyses may be indicative of xenotime inclusions.

The strong partitioning of REE between core and rim in sample 187323 is not reflected by sample 155735. Both domains exhibit a similarly strong HREE enrichment, despite the existence of abundant garnet in the peak metamorphic assemblage. Furthermore, there is limited evidence of LREE or MREE flattening, notwithstanding the widespread growth of titanite during mylonitisation. There is, however, a marginal drop in the negative Eu anomaly consistent with limited anorthite breakdown during titanite formation. Strong reduction of the positive Ce anomaly may also be indicative of the incorporation of apatite into the equilibrium mineral assemblage, or the restricted replacement of clinozoisite by garnet. However, the extent of apparent Ce depletion in rim domains is heavily influenced by one analysis, and is probably much more conservative.

The lack of distinctive REE partitioning exhibited by sample 155735 suggests that it preserves a strong memory of the protolith (igneous) zircon chemistry (Hoskin & Black, 2000). Its characteristic REE enrichment, jagged LREE and MREE patterns, negative Eu and positive Ce anomalies are all hallmarks of magmatic zircon. This is exemplified by its overall similarity with the core signature from sample 187323. Such limited REE diffusion during Petermann-aged mylonitisation is consistent with the lack of Zr partitioning discussed previously, which resulted in the preservation of an inherited thermal signature. It also explains the lack of 'ghost' texturing exhibited by the recrystallised rim domains. These combined observations again suggest that this sample experienced rapid cooling and exhumation, preventing extensive diffusion of the sluggish REE. It follows, therefore, that the extensive REE diffusion displayed by sample 187323 is indicative of a much slower cooling history. Evidently, however, both samples must have undergone Pb diffusion, in order to enable resetting of the U-Pb systematics during Petermann times. This is consistent with the much faster diffusivity of Pb compared to Zr and REE in zircon (Cherniak & Watson, 2001).

10. Discussion

10.1. Thermobarometric evolution and exhumation history of the Petermann Orogeny

The average geothermal gradient (defined as the ratio of temperature over depth) calculated from equilibrium mineral assemblages throughout Bates varies between *c.* 17–26°C km^{-1} (ave. *c.* 20°C km^{-1}), assuming a pressure gradient of 0.3 kbar per kilometre (Table 3). The lowest estimates are obtained in the immediate hanging wall to the Woodroffe Thrust, and become progressively higher moving south of this location. All estimates are comparable to gradients obtained from the Mann Ranges (*c.* 17°C km^{-1}; Scrimgeour & Close, 1999) and the Musgrave Ranges (*c.* 16–18°C km^{-1}; Camacho et al., 1997), situated in the same crustal block between the Woodroffe Thrust and Mann Fault (see Figure 22). Furthermore, they are compatible with current geothermal gradients in stable Proterozoic cratons, suggesting that the geotherm was not affected by transient heat sources during orogenesis (Lambert, 1983). This implies that cooling subsequent to peak metamorphism was dominantly controlled by exhumation (Camacho et al., 1997; Scrimgeour & Close, 1999). The increase in geothermal gradient moving south of the Woodroffe Thrust therefore suggests that deeper crustal sections experienced more rapid exhumation, preventing uniform thermal equilibration from being maintained during uplift and denudation. This agrees with the contrasting histories of Ti, Zr and REE diffusion retained by zircon and titanite samples. Higher crustal sections were able to effectively diffuse these trace elements during slow retrograde cooling, preserving lower thermal signatures and 'ghost' texturing in zircon rims. Conversely, lower crustal sections experienced complete diffusive closure at peak conditions due to more rapid cooling, recording thermal signatures of crystallisation in titanites and very limited re-equilibration of REE and Ti in zircons.

An estimate of the approximate cooling rate experienced during exhumation can be determined using the thermal and temporal separation between titanite formation and subsequent Pb closure. If the age and trace element temperature estimates from titanite grains with large diffusive radii are interpreted to represent the timing and metamorphic conditions of crystallisation, then a reasonable constraint of *c.* 740–760°C can be placed at *c.* 570

Ma. Similarly, if the age determined from titanite grains with smaller diffusive radii corresponds to the timing of cooling below Pb closure, then an estimate of *c.* 600–660°C can be placed at *c.* 540 Ma (Frost et al., 2000; Cherniak & Watson, 2001). This implies a temperature drop of *c.* 80–160°C in *c.* 30 Ma at an average rate of *c.* 3–5°C per million years, which is indicative of near-isobaric cooling (Harley & Kelly, 2007). It is nevertheless comparable to estimates obtained from the Musgrave Ranges using the discrepancy between garnet (Sm–Nd) and muscovite/biotite/K-feldspar (^{40}Ar–^{39}Ar) closure, which indicate an average rate of *c.* 3°C per million years between 630–530 Ma, and *c.* 4°C per million years between 525–490 Ma. This corresponds to an exhumation rate of *c.* 0.2 mm per year (Camacho et al., 1997). Given such a prolonged *P-T* evolution in both terranes, it is surprising that near-peak equilibrium mineral assemblages are preserved. This may indicate a non-linear cooling path, with rapid initial cooling and exhumation followed by a dramatic slowing towards the termination of orogenesis. In this case, average cooling rates would not be representative of short-lived fluctuations in the bulk exhumation history. An additional estimate of *c.* 23°C per million years between 550–535 Ma in the Musgrave Ranges (Camacho et al., 1997) suggests that episodic changes in the rate of exhumation may be applicable to the inferred thermobarometric evolution in Bates.

10.2. Fluid partitioning and zircon recrystallisation

The overall lack of Petermann-aged zircon recrystallisation throughout Bates is consistent with shearing conditions being dominantly anhydrous during this orogenic event. Zircon growth was thus suppressed during peak metamorphic conditions due to a lack of fluid infiltration, preserving evidence of Musgravian-aged granulite facies metamorphism. This is consistent with a number of metamorphic studies throughout the Musgrave Block, which note the general absence of partial melting in high grade terranes (Clarke et al., 1995; Camacho et al., 1997; Scrimgeour & Close, 1999). However, it is evident that discrete shear zones must have been associated with significantly elevated fluid influx, driving thermal diffusion of trace elements and the recrystallisation of relict magmatic zircons in the solid-state. This is supported by thermobarometric modelling of their associated equilibrium mineral assemblages, which indicate considerably elevated water activities ($a\mathrm{H_2O}$ = 0.75) compared to samples which show no evidence of Petermann-aged alteration ($a\mathrm{H_2O}$ = 0.25). Such shear zones are characterised by a higher proportion of hydrous phases, in contrast to the dominantly quartzofeldspathic (± clinopyroxene) assemblages of reactivated fabrics. Furthermore, they contain limited evidence of migmatisation, which further suggests that water activities must have been significantly elevated in order to allow partial melting of a granitic bulk composition at 700–750°C (Clemens & Vielzeuf, 1987).

The partitioning of fluid into discrete shear zones suggests that fluid pathways were restricted between mylonitised domains. This is despite the pre-existence of structural conduits produced during Musgravian-aged deformation, implying that the shear zones possessed a complex structural arrangement and relationship to fluid sources in the deep crust. It is unlikely that significant influx was generated from the dehydration of Mesoproterozoic granites, because such lithologies preserve a high proportion of relict igneous hornblende and biotite in outcrops adjacent to mylonitic shear zones. Magmatic sources are also inappropriate, given that no igneous suites of an equivalent age have been identified in the western Musgraves (Scrimgeour & Close, 1999;

Edgoose et al., 2004). This highlights the enigmatic nature of fluid infiltration into lower crustal volumes within intracontinental settings, since external sources such as subduction are clearly precluded. As such, the penetration of meteoric fluids and underthrusting of juvenile sedimentary rocks are two possibilities that should be considered as viable alternatives (Miller & Cartwright, 1997; Cartwright & Buick, 1999; Clark et al., 2006).

10.3. Strain partitioning within mylonitic shear zones

The correlation between distinctive structural arrangements and different strain gradients is commonly reported in mylonitic shear zones (e.g. Curtis, 1998; Bailey et al., 2004; Pereira & Silva, 2004). In such cases, highly variable structural fabrics and linear elements may develop within discrete rock packages in response to a single deformational event. Such variability is usually attributed to simultaneous pure and simple shearing, which results in the progressive partitioning of strain into coaxial and non-coaxial components (Fossen & Tikoff, 1993, 1998; Jiang et al., 2001). Higher strains will result in dominantly non-coaxial deformation, producing rotational kinematics where linear fabrics (e.g. stretching lineations) develop parallel to the bulk shearing direction. In contrast, lower strains will characteristically produce coaxial deformation, where material extends perpendicular to the shortening direction and linear elements are thus aligned in this orientation. Intermediate between these two strain end-members is a spectrum of deformational modes which correspond to incremental changes in strain gradient and orientation of finite strain axes, resulting in the progressive rotation of linear fabrics between axes orthogonal and parallel to the bulk shearing direction (Fossen & Tikoff, 1993, 1998; Dewey et al., 1998).

The juxtaposition of contrasting structural patterns is clearly observed at Heather's Hill (Figure 5). Highly strained mylonitic zones display well-developed rotational kinematics, with asymmetric sigma clasts consistently recording top to the southwest tectonic transport. Conversely, weakly strained protomylonitic zones exhibit symmetrical flattening fabrics, with prominent mineral stretching lineations (plunging southeast) developed parallel to fold hinges and perpendicular to the inferred shearing direction in high strain zones. Two hypotheses are available to explain the disagreement between the alignment and type of structural elements in these two domains. Firstly, protomylonitic zones preserve evidence of an earlier, weaker phase of deformation, which has been subsequently overprinted by the discrete development of an intense mylonitic fabric. Each structural arrangement can thus be attributed to a single, temporally distinct deformational event with contrasting strain characteristics, resulting in the superposition of linear markers with highly discrepant orientations. Secondly, both structural domains developed simultaneously in response to progressive strain partitioning within a single shear system. High strain zones were dominated by simple shear, and generated rotational kinematics and stretching lineations parallel to the bulk shearing vector. Alternatively, protomylonitic zones were dominated by pure shear, and involved a component of extension perpendicular to the shortening direction and parallel to the extrusion direction of fold hinges.

A crucial observation which allows the latter hypothesis to be preferred over the former is the progressive change in orientation of the stretching lineation between high and low strain zones (Figure 5b). If two distinct deformational events had resulted in the juxtaposition of linear fabrics with highly oblique angular relationships,

some evidence of overprinting or truncation would be expected. Instead, however, there is a clearly defined progression between both southeast- and southwest-plunging lineations. The gradual rotation of linear markers is thus interpreted to represent an incremental change in orientation of the principal axes of the finite strain ellipsoid (Figure 24). The maximum principal strain (*X*) axis would be perpendicular to the bulk shearing direction (NW/SE) within the pure shear system, and parallel (NE/SW) within the simple shear system.

The identification of progressive strain partitioning within mylonitic shear zones affected by the Petermann Orogeny has important implications for structural patterns observed in areas of the western Musgraves directly adjacent to Bates (see Figure 1). In particular, it may assist in determining the origin of linear fabrics oriented at a high angle to the predominant regional alignment. Figure 25 is a compilation of measurements from Petermann-aged mylonitic foliations and stretching lineations in the eastern Bates Sheet (this study), the western and eastern Mann Ranges in the NTGS Petermann Ranges 1:250 000 Sheet (Scrimgeour et al., 1999), and the Angatja Region in the PIRSA Mann 1:250 000 Sheet (Hallett, 2007). It shows a marked similarity in the structural arrangement of these domains. The western Mann Ranges is perhaps the most appropriate analogue to Bates, with similar subhorizontal west- to southwest- and east- to northeast-plunging stretching lineations on fabrics which dip variably southeast to southwest. It also contains a distinct group of south-plunging lineations attributed to reverse dip-slip movement within an overall north-vergent compressional system (Scrimgeour & Close, 1999; Edgoose et al., 2004). This interpretation is largely based on pervasive south-plunging stretching lineations recorded in the eastern Mann Ranges, south of the Mount Charles Thrust, which exhibit north vergent kinematic indicators. No equivalent indicators are reported from the western Mann Ranges, but it has been suggested that the progressive development of west to southwest-plunging lineations within this region is indicative of strain partitioning into both dip-slip and strike-slip movement during dextral transpression (Scrimgeour & Close, 1999; Edgoose et al., 2004).

Regional strike-slip tectonics, however, are irreconcilable with the structural arrangement in Bates, where top to the southwest kinematics are consistently observed on fabrics dipping shallowly to moderately southeast. Rather than invoking multiple phases of deformation in order to explain this kinematic and structural divergence, it is possible that the progressive switching of deformational modes proposed for Heather's Hill is more widely applicable within the western Musgraves. This would imply that the origin of linear fabrics developed at a high angle to the prevailing NE/SW orientation observed in both Bates and the western Mann Ranges may be related to progressive coaxial strain partitioning within an overall non-coaxial shear system. In other words, the south-plunging stretching lineations reported in both these regions do not correspond to north-vergent emplacement of the Petermann Nappe Complex, because they do not originate parallel to the bulk tectonic movement of the shear system. Rather, they develop at an oblique angle to the pervasive southwest shearing vector, with their precise orientation determined by an intermediate strain intensity involving both pure and simple shear components. This is not to say that all south-plunging lineations within the western Musgraves are generated as a direct result of strain partitioning. Evidently, the north-vergent kinematic indicators observed in the eastern Mann Ranges attest that linear fabrics within this region developed parallel to north-south compression, and are thus representative of the bulk tectonic transport of the Petermann Orogen. Nevertheless, in areas further west of this location, where equivalent kinematics indicate that the bulk shearing vector was oriented NE-SW, it is quite

feasible that south-plunging lineations developed oblique to the inferred tectonic transport direction in response to a stronger component of pure shear, and not as a result of either dip-slip movement or a separate deformational phase.

10.4. Structural and tectonic evolution of the Petermann Orogeny

In the previous section, a mechanism was discussed which potentially explains the contrasting structural organisation of sections of Bates and the western Mann Ranges. Both regions appear to be dominantly shaped by pervasive simple shearing in a NE-SW orientation, but nevertheless feature discrete domains which are characterised by progressive strain partitioning into both pure and simple shear components. This conclusion, however, has limited applicability to the macroscopic architecture of the Petermann Orogen as a whole (Jones et al., 2005). Primarily, this is because the southwest-directed transport inferred from widespread shear zones within the western Musgraves appears incompatible with the gross tectonic development of this orogenic system. Numerous studies have established that the majority of shortening during the Petermann Orogeny was accommodated by north-directed overthrusting along the south-dipping Woodroffe Thrust, resulting in the exhumation of deeply buried rocks and the exposure of a high pressure orogenic core in its hanging wall (Stewart, 1997; Scrimgeour & Close, 1999; Edgoose et al., 2004). Furthermore, the Petermann Nappe Complex, located further north, incorporates interleaved basement and cover successions which contact the essentially undeformed foreland sequences of the Amadeus Basin. The emplacement of this crustal-scale thrust stack involved over 100 km of north-vergent shortening in response to north-south compression of the Australian plate (Lambeck & Burgess, 1992; Sandiford et al., 2001; Flöttmann et al., 2004). In short, there is seemingly incontrovertible evidence that both Bates and the western Mann Ranges, situated in the hanging wall to the Woodroffe Thrust, must have undergone north-directed tectonic transport during the Petermann Orogeny.

The question of how to resolve the apparently contradictory kinematic partitioning throughout the western Musgraves has a number of possible answers, three of which will be considered here. The first two attribute its current kinematic expression to the superposition of multiple deformation episodes. In this case, the juxtaposition of conflicting transport vectors is either the product of an extensive overprinting pattern, or the passive incorporation of pre-deformed structural blocks into an actively evolving orogenic system. Presumably, southwest-directed shearing would represent the earlier phase of deformation that is passively carried, given that the bulk structural architecture of the orogen in which it is preserved records north-directed transport. The opposite is true for a systematic overprinting pattern, given that southwest-directed superposition would reflect limited regional reworking subsequent to orogenesis. An immediate problem with the latter interpretation is that no definitive overprinting relationships are observed, either in Bates or the western Mann Ranges. Admittedly, this could be due to the relatively limited exposure of these terranes, decreasing the likelihood of such relationships being readily identifiable. Indeed, it is a persistent frustration for any explanation of kinematic partitioning that neither a progressive nor discrete shift between the opposing shearing vectors has been observed.

Nevertheless, a more significant criticism of temporally separated structural juxtaposition is that geochronological data acquired in this study does not resolve into two distinct deformational phases. As documented earlier, the spread of ages across *c.* 570–540 Ma is interpreted to represent a progressive cooling history, rather than the stepped growth or recrystallisation of accessory phases. As such, it does not reveal any evidence of thermal or deformational pulses within the Petermann Orogeny. Furthermore, no suggestion of episodic behaviour has been recognised in additional studies in the Mann Ranges (Scrimgeour et al., 1999; Edgoose et al., 2004), or in surrounding regions of the Musgrave Block (Maboko et al., 1992; Camacho & Fanning, 1995; Sun et al., 1996; Camacho et al., 1997). This is equally true of the thermobarometric history retained by metamorphic mineral assemblages throughout Bates, which largely agree with *P-T* trends established in both the western (potentially southwest-directed) and eastern (north-directed) Mann Ranges (Scrimgeour & Close, 1999). In all cases, the recrystallised assemblages are restricted to shear zones and evidently synkinematic, ruling out the possibility of a disjunction between deformation and metamorphism. Nevertheless, the disagreement between the preservation of deep crustal assemblages and a prolonged *P-T* evolution inferred from average cooling rates may indicate a non-linear cooling history punctuated by short-lived deformational episodes (Wade et al., 2005). Whether such phases could be correlated to distinctive structural expressions is another matter entirely. Based solely on the overlap between geochronological data obtained from various parts of the western Musgraves, this appears unlikely.

Evidently, the structural, metamorphic and geochronological framework of the western Musgraves does not easily lend itself to interpretations involving two distinct phases of deformation during the Petermann Orogeny. This leaves the third possibility that its contrasting kinematic expressions developed synchronously. In order to evaluate this hypothesis appropriately, it is necessary to consider the overall structural geometry of the Woodroffe Thrust, along which the divergence in tectonic movement must have occurred. In plan view, the Woodroffe Thrust is characterised by a pronounced lobate outline throughout the western Musgraves (Figures 1 and 2), which is convex towards the foreland (in the direction of vergence). This curved geometry is matched by a lateral variation in structural trends. In the eastern Mann Ranges, situated at the point of initial curvature, the structural grain is oriented directly perpendicular to the bulk shortening direction of the orogen. Mylonitic fabrics invariably dip shallowly to moderately south, and are associated with subhorizontal south-plunging stretching lineations (Figure 25a). In the western Mann Ranges, thrust curvature becomes much more pronounced and the structural grain rotates slightly west. Mylonitic fabrics define a corrugated fold profile which plunges subhorizontally WSW (Figure 25b), suggesting a component of NNW/SSE shortening normal to the thrust trace in this region. Finally, at the western edge of the lobe, Bates exhibits increased strike rotation towards the west, with fold corrugations plunging shallowly southwest (Figure 25c). Like the western Mann Ranges, there is good correspondence between the best fit pole to the fold profile plane (Beta axis) and the greatest population of lineation data. This suggests that stretching lineations in both regions developed synchronously with fold corrugations, and potentially represent extension orthogonal to the shortening direction of the orogenic system. In each case, this inferred spreading direction is parallel to the lobate outline of the Woodroffe Thrust.

There is clearly a marked difference in the structural arrangement of regions directly south of an anomalous curvature exhibited by the Woodroffe Thrust. This is consistent with the structural complexity exhibited by other

orogenic belts which contain curved thrust traces, such as the Appalachians and the western Alps (Dietrich, 1989; Marshak & Tabor, 1989). Several models have been proposed which attribute this curvature to bending, shearing and shortening mechanisms largely controlled by bulk rheology, pre-existing structural obstacles, and regional variations in sediment thickness (Marshak et al., 1992; Ferrill & Groshong, 1993). In each case, however, all material movement is ultimately governed by the bulk tectonic transport of the orogenic system. This appears incompatible with the kinematic record observed in the western Musgraves. The consistent identification of southwest-directed tectonic transport in Bates, and a similar kinematic development proposed for the western Mann Ranges, suggests that their evolution cannot be ascribed to a simple thrust mechanism in which movement is uniformly orogen parallel.

The failure of conventional thrust curvature models to adequately account for kinematic partitioning in the western Musgraves highlights the need for an orogenic mechanism which links the anomalous geometry of the Woodroffe Thrust to heterogeneous deformation in its hanging wall. An additional challenge is to successfully integrate this mechanism into a combined understanding of the tectonic development of the Petermann Orogen as a whole. With this in mind, a potential orogenic model will now be considered which attributes the kinematically and structurally distinct evolution of this region to the westward propagation of a spreading thrust sheet. It is proposed that the progressive rotation of the gross regional lineation pattern, from orogen-parallel adjacent to the approximately linear trace of the Woodroffe Thrust to highly oblique at the point of its greatest curvature further west, represents a change in the trajectory of material flow caused by lateral escape towards the orogen margin. In this scenario, the arcuate expansion of the overriding thrust sheet was accompanied by gravitational collapse, resulting in the widespread movement of material away from its net transport direction towards the north. The interaction of this ductile material with the relatively rigid upper crustal sections in the footwall may have generated shortening orthogonal to the curved thrust trace, resulting in the development of broad fold corrugations and the extrusion of material towards the southwest. Pervasive extensional deformation was thus produced in the hanging wall whose kinematic polarity is decoupled from the bulk tectonic transport of the orogen.

The existence of anomalously oblique lineation arrays throughout Bates and the western Mann Ranges, coupled with the lobate geometry of the nearby Woodroffe Thrust, suggests that both areas were affected by gravity spreading. Similar lineation patterns are also observed in the Angatja Region, south of the eastern Mann Ranges, accompanied by a regional spread of mylonitic fabrics which define a southwest-plunging fold profile (Figure 25d). However, the very discrete nature of deformation is in this domain is indicative of highly focused strain in competent rock units, which is not readily compatible with widespread extrusional escape. This suggests that the extent of thrust spreading, which is intimately linked to the development of pervasive regional deformation, may be ultimately controlled by strength contrasts induced by lithospheric weakening.

The development of kinematic partitioning within broad thrust sheets is not unique to the Petermann Orogen. Several examples have been documented worldwide in which gravitational instabilities and lateral extrusion produce divergent rock flow during thrust emplacement. These include the Moine Thrust in northwest Scotland (Thigpen et al., 2007), the Caledonides in northeast Greenland (Andresen et al., 2007) and the Kaoko Belt in

northwest Namibia (Goscombe et al., 2002). In each case, contemporaneous strain fields in different vertical and horizontal sections of the crust are highly discrepant, and not necessarily representative of the bulk tectonic evolution or kinematic expression of the orogenic system. This emphasises the fact that the existence of regional southwest-directed tectonic transport in areas of the western Musgraves affected by extrusional flow remains compatible with the overall north-directed emplacement of the Petermann Nappe Complex at the same time.

Unlike its distinctive kinematic expression, however, the metamorphic record of gravity spreading is not as easily distinguished from the bulk exhumation history of Petermann Orogen. As mentioned previously, similar trends in *P-T* conditions are apparent in Bates and the western Mann Ranges compared to areas further east, where thrust emplacement has evidently been unaffected by lateral extrusion. Furthermore, average geothermal gradients calculated within Bates are comparable to those from both the Mann and Musgrave Ranges. There is thus no distinctive record of opposing material flow into lower crustal levels during thrust emplacement, nor an apparent record of contrasting particle paths. This is despite the overall slow rate of exhumation, which should permit thermal equilibration to be maintained at all levels of the uplifted slab. However, it should be remembered that this parameter is both poorly constrained and necessarily generalised, and is probably not representative of the exhumation history at smaller temporal scales.

Besides its lack of a distinctive metamorphic imprint, another criticism of the gravity spreading orogenic mechanism is the absence of north-vergent kinematics in either Bates or the western Mann Ranges. The high pressure (*c.* 10–14 kbar) metamorphic architecture of these regions suggests that southwest-directed extrusion involved substantial parts of the ductile lower crust. Nevertheless, higher crustal sections should be expected to preserve evidence of the ultimately north-directed emplacement of the Petermann Nappe Complex along the Woodroffe Thrust. It is therefore problematic that north-vergent kinematics have not been identified in its immediate hanging wall (Scrimgeour & Close, 1999; Edgoose et al., 2004). There are two possible explanations which may mitigate this dilemma. Firstly, it is possible that north-vergent kinematics do actually exist in these areas, but have not been identified due to extremely limited exposure. Secondly, north-directed thrust emplacement may have been transferred to the Wankari Detachment Zone (Figure 1), north of the Woodroffe Thrust, which does exhibit north- to northwest-vergent structures along its western edge (Edgoose et al., 2004; Flöttmann et al., 2004). In this case, gravitational collapse could have pervasively affected the deep crustal rocks in the hanging wall of the Woodroffe Thrust, but had little effect on overall thrust emplacement along an adjacent crustal boundary. Further study of field relationships throughout the western Musgraves, in particular the detailed mapping of regional lineation arrays, is needed to decide which (if any) of these options is most valid.

11. Conclusion

The main findings of this study are:

- The western Musgraves are characterised by pervasive mylonitic deformation which formed at deep crustal levels (P = 10–13 kbar and T = 700–780°C);

- Peak metamorphic conditions were attained at *c.* 570 Ma and were followed by cooling to *c.* 600–660°C by *c.* 540 Ma, at an average rate of *c.* 3–5°C per million years;
- Cooling was largely driven by slow uplift and denudation, although contrasting records of trace element diffusion and thermal equilibration suggest that deeper crustal sections experienced more rapid exhumation;
- Shearing conditions were dominantly anhydrous, but discrete shear zones feature increased water activities consistent with a complex pattern of fluid partitioning;
- Distinctive structural arrangements developed in response to changes in strain intensity, with simultaneous pure and simple shearing resulting in the progressive partitioning of coaxial and non-coaxial strain components into discrete rock packages;
- Oblique regional lineation arrays and reverse polarity tectonic transport vectors suggest that north-directed emplacement of the Petermann Nappe Complex along the Woodroffe Thrust involved substantial extrusion of deep crustal material towards the southwest. The westward spreading of this broad thrust towards the orogen margin was followed by gravitational collapse, producing an anomalous lobate thrust trace geometry.

12. Acknowledgements

First and foremost, I thank my supervisors, Alan Collins and Martin Hand, for all their assistance and guidance, both in the field and back in Adelaide. I am also grateful to the Ngaanyatjarra Council and the people of the Blackstone and Wingellina communities for allowing access to their lands. Many thanks must go to GSWA for providing generous logistical and financial support for this project. In particular, Hugh Smithies, Paul Evins and Trevor Holland are thanked for their great help and camaraderie out in the field, and Simon Bodorkos and Mike Wingate for their assistance on the SHRIMP and patient answers to countless questions about the perils of geochronology. I am greatly indebted to Ben Wade and Justin Payne for all their help on the laser, and to Angus Netting and Peter Self from Adelaide Microscopy for all their technical expertise. Dot Close and Ian Scrimgeour of NTGS are thanked for providing structural data from the Mann Ranges, and for being very willing to assist my interpretation. Thanks must also go to Rian Dutch, Kathryn Cutts, Katie Howard, Ailsa Schwarz, Althea Walker, Michael Spzunar and Kate Selway, and the Honours students of 2007, particularly Kylie Matonia and Lachlan Hallett. The Australian Institute of Geoscientists is gratefully acknowledged for providing a generous Honours bursary. Oh yeah, and Rodney King is thanked for being the rude, smelly bastard I had to put up with for five weeks, and who proved time and time again that real men don't drink soy milk. Last but by no means least, I thank my family, in particular Ashlea Doolette for all her support and dedication throughout the year, and most importantly for giving me something worthwhile to aim for.

Appendix 1 – Microprobe analyses used for *P-T* estimates

Sample 184464

	Grt core	Grt rim	Bt core	Bt rim	Hbl core	Hbl rim	Cpx core	Cpx rim	Ksp core	Ksp rim	Pl core	Pl rim	Mag	Spl
SiO_2	37.40	37.54	36.35	36.04	40.57	39.86	50.90	50.14	64.75	63.94	61.94	62.58	0.04	0.05
TiO_2	0.05	0.09	4.68	4.28	1.68	1.94	0.18	0.19	0.03	0.01	0.04	0.00	0.08	13.75
Al_2O_3	21.11	21.01	14.14	14.44	12.13	12.08	3.56	3.48	18.98	18.75	22.55	23.38	0.09	0.07
Cr_2O_3	0.00	0.02	0.00	0.00	0.00	0.00	0.00	0.00	0.04	0.00	0.03	0.00	0.01	0.00
FeO	25.68	25.94	14.68	14.99	16.47	17.88	12.58	11.68	0.32	0.20	0.17	0.07	94.88	77.47
MnO	1.96	1.95	0.01	0.02	0.01	0.04	0.15	0.22	0.00	0.00	0.06	0.00	0.00	0.00
MgO	3.66	3.59	14.92	15.39	10.39	10.27	9.84	11.02	0.01	0.02	0.03	0.01	0.00	0.08
CaO	9.36	9.46	0.06	0.06	11.59	11.24	19.26	20.76	0.03	0.02	3.63	4.60	0.00	0.04
Na_2O	0.01	0.00	0.02	0.08	1.54	1.26	2.31	1.68	1.36	1.01	9.14	9.05	0.03	0.00
K_2O	0.01	0.00	8.93	8.32	1.72	1.75	0.01	0.02	13.31	14.92	0.22	0.23	0.02	0.01
Totals	99.41	99.78	93.83	93.87	96.41	96.97	99.30	99.84	98.90	98.92	97.85	99.93	102.19	95.38
Oxygens	12	12	11	11	23	23	6	6	8	8	8	8	4	4
Si	2.96	2.97	2.75	2.72	6.20	6.07	1.93	1.89	2.99	2.98	2.80	2.77	0.00	0.00
Ti	0.00	0.01	0.27	0.24	0.19	0.22	0.01	0.01	0.00	0.00	0.00	0.00	0.00	0.41
Al	1.97	1.96	1.26	1.28	2.19	2.17	0.16	0.15	1.03	1.03	1.20	1.22	0.00	0.00
Cr	0.00	0.00	0.00	0.00	0.00	0.00	0.00	0.00	0.00	0.00	0.00	0.00	0.00	0.00
Fe^{3+}	0.10	0.10	0.02	0.14	0.35	0.72	0.15	0.19	0.01	0.01	0.01	0.00	1.99	1.17
Fe^{2+}	1.60	1.62	0.91	0.80	1.75	1.56	0.25	0.18	0.00	0.00	0.00	0.00	1.00	1.41
Mn	0.13	0.13	0.00	0.00	0.00	0.01	0.01	0.01	0.00	0.00	0.00	0.00	0.00	0.00
Mg	0.43	0.42	1.69	1.73	2.37	2.33	0.56	0.62	0.00	0.00	0.00	0.00	0.00	0.01
Ca	0.79	0.80	0.01	0.01	1.90	1.83	0.78	0.84	0.00	0.00	0.18	0.22	0.00	0.00
Na	0.00	0.00	0.00	0.01	0.46	0.37	0.17	0.12	0.12	0.09	0.80	0.78	0.00	0.00
K	0.00	0.00	0.86	0.80	0.34	0.34	0.00	0.00	0.78	0.89	0.01	0.01	0.00	0.00
Sum	8.00	8.00	7.77	7.73	15.74	15.62	4.00	4.00	4.94	5.00	5.00	5.01	3.00	3.00

Sample 184468

	Grt core	Grt rim	Bt core	Bt rim	Hbl core	Hbl rim	Cpx core	Cpx rim	Ksp core	Ksp core	Ksp rim	Pl core	Pl rim	Ilm
SiO_2	37.27	37.04	34.83	35.54	40.44	40.86	50.17	49.68	63.34	63.45	64.25	63.84	63.45	0.01
TiO_2	0.08	0.06	5.42	6.08	1.97	2.05	0.18	0.13	0.00	0.00	0.01	0.03	0.02	46.18
Al_2O_3	20.85	20.88	13.54	13.29	12.01	11.63	2.22	3.17	18.43	18.70	18.60	21.85	23.09	0.00
Cr_2O_3	0.00	0.00	0.04	0.00	0.00	0.00	0.00	0.00	0.06	0.04	0.00	0.00	0.00	0.00
FeO	31.25	28.16	22.90	21.71	20.24	20.24	16.74	14.09	0.18	0.14	0.18	0.15	0.29	50.97
MnO	1.12	1.50	0.04	0.09	0.11	0.13	0.14	0.15	0.04	0.00	0.00	0.00	0.03	0.37
MgO	2.74	2.32	9.15	9.01	8.11	8.07	8.83	9.42	0.00	0.00	0.01	0.00	0.01	0.05
CaO	7.66	9.90	0.04	0.12	11.23	11.18	19.10	20.29	0.01	0.08	0.01	3.29	3.89	0.00
Na_2O	0.01	0.00	0.07	0.07	1.76	1.59	1.71	1.50	1.36	0.76	1.10	9.83	9.77	0.00
K_2O	0.01	0.03	8.09	9.13	1.74	1.72	0.02	0.01	14.50	14.65	14.88	0.11	0.13	0.00
Totals	101.29	100.13	94.12	95.04	97.86	97.69	99.66	98.94	97.96	97.86	99.06	99.11	100.71	98.69
Oxygens	12	12	11	11	23	23	6	6	8	8	8	8	8	3
Si	2.94	2.95	2.74	2.76	6.20	6.27	1.93	1.91	2.98	2.98	2.99	2.84	2.79	0.00
Ti	0.01	0.00	0.32	0.36	0.23	0.24	0.01	0.00	0.00	0.00	0.00	0.00	0.00	0.89
Al	1.94	1.96	1.26	1.22	2.17	2.10	0.10	0.14	1.02	1.04	1.02	1.15	1.20	0.00
Cr	0.00	0.00	0.00	0.00	0.00	0.00	0.00	0.00	0.00	0.00	0.00	0.00	0.00	0.00
Fe^{3+}	0.17	0.15	0.00	0.00	0.28	0.26	0.16	0.15	0.01	0.01	0.01	0.01	0.01	0.21
Fe^{2+}	1.89	1.72	1.51	1.41	2.31	2.33	0.38	0.31	0.00	0.00	0.00	0.00	0.00	0.88
Mn	0.08	0.10	0.00	0.01	0.01	0.02	0.01	0.01	0.00	0.00	0.00	0.00	0.00	0.01
Mg	0.32	0.28	1.07	1.04	1.85	1.84	0.51	0.54	0.00	0.00	0.00	0.00	0.00	0.00
Ca	0.65	0.84	0.00	0.01	1.85	1.84	0.79	0.84	0.00	0.00	0.00	0.16	0.18	0.00
Na	0.00	0.00	0.01	0.01	0.52	0.47	0.13	0.11	0.12	0.07	0.10	0.85	0.83	0.00
K	0.00	0.00	0.81	0.91	0.34	0.34	0.00	0.00	0.87	0.88	0.88	0.01	0.01	0.00
Sum	8.00	8.00	7.72	7.73	15.78	15.71	4.00	4.00	5.00	4.97	4.99	5.01	5.03	2.00

Sample 184484

	Grt core	Grt rim	Grt core	Grt rim	Bt core	Hbl core	Hbl rim	Hbl core	Cpx core	Cpx rim	Ksp core	Ksp rim	Ksp core	Pl core	Pl rim	Mag	Spl
SiO_2	36.87	37.02	36.81	37.05	37.28	41.79	40.58	41.08	51.51	51.85	63.63	64.24	62.90	62.34	59.09	0.02	0.00
TiO_2	0.01	0.00	0.21	0.04	5.44	1.81	1.55	1.86	0.13	0.08	0.04	0.02	0.01	0.00	0.01	0.09	16.23
Al_2O_3	21.82	21.50	21.23	21.02	13.51	12.10	13.25	11.65	1.65	1.61	18.42	18.50	18.53	24.19	24.01	0.24	0.09
Cr_2O_3	0.05	0.00	0.00	0.07	0.00	0.05	0.02	0.00	0.00	0.03	0.01	0.00	0.00	0.07	0.02	0.17	0.03
FeO	26.60	26.25	27.48	25.49	12.81	12.40	12.76	13.29	8.58	9.33	0.29	0.31	0.17	0.15	1.89	93.95	73.83
MnO	1.19	1.04	2.40	2.37	0.15	0.10	0.11	0.11	0.19	0.15	0.01	0.00	0.00	0.03	0.00	0.02	0.06
MgO	5.84	6.14	5.57	5.48	15.85	13.65	12.95	12.45	13.76	13.87	0.00	0.04	0.02	0.00	0.38	0.09	0.27
CaO	6.56	6.62	6.71	6.82	0.04	11.72	11.46	11.58	22.13	22.05	0.11	0.08	0.03	5.41	5.17	0.02	0.03
Na_2O	0.00	0.00	0.00	0.02	0.03	1.53	1.37	1.35	0.83	0.71	1.00	1.17	1.00	8.84	7.18	0.06	0.00
K_2O	0.00	0.04	0.00	0.02	9.63	1.72	1.96	1.89	0.00	0.01	14.99	14.83	15.30	0.13	0.33	0.00	0.00
Totals	99.22	98.89	100.89	98.62	94.74	97.32	96.56	95.59	99.20	100.11	98.55	99.24	98.00	101.18	98.29	101.63	93.87
Oxygens	12	12	12	12	11	23	23	23	6	6	8	8	8	8	8	4	4
Si	2.90	2.92	2.87	2.94	2.78	6.18	6.07	6.24	1.93	1.93	2.98	2.98	2.97	2.74	2.68	0.00	0.00
Ti	0.00	0.00	0.01	0.00	0.31	0.20	0.18	0.21	0.00	0.00	0.00	0.00	0.00	0.00	0.00	0.00	0.49
Al	2.03	2.00	1.95	1.97	1.19	2.11	2.34	2.09	0.07	0.07	1.02	1.01	1.03	1.25	1.28	0.01	0.00
Cr	0.00	0.00	0.00	0.00	0.00	0.01	0.00	0.00	0.00	0.00	0.00	0.00	0.00	0.00	0.00	0.01	0.00
Fe^{3+}	0.17	0.17	0.28	0.15	0.00	0.51	0.60	0.40	0.12	0.12	0.01	0.01	0.01	0.01	0.07	1.98	1.01
Fe^{2+}	1.59	1.56	1.52	1.55	0.80	1.02	1.00	1.29	0.15	0.18	0.00	0.00	0.00	0.00	0.00	0.99	1.47
Mn	0.08	0.07	0.16	0.16	0.01	0.01	0.01	0.01	0.01	0.01	0.00	0.00	0.00	0.00	0.00	0.00	0.00
Mg	0.69	0.72	0.65	0.65	1.76	3.01	2.88	2.82	0.77	0.77	0.00	0.00	0.00	0.00	0.03	0.01	0.02
Ca	0.55	0.56	0.56	0.58	0.00	1.86	1.84	1.88	0.89	0.88	0.01	0.00	0.00	0.26	0.25	0.00	0.00
Na	0.00	0.00	0.00	0.00	0.00	0.44	0.40	0.40	0.06	0.05	0.09	0.11	0.09	0.75	0.63	0.00	0.00
K	0.00	0.00	0.00	0.00	0.92	0.32	0.37	0.37	0.00	0.00	0.90	0.88	0.92	0.01	0.02	0.00	0.00
Sum	8.00	8.00	8.00	8.00	7.78	15.68	15.68	15.69	4.00	4.00	5.00	5.00	5.02	5.01	4.97	3.00	3.00

Sample 184486 B

	Grt core	Grt rim	Grt core	Bt core	Bt rim	Bt core	Ksp core	Ksp rim	Pl core	Pl rim	Mag
SiO_2	37.38	37.16	37.21	35.92	36.17	35.72	64.04	63.03	63.11	62.31	0.13
TiO_2	0.00	0.02	0.03	5.47	5.60	5.21	0.01	0.02	0.03	0.04	0.07
Al_2O_3	21.69	21.11	21.72	14.42	14.42	14.48	18.58	18.48	23.28	23.13	0.15
Cr_2O_3	0.01	0.00	0.00	0.01	0.00	0.00	0.00	0.00	0.01	0.00	0.02
FeO	27.67	27.29	26.36	14.81	15.11	14.98	0.09	0.23	0.23	0.39	93.05
MnO	1.32	1.20	1.01	0.04	0.01	0.02	0.00	0.00	0.02	0.00	0.01
MgO	5.30	5.22	4.92	13.62	13.67	14.11	0.01	0.00	0.01	0.03	0.01
CaO	6.77	7.33	8.20	0.03	0.02	0.06	0.01	0.04	4.38	4.43	0.03
Na_2O	0.03	0.06	0.03	0.05	0.05	0.00	0.84	0.70	9.10	9.12	0.00
K_2O	0.00	0.00	0.03	9.29	9.38	9.02	15.24	15.34	0.15	0.14	0.01
Totals	100.46	99.73	99.77	93.67	94.44	93.60	98.84	97.88	100.34	99.64	100.36
Oxygens	12	12	12	11	11	11	8	8	8	8	4
Si	2.92	2.93	2.92	2.74	2.74	2.72	2.99	2.97	2.78	2.77	0.01
Ti	0.00	0.00	0.00	0.31	0.32	0.30	0.00	0.00	0.00	0.00	0.00
Al	2.00	1.96	2.01	1.30	1.29	1.30	1.02	1.03	1.21	1.21	0.01
Cr	0.00	0.00	0.00	0.00	0.00	0.00	0.00	0.00	0.00	0.00	0.00
Fe^{3+}	0.17	0.20	0.16	0.00	0.00	0.00	0.00	0.01	0.01	0.01	1.98
Fe^{2+}	1.64	1.60	1.58	0.94	0.96	0.96	0.00	0.00	0.00	0.00	1.00
Mn	0.09	0.08	0.07	0.00	0.00	0.00	0.00	0.00	0.00	0.00	0.00
Mg	0.62	0.61	0.58	1.55	1.54	1.60	0.00	0.00	0.00	0.00	0.00
Ca	0.57	0.62	0.69	0.00	0.00	0.01	0.00	0.00	0.21	0.21	0.00
Na	0.00	0.01	0.01	0.01	0.01	0.00	0.08	0.06	0.78	0.79	0.00
K	0.00	0.00	0.00	0.91	0.91	0.88	0.91	0.92	0.01	0.01	0.00
Sum	8.00	8.00	8.00	7.76	7.76	7.77	4.99	5.00	5.00	5.01	3.00

Sample 185674

	Grt core	Grt rim	Grt core	Grt rim	Bt core	Bt rim	Ksp core	Ksp rim	Ksp core	Pl core	Pl rim	Mag	Mag	Mag
SiO_2	37.08	36.57	36.62	36.20	38.31	38.30	62.16	64.08	62.73	62.78	62.97	0.12	0.17	0.04
TiO_2	0.01	0.00	0.03	0.02	2.42	2.89	0.00	0.00	0.00	0.00	0.03	0.07	0.05	0.04
Al_2O_3	21.39	21.38	21.65	20.85	12.13	12.37	18.04	18.41	18.27	23.05	22.88	0.08	0.10	0.01
Cr_2O_3	0.00	0.02	0.00	0.04	0.00	0.01	0.00	0.08	0.00	0.00	0.00	0.00	0.00	0.00
FeO	28.44	27.13	27.90	28.14	15.80	15.48	0.05	0.00	0.03	0.13	0.16	92.00	92.97	94.55
MnO	1.44	1.66	1.39	1.57	0.03	0.07	0.00	0.00	0.00	0.00	0.06	0.00	0.02	0.05
MgO	4.12	3.94	3.92	3.64	16.08	15.37	0.00	0.01	0.00	0.00	0.00	0.01	0.00	0.00
CaO	7.19	7.47	7.66	7.65	0.00	0.00	0.03	0.01	0.00	3.76	3.56	0.03	0.03	0.02
Na_2O	0.09	0.06	0.00	0.03	0.08	0.08	0.97	1.01	0.91	8.55	8.90	0.07	0.06	0.21
K_2O	0.00	0.01	0.01	0.04	9.36	9.21	15.28	15.03	15.02	0.13	0.12	0.02	0.06	0.03
Totals	100.04	98.45	99.44	98.53	94.49	93.89	96.55	98.65	96.98	98.40	98.70	99.23	100.35	102.06
Oxygens	12	12	12	12	11	11	8	8	8	8	8	4	4	4
Si	2.93	2.93	2.91	2.91	2.89	2.91	2.98	2.99	2.98	2.81	2.81	0.01	0.01	0.00
Ti	0.00	0.00	0.00	0.00	0.14	0.17	0.00	0.00	0.00	0.00	0.00	0.00	0.00	0.00
Al	1.99	2.02	2.03	1.98	1.08	1.11	1.02	1.01	1.02	1.22	1.20	0.00	0.00	0.00
Cr	0.00	0.00	0.00	0.00	0.00	0.00	0.00	0.00	0.00	0.00	0.00	0.00	0.00	0.00
Fe^{3+}	0.17	0.13	0.15	0.20	0.15	0.05	0.00	0.00	0.00	0.01	0.01	1.99	1.99	2.01
Fe^{2+}	1.71	1.69	1.70	1.69	0.85	0.93	0.00	0.00	0.00	0.00	0.00	0.99	0.99	0.97
Mn	0.10	0.11	0.09	0.11	0.00	0.01	0.00	0.00	0.00	0.00	0.00	0.00	0.00	0.00
Mg	0.49	0.47	0.46	0.44	1.81	1.74	0.00	0.00	0.00	0.00	0.00	0.00	0.00	0.00
Ca	0.61	0.64	0.65	0.66	0.00	0.00	0.00	0.00	0.00	0.18	0.17	0.00	0.00	0.00
Na	0.01	0.01	0.00	0.01	0.01	0.01	0.09	0.09	0.08	0.74	0.77	0.01	0.00	0.02
K	0.00	0.00	0.00	0.00	0.90	0.89	0.93	0.90	0.91	0.01	0.01	0.00	0.00	0.00
Sum	8.00	8.00	8.00	8.00	7.82	7.80	5.03	5.00	5.00	4.96	4.97	3.00	3.00	3.00

Sample 185679

	Grt core	Grt rim	Grt rim	Grt core	Bt core	Bt core	Bt rim	Ksp core	Ksp rim	Ksp core	Pl core	Pl rim	Mag	Spl
SiO_2	37.74	37.72	37.42	37.72	40.15	40.58	39.17	64.62	67.39	64.07	64.27	63.88	0.06	0.08
TiO_2	0.03	0.00	0.03	0.05	0.27	0.31	1.68	0.04	0.00	0.02	0.00	0.00	0.02	14.91
Al_2O_3	21.50	21.78	21.66	21.48	13.20	13.00	13.51	18.61	16.57	18.54	22.84	22.47	0.24	0.05
Cr_2O_3	0.03	0.06	0.02	0.08	0.04	0.03	0.00	0.00	0.00	0.00	0.00	0.00	0.00	0.09
FeO	28.49	29.35	29.21	27.78	9.05	8.29	9.09	0.24	0.19	0.60	0.05	0.09	93.92	76.27
MnO	0.70	0.75	0.84	1.08	0.06	0.08	0.00	0.00	0.03	0.12	0.00	0.00	0.00	0.37
MgO	5.92	5.76	5.19	5.11	22.77	22.85	20.71	0.02	0.02	0.11	0.00	0.00	0.02	0.06
CaO	5.49	5.08	4.72	7.02	0.01	0.03	0.02	0.00	0.03	0.08	3.67	3.41	0.00	0.08
Na_2O	0.00	0.00	0.02	0.04	0.04	0.06	0.11	0.93	0.63	1.86	9.75	10.02	0.04	0.00
K_2O	0.33	0.00	0.05	0.00	9.63	9.52	9.59	14.85	14.30	14.02	0.15	0.08	0.02	0.02
Totals	100.53	100.71	99.24	100.59	95.39	94.90	94.03	99.35	99.18	99.51	100.73	99.95	101.29	95.63
Oxygens	12	12	12	12	11	11	11	8	8	8	8	8	4	4
Si	2.94	2.94	2.96	2.94	2.90	2.93	2.87	2.99	3.10	2.97	2.82	2.82	0.00	0.00
Ti	0.00	0.00	0.00	0.00	0.02	0.02	0.09	0.00	0.00	0.00	0.00	0.00	0.00	0.44
Al	1.97	2.00	2.02	1.98	1.12	1.11	1.17	1.02	0.90	1.01	1.18	1.17	0.01	0.00
Cr	0.00	0.00	0.00	0.01	0.00	0.00	0.00	0.00	0.00	0.00	0.00	0.00	0.00	0.00
Fe^{3+}	0.17	0.12	0.06	0.13	0.08	0.08	0.08	0.01	0.01	0.02	0.00	0.00	1.99	1.10
Fe^{2+}	1.68	1.80	1.88	1.68	0.46	0.43	0.47	0.00	0.00	0.00	0.00	0.00	1.00	1.43
Mn	0.05	0.05	0.06	0.07	0.00	0.01	0.00	0.00	0.00	0.01	0.00	0.00	0.00	0.01
Mg	0.69	0.67	0.61	0.60	2.45	2.46	2.26	0.00	0.00	0.01	0.00	0.00	0.00	0.00
Ca	0.46	0.42	0.40	0.59	0.00	0.00	0.00	0.00	0.00	0.00	0.17	0.16	0.00	0.00
Na	0.00	0.00	0.00	0.01	0.01	0.01	0.02	0.08	0.06	0.17	0.83	0.86	0.00	0.00
K	0.03	0.00	0.01	0.00	0.89	0.88	0.90	0.88	0.84	0.83	0.01	0.00	0.00	0.00
Sum	8.00	8.00	8.00	8.00	7.93	7.91	7.87	4.98	4.90	5.01	5.01	5.02	3.00	3.00

Sample 187305

	Grt core	Grt rim	Bt core	Bt rim	Hbl core	Hbl rim	Ksp core	Ksp rim	Ksp core	Pl core	Pl rim	Mag	Ilm
SiO_2	36.50	36.81	36.20	36.01	39.36	39.36	64.07	63.70	63.66	62.25	62.07	0.09	0.03
TiO_2	0.03	0.04	4.12	4.18	1.22	1.49	0.03	0.01	0.02	0.00	0.00	0.09	51.30
Al_2O_3	20.40	20.71	13.73	13.36	12.09	12.27	18.70	18.56	18.35	23.71	23.42	0.27	0.00
Cr_2O_3	0.00	0.04	0.00	0.00	0.03	0.00	0.00	0.00	0.05	0.00	0.00	0.03	0.00
FeO	28.50	27.91	21.58	21.58	21.24	21.29	0.18	0.20	0.30	1.41	1.30	95.40	45.12
MnO	2.66	3.67	0.23	0.11	0.25	0.23	0.00	0.00	0.07	0.00	0.00	0.06	1.29
MgO	1.94	1.73	10.12	10.40	7.37	7.18	0.00	0.00	0.01	0.01	0.02	0.01	0.06
CaO	9.88	9.53	0.02	0.00	11.08	11.14	0.01	0.00	0.02	4.81	4.47	0.01	0.02
Na_2O	0.05	0.03	0.06	0.06	1.77	1.71	1.18	1.05	1.02	8.59	8.37	0.00	0.00
K_2O	0.00	0.00	9.36	9.31	2.02	1.97	14.95	14.66	15.01	0.13	0.17	0.02	0.00
Totals	100.39	100.82	95.42	95.02	96.80	96.98	99.15	98.22	98.55	99.56	98.62	103.02	97.86
Oxygens	12	12	11	11	23	23	8	8	8	8	8	4	3
Si	2.91	2.93	2.80	2.80	6.15	6.14	2.98	2.98	2.98	2.77	2.78	0.00	0.00
Ti	0.00	0.00	0.24	0.24	0.14	0.18	0.00	0.00	0.00	0.00	0.00	0.00	1.00
Al	1.92	1.94	1.25	1.22	2.23	2.26	1.02	1.02	1.01	1.24	1.24	0.01	0.00
Cr	0.00	0.00	0.00	0.00	0.00	0.00	0.00	0.00	0.00	0.00	0.00	0.00	0.00
Fe^{3+}	0.26	0.20	0.00	0.00	0.43	0.38	0.01	0.01	0.01	0.00	0.00	1.98	0.01
Fe^{2+}	1.64	1.65	1.40	1.40	2.35	2.40	0.00	0.00	0.00	0.00	0.00	1.00	0.97
Mn	0.18	0.25	0.02	0.01	0.03	0.03	0.00	0.00	0.00	0.00	0.00	0.00	0.03
Mg	0.23	0.21	1.17	1.21	1.72	1.67	0.00	0.00	0.00	0.00	0.00	0.00	0.00
Ca	0.85	0.81	0.00	0.00	1.86	1.86	0.00	0.00	0.00	0.23	0.22	0.00	0.00
Na	0.01	0.01	0.01	0.01	0.54	0.52	0.11	0.10	0.09	0.74	0.73	0.00	0.00
K	0.00	0.00	0.93	0.92	0.40	0.39	0.89	0.88	0.90	0.01	0.01	0.00	0.00
Sum	8.00	8.00	7.80	7.81	15.85	15.82	5.00	4.99	5.00	4.99	4.97	3.00	2.00

Sample 187314

	Grt core	Grt rim	Bt core	Bt rim	Bt core	Bt rim	Ksp core	Ksp rim	Pl core	Pl rim	Mag	Mag
SiO_2	37.14	36.76	35.74	34.89	35.21	34.31	64.69	64.76	62.11	61.77	5.07	1.00
TiO_2	0.00	0.00	2.90	3.03	3.60	3.52	0.03	0.00	0.03	0.01	0.01	0.07
Al_2O_3	20.88	21.07	17.23	16.89	16.88	17.03	18.71	18.43	23.91	24.26	0.03	0.56
Cr_2O_3	0.00	0.00	0.00	0.01	0.00	0.00	0.00	0.00	0.07	0.01	0.00	0.00
FeO	28.66	27.87	20.42	19.09	20.26	21.10	0.12	0.14	0.03	0.15	88.30	91.95
MnO	6.43	6.79	0.20	0.19	0.15	0.27	0.01	0.04	0.04	0.00	0.02	0.00
MgO	2.67	2.22	9.86	9.38	9.31	9.30	0.00	0.00	0.00	0.00	0.00	0.21
CaO	4.55	5.27	0.01	0.07	0.00	0.13	0.01	0.00	5.35	5.06	0.03	0.00
Na_2O	0.02	0.02	0.05	0.05	0.03	0.04	0.53	0.58	8.78	8.58	0.00	0.00
K_2O	0.00	0.01	9.46	9.21	9.61	7.83	15.77	15.85	0.08	0.15	0.11	0.39
Totals	100.51	100.19	95.88	92.83	95.06	93.70	99.89	99.83	100.39	100.01	99.25	100.94
Oxygens	12	12	11	11	11	11	8	8	8	8	4	4
Si	2.97	2.95	2.72	2.74	2.71	2.67	2.99	3.00	2.75	2.74	0.19	0.04
Ti	0.00	0.00	0.17	0.18	0.21	0.21	0.00	0.00	0.00	0.00	0.00	0.00
Al	1.97	1.99	1.55	1.56	1.53	1.56	1.02	1.01	1.25	1.27	0.00	0.03
Cr	0.00	0.00	0.00	0.00	0.00	0.00	0.00	0.00	0.00	0.00	0.00	0.00
Fe^{3+}	0.10	0.11	0.00	0.00	0.00	0.09	0.00	0.01	0.00	0.01	1.62	1.92
Fe^{2+}	1.82	1.76	1.30	1.25	1.31	1.28	0.00	0.00	0.00	0.00	1.18	0.99
Mn	0.44	0.46	0.01	0.01	0.01	0.02	0.00	0.00	0.00	0.00	0.00	0.00
Mg	0.32	0.27	1.12	1.10	1.07	1.08	0.00	0.00	0.00	0.00	0.00	0.01
Ca	0.39	0.45	0.00	0.01	0.00	0.01	0.00	0.00	0.25	0.24	0.00	0.00
Na	0.00	0.00	0.01	0.01	0.00	0.01	0.05	0.05	0.75	0.74	0.00	0.00
K	0.00	0.00	0.92	0.92	0.95	0.78	0.93	0.94	0.01	0.01	0.01	0.02
Sum	8.00	8.00	7.80	7.77	7.79	7.70	4.99	5.00	5.01	5.00	3.00	3.00

Sample 187323

	Grt core	Bt core	Bt rim	Hbl core	Hbl rim	Hbl core	Hbl rim	Hbl core	Hbl rim	Pl core	Pl rim	Mag	Mag
SiO_2	36.72	34.65	34.64	37.99	37.86	38.52	37.73	37.76	37.73	63.85	63.02	0.05	0.03
TiO_2	0.11	2.31	2.34	0.73	0.37	0.67	0.65	0.68	0.58	0.00	0.00	0.04	0.19
Al_2O_3	20.28	14.63	15.28	12.72	12.83	12.52	12.58	13.08	13.13	23.99	23.07	0.15	0.09
Cr_2O_3	0.01	0.00	0.02	0.07	0.06	0.04	0.00	0.00	0.00	0.00	0.00	0.00	0.06
FeO	20.25	25.14	24.84	26.08	26.56	25.44	25.07	25.64	25.20	0.13	0.15	94.71	93.28
MnO	6.36	0.40	0.52	0.75	0.62	0.76	0.65	0.73	0.61	0.00	0.00	0.16	0.08
MgO	0.68	6.88	6.77	4.32	3.71	4.27	4.25	4.22	4.16	0.00	0.01	0.00	0.02
CaO	14.61	0.04	0.00	10.73	10.81	10.83	10.87	11.07	11.00	5.07	4.56	0.04	0.09
Na_2O	0.00	0.06	0.03	1.65	1.44	1.74	1.50	1.63	1.59	4.46	9.06	0.01	0.00
K_2O	0.01	9.38	9.40	1.99	2.03	1.93	1.90	1.94	2.00	0.17	0.19	0.02	0.01
Totals	99.33	93.48	93.85	97.72	96.92	97.22	95.75	97.38	96.53	97.69	100.08	102.23	100.77
Oxygens	12	11	11	23	23	23	23	23	23	8	8	4	4
Si	2.95	2.80	2.78	6.01	6.05	6.11	6.07	5.99	6.03	2.84	2.79	0.00	0.00
Ti	0.01	0.14	0.14	0.09	0.04	0.08	0.08	0.08	0.07	0.00	0.00	0.00	0.01
Al	1.92	1.39	1.45	2.37	2.42	2.34	2.39	2.45	2.47	1.26	1.20	0.01	0.00
Cr	0.00	0.00	0.00	0.01	0.01	0.00	0.00	0.00	0.00	0.00	0.00	0.00	0.00
Fe^{3+}	0.18	0.00	0.00	0.82	0.77	0.61	0.67	0.74	0.63	0.01	0.01	1.99	1.98
Fe^{2+}	1.18	1.70	1.67	2.63	2.78	2.77	2.70	2.66	2.74	0.00	0.00	0.99	1.00
Mn	0.43	0.03	0.04	0.10	0.08	0.10	0.09	0.10	0.08	0.00	0.00	0.01	0.00
Mg	0.08	0.83	0.81	1.02	0.88	1.01	1.02	1.00	0.99	0.00	0.00	0.00	0.00
Ca	1.26	0.00	0.00	1.82	1.85	1.84	1.88	1.88	1.88	0.24	0.22	0.00	0.00
Na	0.00	0.01	0.01	0.51	0.45	0.54	0.47	0.50	0.49	0.38	0.78	0.00	0.00
K	0.00	0.97	0.96	0.40	0.41	0.39	0.39	0.39	0.41	0.01	0.01	0.00	0.00
Sum	8.00	7.86	7.84	15.76	15.74	15.79	15.75	15.79	15.80	4.73	5.00	3.00	3.00

Sample 187330 A

	Grt core	Grt rim	Grt core	Grt rim	Bt core	Bt rim	Hbl core	Hbl rim	Hbl core	Hbl rim	Ksp core	Ksp rim	Pl core	Pl rim	Mag	Ilm
SiO_2	36.41	36.65	36.25	36.84	37.47	36.41	39.17	40.57	40.51	40.86	63.84	64.26	62.19	61.04	0.07	0.03
TiO_2	0.00	0.03	0.08	0.04	3.51	3.41	1.63	1.80	1.75	1.76	0.00	0.02	0.00	0.00	0.40	49.71
Al_2O_3	20.98	20.58	20.39	20.95	14.58	15.27	11.92	11.74	11.67	12.48	18.58	18.71	23.27	23.66	0.99	0.00
Cr_2O_3	0.01	0.01	0.00	0.00	0.00	0.05	0.00	0.08	0.00	0.00	0.03	0.02	0.04	0.02	0.00	0.00
FeO	26.25	26.37	26.14	26.67	15.74	18.22	19.70	17.97	18.27	17.77	0.02	0.08	0.21	0.49	93.40	46.07
MnO	2.30	2.75	3.95	3.05	0.04	0.08	0.22	0.17	0.14	0.22	0.01	0.03	0.00	0.03	0.10	1.53
MgO	2.05	2.27	1.22	2.38	13.68	12.57	9.02	9.24	9.21	9.67	0.00	0.00	0.00	0.00	0.08	0.36
CaO	10.65	10.87	11.13	9.80	0.05	0.08	10.70	11.08	10.85	11.19	0.00	0.01	4.57	5.30	0.03	0.01
Na_2O	0.01	0.04	0.03	0.01	0.03	0.08	1.62	1.80	1.74	1.64	1.37	1.12	8.84	8.52	0.00	0.03
K_2O	0.00	0.01	0.01	0.02	9.64	8.80	1.85	1.89	1.80	1.89	14.43	14.86	0.27	0.35	0.00	0.00
Totals	98.92	99.98	99.57	100.06	94.75	95.07	96.46	96.53	96.22	97.80	98.30	99.15	99.41	99.47	101.91	98.15
Oxygens	12	12	12	12	11	11	23	23	23	23	8	8	8	8	4	3
Si	2.93	2.92	2.92	2.93	2.83	2.76	6.07	6.25	6.26	6.19	2.98	2.98	2.77	2.73	0.00	0.00
Ti	0.00	0.00	0.01	0.00	0.20	0.19	0.19	0.21	0.20	0.20	0.00	0.00	0.00	0.00	0.01	0.96
Al	1.99	1.93	1.94	1.97	1.30	1.36	2.18	2.13	2.13	2.23	1.02	1.02	1.22	1.25	0.04	0.00
Cr	0.00	0.00	0.00	0.00	0.00	0.00	0.00	0.01	0.00	0.00	0.00	0.00	0.00	0.00	0.00	0.00
Fe^{3+}	0.16	0.23	0.22	0.17	0.00	0.05	0.73	0.23	0.31	0.38	0.00	0.00	0.01	0.02	1.93	0.08
Fe^{2+}	1.60	1.52	1.54	1.60	0.99	1.10	1.82	2.09	2.05	1.87	0.00	0.00	0.00	0.00	1.01	0.91
Mn	0.16	0.19	0.27	0.21	0.00	0.01	0.03	0.02	0.02	0.03	0.00	0.00	0.00	0.00	0.00	0.03
Mg	0.25	0.27	0.15	0.28	1.54	1.42	2.08	2.12	2.12	2.18	0.00	0.00	0.00	0.00	0.01	0.01
Ca	0.92	0.93	0.96	0.84	0.00	0.01	1.78	1.83	1.80	1.82	0.00	0.00	0.22	0.25	0.00	0.00
Na	0.00	0.01	0.00	0.00	0.00	0.01	0.49	0.54	0.52	0.48	0.12	0.10	0.76	0.74	0.00	0.00
K	0.00	0.00	0.00	0.00	0.93	0.85	0.37	0.37	0.36	0.36	0.86	0.88	0.02	0.02	0.00	0.00
Sum	8.00	8.00	8.00	8.00	7.79	7.77	15.72	15.81	15.76	15.73	5.00	4.99	5.00	5.01	3.00	2.00

Sample 155733

	Grt core	Grt rim	Bt core	Bt rim	Hbl core	Pl core	Pl rim	Pl core	Pl rim	Mag	Mag	Mag
SiO_2	37.10	37.11	35.21	35.81	37.96	62.50	62.92	62.10	62.10	0.17	0.02	0.06
TiO_2	0.15	0.05	3.53	2.93	1.01	0.01	0.00	0.13	0.00	0.11	0.01	0.05
Al_2O_3	20.04	20.13	13.64	13.76	12.36	22.56	22.91	23.01	22.40	0.21	0.23	0.21
Cr_2O_3	0.01	0.00	0.08	0.00	0.02	0.05	0.03	0.02	0.00	0.00	0.00	0.03
FeO	26.60	25.54	24.78	24.30	24.04	0.05	0.07	0.17	0.13	90.60	92.51	91.07
MnO	1.72	3.94	0.35	0.40	0.58	0.01	0.00	0.02	0.02	0.06	0.10	0.08
MgO	1.77	1.51	7.81	8.17	5.24	0.01	0.00	0.00	0.01	0.00	0.00	0.00
CaO	11.19	11.31	0.05	0.00	10.58	4.67	4.69	4.84	4.63	0.00	0.00	0.03
Na_2O	0.01	0.03	0.04	0.10	1.60	8.84	8.64	8.53	8.66	0.00	0.00	0.00
K_2O	0.01	0.00	9.26	9.33	2.06	0.27	0.29	0.27	0.21	0.00	0.00	0.00
Totals	98.60	99.62	94.76	94.80	95.46	98.99	99.56	99.11	98.18	91.15	92.88	91.53
Oxygens	12	12	11	11	23	8	8	8	8	4	4	4
Si	2.99	2.97	2.79	2.83	6.08	2.80	2.80	2.78	2.80	0.01	0.00	0.00
Ti	0.01	0.00	0.21	0.17	0.12	0.00	0.00	0.00	0.00	0.00	0.00	0.00
Al	1.91	1.90	1.28	1.28	2.33	1.19	1.20	1.21	1.19	0.01	0.01	0.01
Cr	0.00	0.00	0.01	0.00	0.00	0.00	0.00	0.00	0.00	0.00	0.00	0.00
Fe^{3+}	0.09	0.16	0.00	0.00	0.54	0.00	0.00	0.01	0.01	1.97	1.99	1.98
Fe^{2+}	1.70	1.55	1.64	1.61	2.68	0.00	0.00	0.00	0.00	1.01	1.00	1.00
Mn	0.12	0.27	0.02	0.03	0.08	0.00	0.00	0.00	0.00	0.00	0.00	0.00
Mg	0.21	0.18	0.92	0.96	1.25	0.00	0.00	0.00	0.00	0.00	0.00	0.00
Ca	0.97	0.97	0.01	0.00	1.82	0.22	0.22	0.23	0.22	0.00	0.00	0.00
Na	0.00	0.01	0.01	0.02	0.50	0.77	0.74	0.74	0.76	0.00	0.00	0.00
K	0.00	0.00	0.94	0.94	0.42	0.02	0.02	0.02	0.01	0.00	0.00	0.00
Sum	8.00	8.00	7.83	7.83	15.82	5.00	4.98	4.99	4.99	3.00	3.00	3.00

Sample 155735

	Grt core	Grt rim	Bt core	Bt rim	Hbl core	Hbl rim	Pl core	Pl rim	Mag	Mag
SiO_2	38.85	39.09	37.81	37.22	40.43	40.90	64.67	64.79	0.23	0.06
TiO_2	0.03	0.07	1.99	2.33	1.09	1.18	0.05	0.02	0.45	0.17
Al_2O_3	19.23	19.34	15.42	14.91	13.17	12.78	23.57	23.50	0.34	0.17
Cr_2O_3	0.00	0.01	0.00	0.00	0.00	0.01	0.00	0.09	0.04	0.01
FeO	22.87	22.68	21.78	23.06	22.76	22.75	0.21	0.06	94.12	95.79
MnO	6.67	5.74	0.33	0.50	0.70	0.52	0.01	0.04	0.08	0.00
MgO	1.29	1.25	8.37	8.41	5.69	5.96	0.00	0.00	0.02	0.03
CaO	11.48	12.32	0.09	0.28	10.70	10.61	5.25	4.79	0.21	0.06
Na_2O	0.03	0.02	0.12	0.08	1.57	1.59	8.44	8.79	0.00	0.00
K_2O	0.00	0.00	8.12	8.99	2.00	1.94	0.16	0.18	0.03	0.00
Totals	100.41	100.52	94.04	95.80	97.87	97.98	102.36	102.25	89.08	89.72
Oxygens	12	12	11	11	23	23	8	8	4	4
Si	3.09	3.10	2.92	2.87	6.25	6.30	2.79	2.80	0.01	0.00
Ti	0.00	0.00	0.12	0.14	0.13	0.14	0.00	0.00	0.01	0.01
Al	1.80	1.81	1.41	1.36	2.40	2.32	1.20	1.20	0.02	0.01
Cr	0.00	0.00	0.00	0.00	0.00	0.00	0.00	0.00	0.00	0.00
Fe^{3+}	0.02	0.00	0.00	0.00	0.29	0.29	0.01	0.00	1.94	1.98
Fe^{2+}	1.50	1.50	1.41	1.49	2.62	2.60	0.00	0.00	1.01	1.00
Mn	0.45	0.39	0.02	0.03	0.09	0.07	0.00	0.00	0.00	0.00
Mg	0.15	0.15	0.96	0.97	1.31	1.37	0.00	0.00	0.00	0.00
Ca	0.98	1.05	0.01	0.02	1.77	1.75	0.24	0.22	0.01	0.00
Na	0.00	0.00	0.02	0.01	0.47	0.47	0.71	0.74	0.00	0.00
K	0.00	0.00	0.80	0.89	0.40	0.38	0.01	0.01	0.00	0.00
Sum	8.00	8.00	7.67	7.77	15.72	15.69	4.96	4.97	3.00	3.00

Appendix 2 - Representative output file from AX

Calculations for P = 11.0 kbar and T = 700°C

```
g circle
  2-site mixing + Regular solution gammas
  Ferric from:  Cation Sum = 8 for 12 oxygens
  W: py.alm=2.5, gr.py=33, py.andr=73, alm.andr=60, spss.andr=60 kJ

oxide    wt % cations               activity         ±sd    ±%

 SiO2   36.87   2.903         py       0.027     0.00787    30
 TiO2    0.01   0.001         gr      0.0125     0.00443    35
Al2O3   21.82   2.025        alm        0.12      0.0187    15
Cr2O3    0.05   0.003       spss    0.000015   0.0000084    57
Fe2O3    2.79   0.165       andr           -           -     -
  FeO   24.09   1.586
  MnO    1.19   0.079
  MgO    5.84   0.685
  CaO    6.56   0.553
 Na2O    0.00   0.000
  K2O    0.00   0.000

totals  99.22   8.000
_____________________________________________________________________________
g circle
  2-site mixing + Regular solution gammas
  Ferric from:  Cation Sum = 8 for 12 oxygens
  W: py.alm=2.5, gr.py=33, py.andr=73, alm.andr=60, spss.andr=60 kJ

oxide    wt % cations               activity         ±sd    ±%

 SiO2   37.02   2.918         py       0.031      0.0087    28
 TiO2    0.00   0.000         gr      0.0133     0.00466    35
Al2O3   21.50   1.998        alm        0.12      0.0184    16
Cr2O3    0.00   0.000       spss    0.000010   0.0000056    57
Fe2O3    2.87   0.170       andr           -           -     -
  FeO   23.66   1.560
  MnO    1.04   0.070
  MgO    6.14   0.721
  CaO    6.62   0.559
 Na2O    0.00   0.000
  K2O    0.04   0.004

totals  98.89   8.000
_____________________________________________________________________________
g circle
  2-site mixing + Regular solution gammas
  Ferric from:  Cation Sum = 8 for 12 oxygens
  W: py.alm=2.5, gr.py=33, py.andr=73, alm.andr=60, spss.andr=60 kJ

oxide    wt % cations               activity         ±sd    ±%

 SiO2   36.81   2.873         py      0.0222     0.00688    31
 TiO2    0.21   0.012         gr      0.0109     0.00397    36
Al2O3   21.23   1.954        alm        0.11      0.0178    16
Cr2O3    0.00   0.000       spss     0.00012    0.000063    54
Fe2O3    4.71   0.277       andr           -           -     -
  FeO   23.25   1.517
  MnO    2.40   0.159
  MgO    5.57   0.647
  CaO    6.71   0.561
 Na2O    0.00   0.000
  K2O    0.00   0.000

totals 100.89   8.000
_____________________________________________________________________________
g circle
  2-site mixing + Regular solution gammas
  Ferric from:  Cation Sum = 8 for 12 oxygens
  W: py.alm=2.5, gr.py=33, py.andr=73, alm.andr=60, spss.andr=60 kJ

oxide    wt % cations               activity         ±sd    ±%

 SiO2   37.05   2.941         py      0.0219     0.00682    31
 TiO2    0.04   0.002         gr      0.0125     0.00441    35
Al2O3   21.02   1.967        alm        0.12      0.0183    16
Cr2O3    0.07   0.004       spss     0.00012    0.000065    54
Fe2O3    2.45   0.146       andr           -           -     -
  FeO   23.28   1.546
  MnO    2.37   0.159
  MgO    5.48   0.648
  CaO    6.82   0.580
 Na2O    0.02   0.004
  K2O    0.02   0.002

totals  98.62   8.000
_____________________________________________________________________________
```

sp circle
  Ferric from: Cation Sum = 3 for 4 oxygens. Max Ratio = 0.9
  ideal mixing in inverse spinels

oxide	wt %	cations		activity	±sd	±%
SiO2	0.00	0.000	mt	0.25	0.19	75
TiO2	16.23	0.491	usp	0.24	0.0250	11
Al2O3	0.09	0.004	cmt	-	-	-
Cr2O3	0.03	0.001				
Fe2O3	33.44	1.013				
FeO	43.74	1.472				
MnO	0.06	0.002				
MgO	0.27	0.016				
CaO	0.03	0.001				
Na2O	0.00	0.000				
K2O	0.00	0.000				
totals	93.87	3.000				

---

sp circle

  Ferric from: Cation Sum = 3 for 4 oxygens. Max Ratio = 0.9
  ideal mixing in inverse spinels

oxide	wt %	cations		activity	±sd	±%
SiO2	0.02	0.001	mt	0.96	0.096	10
TiO2	0.09	0.002	usp	-	-	-
Al2O3	0.24	0.011	cmt	-	-	-
Cr2O3	0.17	0.005				
Fe2O3	69.68	1.982				
FeO	31.25	0.988				
MnO	0.02	0.001				
MgO	0.09	0.005				
CaO	0.02	0.001				
Na2O	0.06	0.004				
K2O	0.00	0.000				
totals	101.63	3.000				

---

amph circle
  Mixing model of Dale, Holland & Powell (2000)
  Ferric from: Av from max and min constraints. Holland & Blundy 1993

oxide	wt %	cations		activity	±sd	±%
SiO2	41.79	6.184	tr	0.0327	0.00818	25
TiO2	1.81	0.201	fact	0.000010	0.0000082	81
Al2O3	12.10	2.112	ts	0.0002	0.00099	626
Cr2O3	0.05	0.005	parg	0.057	0.0142	25
Fe2O3	4.61	0.513	gl	-	-	-
FeO	8.25	1.021				
MnO	0.10	0.013				
MgO	13.65	3.010				
CaO	11.72	1.858				
Na2O	1.53	0.439				
K2O	1.72	0.324				
totals	97.32	15.681				

---

amph circle
  Mixing model of Dale, Holland & Powell (2000)
  Ferric from: Av from max and min constraints. Holland & Blundy 1993

oxide	wt %	cations		activity	±sd	±%
SiO2	40.58	6.065	tr	0.0324	0.00811	25
TiO2	1.55	0.175	fact	0.000007	0.0000058	82
Al2O3	13.25	2.335	ts	0.0002	0.0014	789
Cr2O3	0.02	0.003	parg	0.080	0.0199	25
Fe2O3	5.33	0.600	gl	-	-	-
FeO	7.96	0.995				
MnO	0.11	0.014				
MgO	12.95	2.883				
CaO	11.46	1.835				
Na2O	1.37	0.398				
K2O	1.96	0.374				
totals	96.56	15.677				

---

amph circle
  Mixing model of Dale, Holland & Powell (2000)
  Ferric from: Av from max and min constraints. Holland & Blundy 1993

oxide	wt %	cations		activity	±sd	±%
SiO2	41.08	6.235	tr	0.0255	0.00689	27
TiO2	1.86	0.212	fact	0.000026	0.000020	77
Al2O3	11.65	2.085	ts	0.0002	0.00083	425
Cr2O3	0.00	0.000	parg	0.043	0.0108	25
Fe2O3	3.48	0.397	gl	-	-	-
FeO	10.16	1.289				
MnO	0.11	0.014				
MgO	12.45	2.816				
CaO	11.58	1.883				
Na2O	1.35	0.397				
K2O	1.89	0.366				
totals	95.59	15.693				

---

fsp circle
  Waldbaum & Thompson 1969
  Ferric from: all ferric

oxide	wt %	cations		activity	±sd	±%
SiO2	63.63	2.978	san	0.91	0.0454	5
TiO2	0.04	0.001	ab	0.328	0.0296	9
Al2O3	18.42	1.016				
Cr2O3	0.01	0.000				
Fe2O3	0.32	0.011				
FeO	0.00	0.000				
MnO	0.01	0.001				
MgO	0.00	0.000				
CaO	0.11	0.005				
Na2O	1.00	0.090				
K2O	14.99	0.896				
totals	98.55	5.000				

---

fsp circle
  Waldbaum & Thompson 1969
  Ferric from: all ferric

oxide	wt %	cations		activity	±sd	±%
SiO2	64.24	2.982	san	0.90	0.0448	5
TiO2	0.02	0.001	ab	0.38	0.0293	8
Al2O3	18.50	1.012				
Cr2O3	0.00	0.000				
Fe2O3	0.35	0.012				
FeO	0.00	0.000				
MnO	0.00	0.000				
MgO	0.04	0.003				
CaO	0.08	0.004				
Na2O	1.17	0.105				
K2O	14.83	0.879				
totals	99.24	4.998				

---

fsp circle
  Waldbaum & Thompson 1969
  Ferric from: all ferric

oxide	wt %	cations		activity	±sd	±%
SiO2	62.90	2.967	san	0.91	0.0456	5
TiO2	0.01	0.000	ab	0.325	0.0296	9
Al2O3	18.53	1.031				
Cr2O3	0.00	0.000				
Fe2O3	0.18	0.007				
FeO	0.00	0.000				
MnO	0.00	0.000				
MgO	0.02	0.002				
CaO	0.03	0.001				
Na2O	1.00	0.092				
K2O	15.30	0.922				
totals	98.00	5.021				

---

fsp circle
  Holland & Powell 1992 model 1
  Ferric from: all ferric
  plag is C1 structure

oxide	wt %	cations		activity	±sd	±%
SiO2	62.34	2.737	an	0.36	0.0295	8
TiO2	0.00	0.000	ab	0.75	0.0374	5
Al2O3	24.19	1.252				
Cr2O3	0.07	0.003				
Fe2O3	0.16	0.005				
FeO	0.00	0.000				
MnO	0.03	0.001				
MgO	0.00	0.000				
CaO	5.41	0.255				
Na2O	8.84	0.753				
K2O	0.13	0.007				
totals	101.18	5.013				

---

fsp circle
  Holland & Powell 1992 model 1
  Ferric from: all ferric
  plag is C1 structure

oxide	wt %	cations		activity	±sd	±%
SiO2	59.09	2.681	an	0.40	0.0289	7
TiO2	0.01	0.000	ab	0.71	0.0354	5
Al2O3	24.01	1.284				
Cr2O3	0.02	0.001				
Fe2O3	2.10	0.072				
FeO	0.00	0.000				
MnO	0.00	0.000				
MgO	0.38	0.026				
CaO	5.17	0.251				
Na2O	7.18	0.632				
K2O	0.33	0.019				
totals	98.29	4.966				

---

bi circle
  Al-M1 ordered, site-mixing model + macroscopic RS gammas: (ann, phl, east, obi)
  Ferric from: Tet + Oct cation sum = 6.9 for 11 oxygens. Max Ratio = 0.15
  SF model parameters: Wpa=9, Wpe=10, Wpo=3, Wao=6, Wae=-1, Woe=10 (kJ)

oxide	wt %	cations		activity	±sd	±%
SiO2	37.28	2.784	phl	0.16	0.0242	15
TiO2	5.44	0.305	ann	0.0129	0.00454	35
Al2O3	13.51	1.189	east	-	-	-
Cr2O3	0.00	0.000				
Fe2O3	0.00	0.000				
FeO	12.81	0.800				
MnO	0.15	0.009				
MgO	15.85	1.764				
CaO	0.04	0.004				
Na2O	0.03	0.004				
K2O	9.63	0.918				
totals	94.74	7.777				

---

cpx circle
  C2/c Ca-pyroxene. Projected into di-hed-en-cats-jd-acm for gammas
  Ferric from: Cation Sum = 4 for 6 oxygens

oxide	wt %	cations		activity	±sd	±%
SiO2	51.51	1.931	di	0.66	0.066	10
TiO2	0.13	0.004	hed	0.17	0.0236	14
Al2O3	1.65	0.073	cats	-	-	-
Cr2O3	0.00	0.000				
Fe2O3	4.20	0.118				
FeO	4.81	0.151				
MnO	0.19	0.006				
MgO	13.76	0.769				
CaO	22.13	0.889				
Na2O	0.83	0.060				
K2O	0.00	0.000				
totals	99.20	4.000				

---

cpx circle
C2/c Ca-pyroxene. Projected into di-hed-en-cats-jd-acm for gammas
Ferric from: Cation Sum = 4 for 6 oxygens

oxide	wt %	cations		activity	±sd	±%
SiO2	51.85	1.930	di	0.64	0.064	10
TiO2	0.08	0.002	hed	0.19	0.0243	12
Al2O3	1.61	0.071	cats	-	-	-
Cr2O3	0.03	0.001				
Fe2O3	4.13	0.116				
FeO	5.61	0.175				
MnO	0.15	0.005				
MgO	13.87	0.769				
CaO	22.05	0.880				
Na2O	0.71	0.052				
K2O	0.01	0.000				

Appendix 3 - Representative output file from THERMOCALC v3.26

1. Average P *calculation*

```
THERMOCALC 3.26  running at 0.42 on Tue 25 Sep,2007, with
tcds55.txt produced at 19:29:59 on 22 Nov 2003 (with sigma fit =  1.067)

An independent set of reactions has been calculated

Activities and their uncertainties

                py       gr      alm       tr     fact       ts     parg
a           0.0310   0.0133    0.120   0.0324  7.00e-6 0.000200   0.0800
sd(a)/a    0.28065  0.35038  0.15333  0.25031  0.82857  7.00000  0.24875

               san      phl      ann       an       ab       di      hed
a            0.910    0.160   0.0129    0.400    0.710    0.660    0.170
sd(a)/a    0.05000  0.15125  0.35194  0.07225  0.05000  0.10000  0.13882

                 q      H2O
a             1.00    0.250
sd(a)/a          0

Independent set of reactions
1)  py + 2gr + 3q = 3an + 3di
2)  2gr + alm + 3q = 3an + 3hed
3)  2py + 4gr + 3ts + 12q = 3tr + 12an
4)  6tr + 21an = 10py + 11gr + 27q + 6H2O
5)  4gr + 5alm + 3ts + 12q = 3py + 3fact + 12an
6)  3ann + 12an + 18hed = 8gr + 4alm + 3fact + 3san
7)  3phl + 12an + 18di = 4py + 8gr + 3tr + 3san
8)  py + 2gr + 3phl + 3ab = 3parg + 3san

Calculations for the independent set of reactions
 at T = 750¡C  (for a(H2O) = 0.25)
       P(T)   sd(P)       a   sd(a)         b        c     ln_K sd(ln_K)
1      10.2    1.08   -0.27    0.83  -0.13382    6.685    8.118    0.841
2      11.5    1.08   54.03    2.05  -0.15450    7.041    2.696    0.857
3       8.1    8.51  -31.41    6.48  -0.37235   21.087   28.495   21.085
4      11.2    0.92  548.42    4.63   0.34840  -48.680  -42.438    5.224
5      10.5    7.78  250.81    8.28  -0.45446   23.254   -3.593   21.241
6       9.7    1.61 -214.35    8.62   0.64381  -25.613  -22.990    4.748
7       9.7    1.29  -38.11    3.55   0.56236  -24.769  -35.054    3.728
8      12.3    3.69  -27.91    2.98  -0.09644    2.824   10.779    1.174

corresponding average P

        avP     sd   fit
lsq   11.70   0.95  1.28

diagnostics on this average P

for 95% confidence, fit (= sd(fit) = sqrt(MSWD)) < 1.42 (but larger may be OK)

column:
1-3: result of doubling the uncertainty on ln a.
4: e* = ln a residuals normalised to sd(ln a) : |e*| >2.5 suspect?
5: hat = diagonal elements of the hat matrix : hat >0.50 influential.
6-7: observed and calculated activities of endmembers.
8-9: regression-through-origin x,y values

             P     sd    fit     e*   hat    a(obs)   a(calc)      x      y
     py  11.70   0.99   1.28    0.0  0.09    0.0310    0.0311   0.40   4.69
     gr  12.19   1.15   1.23    0.7  0.40    0.0133    0.0173   0.85   9.23
    alm  11.52   0.97   1.24   -0.5  0.05     0.120     0.110   0.29   3.89
     tr  11.68   0.98   1.27    0.1  0.06    0.0324    0.0332  -0.34  -4.05
   fact  11.39   0.81   1.06    2.0  0.06   7.00e-6   3.71e-5  -0.32  -5.71
     ts  11.70   0.95   1.27    0.4  0.00  0.000200   0.00277   0.02  -0.19
   parg  11.86   0.94   1.22    0.9  0.05    0.0800     0.100   0.30   2.56
    san  11.70   0.96   1.28    0.0  0.01     0.910     0.911   0.11   1.29
    phl  11.68   0.96   1.27    0.2  0.02     0.160     0.164  -0.19  -2.37
    ann  11.81   0.97   1.26   -0.6  0.07    0.0129    0.0106  -0.35  -3.54
     an  11.84   1.12   1.27   -0.2  0.14     0.400     0.395  -0.50  -5.69
     ab  11.72   0.95   1.27   -0.2  0.00     0.710     0.704  -0.06  -0.52
     di  11.54   0.76   1.01   -2.0  0.01     0.660     0.538   0.14   3.68
    hed  11.67   0.94   1.26    0.5  0.01     0.170     0.181  -0.10  -1.60
      q  11.70   0.95   1.28      0     0      1.00      1.00      0      0
    H2O  11.70   0.95   1.28      0     0      1.00      1.00      0      0

Average pressures  (for a(H2O) = 0.25)

T¡C       600   625   650   675   700   725   750   775   800   825   850   875   900
av P     11.3  11.4  11.5  11.5  11.6  11.6  11.7  11.8  11.8  11.9  12.0  12.1  12.2
sd       1.85  1.66  1.47  1.30  1.15  1.03  0.95  0.92  0.97  1.06  1.21  1.37  1.55
sigfit    2.9   2.6   2.2   1.9   1.6   1.4   1.3   1.2   1.2   1.3   1.4   1.6   1.8

**************************************
```

2. Average T *calculation*

An independent set of reactions has been calculated

Activities and their uncertainties

	py	gr	alm	tr	fact	ts	parg
a	0.0310	0.0133	0.120	0.0324	7.00e-6	0.000200	0.0800
sd(a)/a	0.28065	0.35038	0.15333	0.25031	0.82857	7.00000	0.24875

	san	phl	ann	an	ab	di	hed
a	0.910	0.160	0.0129	0.400	0.710	0.660	0.170
sd(a)/a	0.05000	0.15125	0.35194	0.07225	0.05000	0.10000	0.13882

	q	H2O
a	1.00	0.250
sd(a)/a	0	

Independent set of reactions
1) 2gr + alm + 3q = 3an + 3hed
2) gr + 2tr = py + 7di + 2q + 2H2O
3) 6gr + 7tr = 3ts + 26di + 4q + 4H2O
4) 5py + 3fact = 5alm + 3tr
5) 2py + 3ts + 12hed = 4gr + 4alm + 3tr
6) 3ann + 12an + 18hed = 8gr + 4alm + 3fact + 3san
7) py + ann = alm + phl
8) 4py + 2gr + 3ann + 3ab = 3alm + 3parg + 3san

Calculations for the independent set of reactions
at P = 11.0 kbar (for a(H2O) = 0.25)

	T(P)	sd(T)	a	sd(a)	b	c	ln_K	sd(ln_K)
1	722.5	49	54.45	2.05	-0.15483	7.034	2.696	0.857
2	849.0	43	181.12	0.87	-0.19419	-0.714	4.797	0.971
3	728.2	330	391.79	7.48	-0.55034	4.204	13.572	21.337
4	604.2	323	-282.04	5.23	0.08190	-2.164	32.088	3.050
5	552.1	737	-246.63	10.07	0.24451	-7.052	17.713	21.142
6	822.7	64	-214.39	8.62	0.64311	-25.541	-22.990	4.748
7	772.9	331	-44.18	0.92	0.01313	-0.292	3.871	0.499
8	803.2	285	-158.67	4.06	-0.05908	1.976	22.393	1.918

Average temperatures (for a(H2O) = 0.25)

corresponding average T

	avT	sd	fit
lsq	774	38	1.31

diagnostics on this average T

for 95% confidence, fit (= sd(fit) = sqrt(MSWD)) < 1.42 (but larger may be OK)

column:
1-3: result of doubling the uncertainty on ln a.
4: e* = ln a residuals normalised to sd(ln a) : |e*| >2.5 suspect?
5: hat = diagonal elements of the hat matrix : hat >0.50 influential.
6-7: observed and calculated activities of endmembers.
8-9: regression-through-origin x,y values

	T	sd	fit	e*	hat	a(obs)	a(calc)	x	y
py	778	48	1.31	0.1	0.37	0.0310	0.0322	0.02	21.61
gr	777	42	1.30	-0.2	0.18	0.0133	0.0124	-0.01	-14.75
alm	777	36	1.23	-0.8	0.00	0.120	0.106	-0.00	-0.98
tr	774	38	1.30	0.3	0.00	0.0324	0.0350	0.00	0.25
fact	780	30	1.02	2.4	0.01	7.00e-6	4.92e-5	0.00	1.05
ts	774	38	1.30	0.4	0.00	0.000200	0.00239	-0.00	-0.75
parg	770	40	1.29	0.5	0.08	0.0800	0.0902	-0.01	-10.61
san	774	39	1.31	-0.0	0.01	0.910	0.910	0.00	4.09
phl	773	40	1.30	0.2	0.08	0.160	0.164	-0.01	-9.94
ann	776	39	1.30	-0.4	0.03	0.0129	0.0114	-0.01	-5.65
an	775	38	1.30	0.2	0.00	0.400	0.407	0.00	1.03
ab	774	39	1.31	-0.1	0.00	0.710	0.707	0.00	2.13
di	754	33	1.06	-1.9	0.10	0.660	0.546	0.01	13.21
hed	781	39	1.27	0.7	0.07	0.170	0.187	0.01	8.46
q	774	38	1.31	0	0	1.00	1.00	0	0
H2O	774	38	1.31	0	0	1.00	1.00	0	0

P	9.0	9.2	9.5	9.8	10.0	10.2	10.5	10.8	11.0	11.2	11.5	11.8	12.0	12.2	12.5	12.8	13.0
av T	764.9	766.1	767.3	768.5	769.7	770.9	772.0	773.2	774.2	775.3	775.9	776.6	777.4	778.3	779.2	780.1	
sd	53	51	49	47	45	43	41	40	38	38	37	37	37	38	39	41	
sigfit	1.9	1.8	1.7	1.6	1.5	1.5	1.4	1.4	1.3	1.3	1.2	1.2	1.2	1.3	1.3	1.3	

****

3. Average P-T *calculation*

```
An independent set of reactions has been calculated

Activities and their uncertainties

                py       gr      alm       tr     fact       ts     parg
a           0.0310   0.0133    0.120   0.0324  7.00e-6 0.000200   0.0800
sd(a)/a    0.28065  0.35038  0.15333  0.25031  0.82857  7.00000  0.24875

               san      phl      ann       an       ab       di      hed
a            0.910    0.160   0.0129    0.400    0.710    0.660    0.170
sd(a)/a    0.05000  0.15125  0.35194  0.07225  0.05000  0.10000  0.13882

                 q      H2O
a             1.00    0.250
sd(a)/a          0

Independent set of reactions
1)  py + 2gr + 3q = 3an + 3di
2)  2gr + alm + 3q = 3an + 3hed
3)  6tr + 21an = 10py + 11gr + 27q + 6H2O
4)  4gr + 5alm + 3ts + 12q = 3py + 3fact + 12an
5)  5py + 10gr + 3fact + 15q = 3tr + 15an + 15hed
6)  3ann + 12an + 18hed = 8gr + 4alm + 3fact + 3san
7)  3phl + 12an + 18di = 4py + 8gr + 3tr + 3san
8)  py + 2gr + 3phl + 3ab = 3parg + 3san

Calculations for the independent set of reactions
 (for a(H2O) = 0.25)
       P(T)   sd(P)       a   sd(a)         b        c     ln_K sd(ln_K)
1     10.19    1.08    0.18    0.83  -0.13419    6.679    8.118    0.841
2     11.52    1.08   54.45    2.05  -0.15483    7.034    2.696    0.857
3     11.17    0.91  542.09    4.63   0.35677  -48.894  -42.438    5.224
4     10.52    7.78  253.19    8.28  -0.45672   23.246   -3.593   21.241
5     10.01    1.34   -9.80    6.99  -0.69225   33.004   45.565    5.148
6      9.71    1.62 -214.39    8.62   0.64311  -25.541  -22.990    4.748
7      9.65    1.29  -38.28    3.55   0.56181  -24.699  -35.054    3.728
8     12.33    3.65  -26.13    2.98  -0.09846    2.852   10.779    1.174

Average PT  (for a(H2O) = 0.25)

Single end-member diagnostic information

avP, avT, sd's, cor, fit are result of doubling the uncertainty on ln a :
a ln a suspect if any are v different from lsq values.
e* are ln a residuals normalised to ln a uncertainties :
large absolute values, say >2.5, point to suspect info.
hat are the diagonal elements of the hat matrix :
large values, say >0.50, point to influential data.
For 95% confidence, fit (= sd(fit)) < 1.45
however a larger value may be OK - look at the diagnostics!

          avP    sd    avT    sd   cor   fit
    lsq  11.8   1.0    782    40 0.126  1.31

             P  sd(P)      T  sd(T)    cor    fit     e*   hat
     py  12.17   1.09    807     50  0.376   1.25  -0.70  0.49
     gr  12.08   1.26    776     44 -0.164   1.29  -0.36  0.53
    alm  11.62   1.03    783     39  0.116   1.26   0.57  0.04
     tr  11.79   1.05    782     40  0.125   1.31  -0.08  0.07
   fact  11.49   0.84    783     32  0.120   1.05  -2.03  0.06
     ts  11.81   1.01    782     40  0.126   1.30  -0.36  0.00
   parg  11.91   1.01    776     41  0.058   1.28  -0.62  0.13
    san  11.83   1.02    784     41  0.152   1.30  -0.15  0.02
    phl  11.83   1.03    784     42  0.180   1.31   0.13  0.10
    ann  11.97   1.02    786     40  0.168   1.27   0.75  0.10
     an  11.95   1.20    782     40  0.108   1.30   0.18  0.14
     ab  11.82   1.02    782     40  0.119   1.30   0.12  0.01
     di  11.58   0.85    760     36  0.176   1.08   1.64  0.15
    hed  11.78   0.99    788     40  0.110   1.27  -0.72  0.06
      q  11.81   1.02    782     40  0.126   1.31      0     0
    H2O  11.81   1.02    782     40  0.126   1.31      0     0


T = 782¡C, sd = 40,
P = 11.8 kbars, sd = 1.0, cor = 0.126, sigfit = 1.31

************************************
```

14. References

Andersen, T. 2002. Correction of common lead in U-Pb analyses that do not report Pb-204. *Chemical Geology* **192**(1-2), 59-79.

Andresen, A., Rehnström, E. F. & Holte, M. 2007. Evidence for simultaneous contraction and extension at different crustal levels during the Caledonian orogeny in NE Greenland. *Journal of the Geological Society of London* **164**, 869-880.

Bailey, C. M., Francis, B. E. & Fahrney, E. 2004. Strain and vorticity analysis of transpressional high-strain zones from the Virginia Piedmont, USA. In: *Flow Processes in Faults and Shear Zones* (edited by Alsop, G. I., Holdsworth, R. E., McCaffrey, K. J. W. & Hand, M.). Geological Society of London, Special Publications **224**, 249-264.

Bodorkos, S., Love, G. J. & Wingate, M. T. D. 2006. 180300: porphyritic metamonzogranite, Mount Gosse Geochronology dataset 653. In: *Compilation of geochronology data, June 2006 update*. Western Australia Geological Survey.

Camacho, A., Compston, W., McCullough, M. & McDougall, I. 1997. Timing and exhumation of eclogite facies shear zones, Musgrave Block, central Australia. *Journal of Metamorphic Geology* **15**, 735-751.

Camacho, A. & Fanning, C. M. 1995. Some isotopic constraints on the evolution of the granulite and upper amphibolite facies terranes in the eastern Musgrave Block, central Australia. *Precambrian Research* **71**, 155-181.

Camacho, A. & McDougall, I. 2000. Intracratonic, strikeslip partitioned transpression and the formation of eclogite facies rocks: An example from the Musgrave Block, central Australia. *Tectonics* **19**, 978-996.

Camacho, A., McDougall, I., Armstrong, R. & Braun, J. 2001. Evidence for shear heating, Musgrave Block, central Australia. *Journal of Structural Geology* **23**, 1007-1013.

Camacho, A., Vernon, R. H. & Fitzgerald, J. D. 1995. Large volumes of pseudotachylite in the Woodroffe Thrust, eastern Musgrave Ranges, Australia. *Journal of Structural Geology* **17**, 371-383.

Cartwright, I. & Buick, I. S. 1999. Meteoric fluid flow within Alice Springs age shear zones, Reynolds Range, central Australia. *Journal of Metamorphic Geology* **17**, 397-414.

Cherniak, D. J. 1993. Lead diffusion in titanite and preliminary results on the effects of radiation damage on Pb transport. *Chemical Geology* **110**(1-3), 177-194.

Cherniak, D. J. 2006. Zr diffusion in titanite. *Contributions to Mineralogy and Petrology* **152**, 639-647.

Cherniak, D. J., Hanchar, J. M. & Watson, E. B. 1997a. Diffusion of tetravalent cations in zircon. *Contributions to Mineralogy and Petrology* **127**, 383-390.

Cherniak, D. J., Hanchar, J. M. & Watson, E. B. 1997b. Rare-earth diffusion in zircon. *Chemical Geology* **134**, 289–301.

Cherniak, D. J. & Watson, E. B. 2001. Pb diffusion in zircon. *Chemical Geology* **172**, 5-24.

Clark, C., Hand, M., Faure, K. & Schmidt-Mumm, A. 2006. Up-Temperature flow of surface-derived fluids in the mid crust: the role of pre-orogenic burial of hydrated fault rocks. *Journal of Metamorphic Geology* **24**, 367-386.

Clarke, G. L., Buick, I. S., Glikson, A. Y. & Stewart, A. J. 1995. Structural and pressure–temperature evolution of host rocks of the Giles Complex, central Australia: evidence for multiple high pressure events. *AGSO Journal of Australian Geology and Geophysics* **16**, 127-146.

Clemens, J. D. & Vielzeuf, D. 1987. Constraints on melting and magma production in the crust. *Earth and Planetary Science Letters* **86**, 287-306.

Collins, A. S. & Pisarevsky, S. A. 2005. Amalgamating eastern Gondwana: The evolution of the Circum-Indian Orogens. *Earth Science Reviews* **71**, 229-270.

Collins, A. S., Santosh, M., Braun, I. & Clark, C. 2007. Age and sedimentary provenance of the Southern Granulites, South India: U-Th-Pb SHRIMP secondary ion mass spectrometry. *Precambrian Research* **155**(1-2), 125-138.

Corfu, F., Hanchar, J. M., Hoskin, P. W. O. & Kinny, P. D. 2003. Atlas of Zircon Textures. In: *Zircon* (edited by Hanchar, J. M. & Hoskin, P. W. O.) Reviews in Mineralogy and Geochemistry **53**, 469-500.

Curtis, M. L. 1998. Development of kinematic partitioning within a pure-shear dominated dextral transpression zone: the southern Ellsworth Mountains, Antarctica. In: *Continental Transpressional and Transtensional Tectonics* (edited by Holdsworth, R. E., Strachan, R. A. & Dewey, J. F.) Geological Society of London, Special Publications **135**, 289-306.

Dewey, J. F. 1998. Transpression and transtension zones. In: *Continental Transpressional and Transtensional Tectonics* (edited by Holdsworth, R. E., Strachan, R. A. & Dewey, J. F.) Geological Society of London, Special Publications **135**, 1-14.

Dietrich, D. 1989. Fold-axis parallel extension in an arcuate fold-and-thrust belt: the case of the Helvetic nappes. *Tectonophysics* **170**, 183-212.

Droop, G. T. R. 1987. A general equation for estimating Fe^{3+} concentrations in ferromagnesian silicates and oxides from microprobe analysis, using stoichiometric criteria. *Mineralogical Magazine* **51**, 431-435.

Eckert, J. O. J., Newton, R. C. & Kleppa, O. J. 1991. The reaction and recalibration of garnet–pyroxene–plagioclase–quartz geobarometers in the CMAS system by solution calorimetry. *American Mineralogist* **76**, 148-160.

Edgoose, C. J., Scrimgeour, I. R. & Close, D. F. 2004. Geology of the Musgrave Block, Northern Territory. Northern Territory Geological Survey, Report 15.

Ellis, D. J. & Green, D. H. 1979. An experimental study on the effect of Ca upon garnet–clinopyroxene Fe–Mg exchange equilibria. *Contributions to Mineralogy and Petrology* **71**, 13-22.

Ferrill, D. A. & Groshong, R. H. J. 1993. Kinematic model for the curvature of the northern Subalpine Chain, France. *Journal of Structural Geology* **15**(3-5), 523-541.

Flöttmann, T. & Hand, M. 1999. Folded basement-cored tectonic wedges along the northern edge of the Amadeus Basin, central Australia; evaluation of orogenic shortening. *Journal of Structural Geology* **21**(4), 399-412.

Flöttmann, T., Hand, M., Close, D., Edgoose, C. J. & Scrimgeour, I. R. 2004. Thrust tectonic styles of the intracratonic Alice Springs and Petermann Orogenies, Central Australia. In: *Thrust tectonics and hydrocarbon systems* (edited by McClay, K. R.) AAPG Memoir **82**, 538-557.

Fossen, H. & Tikoff, B. 1993. The deformation matrix for simultaneous simple shearing, pure shearing and volume change, and its application to transpression-transtension tectonics. *Journal of Structural Geology* **15**(3-5), 413-422.

Fossen, H. & Tikoff, B. 1998. Extended models of transpression and transpression, and application to tectonic settings. In: *Continental Transpressional and Transtensional Tectonics* (edited by Holdsworth, R. E., Strachan, R. A. & Dewey, J. F.) Geological Society of London, Special Publications **135**, 15-33.

Frost, R. B., Chamberlain, K. R. & Schumacher, J. C. 2000. Sphene (titanite): phase relations and use as a geochronometer. *Chemical Geology* **172**, 131-148.

Geological Survey of Western Australia. 2006. West Musgrave: Western Australia Geological Survey, 1:100 000 Geological Information Series.

Glikson, A. Y., Ballhaus, C. G., Clarke, G. L., Sheraton, J. W., Stewart, A. J. & Sun, S. S. 1995. Geological framework and crustal evolution of the Giles mafic–ultramafic complex and environs, western Musgrave Block, central Australia. *AGSO Journal of Australian Geology and Geophysics* **16**, 41-67.

Goscombe, B., Gray, D. & Hand, M. 2002. Extrusional Tectonics in the Core of a Transpressional Orogen; the Kaoko Belt, Namibia. *Journal of Petrology* **46**(6), 1203-1241.

Graham, C. M. & Powell, R. 1984. A garnet–hornblende geo-thermometer: calibration, testing and application to the Pelona Schist, Southern California. *Journal of Metamorphic Geology* **2**, 13-31.

Haines, P. W., Hand, M. & Sandiford, M. 2001. Palaeozoic synorogenic sedimentation in central and northern Australia; a review of distribution and timing with implications for the evolution of intracontinental orogens. *Australian Journal of Earth Sciences* **48**(6), 911-928.

Hallett, L. 2007. Pressure-temperature conditions and kinematic framework of the Petermann Orogeny in the central Musgrave Province, University of Adelaide Honours Thesis.

Hand, M. & Sandiford, M. 1999. Intraplate deformation in central Australia, the link between subsidence and fault reactivation. *Tectonophysics* **305**, 121-140.

Harley, S. L. & Kelly, N. M. 2007. The impact of zircon–garnet REE distribution data on the interpretation of zircon U–Pb ages in complex high-grade terrains: An example from the Rauer Islands, East Antarctica. *Chemical Geology* **241**, 62-87.

Hayden, L. A., Watson, E. B. & Wark, D. A. 2006. A thermobarometer for sphene. Abstract, 16th V.M. Goldschmidt Conference.

Holland, T. J. P. & Powell, R. 1998. An internally consistent thermodynamic data set for phases of petrological interest. *Journal of Metamorphic Geology* **13**(3), 309-343.

Hoskin, P. W. O. & Black, L. P. 2000. Metamorphic zircon formation by solid-state recrystallization of protolith igneous zircon. *Journal of Metamorphic Geology* **18**, 423-439.

Hoskin, P. W. O. & Schaltegger, U. 2003. The composition of zircon and igneous and metamorphic petrogenesis. In: *Zircon* (edited by Hanchar, J. M. & Hoskin, P. W. O.) Reviews in Mineralogy and Geochemistry, Mineralogical Society of America **53**, 27-62.

Howard, H. M., Smithies, R. H., Pirajno, F. & Skwarnecki, M. S. 2006. Bates, W.A. Sheet 4646. Western Australia Geological Survey, 1:100 000 Geological Information Series.

Ireland, T. R., Flöttmann, T., Fanning, C. M., Gibson, G. M. & Preiss, W. V. 1998. Development of the early Paleozoic Pacific margin of Gondwana from detrital-zircon ages across the Delamerian orogen. *Geology* **26**(3), 243-246.

Jackson, S. E., Pearson, N. J., Griffin, W. L. & Belousova, E. A. 2004. The application of laser ablation-inductively coupled plasma-mass spectrometry to in situ U-Pb zircon geochronology. *Chemical Geology* **211**(1-2), 47-69.

Jiang, D., Lin, S. & Williams, P. F. 2001. Deformation path in high-strain zones, with reference to slip partitioning in transpressional plate-boundary regions. *Journal of Structural Geology* **23**, 991-1005.

Jones, R. R., Holdsworth, R. E., McCaffrey, K. J. W., Clegg, P. & Tavarnelli, E. 2005. Scale dependence, strain compatibility and heterogeneity of three-dimensional deformation during mountain building: a discussion. *Journal of Structural Geology* **27**, 1190-1204.

Kelly, N. M., Clarke, G. L. & Harley, S. L. 2006. Monazite behaviour and age significance in poly-metamorphic high-grade terrains: A case study from the western Musgrave Block, central Australia. *Lithos* **88**, 100-134.

Kelsey, D. E., Wade, B. P., Collins, A. S., Hand, M., Sealing, C. R. & Netting, A. 2007. Discovery of a Neoproterozoic basin in the Prydz belt in East Antarctica and its implications for Gondwana assembly and ultrahigh temperature metamorphism. *Precambrian Research*, in press.

Kinny, P. D. 1997. Users guide to U-Th-Pb dating of titanite, perovskite, monazite and baddeleyite using the W.A. SHRIMP. W.A. Isotope Science Research Centre Report no. SPS 693/1997/AP72, Curtin University of Technology, Perth, 21pp.

Kinny, P. D., McNaughton, N. J., Fanning, C. M. & Maas, R. 1994. 518 Ma sphene (titanite) from the Khan pegmatite, Namibia, southwest Africa: A potential ion-microprobe standard. In: *Eighth International Conference on Geochronology, Cosmochronology and Isotope Geology Abstracts*. US Geological Survey Circular 1107, Berkeley, 171.

Kohn, M. J. & Spear, F. S. 1990. Two new geobarometers for garnet amphibolites with applications to southeastern Vermont. *American Mineralogist* **75**, 89-96.

Koschek, G. 1993. Origin and significance of the SEM cathodoluminescence from zircon. *Journal of Microscopy* **171**, 223-232.

Kretz, R. 1983. Symbols for rock-forming minerals. *American Mineralogist* **68**, 277-279.

Krogh, E. J. 1988. The garnet–clinopyroxene Fe–Mg geo-thermometer—a reinterpretation of existing experimental data. *Contributions to Mineralogy and Petrology* **99**, 44-48.

Lambeck, K. & Burgess, G. 1992. Deep crustal structure of the Musgrave Block, central Australia: results from teleseismic travel-time anomalies. *Australian Journal of Earth Sciences* **39**, 1-20.

Lambert, R. S. J. 1983. Metamorphism and thermal gradients in the Proterozoic continental crust. *Geological Society of America, Memoir* **161**, 155-165.

Leake, B. E., Woolley, A. R., Arps, C. E. S., Birch, W. D., Gilbert, M. C., Grice, J. D., Hawthorne, F. C., Kato, A., Kisch, H. J., Krivovichev, V. G., Linthout, K., Laird, J., Mandarino, J. A., Maresch, W. V., Nickel, E. H., Rock, N. M. S., Schumacher, J. C., Smith, D. C., Stephenson, N. C. N., Ungaretti, L., Whittaker, E. J. W. & Youzhi, G. 1997. Nomenclature of Amphiboles: Report of the Subcommittee on Amphiboles of the International Mineralogical Association, Commission on New Minerals and Mineral Names. *The Canadian Mineralogist* **35**, 219-246.

Ludwig, K. R. 2003. Isoplot/Ex, rev. 3.00: A Geochronological Toolkit for Microsoft Excel. *Berkeley Geochronology Center Special Publication* **4**, 71pp.

Maboko, M. A. H., McDougall, I., Zeitler, P. K. & Williams, I. S. 1992. Geochronological evidence for ~530-550 Ma juxtaposition of two Proterozoic metamorphic terranes in the Musgrave Ranges, central Australia. *Australian Journal of Earth Sciences* **39**, 457-471.

Marshak, S. & Tabor, J. R. 1989. Structure of the Kingston orocline in the Appalachian fold-thrust belt, New York. *Geological Society of America Bulletin* **101**, 683-701.

Marshak, S., Wilkerson, M. S. & Hsui, A. T. 1992. Generation of curved fold-thrust belts: Insight from simple physical and analytical models. In: *Thrust Tectonics* (edited by McClay, K. R.). Chapman and Hall, London.

Mawby, J. 2000. Metamorphic and geochronologic constraints on Palaeozoic tectonism in the eastern Arunta Inlier, University of Adelaide PhD Thesis.

Miller, J. & Cartwright, I. 1997. Early meteoric fluid flow in the high-grade, low-^{18}O gneisses from the Mallee Bore area, northern Harts Range, central Australia. *Journal of the Geological Society of London* **159**, 839-848.

Moecher, D. P., Anovitz, L. M. & Essene, E. J. 1988. Calculation of clinopyroxene–garnet–plagioclase–quartz geobarometers and application to high grade metamorphic rocks. *Contributions to Mineralogy and Petrology* **100**, 92-106.

Morimoto, N., Fabries, J., Ferguson, A. K., Ginzburg, I. V., Ross, M., Seifert, F. A., Zussman, J., Aoki, K. & Gottardi, G. 1988. Nomenclature of pyroxenes. *Mineralogical Magazine* **52**, 535-550.

Newton, R. C. & Perkins, D. 1982. Thermodynamic calibration of geobarometers based on the assemblages garnet–plagioclase–orthopyroxene–(clinopyroxene)–quartz. *American Mineralogist* **67**, 203-222.

Payne, J., Wade, B. P., Hand, M., Barovich, K., Maidment, D. & Netting, A. 2007. On the optimisation and accuracy of LA-ICP-MS for U-Pb monazite geochronology: Applications from the earliest Palaeoproterozoic to Palaeozoic. *Chemical Geology*, in review.

Payne, J. L., Barovich, K. & Hand, M. 2006. Provenance of metasedimentary rocks in the northern Gawler Craton, Australia: Implications for Palaeoproterozoic reconstructions. *Precambrian Research* **148**, 275-291.

Pearce, N. J. G., Perkins, W. T., Westgate, J. A., Gorton, M. P., Jackson, S. E., Neal, C. R. & Chenery, S. P. 1997. A compilation of new and published major and trace element data for NIST SRM 610 and NIST SRM 612 glass reference materials. *Geostandards Newsletter - Journal of Geostandards and Geoanalysis* **21**(1), 115-144.

Pereira, M. F. & Silva, J. B. 2004. Development of local orthorhombic fabrics within a simple-shear dominated sinistral transpression zone: the Arronches sheared gneisses (Iberian Massif, Portugal). In: *Flow Processes in Faults and Shear Zones* (edited by Alsop, G. I., Holdsworth, R. E., McCaffrey, K. J. W. & Hand, M.) Geological Society of London, Special Publications **224**, 215-227.

Powell, R. 1985. Regression diagnostics and robust regression in geothermometer/geobarometer calibration: the garnet–clinopyroxene thermometer revisited. *Journal of Metamorphic Geology* **3**, 327-342.

Powell, R. & Holland, T. J. P. 1988. An internally consistent thermodynamic dataset with uncertainties and corrections: 3 Applications to geobarometry, worked examples and a computer program. *Journal of Metamorphic Geology* **6**, 173-204.

Powell, R. & Holland, T. J. P. 1994. Optimal geothermometry and geobarometry. *American Mineralogist* **79**(1-2), 120-133.

Powell, R., Holland, T. J. P. & Worley, B. 1998. Calculating phase diagrams involving solid solutions via non-linear equations with examples using THERMOCALC. *Journal of Metamorphic Geology* **16**, 257-271.

Rubatto, D. 2002. Zircon trace element geochemistry: partitioning with garnet and the link between U–Pb ages and metamorphism. *Chemical Geology* **184**, 123-138.

Sandiford, M. & Hand, M. 1998. Controls on the locus of intraplate deformation in central Australia. *Earth and Planetary Science Letters* **162**(1-4), 97-110.

Sandiford, M., Hand, M. & McLaren, S. 2001. Tectonic feedback, intraplate orogeny and the geochemical structure of the crust: a central Australian perspective. In: *Continental reactivation and reworking.* (edited by Miller, J. A., Holdsworth, R. E., Buick, I. S. & Hand, M.). Geological Society of London, Special Publications **184**, 219-236.

Schaltegger, U., Fanning, C. M., Gunther, D., Maurin, J. C., Schulmann, K. & Gebauer, D. 1999. Growth, annealing and recrystallization of zircon and preservation of monazite in high-grade metamorphism: conventional and in-situ U-Pb isotope, cathodoluminescence and microchemical evidence. *Contributions to Mineralogy and Petrology* **134**(2-3), 186-201.

Scrimgeour, I. R. & Close, D. 1999. Regional high-pressure metamorphism during intracratonic deformation: the Petermann Orogeny, central Australia. *Journal of Metamorphic Geology* **17**, 557-572.

Scrimgeour, I. R., Close, D. & Edgoose, C. J. 1999. Petermann Ranges, Northern Territory (Second Edition). 1:250 000 geological map series explanatory notes, SG 52-07. Northern Territory Geological Survey, Darwin.

Shaw, R. D. & Black, L. P. 1991. The history and tectonic implications of the Redbank thrust zone, central Australia, based on structural, metamorphic and Rb-Sr isotopic evidence. *Australian Journal of Earth Sciences* **38**(3), 307-332.

Stacey, J. S. & Kramers, J. D. 1975. Approximation of terrestrial lead isotope evolution by a two-stage model. *Earth and Planetary Science Letters* **26**, 207-221.

Stewart, A. J. 1995. Resolution of conflicting structures and deformation history of the Mount Aloysius granulite massif, western Musgrave Block, central Australia. *AGSO Journal of Australian Geology and Geophysics* **16**, 91-105.

Stewart, A. J. 1997. Geology of the Bates 1:100 000 sheet area (4646), Musgrave Block, Western Australia. Australian Geological Survey Organisation Record, 36 pp.

Stewart, A. J. 1998. Subeclogitic rocks and their implications for crustal structure in the western Musgrave Block, central Australia. *AGSO Research Newsletter* **29**.

Storkey, A. C., Hermann, J., Hand, M. & Buick, I. S. 2005. Using *In Situ* Trace-Element Determinations to Monitor Partial Melting Processes in Metabasites. *Journal of Petrology* **46**(6), 1283-1308.

Sun, S. S., Gray, C. M., Sheraton, J. W. & Glikson, A. Y. 1996. Zircon U–Pb chronology and neodymium isotopic study of tectonothermal and crust-forming events in the Tomkinson Ranges, western Musgrave Block, Western Australia. *AGSO Journal of Australian Geology and Geophysics* **24**, 13-15.

Sun, S. S. & Sheraton, J. W. 1992. Zircon U/Pb chronology, tectonothermal and crust-forming events in the Tomkinson Ranges, Musgrave Block, central Australia. *AGSO Research Newsletter* **17**, 9-10.

Taylor, S. R. & McClennan, S. M. 1985. *The Continental Crustal: Its Composition and Evolution*. Blackwell, Oxford, 312 pp.

Tera, F. & Wasserburg, G. J. 1972. U-Th-Pb systematics in three Apollo-14 basalts and the problem of initial Pb in lunar rocks. *Earth and Planetary Science Letters* **14**, 281-304.

Thigpen, J. R., Law, R. D. & Brown, S. J. 2007. 3-D strain symmetry and vorticity of flow along the Moine Thrust, northwest Scotland: Implications for thrust sheet evolution at mid-crustal levels. *Geological Society of America, Abstracts with Programs* **39**(6), 94.

Van Achterbergh, E., Ryan, C. G., Jackson, S. E. & Griffin, W. L. 2001. Data reduction software for LA-ICP-MS. In: *Laser-ablation-ICPMS in the earth sciences; principles and applications.* (edited by Paul, J. S.). Mineralogical Association of Canada, Ottowa, ON, Canada.

Wade, B. P., Hand, M. & Barovich, K. M. 2005. Nd isotopic and geochemical constraints on provenance of sedimentary rocks in the eastern Officer Basin, Australia: implications for the duration of the intracratonic Petermann Orogeny. *Journal of the Geological Society of London* **162**, 513-530.

Walker-Hallam, A. 2006. Complex strain in mylonites from the western Musgraves, North of the Mann Fault, Western Australia, University of Adelaide Honours Thesis.

Watson, E. B., Wark, D. A. & Thomas, J. B. 2006a. Crystallization thermometers for zircon and rutile. *Contributions to Mineralogy and Petrology* **151**, 413-433.

Watson, E. B., Hayden, L. A., Wark, D. A., Cherniak, D. J., Thomas, J. B. & Manchester, J. E. 2006b. New crystallisation thermometers for zircon, rutile and sphene: calibrations, diffusion considerations, and applications. *Geological Society of America, Abstracts with Programs* **38**, 5.

Wayne, D. M. & Sinha, A. K. 1988. Physical and chemical response of zircons to deformation. *Contributions to Mineralogy and Petrology* **98**, 109-121.

White, R. W. & Clarke, G. L. 1997. The Role of Deformation in Aiding Recrystallisation: an Example from a High-pressure Shear Zone, Central Australia. *Journal of Petrology* **38**(10), 1307-1329.

White, R. W., Clarke, G. L. & Nelson, D. R. 1999. SHRIMP U–Pb zircon dating of Grenville-age events in the western part of the Musgrave Block, central Australia. *Journal of Metamorphic Geology* **17**, 465-481.

White, R. W., Powell, R. & Clarke, G. L. 2002. The interpretation of reaction textures in Fe-rich metapelitic granulites of the Musgrave Block, central Australia: constraints from mineral equilibria calculations in the system K_2O–FeO–MgO–Al_2O_3–SiO_2–H_2O–TiO_2–Fe_2O. *Journal of Metamorphic Geology* **20**, 41-55.

Williams, I. S. 1998. U-Th-Pb Geochronology by Ion Microprobe. In: *Applications of microanalytical techniques to understanding mineralising processes* (edited by McKibben, M. A., Shanks III, W. C. & Ridley, W. I.) Reviews in Economic Geology **7**, 1-35.

15. Figure captions

Figure 1. (a) Regional geological map of the Musgrave Block, showing its position relative to the Amadeus and Officer Basins. Also shown are the locations of the Woodroffe Thrust, Mann Fault, Wankari Detachment Zone and the Petermann Nappe Complex, along with the map sheet areas referred to in Figure 24; (b) Schematic cross section of the western Musgraves, showing the transport directions on major faults and inferred structural arrangement of the Petermann Nappe Complex. Approximate location of section line X-Y is shown in Figure 1a. Both (a) and (b) modified after Edgoose et al., 2004.

Figure 2. Simplified geology of the western Musgrave Block, showing fault trace geometry of the Woodroffe Thrust and Mann Fault, and various locations mentioned in the text. Modified after Scrimgeour & Close (1999) and White et al. (2002).

Figure 3. Outcrop photographs from various locations throughout Bates. (a) Minute mylonitic shear band developed in Pitjantjatjara Supersuite granite 2 km SSE of Mount Daisy Bates. Note that rock adjacent to shear band remains essentially undeformed. Location of sample 187330 A. Length of scale bar is 10 cm; (b) Moderately SE dipping mylonitic shear zone 3 km NNE of Mount Daisy Bates. Shear zone is approximately 50 m wide; (c) Rotated delta porphyroclast in hornblende-bearing felsic mylonite 5 km north of Mount Daisy Bates. Photograph faces NW, indicating top to SW tectonic transport direction of upper plate. Location of sample 187323. Length of scale bar is 10 cm; (d) Isoclinal intrafoliar folds developed in garnet-bearing mylonite on western face of Mount Gosse (lower and upper parts of photograph), separated by a planar mylonitic fabric (centre of photograph). Location of sample 184495. Length of scale bar is 10 cm; (e) Intensely deformed felsic mylonite from northern Bates, 1 km south of inferred Woodroffe Thrust location, containing extensive pseudotachylite veining. Length of scale bar is 10cm; (f) Migmatitic shear zone 4 km SW of Mount Gosse, showing dark plagioclase-rich layers separated by garnetiferous layers. Location of sample 184484. Length of scale bar is 10 cm.

Figure 4. Regional geological map of the eastern Bates 1:100 000 Sheet, showing the distribution of mylonitic outcrops and key locations mentioned in the text. Also shown are structural measurements of mylonitic fabrics and mineral stretching lineations, and the orientation of tectonic transport vectors. Note the location of Figure 5

at Heather's Hill. Modified after Howard et al., 2006. Inset: Stereographic projections of poles to mylonitic fabrics and stretching lineations (left) and equivalent contoured data (right). All structural measurements shown.

Figure 5. (a) Geological map of Heather's Hill, showing the location of NW/SE trending shear zone containing mylonitised granitic gneiss. Modified after Howard et al., 2006; (b) Detailed structural map of the mylonitic shear zone, showing the distribution of mylonite subunits and their associated strain gradients. Also shown is the structural arrangement of planar and linear fabrics.

Figure 6. Photomicrographs of key petrological relationships. All photomicrographs except (c) are in plane polarised light and have a mylonitic foliation parallel to their base. (a) Fine-grained aggregates of recrystallised garnet associated with small biotite needles and magnetite. Sample 184486 B. Width of field of view is 1.5 mm; (b) Relict porphyroclastic garnet in contact with metamorphic biotite and hornblende needles, and separated from fragmented primary hornblende grains by a plagioclase moat. Sample 187305. Width of field of view is 2.5 mm; (c) Linear inclusion trails in primary igneous hornblende surrounded by a fine recrystallised matrix of biotite, hornblende, plagioclase, K-feldspar and quartz. Note associations between titanite, clinozoisite and ilmenite. Sample 155733. Width of field of view is 2 mm; (d) Diamond-shaped titanite porphyroblasts parallel to mylonitic foliation defined by elongate biotite and hornblende needles. Sample 187323. Width of field of view is 1.5 mm; (e) Relict igneous clinopyroxene associated with fine recrystallised aggregates of garnet and hornblende. Sample 184464. Width of field of view is 1.5 mm; (f) Relict igneous orthopyroxene and titanomagnetite enveloped by a corona containing fine-grained garnet, biotite, hornblende and metamorphic clinopyroxene (not visible). Sample 184484. Width of field of view is 1 mm.

Figure 7. Comparison of *P-T* estimates for samples 184464 and 187323 using variable water activities. Each error ellipse represents the average *P-T* conditions (and their associated 1 sigma errors) calculated using progressively increasing aH_2O input values in THERMOCALC v. 3.26, as summarised in Table 2. Superimposed symbols correspond to temperature estimates calculated using garnet-clinopyroxene, garnet-hornblende and garnet-biotite mineral equilibria thermometers for progressively increasing pressure values, also summarised in Table 2. For both samples, plotted symbols jointly fall within one error ellipse (shaded black), making its associated aH_2O value a logical selection for modelled water activity.

Figure 8. Regional geological map of the eastern Bates 1:100 000 Sheet, showing the location of samples selected for thermobarometry and their associated *P-T* estimates. Also shown are *P-T* estimates obtained using the recalculated assemblages of White & Clarke (1997) for samples M010, M213 and M214. All errors quoted are ± 1 sigma. Modified after Howard et al., 2006. Inset: Graphical representation of the variation in *P-T* conditions moving southeast of the immediate hanging wall to the Woodroffe Thrust.

Figure 9. Plots of $^{206}Pb/^{238}U$ age vs. *f* 204 for all titanite samples. (a) Strong positive correlation for samples 184495, 187323 and 187337, obtained in a single SHRIMP session during 2007. Filled symbols represent analyses excluded from the linear regression; (b) Strong negative correlation for sample 155731, obtained in previous SHRIMP session during 2006.

Figure 10. Cathodoluminescence images of representative zircon grains extracted from (a) sample 187325; (b) sample 184468; (c) sample 184464. Displayed spot ages are $^{207}Pb/^{206}Pb$ ages, and spot size shown is 30 μm.

Figure 11. Cathodoluminescence images of representative zircon grains extracted from sample 187323. Displayed spot ages <1000 Ma and >1000 Ma are $^{206}Pb/^{238}U$ and $^{207}Pb/^{206}Pb$ ages, respectively. Spot size shown is 30 μm.

Figure 12. Diagrammatic representations of SHRIMP titanite age data from samples 184495, 187323 and 187337. $^{206}Pb/^{238}U$ weighted averages using 204-corrected age estimates are shown in (a), (c) and (e), with some analyses omitted for reasons mentioned in the text. Tera-Wasserburg concordia plots using uncorrected isotope ratios are shown in (b), (d) and (e), with some analyses excluded for reasons mentioned in the text. Anchor values for each regression line are also shown, along with their associated errors.

Figure 13. Diagrammatic representations of SHRIMP titanite age data from sample 155731. (a) $^{206}Pb/^{238}U$ weighted average using 204-corrected age estimates; (b) Tera-Wasserburg concordia plot using uncorrected isotope ratios, with one analysis excluded for reasons mentioned in the text. Anchor value for the linear regression is also shown with its associated error.

Figure 14. Regional geological map of the eastern Bates 1:100 000 Sheet, showing the location of samples selected for geochronology and their associated age estimates. Also shown are additional age estimates obtained from Spaghetti Hill by Walker-Hallam (2006). All errors quoted are ± 1 sigma. Modified after Howard et al., 2006.

Figure 15. Diagrammatic representations of LA-ICPMS zircon data obtained from sample 187323. (a) Conventional U-Pb concordia plot of all zircon data. Black ellipses indicate data included in additional concordia plots (c) and (e) below. Grey ellipses indicate data excluded from subsequent regressions for reasons mentioned in the text. Inset: Probability density plot of zircons included in the regressions. For data <1000 Ma and >1000 Ma, $^{206}Pb/^{238}U$ and $^{207}Pb/^{206}Pb$ ages are used, respectively; (b) $^{206}Pb/^{238}U$ weighted average of zircon rim analyses included in the regression shown in (c); (c) Tera-Wasserburg U-Pb concordia plot of rim analyses, showing the regression line and age calculations. Common lead composition used as anchor value for regression (0.814 ± 0.023) is based on SHRIMP analysis of titanites from the same sample. See Figure 13d; (d) $^{207}Pb/^{206}Pb$ weighted average of zircon core analyses included in the regression (e) with >90% concordance; (e) Conventional U-Pb concordia plot of core analyses, showing the regression line and age calculations.

Figure 16. Diagrammatic representations of LA-ICPMS zircon data obtained from sample 187325. (a) Conventional U-Pb concordia plot of all zircon data. Black ellipses indicate data included in the regression shown (dash-dotted line). Grey ellipse indicates one analysis excluded from the regression for reasons mentioned in the text. Inset: Probability density plot of zircons included in the regression with >90% concordance. $^{207}Pb/^{206}Pb$ ages are shown as indicated; (b) $^{207}Pb/^{206}Pb$ weighted average of analyses included in the regression with >90% concordance.

Figure 17. Diagrammatic representations of LA-ICPMS zircon data obtained from sample 184464. (a) Conventional U-Pb concordia plot of all zircon data, showing calculated regression line. Black ellipses indicate data included in the concordia calculation shown in (c). Grey ellipses indicate data included in the regression but excluded from the concordia calculation for reasons mentioned in the text. Inset: Probability density plot of zircons included in the regression with >90% concordance. $^{207}Pb/^{206}Pb$ ages are shown as indicated; (b) $^{207}Pb/^{206}Pb$ weighted average of analyses included in the regression with >90% concordance; (c) Conventional U-Pb concordia plot of concordant LA-ICPMS zircon data from Sample 184464, showing the concordia age calculation (grey shaded ellipse).

Figure 18. Diagrammatic representations of LA-ICPMS zircon data obtained from sample 184468. (a) Conventional U-Pb concordia plot of all zircon data. Black ellipses indicate data included in the regression shown (dash-dotted line). Grey ellipses indicate data excluded from the regression for reasons mentioned in the text. Inset: Probability density plot of zircons included in the regression with >90% concordance. $^{207}Pb/^{206}Pb$ ages are shown as indicated; (b) $^{207}Pb/^{206}Pb$ weighted average of analyses included in the regression with >90% concordance.

Figure 19. Graphical comparison of temperature estimates obtained using trace element thermometry and THERMOCALC modelling of equilibrium mineral assemblages. Also shown is the regional pattern of increasing pressures and temperatures moving southeast of the Woodroffe Thrust. Note that the temperature estimates obtained using Ti and Zr thermometry generally conform to the established trend presented in Figure 6. Sample 155735 is an exception for reasons mentioned in the text.

Figure 20. Regional geological map of the eastern Bates 1:100 000 Sheet, showing the location of all samples and their associated *P-T*, age and trace element thermometry temperature estimates. Modified after Howard et al., 2006.

Figure 21. Chondrite normalised REE patterns of titanite (a-d) and zircon (e-f). Zircon cores are shown as shaded patterns, while recrystallised rims are shown as unbroken lines. Normalisation after Taylor and McClennan (1985).

Figure 22. Simplified geology of the western Musgrave Block, showing the distribution of *P-T* estimates obtained from the high grade terrane between the Woodroffe Thrust and Mann Fault. Numbers represent calculated temperatures in °C (± *c.* 50°C) and pressures in kbar (± *c.* 1 kbar). Calculations provided by Camacho et al. (1997) are obtained from the Davenport Shear Zone, Musgrave Ranges, approximately 100 km east of map limit. Modified after Scrimgeour & Close (1999) and White et al. (2002).

Figure 23. Plot of Th/U vs. age estimate for zircon grains on which multiple analyses were conducted. Note that rim analyses are consistently lower in Th than core analyses from the same grain. Grey shaded area indicates rim analyses below conventional cut off for metamorphic zircon (*c.* 0.10). Displayed ages <1000 Ma and >1000 Ma are $^{206}Pb/^{238}U$ and $^{207}Pb/^{206}Pb$ ages, respectively.

Figure 24. Relationship between field observations at Heather's Hill and proposed strain partitioning models. (a) Structural arrangement of mylonitic shear zone at Heather's Hill, showing the progressive rotation of stretching lineations in response to variable strain intensity, and the inferred division of discrete rock packages into coaxial (1) and non-coaxial (2) strain domains; (b) Pure shear model, showing the development of non-coaxial strain and its associated linear and planar fabric elements; (c) Simple shear model, showing the development of rotational strain and its associated linear and planar fabric elements. Also shown are pre- and post-strain configurations of the finite strain ellipsoid in response to both pure and simple shear.

Figure 25. Comparison of structural measurements from Bates with adjacent areas of the western Musgraves. The location of each field area is shown in Figure 1.

Table 1 – Summary of mineral chemistry from all petrological groups

	Group 1	Group 2	Group 3	Group 4
Garnet				
X_{Fe}	0.54 - 0.61	0.40 - 0.57	0.54 - 0.64	0.53 - 0.64
X_{Ca}	0.13 - 0.24	0.28 - 0.43	0.22 - 0.29	0.14 - 0.20
X_{Mg}	0.09 - 0.24	0.03 - 0.10	0.09 - 0.15	0.20 - 0.25
X_{Mn}	0.02 - 0.04	0.04 - 0.15	0.03 - 0.04	0.02 - 0.06
Biotite				
X_{Ti}	0.05 - 0.11	0.04 - 0.08	0.08 - 0.13	0.01 - 0.11
X_{Fe}	0.33 - 0.48	0.35 - 0.60	0.32 - 0.52	0.17- 0.28
X_{Al}^{VI}	0.00 - 0.10	0.01 - 0.12	0.00 - 0.01	0.00 - 0.01
X_{Mg}	0.37 - 0.61	0.29 - 0.54	0.37 - 0.59	0.61 - 0.82
X_{Na}	0.00 - 0.01	0.00 - 0.02	0.00 - 0.01	0.00 - 0.02
Hornblende				
X_{Fe}	-	0.46 - 0.76	0.40 - 0.56	0.25 - 0.31
X_{Mg}	-	0.24 - 0.54	0.44 - 0.60	0.69 - 0.75
Clinopyroxene				
X_{Ca}	-	-	0.45 - 0.46	0.45 - 0.46
X_{Mg}	-	-	0.28 - 0.34	*c.* 0.40
X_{Fe}	-	-	0.20 - 0.30	0.14 - 0.15
Plagioclase				
X_{Na}	0.75 - 0.82	0.56 - 0.78	0.78 - 0.84	0.72 - 0.84
X_{Ca}	0.18 - 0.25	0.22 - 0.39	0.16 - 0.22	0.16 - 0.28
X_{K}	0.005 - 0.009	0.007 - 0.020	0.007 - 0.013	0.004 - 0.021
K-feldspar				
X_{K}	0.91 - 0.95	0.87 - 0.91	0.87 - 0.93	0.83 - 0.94
X_{Na}	0.05 - 0.09	0.09 - 0.13	0.07 - 0.13	0.06 - 0.17
X_{Ca}	0.000 - 0.002	0.000 - 0.001	0.000 - 0.004	0.000 - 0.005
Ilmenite				
X_{Ilm}	-	0.96 - 1.00	*c.* 0.90	-
X_{Fe}	-	0.49 - 0.50	*c.* 0.55	-
X_{Ti}	-	0.48 - 0.50	*c.* 0.45	-
X_{Mn}	-	0.01 - 0.02	-	-
Titanomagnetite				
X_{Fe}	-	-	*c.* 0.86	0.84 - 0.85
X_{Ti}	-	-	*c.* 0.14	0.15 - 0.16

Table 3 – Summary of *P-T* calculations

Sample No.	Average *P* (kbar, ±1σ)	Average *T* (°C, ±1σ)	Average *P-T* (±1σ)	Geothermal gradient (°C km^{-1})	*a*H_2O
Group 1 – Felsic mylonites					
184486 B	10.79 ± 0.90	770 ± 48	776 ± 66, 10.7 ± 1.2	*c.* 22	0.15
185674	11.81 ± 0.88	695 ± 44	712 ± 47, 12.0 ± 0.9	*c.* 18	0.25
187314	9.62 ± 0.78	622 ± 38	622 ± 34, 9.6 ± 0.8	*c.* 19	0.50
Group 2 – Hornblende-bearing felsic mylonites					
155733	11.05 ± 0.75	754 ± 50	760 ± 72, 11.3 ± 1.1	*c.* 20	0.50
155735	10.18 ± 0.57	741 ± 70	739 ± 76, 10.1 ± 0.8	*c.* 22	0.75
187305	11.04 ± 0.67	688 ± 38	692 ± 38, 10.7 ± 0.7	*c.* 19	0.50
187323	10.49 ± 0.65	677 ± 48	676 ± 70, 10.8 ± 1.0	*c.* 19	0.75
187330 A	11.38 ± 0.69	644 ± 30	650 ± 35, 11.8 ± 0.8	*c.* 17	0.50
Group 3 – Clinopyroxene-bearing felsic mylonites					
184464	11.22 ± 0.74	714 ± 27	712 ± 35, 10.7 ± 0.9	*c.* 20	0.25
184468	11.60 ± 0.74	699 ± 32	718 ± 37, 11.8 ± 0.9	*c.* 18	0.25
Group 4 – Migmatitic mylonites					
184484	11.87 ± 0.97	774 ± 38	782 ± 40, 11.8 ± 1.0	*c.* 20	0.25
185679	10.42 ± 1.12	787 ± 44	785 ± 47, 10.7 ± 1.2	*c.* 22	0.50

Recalculated assemblages (White & Clarke, 1997)

Sample No.	Average *P* (kbar, ±1σ)	Average *T* (°C, ±1σ)	Average *P-T* (±1σ)	Geothermal gradient (°C km^{-1})	*a*H_2O
M214					
Core	13.32 ± 0.80	717 ± 32	733 ± 37, 13.1 ± 0.9	*c.* 17	0.25
Rim	11.11 ± 0.79	781 ± 34	795 ± 40, 11.6 ± 0.9	*c.* 21	0.25
M213					
Core	13.13 ± 1.06	710 ± 40	732 ± 46, 13.0 ± 1.2	*c.* 17	0.25
Rim	11.33 ± 0.83	761 ± 34	755 ± 36, 11.4 ± 0.9	*c.* 20	0.25
M010					
Core	10.94 ± 0.64	743 ± 24	752 ± 28, 11.0 ± 0.7	*c.* 21	0.25
Rim	8.98 ± 0.77	791 ± 39	777 ± 33, 9.1 ± 0.8	*c.* 26	0.25

Table 4 – SHRIMP titanite age data

Sample 184495						Isotope Ratios*											Ages (Ma)*				
Spot name	**U (ppm)**	**Th (ppm)**	**Th/U**	**Pb (ppm)**	***f* 204 (%)**	**$^{207}Pb/^{206}Pb$**	**±1σ**	**$^{208}Pb/^{206}Pb$**	**±1σ**	**$^{206}Pb/^{238}U$**	**±1σ**	**$^{207}Pb/^{235}U$**	**±1σ**	**$^{208}Pb/^{232}Th$**	**±1σ**	**rho**	**$^{206}Pb/^{238}U$**	**±1σ**	**$^{207}Pb/^{206}Pb$**	**±1σ**	**Conc. (%)**
495-01.1	432	94	0.22	42	0.0336	0.0593	0.0018	0.0923	0.0043	0.0879	0.0011	0.7186	0.0245	0.0373	0.0018	0.351	543	6	578	66	94
495-02.1	305	101	0.33	34	0.0513	0.0573	0.0032	0.1932	0.0079	0.0871	0.0011	0.6876	0.0402	0.0510	0.0022	0.219	538	7	502	122	107
495-03.1	238	104	0.44	26	0.0588	0.0607	0.0053	0.1563	0.0128	0.0873	0.0013	0.7311	0.0655	0.0313	0.0026	0.164	539	8	630	187	86
495-04.1	165	70	0.42	20	0.0894	0.0626	0.0057	0.1478	0.0138	0.0870	0.0013	0.7513	0.0704	0.0303	0.0029	0.155	538	7	696	194	77
495-05.1	32	8	0.25	12	0.3706	0.1287	0.0268	0.3761	0.0620	0.1054	0.0032	1.8691	0.4004	0.1576	0.0264	0.142	646	19	2080	374	31
495-06.1	249	57	0.23	25	0.0594	0.0560	0.0038	0.0674	0.0092	0.0857	0.0011	0.6610	0.0470	0.0252	0.0035	0.188	530	7	451	152	118
495-07.1	380	137	0.36	44	0.0501	0.0618	0.0027	0.2875	0.0067	0.0867	0.0011	0.7383	0.0345	0.0692	0.0018	0.267	536	6	665	93	81
495-08.1	396	95	0.24	40	0.0396	0.0569	0.0023	0.0973	0.0055	0.0889	0.0011	0.6975	0.0303	0.0362	0.0021	0.283	549	6	487	89	113
495-09.1	243	57	0.23	28	0.0742	0.0563	0.0035	0.1177	0.0084	0.0891	0.0011	0.6909	0.0448	0.0450	0.0033	0.198	550	7	463	138	119
495-10.1	279	79	0.28	30	0.0632	0.0570	0.0040	0.1142	0.0097	0.0870	0.0012	0.6831	0.0499	0.0350	0.0030	0.182	538	7	490	155	110
495-11.1	222	78	0.35	24	0.0663	0.0560	0.0043	0.1222	0.0103	0.0857	0.0012	0.6621	0.0523	0.0300	0.0026	0.170	530	7	454	170	117
495-12.1	374	132	0.35	37	0.0349	0.0601	0.0025	0.1236	0.0061	0.0865	0.0011	0.7164	0.0326	0.0302	0.0016	0.276	535	6	606	91	88
495-13.1	606	168	0.28	54	0.0289	0.0561	0.0018	0.0982	0.0043	0.0807	0.0010	0.6244	0.0219	0.0286	0.0013	0.346	500	6	457	70	110

Sample 187323						Isotope Ratios*											Ages (Ma)*				
Spot name	**U (ppm)**	**Th (ppm)**	**Th/U**	**Pb (ppm)**	***f* 204 (%)**	**$^{207}Pb/^{206}Pb$**	**±1σ**	**$^{208}Pb/^{206}Pb$**	**±1σ**	**$^{206}Pb/^{238}U$**	**±1σ**	**$^{207}Pb/^{235}U$**	**±1σ**	**$^{208}Pb/^{232}Th$**	**±1σ**	**rho**	**$^{206}Pb/^{238}U$**	**±1σ**	**$^{207}Pb/^{206}Pb$**	**±1σ**	**Conc. (%)**
323-01.1	34	5	0.16	9	0.2630	0.0913	0.0213	0.2471	0.0498	0.1049	0.0029	1.3207	0.3140	0.1639	0.0334	0.116	643	17	1453	456	44
323-02.1	112	19	0.17	14	0.1007	0.0458	0.0068	0.0363	0.0163	0.0939	0.0015	0.5923	0.0896	0.0203	0.0091	0.102	579	9	0	17	0
323-03.1	44	8	0.19	8	0.2068	0.0655	0.0171	0.1188	0.0413	0.0967	0.0024	0.8733	0.2321	0.0599	0.0209	0.095	595	14	790	571	75
323-04.1	94	14	0.15	11	0.0829	0.0559	0.0067	0.0511	0.0160	0.0929	0.0015	0.7158	0.0876	0.0316	0.0099	0.129	572	9	448	267	128
323-05.1	43	7	0.16	8	0.2367	0.0505	0.0203	0.0667	0.0489	0.0907	0.0026	0.6312	0.2560	0.0390	0.0286	0.070	559	15	218	732	257
323-06.1	42	8	0.20	9	0.2713	0.0403	0.0212	0.0838	0.0511	0.0936	0.0027	0.5201	0.2755	0.0390	0.0238	0.055	577	16	0	18	0
323-07.1	81	17	0.21	13	0.1505	0.0724	0.0107	0.1430	0.0257	0.0947	0.0018	0.9461	0.1427	0.0648	0.0117	0.125	583	11	998	303	58
323-08.1	27	4	0.17	7	0.3105	0.0989	0.0305	0.2713	0.0713	0.0981	0.0036	1.3374	0.4217	0.1592	0.0423	0.115	603	21	1604	605	38
323-09.1	29	5	0.17	7	0.3180	0.0584	0.0278	0.1329	0.0670	0.0957	0.0034	0.7705	0.3710	0.0769	0.0389	0.075	589	20	545	797	108
323-10.1	69	16	0.23	10	0.1328	0.0670	0.0110	0.1154	0.0264	0.0925	0.0018	0.8547	0.1428	0.0462	0.0106	0.116	570	11	839	346	68
323-11.1	42	8	0.19	9	0.2322	0.0660	0.0184	0.1390	0.0443	0.0989	0.0026	0.9000	0.2544	0.0713	0.0228	0.093	608	15	806	609	75
323-12.1	113	21	0.18	13	0.0603	0.0657	0.0054	0.0897	0.0129	0.0947	0.0014	0.8584	0.0728	0.0462	0.0067	0.173	583	8	798	172	73
323-13.1	54	7	0.14	10	0.2142	0.0633	0.0157	0.1921	0.0380	0.0952	0.0022	0.8317	0.2092	0.1355	0.0270	0.093	586	13	719	544	82
323-14.1	105	18	0.17	12	0.0785	0.0546	0.0061	0.0554	0.0146	0.0925	0.0014	0.6964	0.0795	0.0305	0.0080	0.134	570	8	395	251	144
323-15.1	149	26	0.17	16	0.0518	0.0622	0.0043	0.0675	0.0104	0.0898	0.0012	0.7710	0.0560	0.0354	0.0055	0.191	555	7	682	149	81

Sample 187337						Isotope Ratios*											Ages (Ma)*				
Spot name	**U (ppm)**	**Th (ppm)**	**Th/U**	**Pb (ppm)**	***f* 204 (%)**	**$^{207}Pb/^{206}Pb$**	**±1σ**	**$^{208}Pb/^{206}Pb$**	**±1σ**	**$^{206}Pb/^{238}U$**	**±1σ**	**$^{207}Pb/^{235}U$**	**±1σ**	**$^{208}Pb/^{232}Th$**	**±1σ**	**rho**	**$^{206}Pb/^{238}U$**	**±1σ**	**$^{207}Pb/^{206}Pb$**	**±1σ**	**Conc. (%)**
337-01.1	23	4	0.16	7	0.4271	0.0245	0.0329	-0.0306	0.0795	0.0878	0.0036	0.2967	0.4001	-0.0165	-0.0428	0.030	543	21	0	15	0
337-02.1	60	17	0.29	10	0.1720	0.0694	0.0111	0.1205	0.0269	0.0938	0.0018	0.8976	0.1464	0.0391	0.0088	0.116	578	10	911	334	63
337-03.1	17	3	0.15	7	0.4151	0.0982	0.0388	0.2367	0.0903	0.1030	0.0045	1.3955	0.5617	0.1641	0.0631	0.109	632	26	1591	803	40
337-04.1	39	4	0.11	8	0.2038	0.0953	0.0169	0.1431	0.0391	0.0953	0.0022	1.2521	0.2275	0.1217	0.0334	0.129	587	13	1533	339	38
337-05.1	10	1	0.08	7	0.6028	0.0714	0.0849	0.1104	0.2005	0.1007	0.0094	0.9910	1.1935	0.1437	0.2613	0.077	618	55	969	1447	64
337-06.1	89	17	0.20	13	0.1393	0.0712	0.0098	0.0775	0.0234	0.0968	0.0017	0.9504	0.1336	0.0383	0.0116	0.128	596	10	964	283	62
337-07.1	9	3	0.32	10	0.5172	0.2377	0.0612	0.6237	0.1413	0.1860	0.0108	6.0955	1.6506	0.3650	0.0857	0.214	1100	59	3105	422	35
337-08.1	17	4	0.22	9	0.4818	0.1044	0.0471	0.3186	0.1083	0.1110	0.0054	1.5980	0.7346	0.1584	0.0545	0.106	679	31	1703	930	40
337-09.1	36	28	0.76	9	0.3487	0.0366	0.0248	0.1823	0.0602	0.0852	0.0027	0.4293	0.2928	0.0203	0.0067	0.047	527	16	0	847	0
337-11.1	12	2	0.18	7	0.5583	0.0962	0.0672	0.3109	0.1576	0.1074	0.0077	1.4241	1.0129	0.1813	0.0929	0.101	657	45	1552	940	42
337-12.1	26	10	0.37	6	0.2661	0.0951	0.0247	0.2622	0.0579	0.0953	0.0029	1.2492	0.3321	0.0681	0.0152	0.116	587	17	1530	508	38
337-13.1	10	1	0.13	8	0.7605	0.0127	0.1361	-0.1400	0.3297	0.0679	0.0104	0.1190	1.2759	-0.0750	-0.1771	0.014	423	63	0	16	0
337-14.1	9	1	0.15	9	0.7816	-0.0075	0.1532	-0.0544	0.3720	0.0749	0.0130	-0.0771	-1.5801	-0.0267	-0.1828	0.008	466	78	0	17	0

Sample 155731						Isotope Ratios*											Ages (Ma)*				
Spot name	**U (ppm)**	**Th (ppm)**	**Th/U**	**Pb (ppm)**	***f* 204 (%)**	**$^{207}Pb/^{206}Pb$**	**±1σ**	**$^{208}Pb/^{206}Pb$**	**±1σ**	**$^{206}Pb/^{238}U$**	**±1σ**	**$^{207}Pb/^{235}U$**	**±1σ**	**$^{208}Pb/^{232}Th$**	**±1σ**	**rho**	**$^{206}Pb/^{238}U$**	**±1σ**	**$^{207}Pb/^{206}Pb$**	**±1σ**	**Conc. (%)**
731-01.1	29	5	0.19	7	0.3724	0.0250	0.0419	-0.0428	0.1014	0.0853	0.0045	0.2945	0.4952	-0.0192	-0.0456	0.031	528	27	0	23	0
731-02.1	37	6	0.162	7	0.2918	0.0323	0.0306	-0.0251	0.0740	0.0836	0.0034	0.3719	0.3549	-0.0129	-0.0381	0.043	517	20	0	23	0
731-03.1	41	10	0.254	8	0.2564	0.0429	0.0247	0.0281	0.0597	0.0860	0.0029	0.5087	0.2953	0.0095	0.0202	0.058	532	17	0	21	0
731-04.1	53	9	0.176	10	0.2649	0.0564	0.0252	0.0574	0.0609	0.0822	0.0027	0.6391	0.2890	0.0267	0.0284	0.074	509	16	467	768	109
731-05.1	54	10	0.178	9	0.2204	0.0351	0.0188	-0.0208	0.0454	0.0857	0.0023	0.4141	0.2235	-0.0100	-0.0219	0.050	530	14	0	19	0
731-06.1	12	2	0.182	9	0.7229	0.0182	0.1516	-0.0597	0.3674	0.0765	0.0132	0.1918	1.6037	-0.0251	-0.1544	0.021	475	79	0	23	0
731-07.1	25	5	0.207	7	0.3968	0.0454	0.0462	0.0116	0.1116	0.0809	0.0046	0.5059	0.5193	0.0045	0.0436	0.056	501	28	0	23	0
731-08.1	20	6	0.313	10	0.6578	-0.0470	0.1048	-0.1948	0.2548	0.0691	0.0083	-0.4477	-0.9931	-0.0429	-0.0564	0.054	430	50	0	20	0
731-09.1	21	3	0.127	7	0.4340	0.0748	0.0542	0.1111	0.1309	0.0884	0.0058	0.9118	0.6705	0.0774	0.0915	0.090	546	35	1062	1021	51
731-10.1	25	4	0.166	7	0.3593	0.0788	0.0406	0.0700	0.0979	0.0901	0.0046	0.9790	0.5131	0.0381	0.0533	0.098	556	27	1167	780	48

* All isotope ratios corrected for common Pb following the method of Stacey & Kramers (1975). Displayed ratios and ages are ^{204}Pb corrected.

Table 5 – LA-ICPMS zircon age data

Sample 184468		Isotope Ratios									Ages (Ma)									
Spot name	**Th/U**	**$^{207}Pb/^{206}Pb$**	**±1σ**	**$^{206}Pb/^{238}U$**	**±1σ**	**$^{207}Pb/^{235}U$**	**±1σ**	**$^{208}Pb/^{232}Th$**	**±1σ**	**rho**	**$^{207}Pb/^{206}Pb$**	**±1σ**	**$^{206}Pb/^{238}U$**	**±1σ**	**$^{207}Pb/^{235}U$**	**±1σ**	**$^{208}Pb/^{232}Th$**	**±1σ**	**Conc. (%)**	**Eff. Age***
Spot 1	0.37	0.0794	0.0011	0.1908	0.0026	2.0872	0.0326	0.0465	0.0007	0.864	1182	27	1125	14	1145	11	918	14	95	1182
Spot 2	0.52	0.0792	0.0011	0.1798	0.0021	1.9643	0.0275	0.0578	0.0008	0.850	1178	26	1066	12	1103	9	1135	15	90	1178
Spot 3	0.82	0.0793	0.0009	0.1834	0.0023	2.0061	0.0265	0.0484	0.0005	0.934	1181	23	1085	12	1118	9	956	10	92	1181
Spot 4	0.45	0.0783	0.0011	0.1903	0.0024	2.0548	0.0308	0.0538	0.0008	0.829	1156	28	1123	13	1134	10	1059	16	97	1156
Spot 5	0.30	0.0795	0.0010	0.1958	0.0027	2.1445	0.0323	0.0480	0.0007	0.900	1184	25	1153	14	1163	10	948	14	97	1184
Spot 6	0.46	0.0793	0.0010	0.1928	0.0023	2.1069	0.0292	0.0561	0.0008	0.867	1179	26	1137	13	1151	10	1104	16	96	1179
Spot 7	0.52	0.0792	0.0010	0.1858	0.0023	2.0290	0.0279	0.0528	0.0007	0.902	1178	24	1098	13	1125	9	1040	13	93	1178
Spot 9	0.43	0.0787	0.0010	0.2030	0.0025	2.2026	0.0314	0.0557	0.0008	0.878	1164	26	1192	14	1182	10	1096	16	102	1164
Spot 10	0.51	0.0789	0.0012	0.1952	0.0024	2.1226	0.0320	0.0593	0.0010	0.810	1170	29	1149	13	1156	10	1164	18	98	1170
Spot 11	0.56	0.0791	0.0010	0.1902	0.0024	2.0745	0.0289	0.0527	0.0007	0.916	1175	24	1123	13	1140	10	1038	13	96	1175
Spot 12	0.43	0.0798	0.0011	0.1918	0.0024	2.1087	0.0311	0.0608	0.0010	0.842	1192	27	1131	13	1152	10	1194	19	95	1192
Spot 13	0.39	0.0793	0.0011	0.1946	0.0026	2.1266	0.0329	0.0531	0.0009	0.875	1180	26	1146	14	1158	11	1045	16	97	1180
Spot 14	0.62	0.0789	0.0010	0.1453	0.0018	1.6052	0.0206	0.0456	0.0006	0.851	1172	28	874	10	891	9	901	12	75	1172
Spot 15	0.79	0.0793	0.0009	0.1997	0.0025	2.1827	0.0291	0.0619	0.0008	0.921	1180	23	1174	13	1176	9	1215	15	100	1180
Spot 16	0.44	0.0784	0.0012	0.1899	0.0024	2.0495	0.0315	0.0597	0.0011	0.811	1156	29	1121	13	1132	11	1171	20	97	1156
Spot 17	0.47	0.0793	0.0010	0.1939	0.0025	2.1202	0.0303	0.0602	0.0009	0.889	1180	25	1143	13	1155	10	1182	17	97	1180
Spot 21	0.44	0.0786	0.0017	0.2037	0.0036	2.2077	0.0506	0.0524	0.0012	0.761	1163	41	1195	19	1184	16	1032	24	103	1163
Spot 22	0.52	0.0786	0.0010	0.1922	0.0027	2.0831	0.0321	0.0615	0.0009	0.894	1163	26	1133	14	1143	11	1206	18	97	1163
Spot 23	0.46	0.0793	0.0010	0.1883	0.0026	2.0589	0.0318	0.0598	0.0009	0.907	1181	25	1112	14	1135	11	1174	17	94	1181
Spot 24	0.63	0.0792	0.0011	0.1931	0.0027	2.1075	0.0337	0.0610	0.0009	0.878	1176	27	1138	15	1151	11	1196	17	97	1176
Spot 25	0.42	0.0791	0.0016	0.1926	0.0030	2.0994	0.0450	0.0575	0.0014	0.727	1174	39	1135	16	1149	15	1129	26	97	1174
Spot 26	0.43	0.0794	0.0010	0.1910	0.0026	2.0912	0.0316	0.0592	0.0009	0.910	1183	25	1127	14	1146	10	1162	17	95	1183
Spot 27	1.07	0.0810	0.0010	0.1933	0.0026	2.1574	0.0309	0.0628	0.0008	0.940	1221	23	1139	14	1167	10	1231	16	93	1221
Spot 28	0.48	0.0864	0.0010	0.1949	0.0026	2.3202	0.0330	0.0670	0.0010	0.939	1346	23	1148	14	1219	10	1311	18	85	1346
Spot 29	0.45	0.0820	0.0009	0.1926	0.0025	2.1750	0.0298	0.0611	0.0009	0.962	1246	22	1135	14	1173	10	1198	17	91	1246
Spot 30	0.43	0.0792	0.0010	0.1383	0.0020	1.5108	0.0235	0.0441	0.0007	0.909	1178	25	835	11	935	10	872	13	71	1178
Spot 31	0.44	0.0789	0.0011	0.1989	0.0028	2.1627	0.0346	0.0610	0.0010	0.876	1170	27	1169	15	1169	11	1197	19	100	1170
Spot 32	0.60	0.0790	0.0009	0.1915	0.0030	2.0871	0.0332	0.0483	0.0007	0.995	1173	22	1130	16	1145	11	954	14	96	1173

Sample 184464		Isotope Ratios									Ages (Ma)									
Spot name	**Th/U**	**$^{207}Pb/^{206}Pb$**	**±1σ**	**$^{206}Pb/^{238}U$**	**±1σ**	**$^{207}Pb/^{235}U$**	**±1σ**	**$^{208}Pb/^{232}Th$**	**±1σ**	**rho**	**$^{207}Pb/^{206}Pb$**	**±1σ**	**$^{206}Pb/^{238}U$**	**±1σ**	**$^{207}Pb/^{235}U$**	**±1σ**	**$^{208}Pb/^{232}Th$**	**±1σ**	**Conc. (%)**	**Eff. Age***
Spot 1	0.73	0.0807	0.0017	0.1973	0.0030	2.1944	0.0474	0.0660	0.0014	0.704	1214	41	1161	16	1179	15	1291	26	96	1214
Spot 2	0.86	0.0806	0.0029	0.2005	0.0038	2.2263	0.0772	0.0687	0.0021	0.545	1212	69	1178	20	1189	24	1343	39	97	1212
Spot 3	0.94	0.0798	0.0015	0.1812	0.0027	1.9944	0.0403	0.0600	0.0011	0.735	1193	38	1074	15	1114	14	1178	20	90	1193
Spot 4	0.81	0.0814	0.0024	0.2093	0.0037	2.3491	0.0677	0.0703	0.0018	0.605	1231	56	1225	19	1227	21	1374	34	100	1231
Spot 5	1.10	0.0821	0.0014	0.2122	0.0031	2.4010	0.0451	0.0682	0.0011	0.789	1248	33	1240	17	1243	13	1334	20	99	1248
Spot 6	1.47	0.0798	0.0014	0.2031	0.0030	2.2347	0.0422	0.0578	0.0009	0.792	1192	34	1192	16	1192	13	1135	17	100	1192
Spot 7	0.71	0.0806	0.0016	0.1993	0.0030	2.2146	0.0449	0.0597	0.0012	0.738	1212	37	1172	16	1186	14	1172	22	97	1212
Spot 8	0.80	0.0794	0.0035	0.2038	0.0049	2.2338	0.0963	0.0380	0.0016	0.555	1182	85	1196	26	1192	30	753	31	101	1182
Spot 9	0.76	0.0792	0.0014	0.2047	0.0031	2.2334	0.0434	0.0592	0.0011	0.772	1176	35	1200	16	1192	14	1162	20	102	1176
Spot 10	0.75	0.0800	0.0015	0.2022	0.0031	2.2294	0.0440	0.0588	0.0010	0.766	1197	36	1187	16	1190	14	1154	20	99	1197
Spot 11	0.74	0.0818	0.0020	0.2121	0.0034	2.3906	0.0592	0.0583	0.0014	0.644	1240	47	1240	18	1240	18	1146	26	100	1240
Spot 13	1.43	0.0816	0.0020	0.1856	0.0031	2.0852	0.0520	0.0457	0.0012	0.667	1236	47	1097	17	1144	17	904	24	89	1236
Spot 14	1.25	0.0818	0.0018	0.1745	0.0024	1.9716	0.0429	0.0460	0.0009	0.638	1241	43	1037	13	1106	15	910	18	84	1241
Spot 15	0.83	0.0796	0.0021	0.2020	0.0034	2.2222	0.0592	0.0458	0.0011	0.629	1186	52	1186	18	1188	19	905	22	100	1186
Spot 16	0.92	0.0821	0.0011	0.1799	0.0022	2.0319	0.0305	0.0514	0.0007	0.825	1247	27	1067	12	1126	10	1014	13	86	1247

Sample 187323		Isotope Ratios									Ages (Ma)									
Spot name	**Th/U**	**$^{207}Pb/^{206}Pb$**	**±1σ**	**$^{206}Pb/^{238}U$**	**±1σ**	**$^{207}Pb/^{235}U$**	**±1σ**	**$^{208}Pb/^{232}Th$**	**±1σ**	**rho**	**$^{207}Pb/^{206}Pb$**	**±1σ**	**$^{206}Pb/^{238}U$**	**±1σ**	**$^{207}Pb/^{235}U$**	**±1σ**	**$^{208}Pb/^{232}Th$**	**±1σ**	**Conc. (%)**	**Eff. Age***
Spot 1	0.14	0.0830	0.0021	0.0524	0.0009	0.5992	0.0149	0.0167	0.0005	0.654	1269	47	329	5	477	9	335	10	26	329
Spot 2	0.08	0.0743	0.0009	0.0902	0.0012	0.9241	0.0131	0.0203	0.0003	0.956	1050	23	557	7	665	7	406	7	53	557
Spot 3	0.10	0.0801	0.0009	0.0894	0.0012	0.9864	0.0133	0.0544	0.0007	0.961	1198	22	552	7	697	7	1071	13	46	552
Spot 4	0.57	0.0711	0.0016	0.0665	0.0010	0.6513	0.0150	0.0059	0.0002	0.667	961	45	415	6	509	9	119	3	43	415
Spot 5	0.17	0.0819	0.0010	0.1838	0.0025	2.0735	0.0300	0.0578	0.0009	0.942	1242	23	1088	14	1140	10	1137	17	88	1242
Spot 6	0.41	0.0795	0.0013	0.1823	0.0025	2.0000	0.0340	0.0195	0.0005	0.791	1186	31	1079	13	1116	12	391	9	91	1186
Spot 7	0.02	0.0659	0.0019	0.0908	0.0015	0.8241	0.0232	0.0749	0.0056	0.575	802	58	560	9	610	13	1459	105	70	560
Spot 8	0.05	0.0674	0.0012	0.0890	0.0012	0.8269	0.0155	0.0628	0.0019	0.737	849	37	550	7	612	9	1231	35	65	550
Spot 9	0.21	0.0789	0.0008	0.2004	0.0027	2.1780	0.0292	0.0566	0.0007	0.987	1169	21	1177	14	1174	9	1112	14	101	1169
Spot 10	0.24	0.0783	0.0008	0.1928	0.0026	2.0809	0.0272	0.0581	0.0007	0.981	1155	20	1136	14	1143	9	1142	13	98	1155
Spot 11	0.48	0.1074	0.0037	0.0902	0.0018	1.3343	0.0438	0.0625	0.0018	0.614	1755	61	557	11	861	19	1226	34	32	557
Spot 12	0.28	0.0774	0.0011	0.1914	0.0025	2.0423	0.0322	0.0536	0.0011	0.843	1131	28	1129	14	1130	11	1056	20	100	1131
Spot 13	0.13	0.1756	0.0048	0.0864	0.0017	2.0914	0.0550	0.1417	0.0047	0.762	2612	45	534	10	1146	18	2678	82	20	534
Spot 14	0.06	0.0773	0.0014	0.0887	0.0013	0.9450	0.0179	0.0699	0.0022	0.764	1128	35	548	8	676	9	1366	41	49	548
Spot 15	0.53	0.0902	0.0026	0.0940	0.0016	1.1690	0.0328	0.0337	0.0010	0.606	1429	54	579	9	786	15	669	20	41	579
Spot 16	1.08	0.1329	0.0046	0.0725	0.0015	1.3287	0.0427	0.0395	0.0010	0.630	2137	59	451	9	858	19	784	20	21	451
Spot 17	1.16	0.2340	0.0198	0.0399	0.0020	1.2789	0.0910	0.0348	0.0027	0.694	3079	129	252	12	836	41	691	53	8	252
Spot 18	0.04	0.0741	0.0013	0.0886	0.0014	0.9049	0.0176	0.0705	0.0025	0.784	1045	35	547	8	654	9	1377	47	52	547
Spot 19	0.18	0.0744	0.0016	0.1681	0.0025	1.7228	0.0373	0.0420	0.0017	0.673	1051	42	1002	14	1017	14	831	32	95	1051
Spot 20	0.28	0.0830	0.0010	0.0900	0.0012	1.0289	0.0144	0.0265	0.0004	0.954	1268	22	555	7	718	7	529	8	44	555
Spot 21	0.38	0.0789	0.0017	0.1889	0.0028	2.0544	0.0457	0.0472	0.0015	0.668	1169	43	1115	15	1134	15	932	28	95	1169
Spot 22	0.21	0.0812	0.0045	0.0878	0.0022	0.9823	0.0511	0.0604	0.0038	0.473	1226	104	542	13	695	26	1185	72	44	542
Spot 23	0.18	0.0775	0.0008	0.1625	0.0021	1.7366	0.0232	0.0459	0.0006	0.986	1134	21	971	12	1022	9	908	12	86	1134
Spot 24	0.45	0.0790	0.0013	0.1905	0.0029	2.0713	0.0379	0.0537	0.0010	0.821	1171	32	1124	15	1139	13	1057	20	96	1171
Spot 25	0.96	0.0870	0.0015	0.1701	0.0025	2.0382	0.0374	0.0395	0.0007	0.787	1360	32	1013	14	1128	13	782	14	74	1360
Spot 26	0.19	0.0779	0.0008	0.1687	0.0022	1.8115	0.0240	0.0411	0.0006	0.985	1144	21	1005	12	1050	9	813	11	88	1144
Spot 27	0.18	0.0784	0.0008	0.1658	0.0022	1.7928	0.0237	0.0371	0.0005	0.983	1157	21	989	12	1043	9	737	10	85	1157
Spot 28	0.93	0.0814	0.0014	0.0897	0.0013	1.0063	0.0183	0.0087	0.0002	0.786	1230	33	554	8	707	9	174	4	45	554
Spot 29	0.16	0.0778	0.0032	0.0924	0.0019	0.9906	0.0391	0.0596	0.0032	0.510	1141	79	570	11	699	20	1170	61	50	570
Spot 30	0.37	0.0813	0.0026	0.0879	0.0017	0.9847	0.0310	0.0168	0.0008	0.610	1229	60	543	10	696	16	337	15	44	543
Spot 31	0.13	0.0682	0.0012	0.0894	0.0014	0.8400	0.0161	0.0131	0.0004	0.794	874	35	552	8	619	9	263	7	63	552
Spot 32	0.07	0.0774	0.0008	0.1644	0.0022	1.7533	0.0237	0.0352	0.0005	0.988	1130	21	981	12	1028	9	699	9	87	1130
Spot 33	0.09	0.0830	0.0022	0.0991	0.0017	1.1335	0.0298	0.0008	0.0000	0.642	1269	50	609	10	769	14	16	1	48	609
Spot 34	0.52	0.0778	0.0014	0.0879	0.0013	0.9434	0.0186	0.5270	0.0145	0.744	1143	36	543	8	675	10	8556	192	48	543
Spot 35	0.16	0.1127	0.0031	0.0785	0.0015	1.2198	0.0331	0.0158	0.0004	0.685	1843	48	487	9	810	15	318	8	26	487
Spot 36	0.38	0.0720	0.0012	0.0899	0.0013	0.8927	0.0165	0.2492	0.0067	0.793	987	33	555	8	648	9	4498	108	56	555
Spot 37	0.02	0.0724	0.0012	0.0897	0.0013	0.8960	0.0163	0.0859	0.0022	0.808	998	32	554	8	650	9	1665	40	56	554
Spot 38	0.05	0.0890	0.0013	0.0905	0.0013	1.1095	0.0189	0.0054	0.0001	0.842	1404	29	558	8	758	9	110	2	40	558
Spot 39	0.20	0.0794	0.0010	0.0888	0.0012	0.9726	0.0143	0.0146	0.0003	0.920	1182	24	549	7	690	7	292	6	46	549
Spot 40	0.24	0.0787	0.0010	0.1707	0.0023	1.8527	0.0271	0.0355	0.0007	0.908	1165	25	1016	13	1064	10	705	13	87	1165
Spot 41	0.89	0.0783	0.0010	0.1765	0.0024	1.9040	0.0291	0.0217	0.0003	0.894	1154	25	1048	13	1083	10	434	7	91	1154
Spot 42	0.03	0.0635	0.0032	0.0848	0.0018	0.7419	0.0358	0.0520	0.0072	0.444	724	103	525	11	564	21	1025	139	73	525
Spot 43	0.32	0.0783	0.0012	0.1637	0.0023	1.7661	0.0307	0.0322	0.0008	0.810	1154	31	977	13	1033	11	641	15	85	1154
Spot 44	0.16	0.0888	0.0035	0.0928	0.0019	1.1355	0.0426	0.0542	0.0030	0.551	1399	73	572	11	770	20	1067	58	41	572
Spot 45	0.19	0.0650	0.0012	0.0908	0.0013	0.8145	0.0163	0.0161	0.0006	0.737	776	38	560	8	605	9	322	11	72	560
Spot 46	0.36	0.0787	0.0009	0.1813	0.0025	1.9660	0.0278	0.0597	0.0008	0.961	1163	22	1074	13	1104	10	1171	15	92	1163
Spot 47	0.46	0.0898	0.0018	0.0884	0.0013	1.0940	0.0222	0.0236	0.0006	0.731	1421	37	546	8	751	11	472	12	38	546
Spot 48	0.22	0.0783	0.0008	0.1719	0.0023	1.8546	0.0251	0.0545	0.0007	0.978	1154	21	1023	13	1065	9	1073	14	89	1154
Spot 49	0.25	0.0704	0.0022	0.0890	0.0017	0.8615	0.0273	0.0286	0.0012	0.608	940	62	549	10	631	15	569	23	58	549
Spot 50	0.24	0.0783	0.0009	0.1937	0.0029	2.0925	0.0320	0.0498	0.0007	0.975	1154	22	1142	16	1146	11	983	14	99	1154
Spot 51	0.13	0.0789	0.0008	0.1960	0.0028	2.1326	0.0299	0.0625	0.0008	0.999	1169	20	1154	15	1159	10	1225	15	99	1169
Spot 52	0.17	0.0777	0.0010	0.1673	0.0024	1.7930	0.0281	0.0600	0.0011	0.912	1140	25	997	13	1043	10	1177	20	88	1140

Sample 187325		Isotope Ratios									Ages (Ma)									
Spot name	**Th/U**	**$^{207}Pb/^{206}Pb$**	**±1σ**	**$^{206}Pb/^{238}U$**	**±1σ**	**$^{207}Pb/^{235}U$**	**±1σ**	**$^{208}Pb/^{232}Th$**	**±1σ**	**rho**	**$^{207}Pb/^{206}Pb$**	**±1σ**	**$^{206}Pb/^{238}U$**	**±1σ**	**$^{207}Pb/^{235}U$**	**±1σ**	**$^{208}Pb/^{232}Th$**	**±1σ**	**Conc. (%)**	**Eff. Age***
Spot 1	0.32	0.0785	0.0008	0.1814	0.0025	1.9643	0.0270	0.0468	0.0005	0.988	1161	21	1075	13	1103	9	925	10	93	1161
Spot 2	0.49	0.0791	0.0010	0.1960	0.0029	2.1366	0.0340	0.0441	0.0006	0.925	1174	25	1154	16	1161	11	872	11	98	1174
Spot 3	0.38	0.0784	0.0009	0.1871	0.0026	2.0211	0.0290	0.0404	0.0005	0.968	1156	22	1106	14	1123	10	800	10	96	1156
Spot 4	0.55	0.0800	0.0013	0.1961	0.0027	2.1620	0.0390	0.0611	0.0011	0.776	1196	33	1154	15	1169	13	1199	20	97	1196
Spot 5	0.63	0.0791	0.0010	0.1881	0.0026	2.0512	0.0313	0.0550	0.0007	0.891	1175	26	1111	14	1133	10	1081	14	95	1175
Spot 6	0.37	0.0789	0.0009	0.1826	0.0026	1.9845	0.0299	0.0439	0.0006	0.957	1169	23	1081	14	1110	10	868	11	92	1169
Spot 7	0.85	0.0789	0.0012	0.1882	0.0026	2.0490	0.0340	0.0543	0.0008	0.828	1170	29	1112	14	1132	11	1068	15	95	1170
Spot 8	0.63	0.0783	0.0011	0.1726	0.0024	1.8626	0.0308	0.0457	0.0007	0.854	1154	28	1026	13	1068	11	904	13	89	1154
Spot 9	0.73	0.0788	0.0010	0.1962	0.0028	2.1295	0.0324	0.0458	0.0005	0.945	1166	24	1155	15	1158	11	905	10	99	1166
Spot 10	0.42	0.0788	0.0010	0.1964	0.0026	2.1359	0.0314	0.0527	0.0008	0.915	1168	24	1156	14	1161	10	1038	14	99	1168
Spot 11	0.58	0.0789	0.0009	0.1840	0.0026	2.0014	0.0291	0.0483	0.0006	0.959	1170	23	1089	14	1116	10	953	11	93	1170
Spot 12	0.44	0.0784	0.0009	0.1751	0.0024	1.8913	0.0267	0.0483	0.0006	0.971	1156	22	1040	13	1078	9	954	11	90	1156
Spot 13	0.58	0.0783	0.0013	0.1784	0.0026	1.9253	0.0356	0.0521	0.0009	0.779	1154	33	1058	14	1090	12	1027	18	92	1154
Spot 14	0.77	0.0791	0.0013	0.1892	0.0027	2.0628	0.0365	0.0516	0.0008	0.809	1174	31	1117	15	1137	12	1017	16	95	1174
Spot 15	0.41	0.0789	0.0009	0.1940	0.0027	2.1081	0.0311	0.0522	0.0007	0.957	1171	23	1143	15	1152	10	1028	14	98	1171
Spot 16	0.96	0.0789	0.0016	0.1916	0.0033	2.0810	0.0475	0.0570	0.0014	0.754	1170	40	1130	18	1143	16	1121	26	97	1170
Spot 17	0.61	0.0794	0.0013	0.1878	0.0023	2.0625	0.0334	0.0605	0.0014	0.754	1181	31	1109	12	1137	11	1187	27	94	1181
Spot 19	0.40	0.0798	0.0011	0.1854	0.0025	2.0425	0.0315	0.0420	0.0007	0.871	1192	26	1097	14	1130	11	832	13	92	1192
Spot 20	0.69	0.0791	0.0011	0.1947	0.0027	2.1309	0.0339	0.0402	0.0006	0.871	1173	27	1147	15	1159	11	796	12	98	1173
Spot 21	0.70	0.0800	0.0011	0.1910	0.0026	2.1051	0.0332	0.0431	0.0006	0.847	1197	27	1127	14	1151	11	853	12	94	1197
Spot 22	0.81	0.0827	0.0017	0.1606	0.0021	1.8369	0.0370	0.0486	0.0017	0.646	1261	40	960	12	1059	13	960	33	76	1261

* For ages <1000 Ma and >1000 Ma, effective age corresponds to calculated $^{206}Pb/^{238}U$ and $^{207}Pb/^{206}Pb$ ages, respectively.

Table 6 – Zircon and titanite descriptions

Sample	Size (µm)	Colour	Morphology	Features	No. grains/ No. spots	Th/U ratios	Average U (ppm)	Average *f* 204 (%)	Age determination (Ma)
Zircon									
184464	100 - 300	Clear	Elongate to stubby subrounded	Occasionally fractured	15/15	0.30 - 1.07	-	-	1186 ± 5
184468	100 - 350	Clear to light orange-brown	Elongate to stubby subrounded and tabular	Occasional opaque inclusions, occasionally fractured	21/28	0.71 - 1.47	-	-	1173 ± 5
187323	200 - 900	Light pink to light orange-brown	Elongate acicular to subrounded	Abundant opaque inclusions, commonly fractured and re-healed	27/52	0.02 - 1.16	-	-	541 ± 4 1170 ± 6
187325	100 - 300	Clear to light brown	Elongate acicular to subrounded	Common opaque inclusions, occasionally fractured	17/21	0.32 - 0.96	-	-	1178 ± 13
Titanite									
184495	150 - 350	Light yellow to light orange-brown	Irregular circular, angular to subrounded	Very highly fractured, common opaque inclusions	13/13	0.22 - 0.44	302	0.08	539 ± 4
187323	250 - 750	Light yellow to light orange-brown	Irregular circular to ovoid, angular to subrounded	Highly fractured, occasional opaque inclusions	15/15	0.14 - 0.23	69	0.18	572 ± 7
187337	250 - 550	Light brown to medium brown	Irregular circular to ovoid, angular to subrounded	Highly fractured, common opaque inclusions	14/14	0.08 - 0.76	27	0.44	573 ± 14
155731	200 - 500	Clear to light brown	Ovoid, angular to subrounded	Highly fractured	10/10	0.13 - 0.31	32	0.40	552 ± 12

Table 7 – LA-ICPMS titanite trace element data

Sample 187323

Spot name	Ca	Sc	Ti	Ga	Y	Zr	Nb	Cs	Ba	La	Ce	Pr	Nd	Sm	Eu	Gd	Tb	Dy	Ho	Er	Tm	Yb	Lu	Hf	Ta
Spot 1	199810	7.98	178785	5.36	1415.67	72.36	960.19	<0.0184	<0.089	3.58	28.91	8.35	68.39	57.55	15.66	103.13	30.15	238	54.07	146.99	19.42	112.58	10.55	5.18	56.59
Spot 2	203299	7.32	180692	5.89	1285.33	75.7	1001.26	<0.0186	<0.063	5.77	36.36	8.32	56.94	41.85	10.79	73.24	23.19	201.31	48.93	144.61	21.13	124.67	11.62	5.21	57.27
Spot 3	201712	6.87	180305	5.5	1214.87	73.91	1019.69	<0.0157	<0.083	4.08	30.19	7.71	54.72	39.75	12.99	73.74	22.48	196.32	45.19	133.65	19.6	123.43	12.66	4.62	58.92
Spot 4	204373	9.13	184638	5.31	1251.39	75.88	952.13	<0.0167	<0.113	7.65	52.8	12.11	81.29	52.55	13.79	90.82	26.4	217.88	48.95	132.89	16.81	95.92	8.87	4.82	49.41
Spot 5	203535	6.43	187551	5.89	1920.4	90.61	1196.34	<0.0186	<0.082	12.7	86.17	20.56	139.17	90.46	20.36	146.25	38.39	312.56	74.02	225.86	35.64	250.34	29.75	6.33	88.93
Spot 6	202304	5.73	187338	6.3	1000.62	70.83	1025.66	<0.0152	<0.103	2.62	18.99	5.24	37.89	30.51	11.26	60.69	18.68	159.36	36.77	101.64	13.48	80.61	7.15	5.87	74.23
Spot 7	201965	8.54	190886	6.89	3004.59	98.06	984.53	<0.026	<0.125	20	131.22	29.12	195.85	127.4	32.74	204.59	55.67	455.69	112.31	369.99	62.13	487.52	63.92	6.4	44.77
Spot 8	203655	7.69	197627	6.51	2963.91	87.92	954.28	<0.030	0.229	28.7	175.51	38.34	240.22	140.26	37.9	230.1	59.69	471.37	113.47	345.16	54.7	410.64	53.08	6.81	74.75
Spot 9	200844	9.05	195165	6.68	3060.74	96.9	1266.48	0.0177	<0.067	19.65	128.92	30.32	203.7	133.86	34.15	226.12	63.02	498.78	116.38	353.26	54.14	388.37	47.66	7.5	95.83
Spot 10	202508	6.59	187531	5.76	1280.36	66.83	1124.24	<0.0142	<0.128	9.66	241.05	11.04	69.71	45.78	13.66	81.44	23.84	204.64	49.23	149.64	21.37	142.81	15.46	5.1	67.81
Spot 11	202939	9.08	210257	6.1	1863.69	80.81	1124.09	<0.020	<0.060	8.14	56.19	13.59	100.07	69.28	21.44	127.37	37.39	310.01	72.48	210.93	29.21	188.87	20.3	5.55	74.25
Spot 12	198792	7.61	212485	6.56	1567.99	85.07	1094.54	<0.021	<0.184	12.55	71.43	14.75	89.28	54.67	15.55	90.17	26.38	230.51	58.99	183.88	29.25	212.19	25.52	5.77	60.62
Spot 13	199174	8.75	216607	5.81	2618.9	79.73	938.86	0.021	0.109	20.13	131.21	29.81	183.19	111.29	32.95	180.28	49.87	400.2	97.11	298.52	49.09	369.85	48.41	7.35	43.29
Spot 14	202661	7.22	220914	5.82	1517.96	84.74	1059.32	<0.0204	<0.089	9.19	55.6	12.27	82.37	54.39	14.82	92.32	27.82	237.85	56.94	171.73	25.28	166.65	18.6	6.22	76.16
Spot 15	198871	7.26	219319	5.42	1172.06	75.37	1127.7	0.0143	<0.080	6.27	41.33	9.62	63.35	43.55	12.59	77.17	23.14	196.81	43.34	114.79	15.62	98.44	10.15	5.93	84.28

Sample 184495

Spot name	Ca	Sc	Ti	Ga	Y	Zr	Nb	Cs	Ba	La	Ce	Pr	Nd	Sm	Eu	Gd	Tb	Dy	Ho	Er	Tm	Yb	Lu	Hf	Ta
Spot 1	198992	16.6	182444	11.3	3358.51	127.54	1979.41	0.0313	2.02	200.27	844.49	151.85	826.88	366.48	77.34	502.43	115.3	759.87	140.34	305.64	32.56	151.07	13.34	6.82	115.02
Spot 2	199463	18	182672	12.5	3343.38	120.05	2243.53	<0.0213	4.78	197.3	779.66	146.04	859.73	440.47	54.3	623.65	141.9	895.06	152.62	318.47	32.42	153.01	12.39	6.97	164.26
Spot 3	202203	14.3	182186	8.74	3158.66	120.15	1461.57	<0.024	1.44	111.96	450.01	78.96	425.66	185.35	39.49	273.16	74.72	609.45	143.02	419.39	57.36	328.74	32.22	6.9	50.01
Spot 4	201810	18.7	176637	10.8	1759.87	96.53	1584.15	<0.026	1.69	86.68	314.98	51.09	257.33	110.28	22.3	159.97	41.8	329.42	72.52	190.88	24.06	134.07	12.07	5.8	78.05
Spot 5	202755	15.7	177464	8.84	2986.09	74.5	1310.68	0.029	1.67	77.49	364.03	75.58	467.28	241.38	43.11	355.37	87.74	630.85	129.16	325.79	40.1	210.57	20.47	5.42	36
Spot 6	200918	10.7	196060	6.13	1591.73	107.83	1820.14	<0.0202	0.414	45.03	222.55	45.72	275.62	139.72	30.52	206.21	49.85	349.81	68.33	161.54	19.04	94.81	8.38	7.92	96.01
Spot 7	202270	18	185213	11.2	3658.78	152.73	1281.97	0.034	1.29	324.81	1630.8	333.01	1914.5	811.36	130.2	861.97	161.6	924.37	152.16	324.72	34.35	166.63	14.82	9.69	63.45
Spot 8	197586	13.8	176158	10.4	1881.83	94.34	1400.07	0.029	1.35	142.31	660.75	120.57	658.13	283.69	67.77	343.4	72.61	450.99	80.76	168.66	18.24	90.68	7.5	5.3	71.98
Spot 9	202086	17.8	180533	12.3	2061.32	118.93	1185.1	0.0281	5.38	213.53	885.34	152.62	807.97	313.15	70.47	358.28	72.3	451.28	84.43	204.97	24.53	137.87	14.31	6.68	86.03
Spot 10	201068	13.5	179868	10.3	1776.55	110.67	1589.97	0.021	3.15	125.52	464.88	73.07	354.97	139.57	35.83	185.33	45	333.19	71.81	183.15	22.6	120.37	10.92	5.92	86.9
Spot 11	197300	7.22	194804	10.8	2134.01	107.71	1449.33	<0.033	1.45	282.85	1329.7	252.06	1416.1	562.51	115.3	581.32	105.4	553.31	88.76	176.08	17.68	88.88	8.01	7.41	101.17
Spot 12	197300	11.8	193072	17.2	2429.9	142.69	1603.17	0.034	32.7	422.5	1389.5	215.53	1037.1	346.69	86.89	374.54	81.79	511.97	100.07	238.45	30.09	165.22	15.03	11.5	120.02
Spot 13	200524	15.5	176702	8.79	2014.96	92.87	1584.66	<0.047	1.06	111.11	491.28	89.53	493.23	212.86	57.24	260.17	56.68	390.22	81.51	220.93	31.87	212.65	27.26	6.61	47.84
Spot 14	199983	6.59	207858	10.2	1542.17	79.93	1971.7	<0.0161	1.11	225.74	1113.8	228.39	1322.7	518.34	94.03	556.82	95.19	469.09	66.39	121.09	12.78	64.68	6.1	5.8	208.57
Spot 15	201068	13.2	177917	8.71	1975.96	144.71	1622.39	<0.0071	9.2	183.88	748.78	119.66	637.81	249.4	65.16	278.33	62.69	413.02	74.93	168	20.1	95.98	8.42	8.84	80.4

Sample 187337

Spot name	Ca	Sc	Ti	Ga	Y	Zr	Nb	Cs	Ba	La	Ce	Pr	Nd	Sm	Eu	Gd	Tb	Dy	Ho	Er	Tm	Yb	Lu	Hf	Ta
Spot 1	198600	8.67	192263	5.86	2522.67	120.07	1148.31	<0.0169	<0.140	20.44	133.97	32.73	241.99	157.91	51.48	258.71	62.65	463.91	97.89	256.24	33.99	211.44	23.19	8.39	60.77
Spot 2	203421	7.6	191529	5.1	1620.52	106.67	824.49	<0.0147	<0.094	14.85	98.1	23.85	170.73	110.99	41.24	186.2	43.55	312.09	65.12	158.4	18.7	103.45	10.14	6.59	39.19
Spot 3	200206	7.44	190958	5.3	1702.51	113.44	882.24	0.0161	<0.071	13.73	84.36	20.89	157.83	107.03	37.23	191.65	47.22	336.82	68.77	164.23	20.22	109.7	11.36	7.56	51.9
Spot 4	198849	5.51	187894	5.14	1183.02	105.25	849	<0.0172	<0.101	13.86	84.53	19.6	137.42	81.49	29.14	134.23	33.74	237.62	45.92	104.43	12.26	67	6.58	7.33	45.93
Spot 5	205875	6.7	199892	4.46	1514.3	117.61	750.94	<0.0174	<0.083	23.92	145.34	33.28	236.07	131.4	49.89	203.74	44.41	302.77	62.54	155.08	18.92	111.43	11.47	6.75	34.22
Spot 6	201342	6.28	191044	5.54	2660.45	117.5	1128.44	0.0126	<0.071	32.6	210.89	48.96	320.09	184.18	58.19	285.57	66.79	486.63	105.65	288.19	39.93	262.23	29.39	7.66	73.04
Spot 7	204350	6.75	188030	5.11	1029.51	83.5	1089.55	<0.0152	<0.077	7.45	53.03	12.57	88.68	57.13	15.96	101.41	26.06	192.52	39.93	96.12	11.31	62.31	5.18	6.14	78.97
Spot 8	200759	5.42	186992	5.64	913.14	94.76	781.07	<0.0139	<0.047	13.66	95.57	22.17	154.15	92.4	25.37	144.77	33.42	212.33	36.03	72.82	8.41	51.53	5.94	6.64	28.31
Spot 9	198628	6.63	186866	5.55	1377.55	109.63	743.3	<0.0137	<0.102	17.45	109.88	25.66	178.83	107.21	42.74	175.05	38.81	267.76	55.06	136.68	16.76	100.86	10.5	6.69	33.79
Spot 10	204192	5.66	193136	5.45	1256.96	97.21	977.01	<0.0077	<0.111	7.94	57.84	13.79	103.56	69.52	23.42	123.66	32.7	242.98	49.04	114.57	13.05	69.93	6.59	6.12	47.59
Spot 11	196687	7.47	186590	5.71	1248.81	97.78	1081.88	<0.0183	<0.068	10.63	70.74	16.93	119.79	76.55	25.63	125.34	32.52	240.45	47.85	113.49	13.7	76.81	7.17	6.33	57.44
Spot 12	196820	5.71	192964	5.07	1698.92	127.38	1056.66	0.017	<0.054	49.82	210.95	38.67	223.53	112.4	42.6	168.51	41.23	300.73	63.55	165.19	22.44	147.32	16.66	8.02	60.68
Spot 13	204186	6.12	195139	5.1	816.86	106.68	654.04	<0.0169	0.57	15.01	209.75	20.94	146.52	86.47	34.05	139.05	29.68	190.43	32.43	60.41	6.09	31.17	2.65	5.86	27.32
Spot 14	203563	6.72	187500	5.29	1204.77	89.39	1024.15	<0.0170	<0.100	8.6	54.1	12.51	84.1	53.88	18.73	96.71	27.3	221.21	48.07	120.47	13.95	75.73	6.72	5.91	52.37
Spot 15	203472	4.77	193394	6.12	894.66	96.35	640.93	<0.0129	<0.108	10.18	66.22	16.39	118.01	76.1	25.55	123.44	30.59	198.43	33.89	65.25	6.56	30.77	2.37	6.37	27.32

Sample 155731

Spot name	Ca	Sc	Ti	Ga	Y	Zr	Nb	Cs	Ba	La	Ce	Pr	Nd	Sm	Eu	Gd	Tb	Dy	Ho	Er	Tm	Yb	Lu	Hf	Ta
Spot 1	195215	8.17	187750	6.29	3813.09	159.11	1724.3	<0.0066	0.252	86.3	517.93	118.11	792.64	399.91	111.5	513.56	105.9	703.73	146.93	407.02	59.23	409.99	52.38	10.8	152.27
Spot 2	196278	8.59	184730	5.55	2064.33	101.9	1311.03	<0.0085	2.4	34.13	210.58	48.88	333.59	178.83	51.49	248.67	54.71	376.36	79.47	216.36	31.45	216.36	27.64	7.12	151.85
Spot 3	195666	8.68	186932	6.02	2041.6	101.74	1069.84	<0.0084	0.29	58.15	371.05	87.89	602.39	300.76	62.13	378.53	73.43	448.97	83.23	198.42	24.97	147.56	16.49	7.86	61.71
Spot 4	197102	8.29	190016	6.05	3986.03	146.17	1637.65	0.009	<0.038	73.51	440.67	104.01	725.55	385.32	102.8	517.42	109.8	748.45	158.44	439.31	63.6	425.22	52.5	10.3	116.83
Spot 5	197867	9.68	191482	6.22	3319.59	160.17	1350.87	<0.0076	0.315	101.12	594.06	134.68	899.64	425.77	109.5	505.28	97.49	625.74	130.11	362.9	54.17	384.52	50.61	10.7	82.77
Spot 6	199144	8.37	186223	5.51	2316.5	119.2	1276.12	<0.0086	<0.045	28.49	174.24	41.51	291.69	165.39	48.92	244.31	57.11	414.81	90.62	245.94	33.6	209.53	23.49	8.14	90.35
Spot 7	198017	9.38	184892	4.62	1787.7	81.35	1280.23	0.0091	0.658	19.3	120.06	28.03	190.75	106.57	30.58	159.03	38.34	294.15	68.62	204.92	31.6	224.69	27.76	6.57	71.42
Spot 8	196967	8.31	184584	5.56	2364.34	111.47	1226.8	<0.0081	<0.031	30.75	204.18	46.37	319.9	182.33	56.07	261.45	60.6	434.64	93.98	256.96	35.37	228.78	25.38	6.91	89.49
Spot 9	197536	10.8	181246	6.14	1449.2	80.41	1533.07	0.0067	0.661	43.29	264.04	53.22	316.31	128.91	35.54	155.43	33.85	242.78	54.43	158.78	24.36	174.29	21.91	5.72	113.81
Spot 10	198613	5.22	183979	6.31	1375	76.68	523.98	<0.0060	0.216	71.21	430.64	91.06	567.01	219.76	69.68	233.75	42.96	266.37	52.07	135.15	18.49	121.51	13.94	5.36	14.15

Table 8 – LA-ICPMS zircon trace element data

Sample 187323

Spot name	Loc.	Ca	Sc	Ti	Ga	Y	Zr	Nb	Cs	Ba	La	Ce	Pr	Nd	Sm	Eu	Gd	Tb	Dy	Ho	Er	Tm	Yb	Lu	Hf	Ta
Spot 1	Core	<529.59	167	7.43	<0.050	969.98	499959	6.36	<0.0115	0.071	0.843	23.32	0.334	2.29	2.41	0.251	11.33	4.82	68.72	29.64	157.53	44.1	515.84	86.99	14222	4.67
Spot 2	Core	<264.70	166	7.49	0.584	926.58	525157	5.09	0.019	0.618	25.47	216.87	9.32	37.49	12.86	1.609	20.21	6.24	75.58	29.47	145.57	38.88	455.96	71.2	13098	3.16
Spot 3	Rim	<764.18	294	9.01	2.15	598.98	569208	2.42	0.0234	1.36	43.56	758.37	14.57	69.39	25.7	4.96	35.96	7.32	59.19	18.81	88.02	20.1	202.62	40.92	16506	1.135
Spot 4	Rim	585.88	211	10.42	2.81	736.03	600959	15.75	0.029	11.38	16.18	833.01	7.27	39.78	13.21	2.32	18.54	5.37	58.5	23.09	119.78	30.65	352.57	74.41	17194	2.111
Spot 5	Rim	<251.94	180	6.93	0.416	222.45	539601	1.146	0.0059	3.66	5.7	482.08	4.25	23.68	13.6	2.74	21.72	4.3	29.57	7.45	28.32	6.26	62.78	10.09	19782	0.45
Spot 6	Rim	<252.64	224	7.06	0.221	541.48	561613	1.877	0.0065	0.078	6.89	298.62	3.27	13.21	4.33	0.836	6.43	2.223	33.33	16.2	88.62	22.89	229.08	31.62	19264	0.763
Spot 7	Rim	<206.10	176	5.81	0.047	282.23	464382	2.061	<0.0049	0.033	0.0687	0.515	0.0234	0.145	0.109	0.055	0.835	0.599	12.94	7.4	48.33	15.36	205.28	38.26	13647	0.662
Spot 8	Rim	<317.20	223	8.46	1.024	933.5	654577	2.67	0.0174	1.82	26.03	1565.1	18.47	114.8	62.56	12.97	100.04	18.3	124.52	30.14	101.85	21.61	233.24	37.73	18131	1.032
Spot 9	Rim	1180.38	195	7.99	8.1	312.12	502282	1.169	0.096	109.3	18.07	145.4	4.72	22.82	11.4	2.65	17.29	4.3	35.31	10.89	47.9	10.82	112.33	24.15	14007	0.285
Spot 10	Rim	<196.73	183	6.19	<0.024	329.96	485413	2.33	<0.0056	<0.00	0.372	0.458	0.0711	0.313	0.1	0.32	1.24	0.757	15.6	9.27	61.77	20.04	262.37	54.79	13753	1.083
Spot 11	Rim	<206.73	210	6.98	1.501	583.7	539293	2.35	0.0111	1.34	63.1	77.2	11.44	45.53	9.78	1.867	31.72	3.88	36.62	16.15	87.18	25.28	323.11	62.95	15644	1.046
Spot 12	Rim	<225.61	170	8.08	1.97	418.97	570872	2.094	0.0143	22.8	16.21	1085.1	8.88	53.18	33.14	7.22	46.41	10.13	68.41	15.19	46.54	9.03	84.07	11.63	15272	0.601
Spot 13	Rim	<269.38	217	8.00	0.701	270.99	579702	2.34	0.0138	4.24	3.37	50.38	1.191	6.23	3.22	0.645	4.96	1.53	17.28	7.97	44.18	12.18	135.98	27.04	16872	0.772
Spot 14	Rim	<196.42	172	7.39	0.801	348.14	579518	2.7	0.031	2.48	8.72	100.71	3	16.44	8.62	1.546	13.98	3.79	35.43	11.84	54.41	13.88	155.96	29.69	14723	1.481
Spot 15	Core	559.9	189	7.19	0.046	1195.61	590317	2.58	0.0074	0.112	0.224	22.27	0.172	2.25	4.25	0.653	24.17	8.74	110.09	41.62	185.13	42.78	429.74	66.67	12120	1.222
Spot 16	Core	587.25	151	6.65	0.092	961.63	549697	4.94	0.0062	0.112	0.771	31.96	0.492	3.39	3.46	0.394	15.14	5.89	78.02	31.27	156.89	41.18	464.92	75.14	13998	3.28
Spot 17	Rim	<204.25	165	6.59	1.314	839.95	538340	3.06	0.0087	1.12	53.62	1099.5	22.92	120.3	62.95	12.22	87.15	17.26	121.73	29.53	105.2	22.63	233.31	36.4	13568	1.787
Spot 18	Rim	<144.96	121	4.83	0.329	184.59	378356	1.047	0.0082	0.48	3.27	71.21	1.976	11.63	6.72	1.411	9.42	2.163	17.63	5.77	26.51	6.44	70.82	17.17	12672	0.412
Spot 19	Rim	<294.88	159	7.16	2.44	486.95	497566	1.279	0.062	4.44	35.31	303.55	9.97	54.85	27.25	5.81	41.57	9.8	71.47	17.43	63.86	13.87	150.96	37.28	12494	0.31
Spot 20	Rim	<270.56	175	7.86	0.388	338.52	620180	2.61	0.0163	0.964	1.993	77.87	1.725	11.03	5.87	1.022	8.35	2.15	24.73	10.19	55.28	15.86	194.19	36.67	17601	1.611
Spot 21	Rim	<189.67	150	6.03	8.17	831.85	505057	1.519	0.0098	2.61	505.98	1686.1	153.31	649.13	183.82	30.49	171.69	28.38	167.35	32.38	90.39	14.85	125.69	16.45	14094	0.543
Spot 22	Rim	<185.53	146	6.30	13.57	670.18	524917	1.85	0.0174	3.26	789.83	1399.4	130.16	512.42	97.5	15.59	90.43	14.77	96.91	22.66	75.45	16.14	169.1	29.41	13164	0.741
Spot 23	Core	<196.97	144	6.46	0.099	851.76	563360	5.58	0.0091	0.092	1.92	25.53	0.785	2.45	2.12	0.237	9.85	4.25	61.14	26.44	141.19	39.46	462.14	77.56	15707	4.36
Spot 24	Core	<204.94	168	6.76	1.578	906.19	589609	2.8	0.032	0.552	108.37	253.87	25.08	100.42	24.37	3.45	34.34	8.9	88.61	30.07	126.9	28.89	289.32	45.36	11619	1.53
Spot 25	Core	<222.10	165	6.82	0.448	2279.64	577593	6.29	0.0295	0.631	12.53	93.77	3.97	21.54	14.81	1.418	52.29	18.75	221.64	83.09	366.19	82.45	808.96	125.2	12676	3.1
Spot 26	Core	<245.99	168	7.03	0.305	1014.35	603880	4.35	0.0121	1.87	3.41	220.9	2.494	15.86	11.22	1.956	26.99	8.57	92.02	34.15	153.57	37.86	390.49	62.81	14157	2.652
Spot 27	Core	<189.83	166	6.50	0.228	784.66	567988	2.24	0.0054	0.183	10.47	33.38	2.407	10.69	4.95	0.839	23.89	5.96	72.75	27.03	121.83	28.5	293.5	44.56	11664	1.053
Spot 28	Core	17184.7	164	6.38	121.4	1801.29	536993	14.38	0.026	35.41	8470.4	10089	1749.3	6342.4	983.31	116.2	537.46	71.37	369.76	72.56	230.9	48.39	478.11	75.29	14135	3.06
Spot 29	Rim	<364.79	194	7.78	1.73	1574.54	508821	5.99	0.0291	2.67	32.92	1675.4	23.41	147.66	80.67	17.13	136.61	27.66	191.79	46.45	152.71	27.25	252.87	54.5	14095	0.692
Spot 30	Core	183.57	132	5.25	3.56	1138.92	453949	2.54	0.017	59.02	4.07	94.29	2.513	15.91	12.06	2.03	34.41	11.1	121.67	40.85	173.66	38.64	391.19	56.61	9127	1.133
Spot 31	Core	<141.69	119	5.37	0.241	461	462630	4.63	0.0105	2.3	0.177	11.46	0.104	0.86	1.136	0.122	6.05	2.647	37	15.02	76.36	20.8	239.13	38.13	11199	3.14

Sample 155735

Spot name	Loc.	Ca	Sc	Ti	Ga	Y	Zr	Nb	Cs	Ba	La	Ce	Pr	Nd	Sm	Eu	Gd	Tb	Dy	Ho	Er	Tm	Yb	Lu	Hf	Ta
Spot 1	Core	<90.52	373	17.18	0.038	445.82	553302	2.788	<0.0130	<0.065	0.0439	16.65	0.0628	0.795	1.396	0.229	6.99	2.84	36.75	14.92	73.05	18.52	206.31	37.85	12063	1.444
Spot 2	Core	<81.58	367	16.94	0.112	465.23	549504	3.6	0.0116	0.7	<0.0086	16.88	0.0404	0.627	1.324	0.221	6.7	2.875	38.76	15.7	77.46	19.85	222.67	40.11	13039	1.908
Spot 3	Rim	<95.11	362	16.00	0.041	235.04	516870	2.094	<0.0131	<0.074	0.131	7.12	0.0478	0.451	0.659	0.11	3.28	1.34	19.26	7.75	36.74	9	103	16.97	12762	1.032
Spot 4	Core	35250.7	352	17.15	1.538	985.12	515096	4.72	0.0725	12.27	24.97	82.2	7.6	38.25	14.9	3.4	34.24	9.71	100.59	35.01	149.04	34.32	349.59	55.22	10755	1.784
Spot 5	Rim	<82.13	385	15.64	<0.027	95.4	506606	1.443	<0.0126	<0.054	0.0117	0.155	<0.0079	<0.038	0.054	0.05	0.63	0.446	7.02	2.85	11.33	2.068	17.99	2.678	14517	0.797
Spot 6	Rim	<101.58	581	18.52	0.095	535.07	582442	1.851	<0.0176	0.195	1.3	17.17	0.717	4.45	2.55	0.721	6.74	2.381	36.37	15.58	71.25	14.38	124.4	20.72	16309	0.472
Spot 7	Core	<60.90	290	13.39	0.688	756.05	426844	4.08	0.0123	2.38	18.43	159.07	11.48	68.46	31.68	7.17	49.7	9.82	83.29	25.86	107.38	24.28	244.33	42.29	9973	1.835
Spot 8	Core	<86.47	370	16.99	0.07	558.07	552353	4.28	0.0157	0.149	0.087	19.57	0.1087	1.06	1.65	0.285	8.07	3.47	46.04	18.7	93.17	22.92	247.91	46.08	12889	1.992
Spot 9	Rim	<147.62	493	22.19	1.417	516.77	627648	2.86	<0.0199	10.79	6.29	73.95	2.94	14.87	6.35	1.409	11.48	3.46	41.03	16.26	81.79	19.49	208.32	43.96	14058	1.263
Spot 10	Rim	<78.08	352	15.75	0.127	352.72	507060	2.9	<0.0123	1.057	0.502	22.05	0.217	1.421	1.35	0.257	5.65	2.232	29.06	11.49	56.07	14.34	159.25	27.35	11838	1.46
Spot 11	Rim	<170.37	525	22.63	0.229	239.13	651332	1.437	<0.021	1.24	2.152	14.18	1.043	6.35	3.37	0.683	5.36	1.449	18.23	7.06	33.85	8.23	88.5	19.24	15438	0.608
Spot 12	Rim	229.4	429	17.50	0.262	382.5	489597	1.721	<0.0184	1.16	4.58	209.4	5.05	30.91	15.6	3.69	18.48	4.29	36.18	12.13	54.23	12.09	121.82	24.5	11731	0.675
Spot 13	Rim	<76.44	384	15.54	0.071	133.02	500888	1.212	<0.0108	0.102	0.852	28.18	0.523	3.81	1.79	0.534	3.64	0.996	11.15	4.14	15.26	2.91	23.4	3.66	13618	0.428

Table 9 – Summary of thermometry parameters

Zr in sphene thermometer (Hayden et al., 2006)

Sample No.	Zr conc. range (ppm)	Calculated *T* range at 1 GPa (°C)	Average Zr conc. (ppm, ±1σ)	Calculated average *T* (°C, ±1σ, ± 0.1 GPa)	Calculated average *T* (°C, ± max. *T* range)
184495	74.50 - 152.73	734 - 771	120.74 ± 8.45	759 ± 15	759 ± 25
187323	66.83 - 98.06	728 - 748	80.98 ± 4.82	738 ± 14	738 ± 10
187337	83.50 - 127.38	740 - 761	105.55 ± 5.96	752 ± 14	752 ± 12
155731	76.68 - 160.17	735 - 774	113.82 ± 3.60	756 ± 12	756 ± 21

Ti in zircon thermometer (Watson et al., 2006a)

Sample No.	Ti conc. range (ppm)	Calculated *T* range (°C)	Average Ti conc. (ppm, ±1σ)	Calculated average *T* (°C, ±1σ)	Calculated average *T* (°C, ± max. *T* range)
187323					
Cores	5.25 - 7.49	687 - 716	6.61 ± 0.46	706 ± 11	706 ± 19
Rims	4.83 - 10.42	680 - 744	7.31 ± 0.29	714 ± 12	714 ± 34
155735					
Cores	13.39 - 17.18	767 - 791	16.33 ± 0.69	786 ± 13	786 ± 19
Rims	15.54 - 22.63	781 - 818	17.97 ± 0.67	795 ± 13	795 ± 23

(a)

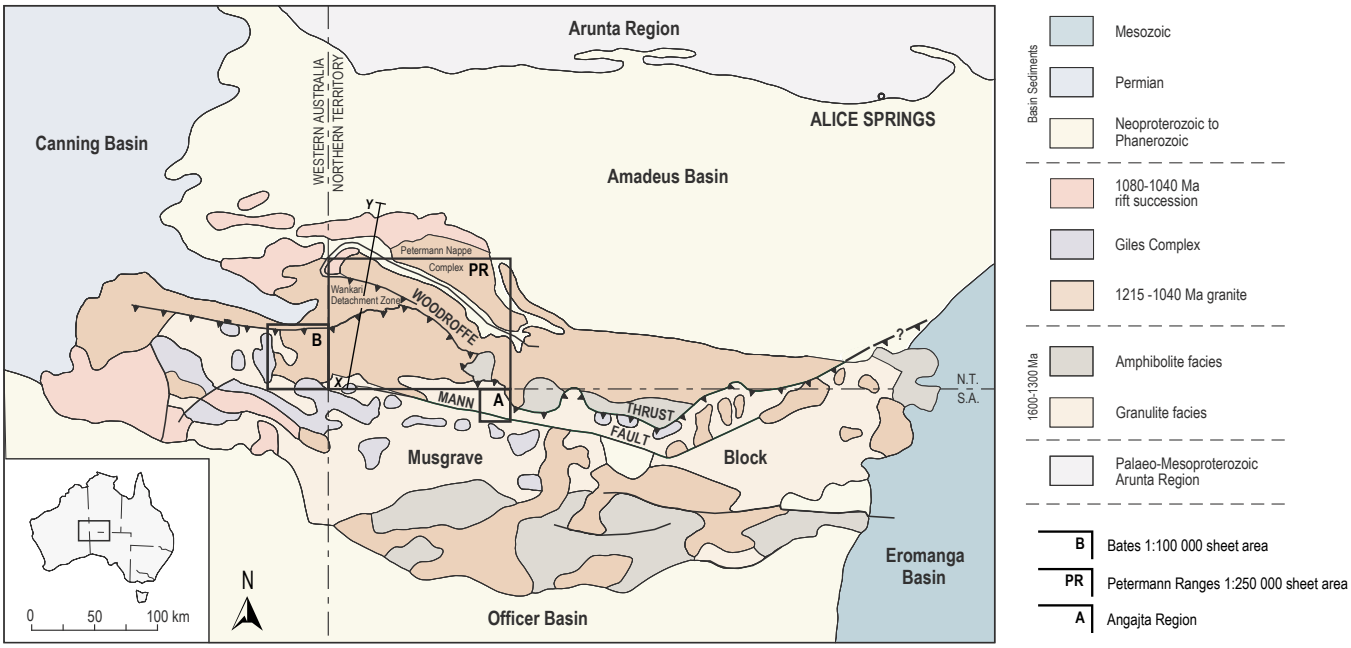
Arunta Region
ALICE SPRINGS
Canning Basin
WESTERN AUSTRALIA
NORTHERN TERRITORY
Amadeus Basin
Y
Petermann Nappe Complex
PR
Wankari Detachment Zone
WOODROFFE
B
X
MANN
A
THRUST FAULT
?
N.T.
S.A.
Musgrave Block
Eromanga Basin
Officer Basin
0 50 100 km
N
Basin Sediments
Mesozoic
Permian
Neoproterozoic to Phanerozoic
1080-1040 Ma rift succession
Giles Complex
1215 -1040 Ma granite
1600-1300 Ma
Amphibolite facies
Granulite facies
Palaeo-Mesoproterozoic Arunta Region
B Bates 1:100 000 sheet area
PR Petermann Ranges 1:250 000 sheet area
A Angajta Region

(b)

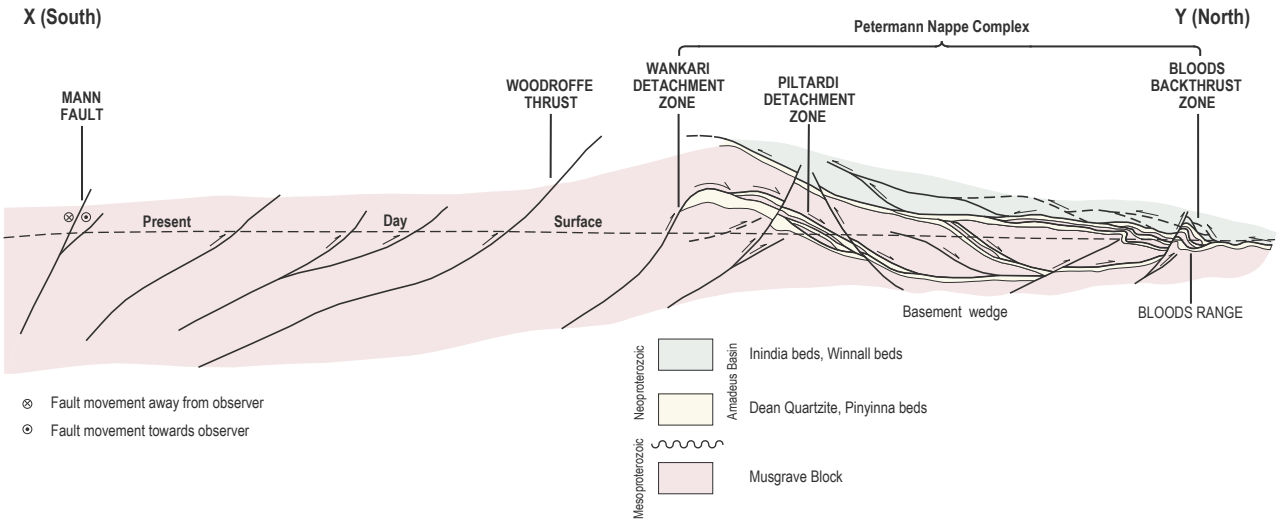
X (South)
Y (North)
Petermann Nappe Complex
MANN FAULT
WOODROFFE THRUST
WANKARI DETACHMENT ZONE
PILTARDI DETACHMENT ZONE
BLOODS BACKTHRUST ZONE
Present
Day
Surface
Basement wedge
BLOODS RANGE
Fault movement away from observer
Fault movement towards observer
Neoproterozoic
Amadeus Basin
Inindia beds, Winnall beds
Dean Quartzite, Pinyinna beds
Mesoproterozoic
Musgrave Block

Figure 1

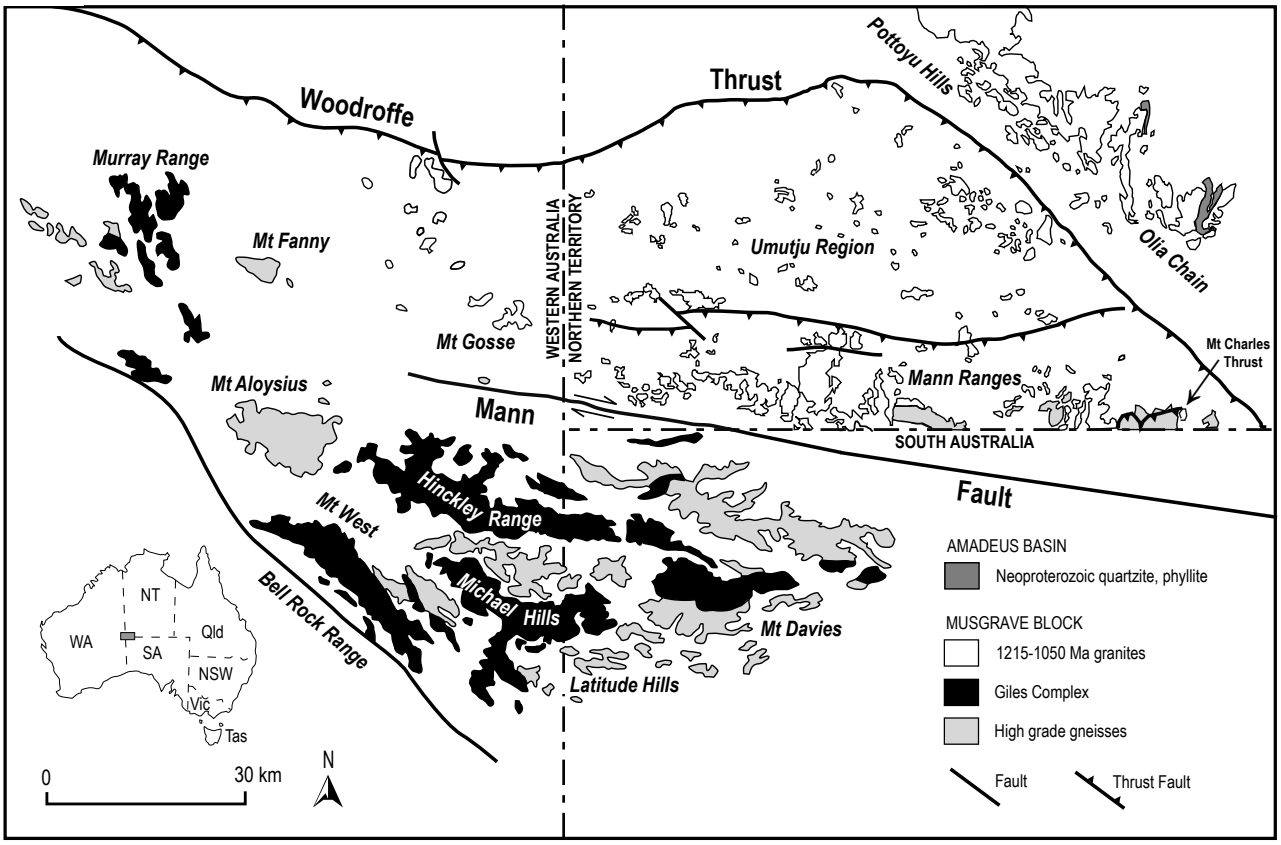
Woodroffe
Thrust
Pottoyu Hills
Murray Range
Mt Fanny
WESTERN AUSTRALIA
NORTHERN TERRITORY
Umutju Region
Olia Chain
Mt Gosse
Mt Charles
Thrust
Mann Ranges
Mt Aloysius
Mann
SOUTH AUSTRALIA
Fault
Hinckley Range
Mt West
Michael Hills
Mt Davies
Bell Rock Range
Latitude Hills
NT
WA
SA
Qld
NSW
Vic
Tas
0
30 km
N
AMADEUS BASIN
Neoproterozoic quartzite, phyllite
MUSGRAVE BLOCK
1215-1050 Ma granites
Giles Complex
High grade gneisses
Fault
Thrust Fault

Figure 2

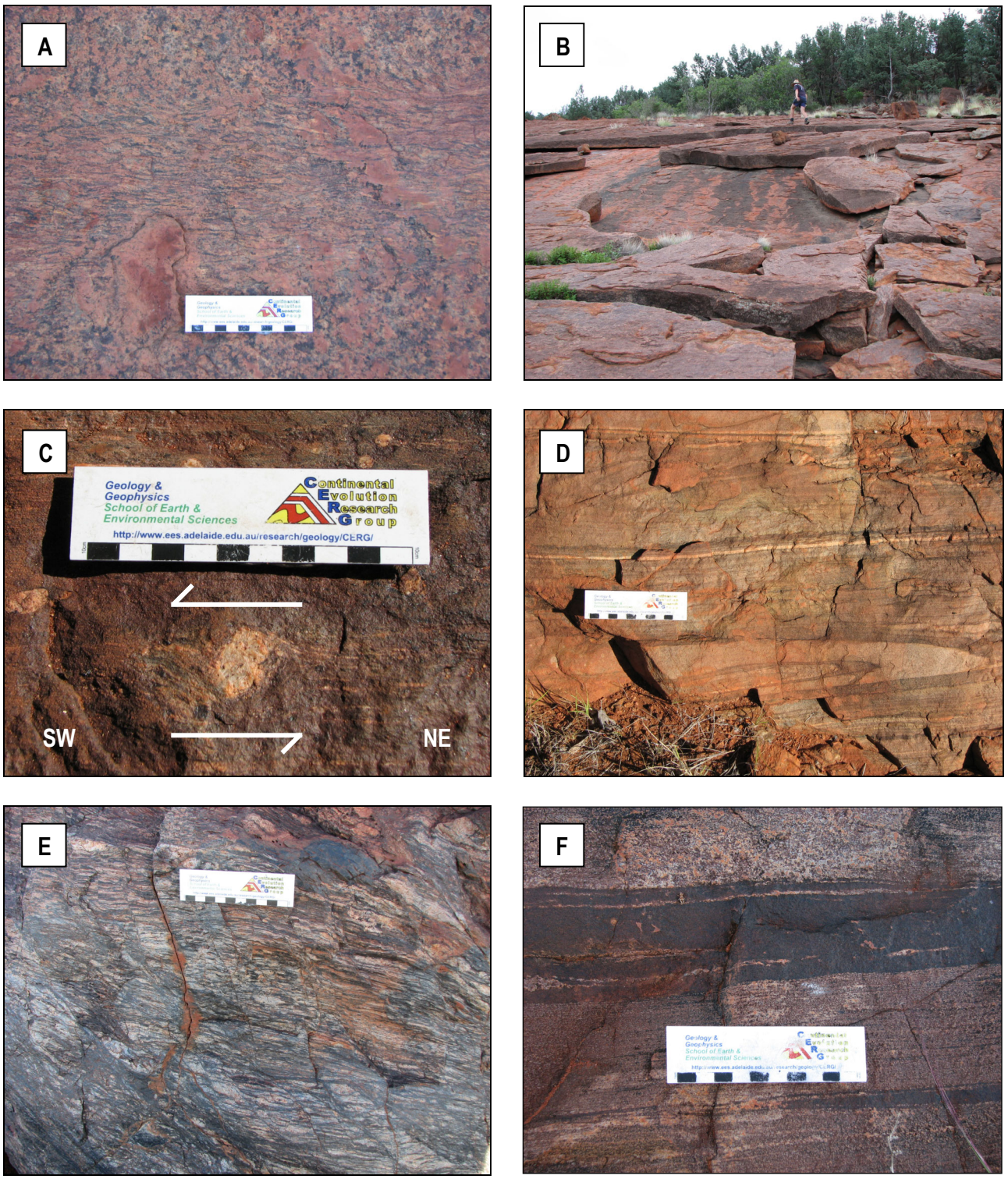
A
B
C
Geology &
Geophysics
School of Earth &
Environmental Sciences
Continental
Evolution
Research
Group
http://www.ees.adelaide.edu.au/research/geology/CERG/
SW
NE
D
E
F

Figure 3

475000 480000 485000 490000 495000

7165000 7160000 7155000 7150000 7145000 7140000 7135000

187314 187323 187325 187305 187330 A 187337

MOUNT DAISY BATES

SPAGHETTI HILL

155731† 155733† 155735† 155737†
† Walker-Hallam, 2006

M010† M213† M214†
† White & Clarke, 1997

184468 184464 184495 184486 B 184484 185679 185674

MOUNT GOSSE

HEATHER'S HILL

FANNY FAULT

Inset to Figure 5a

Poles to foliation planes (mylonitic fabrics)

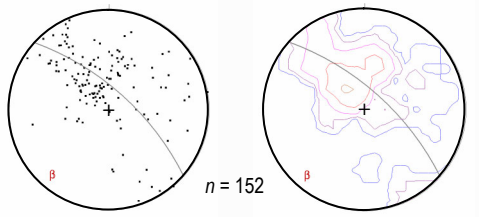

Girdle: 74/042 Beta axis: 16-222

Stretching lineations

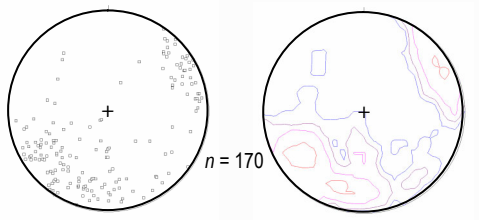

DATA KEY

187323 Sample number

† Reference to previous work

SCALE 1:120 000

0 2 4 8 12 16 20 Kilometers

Map coordinates derived from the Map Grid Of Australia Zone 52 (MGA94)

N

REFERENCE

GEOLOGICAL UNITS

MESOPROTEROZOIC

- Warakuna Supersuite (1050-1078 Ma): predominantly mafic intrusives and gabbros
- Felsic mylonite and blastomylonite; unassigned; typically garnet bearing
- Pitjantjatjara Supersuite (1171-1215 Ma): predominantly metamorphosed seriate to porphyritic granitic rock
- Mylonitic and blastomylonitic seriate to porphyritic granitic rock
- Mylonitic pyroxene granodiorite to quartz monzodiorite
- Mylonitic seriate to porphyritic pyroxene-biotite-hornblende monzogranite
- Mylonitic pyroxene-biotite-hornblende monzogranite with K-feldspar augen relict textures (rapakivi-granite)
- Unassigned group (<1390-1580 Ma): pre-Musgravian Orogeny rocks, including the Birksgate Metamorphics and undifferentiated felsic granulties and granitic gneisses, locally migmatitic and mylonitic
- Mylonitic granitic gneiss; typically augen bearing

SYMBOLS

- Geological boundary
- Fault or shear
- Strike-slip fault, showing relative sinistral horizontal displacement
- Strike-slip fault, showing relative dextral horizontal displacement
- Dyke intrusion, predominantly metadolerite and dolerite of various ages
- 23 Metamorphic foliation, showing strike and dip
- 52 Mineral stretching lineation, showing trend and plunge
- Tectonic transport indicator, showing tectonic transport direction of upper plate

Map compilation: Modified after Howard et al., 2006
Superimposed pseudocolour aeromagnetics image (TMI): Geological Survey of Western Australia, 2006
Structural data compiled by Tom Raimondo & Rodney King (University of Adelaide) and Hugh Smithies & Paul Evins (GSWA)

Figure 4

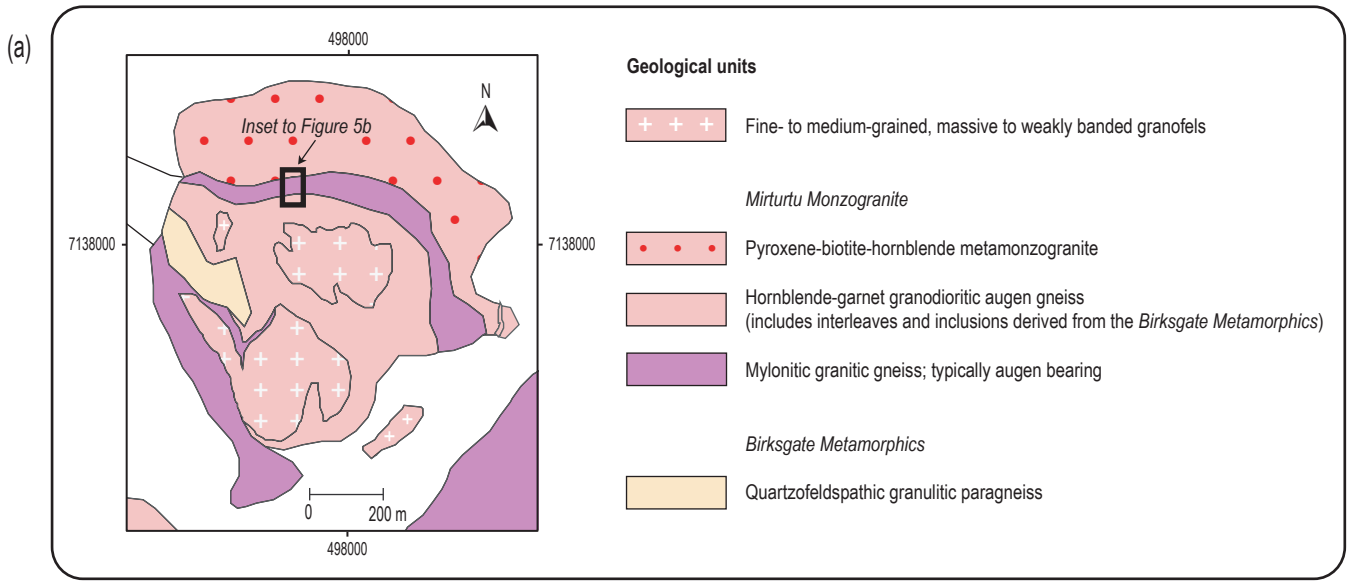
(a)
498000
N
Inset to Figure 5b
7138000
7138000
0
200 m
498000
Geological units
Fine- to medium-grained, massive to weakly banded granofels
Mirturtu Monzogranite
Pyroxene-biotite-hornblende metamonzogranite
Hornblende-garnet granodioritic augen gneiss
(includes interleaves and inclusions derived from the Birksgate Metamorphics)
Mylonitic granitic gneiss; typically augen bearing
Birksgate Metamorphics
Quartzofeldspathic granulitic paragneiss

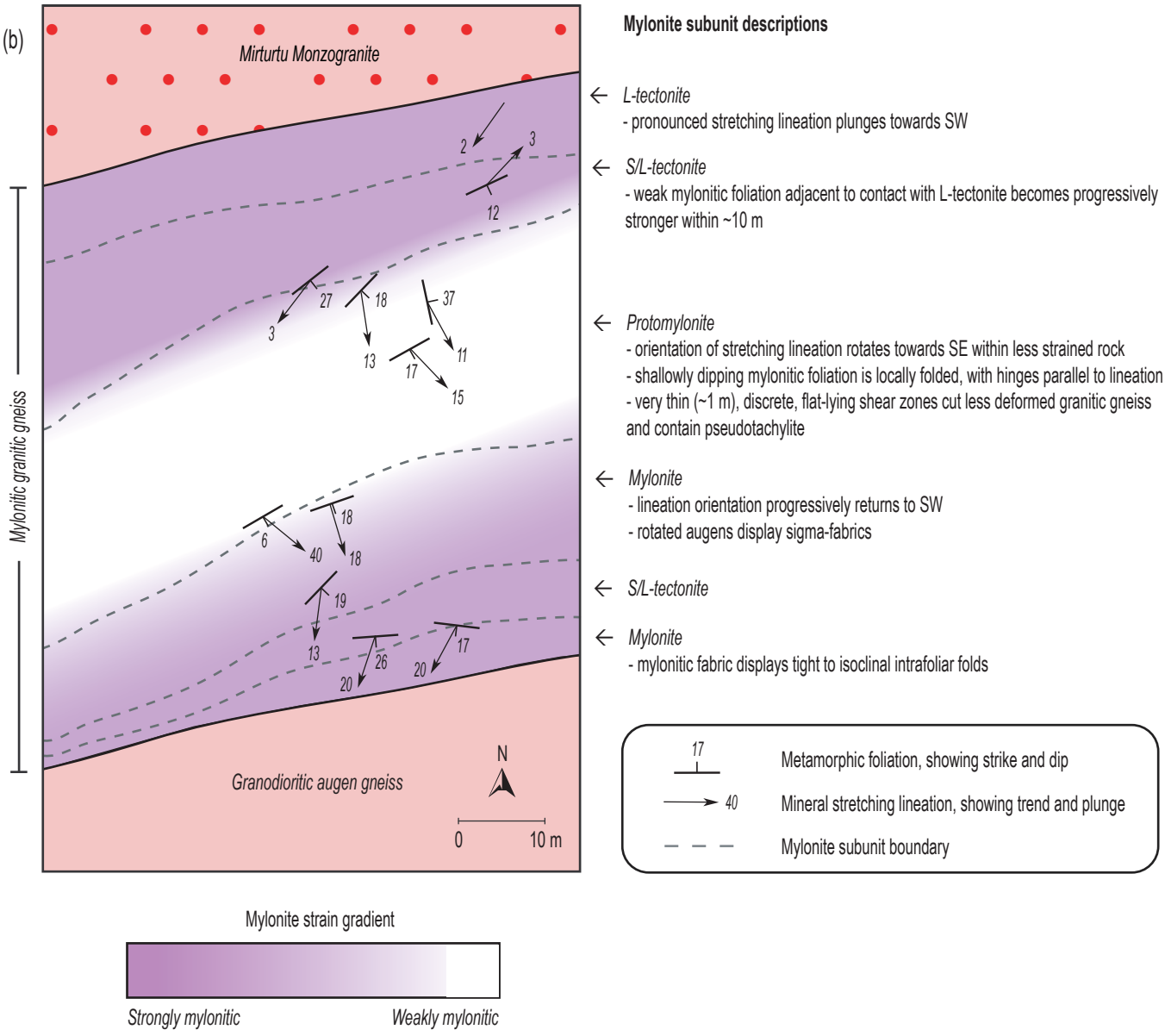
(b)
Mirturtu Monzogranite
Mylonitic granitic gneiss
Granodioritic augen gneiss
N
0
10 m
Mylonite subunit descriptions
L-tectonite
- pronounced stretching lineation plunges towards SW
S/L-tectonite
- weak mylonitic foliation adjacent to contact with L-tectonite becomes progressively stronger within ~10 m
Protomylonite
- orientation of stretching lineation rotates towards SE within less strained rock
- shallowly dipping mylonitic foliation is locally folded, with hinges parallel to lineation
- very thin (~1 m), discrete, flat-lying shear zones cut less deformed granitic gneiss and contain pseudotachylite
Mylonite
- lineation orientation progressively returns to SW
- rotated augens display sigma-fabrics
S/L-tectonite
Mylonite
- mylonitic fabric displays tight to isoclinal intrafoliar folds
Metamorphic foliation, showing strike and dip
Mineral stretching lineation, showing trend and plunge
Mylonite subunit boundary
Mylonite strain gradient
Strongly mylonitic
Weakly mylonitic

Figure 5

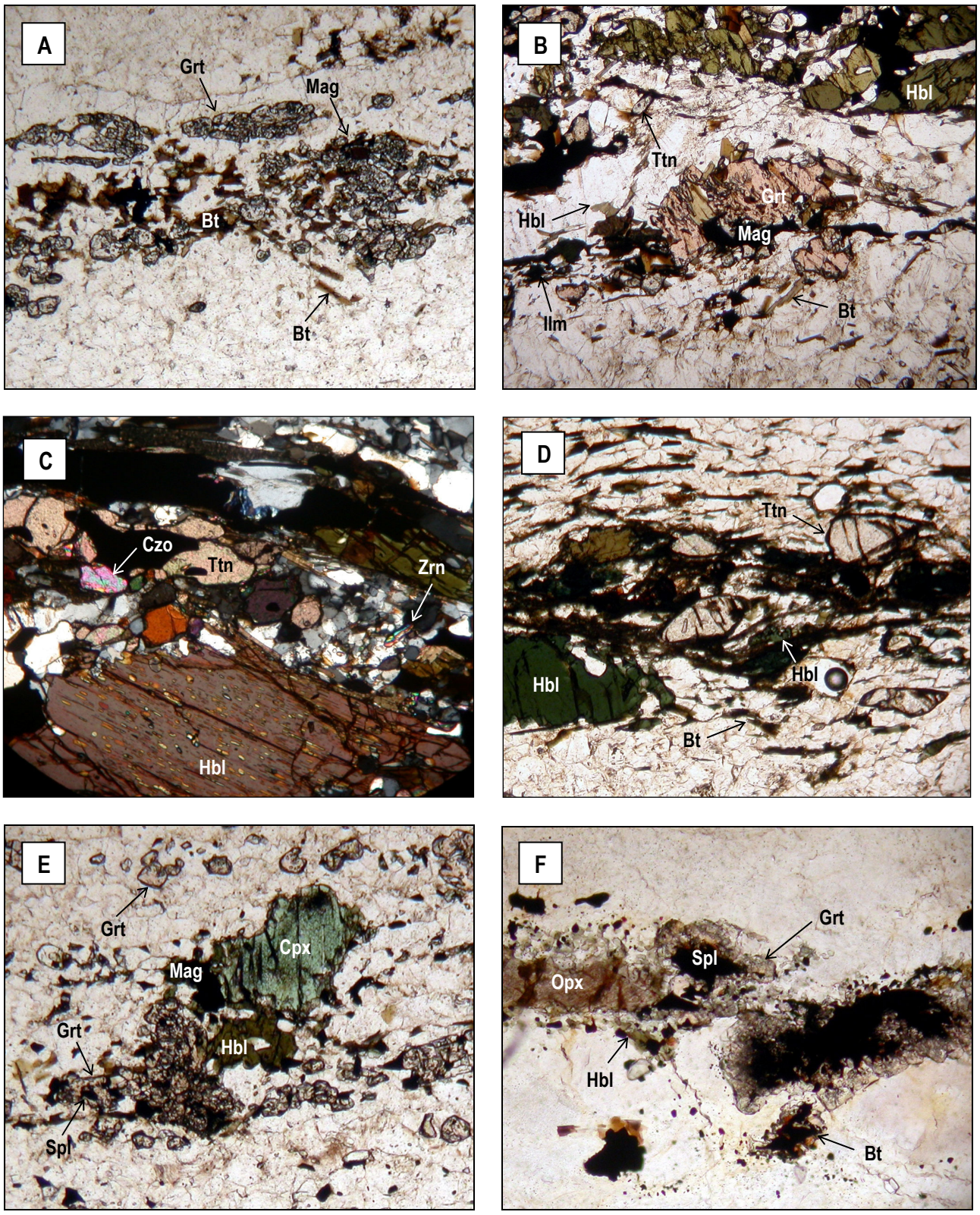
A
Grt
Mag
Bt
Bt
B
Hbl
Ttn
Grt
Hbl
Mag
Ilm
Bt
C
Czo
Ttn
Zrn
Hbl
D
Ttn
Hbl
Hbl
Bt
E
Grt
Cpx
Mag
Grt
Hbl
Spl
F
Grt
Spl
Opx
Hbl
Bt

Figure 6

Table 2 – Water activity selection

Sample 184464 (Group 3)

THERMOCALC Average *P-T* estimates using variable water activities

aH_2O	Average *P* (kbar, ±1σ)	Average *T* (°C, ±1σ)	Error correlation	Fit*
Water absent	11.0 ± 1.9	728 ± 106	0.842	1.43
0.25	10.7 ± 0.9	712 ± 35	0.584	1.32
0.50	12.6 ± 1.1	823 ± 45	0.626	1.38
0.75	13.6 ± 1.3	880 ± 54	0.642	1.48
1.00	14.4 ± 1.5	925 ± 62	0.643	1.57

* Fit value should be <1.42 for 95% confidence.

Mineral equilibria thermometers

	P (kbar)	8.0	9.0	10.0	11.0	12.0	13.0	14.0	15.0
R1 (Grt-Cpx)	*T* (°C)	699	705	711	717	723	729	735	741
R2 (Grt-Hbl)	*T* (°C)	681	688	695	702	709	716	723	729
R3 (Grt-Bt)	*T* (°C)	638	644	649	655	661	666	672	678

R1: py + 3hed = alm + 3di; R2: 5py + 3fact = 5alm + 3tr; R3: py + ann = alm + phl

Sample 187323 (Group 2)

THERMOCALC Average *P-T* estimates using variable water activities

aH_2O	Average *P* (kbar, ±1σ)	Average *T* (°C, ±1σ)	Error correlation	Fit*
Water absent	12.2 ± 2.4	742 ± 123	0.843	0.96
0.25	9.3 ± 1.0	608 ± 67	0.976	1.13
0.50	10.2 ± 1.0	650 ± 66	0.966	0.99
0.75	10.8 ± 1.0	676 ± 66	0.894	0.93
1.00	11.2 ± 1.1	696 ± 73	0.936	0.89

* Fit value should be <1.49 for 95% confidence.

Mineral equilibria thermometers

	P (kbar)	8.0	9.0	10.0	11.0	12.0	13.0	14.0	15.0
R1 (Grt-Hbl)	*T* (°C)	651	658	664	671	677	684	691	697
R2 (Grt-Bt)	*T* (°C)	709	716	722	728	734	740	746	752

R1: 5py + 3fact = 5alm + 3tr; R2: py + ann = alm + phl

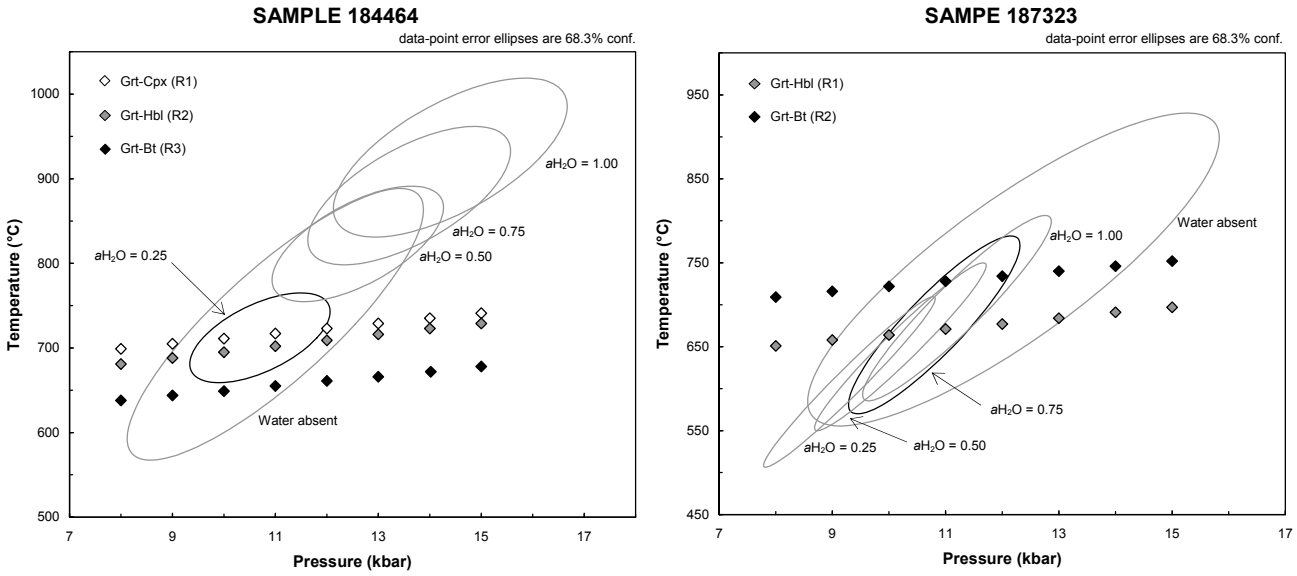

Figure 7

475000 480000 485000 490000 495000

7165000 7160000 7155000 7150000 7145000 7140000 7135000

187314
622 ± 34°C
9.6 ± 0.8 kbar

187323

187323
676 ± 70°C
10.8 ± 1.0 kbar

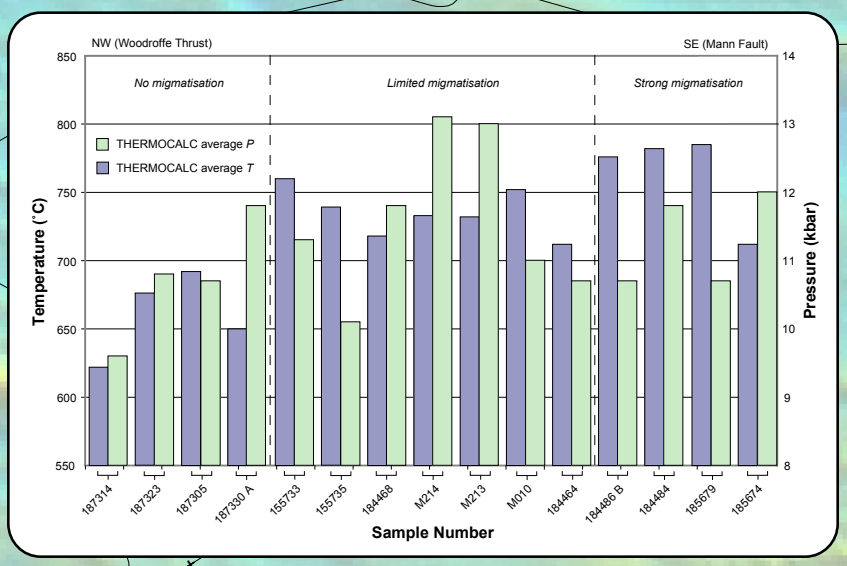

DATA KEY

187323 Sample number

THERMOCALC average *P-T* conditions

† Reference to previous work

MOUNT DAISY BATES

187305
692 ± 38°C
10.7 ± 0.7 kbar

187330 A
650 ± 35°C
11.8 ± 0.8 kbar

M214†
Core 733 ± 37°C, 13.1 ± 0.9 kbar
Rim 795 ± 40°C, 11.6 ± 0.9 kbar

M213†
Core 732 ± 46°C, 13.0 ± 1.2 kbar
Rim 755 ± 36°C, 11.4 ± 0.9 kbar

M010†
Core 752 ± 28°C, 11.0 ± 0.7 kbar
Rim 777 ± 33°C, 9.1 ± 0.8 kbar

† White & Clarke, 1997

SPAGHETTI HILL

155733
760 ± 72°C
11.3 ± 1.1 kbar

155735
739 ± 76°C
10.1 ± 0.8 kbar

184468
718 ± 37°C
11.8 ± 0.9 kbar

184464
712 ± 35°C
10.7 ± 0.9 kbar

MOUNT GOSSE

185674
712 ± 47°C
12.0 ± 0.9 kbar

HEATHER'S HILL

184486 B
776 ± 66°C
10.7 ± 1.2 kbar

Inset to Figure 5a

FANNY FAULT

184484
782 ± 40°C
11.8 ± 1.0 kbar

185679
785 ± 47°C
10.7 ± 1.2 kbar

475000 480000 485000 490000 495000

SCALE 1:120 000

0 2 4 8 12 16 20 Kilometers

Map coordinates derived from the Map Grid Of Australia Zone 52 (MGA94)

N

REFERENCE

GEOLOGICAL UNITS

MESOPROTEROZOIC

- Warakuna Supersuite (1050-1078 Ma): predominantly mafic intrusives and gabbros
- Felsic mylonite and blastomylonite; unassigned; typically garnet bearing
- Pitjantjatjara Supersuite (1171-1215 Ma): predominantly metamorphosed seriate to porphyritic granitic rock
- Mylonitic and blastomylonitic seriate to porphyritic granitic rock
- Mylonitic pyroxene granodiorite to quartz monzodiorite
- Mylonitic seriate to porphyritic pyroxene-biotite-hornblende monzogranite
- Mylonitic pyroxene-biotite-hornblende monzogranite with K-feldspar augen relict textures (rapakivi-granite)
- Unassigned group (<1390-1580 Ma): pre-Musgravian Orogeny rocks, including the Birksgate Metamorphics and undifferentiated felsic granulties and granitic gneisses, locally migmatitic and mylonitic
- Mylonitic granitic gneiss; typically augen bearing

SYMBOLS

- Geological boundary
- Fault or shear
- Strike-slip fault, showing relative sinistral horizontal displacement
- Strike-slip fault, showing relative dextral horizontal displacement
- Dyke intrusion, predominantly metadolerite and dolerite of various ages
- 23 Metamorphic foliation, showing strike and dip
- 52 Mineral stretching lineation, showing trend and plunge
- Tectonic transport indicator, showing tectonic transport direction of upper plate

Map compilation: Modified after Howard et al., 2006
Superimposed pseudocolour aeromagnetics image (TMI): Geological Survey of Western Australia, 2006
Structural data compiled by Tom Raimondo & Rodney King (University of Adelaide) and Hugh Smithies & Paul Evins (GSWA)

Figure 8

(a) Samples 184495, 187323 & 187337

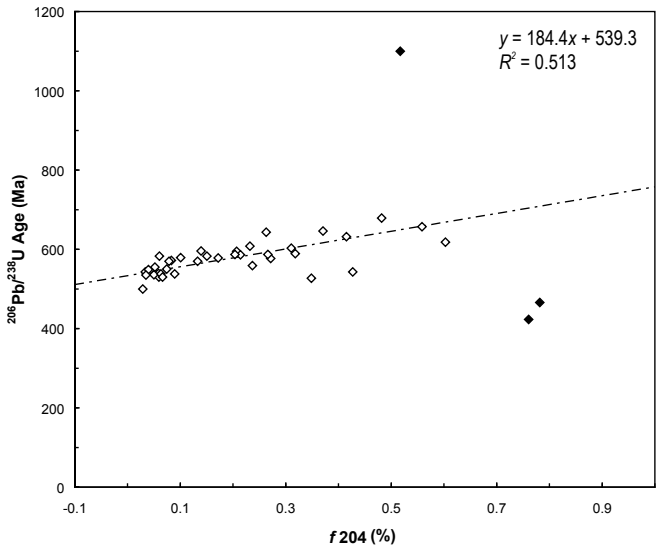

(b) Sample 155731

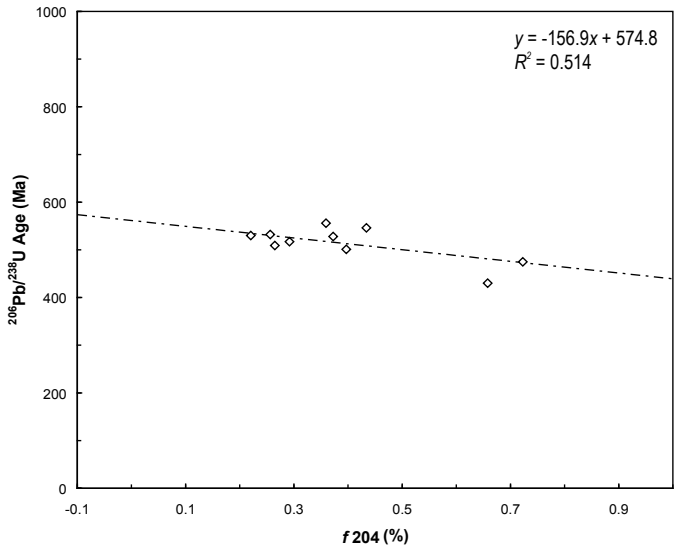

Figure 9

(a) Sample 187325

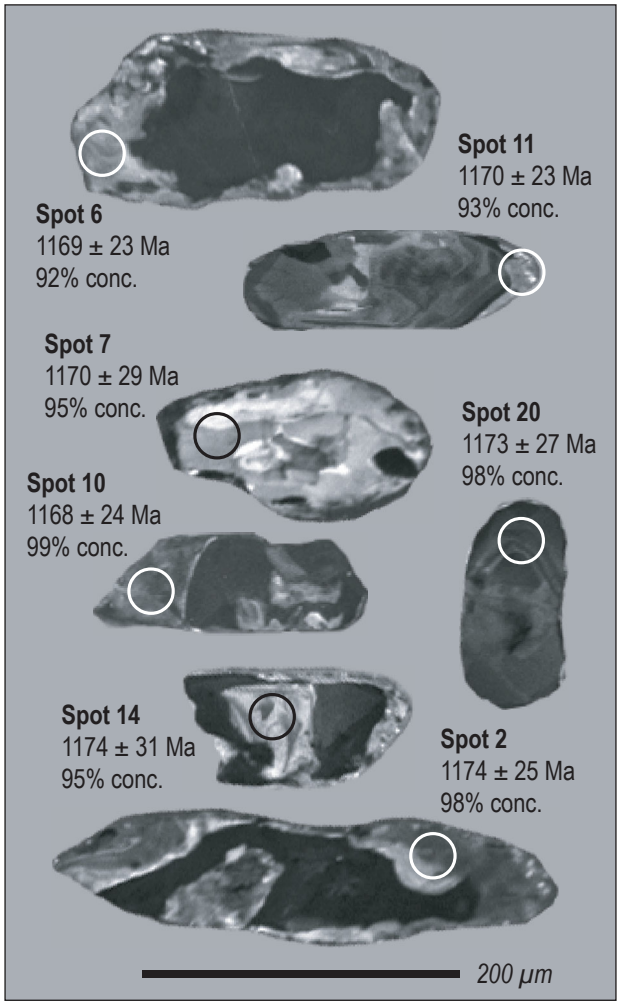

(b) Sample 184468

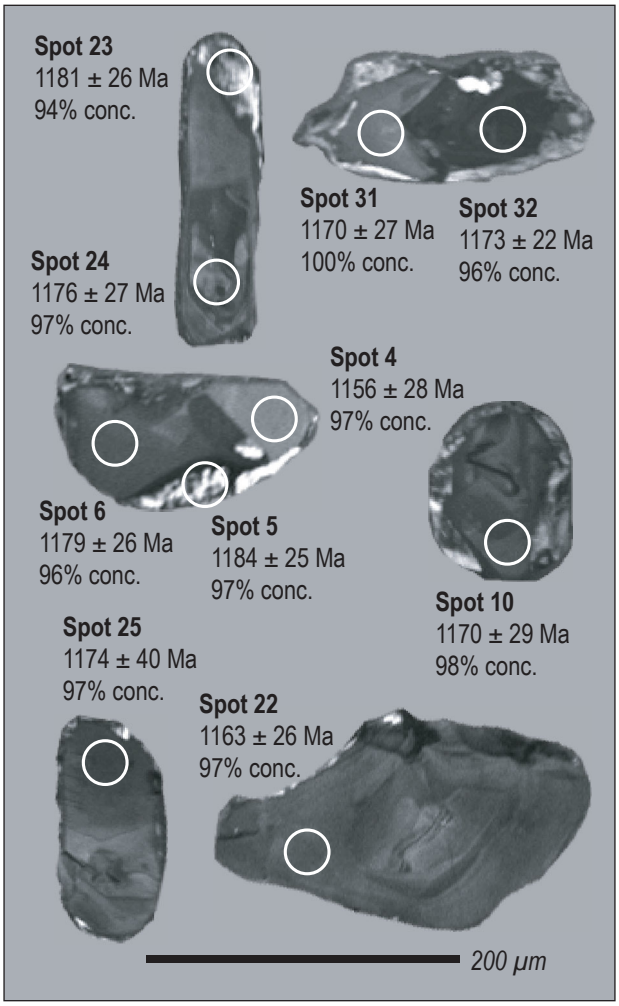

(c) Sample 184464

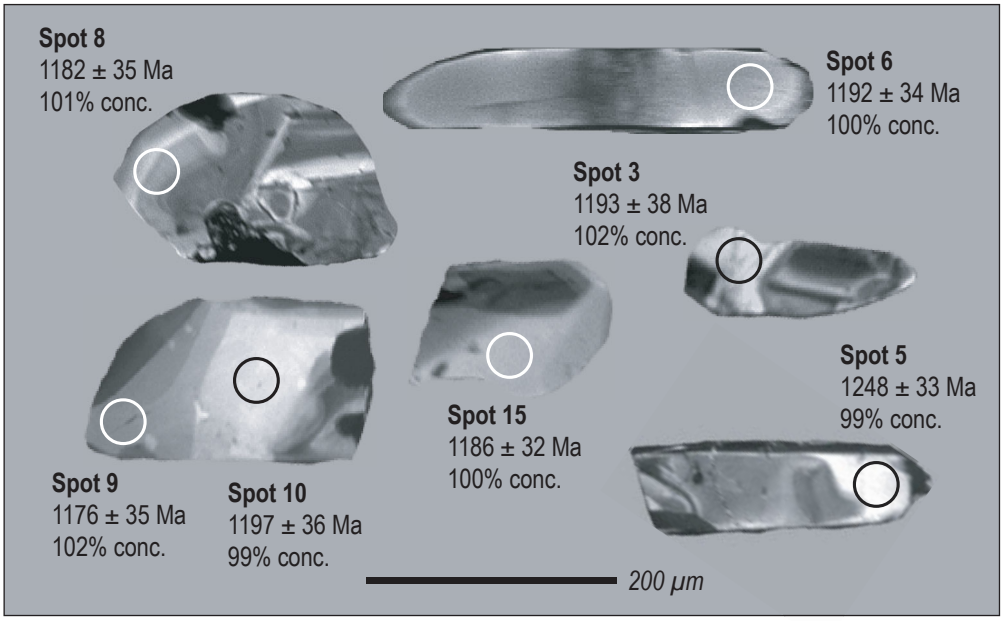

Figure 10

Sample 187323

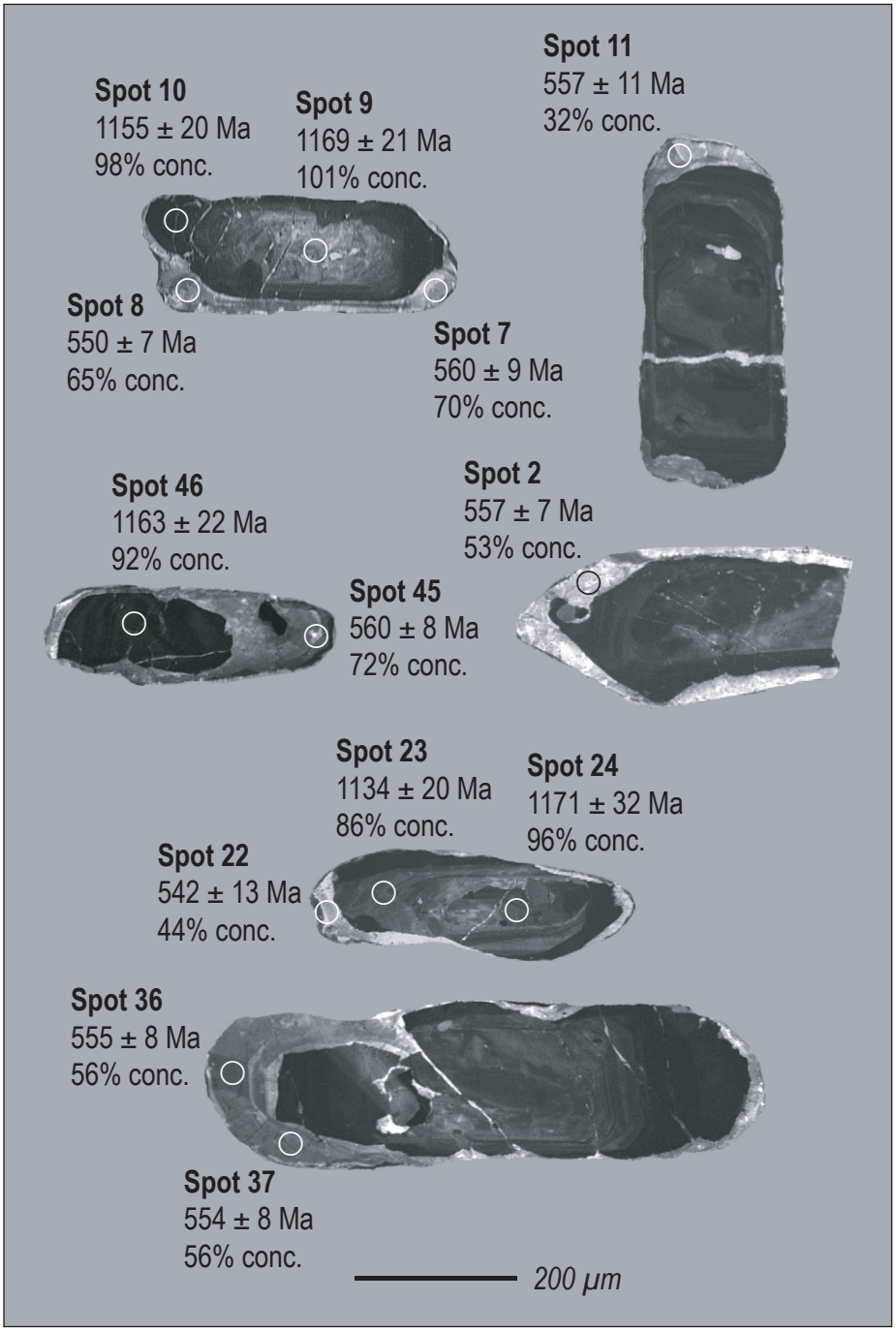

Figure 11

SAMPLE 184495

(a) $^{206}Pb/^{238}U$ weighted average (204-corrected)

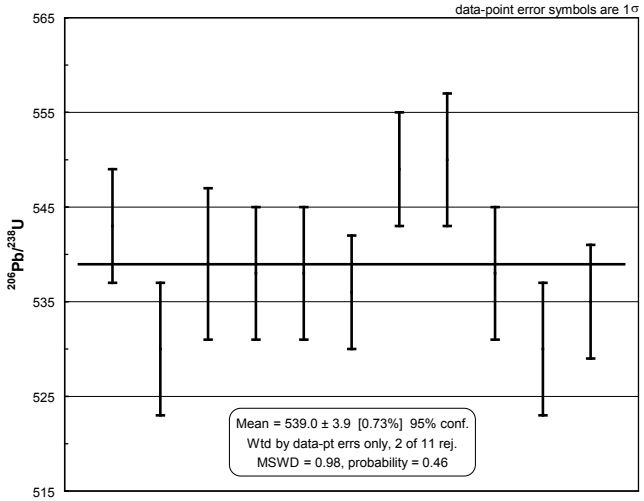

(b) Uncorrected data

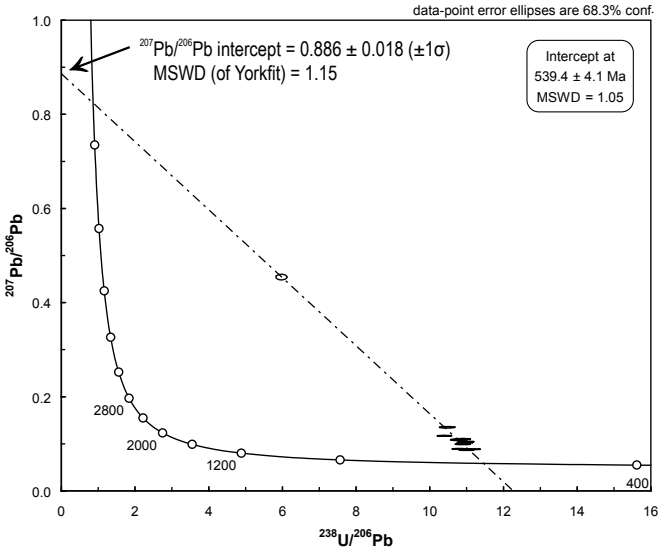

SAMPLE 187323

(c) $^{206}Pb/^{238}U$ weighted average (204-corrected)

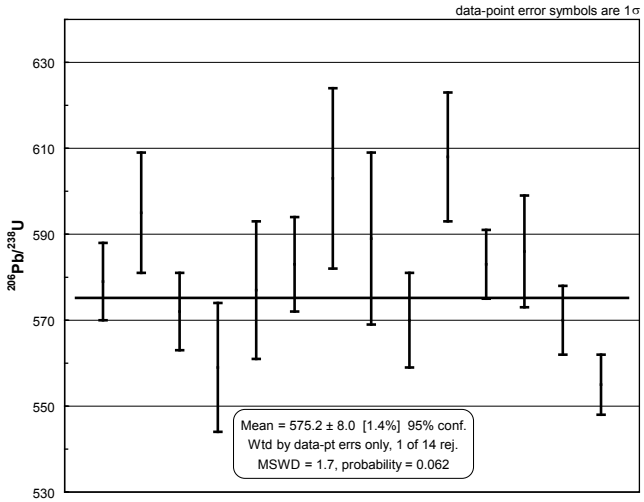

(d) Uncorrected data

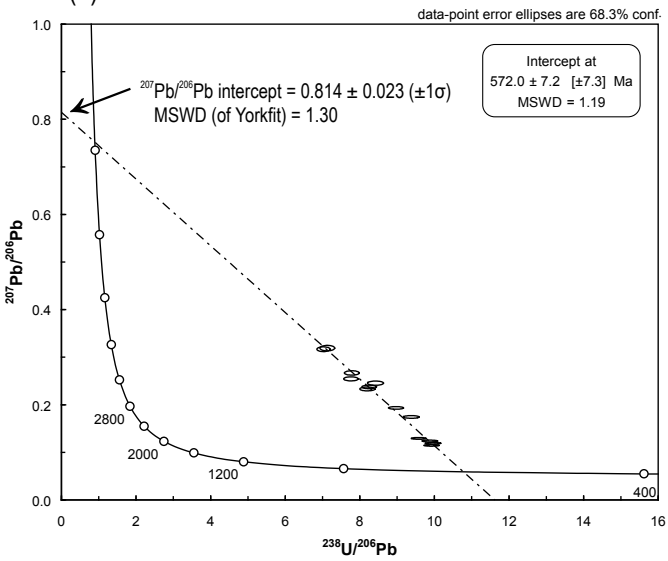

SAMPLE 187337

(e) $^{206}Pb/^{238}U$ weighted average (204-corrected)

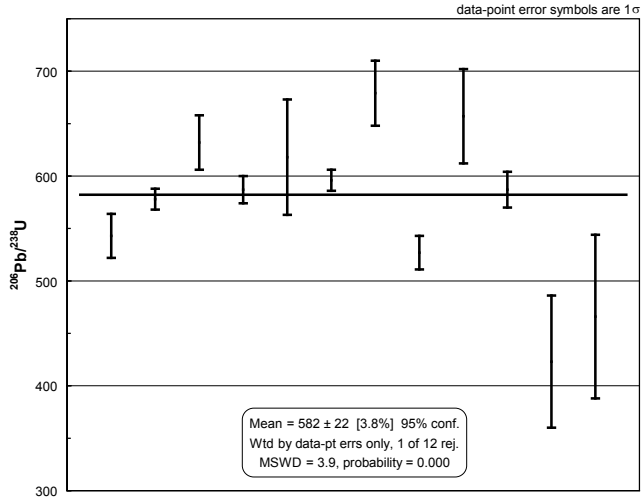

(f) Uncorrected data

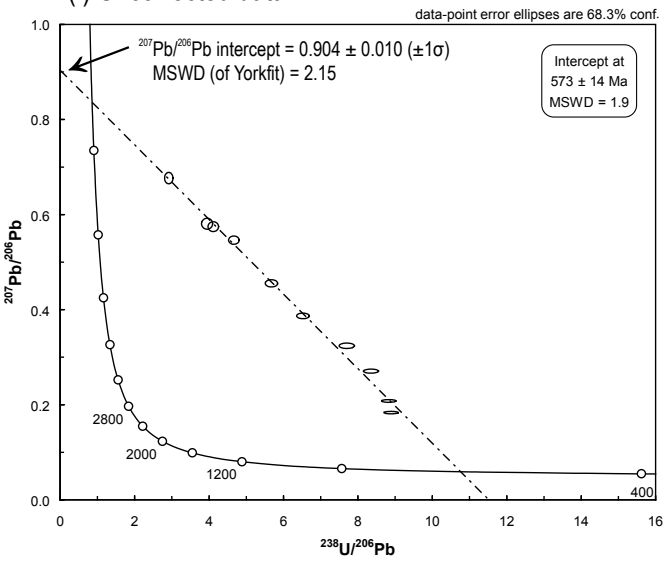

Figure 12

SAMPLE 155731

(a) $^{206}Pb/^{238}U$ weighted average (204-corrected)

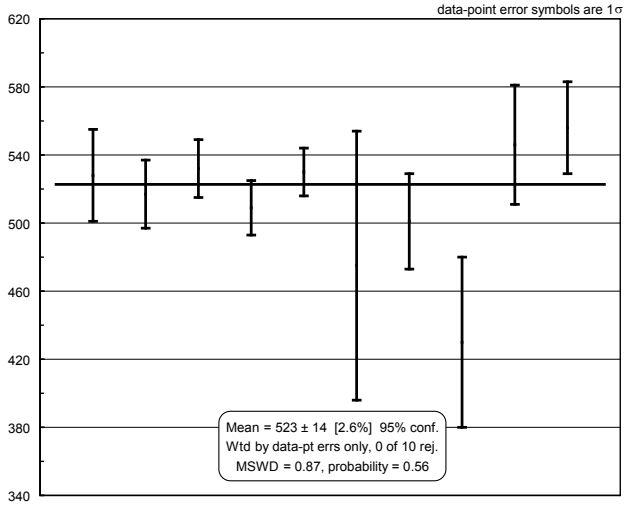

(b) Uncorrected data

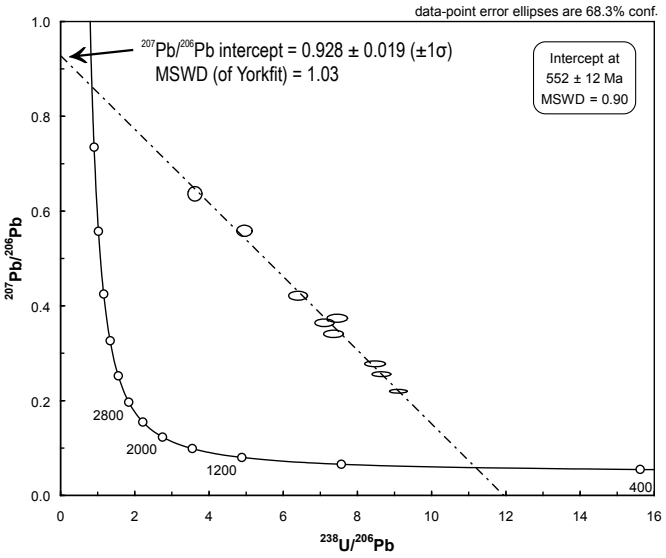

Figure 13

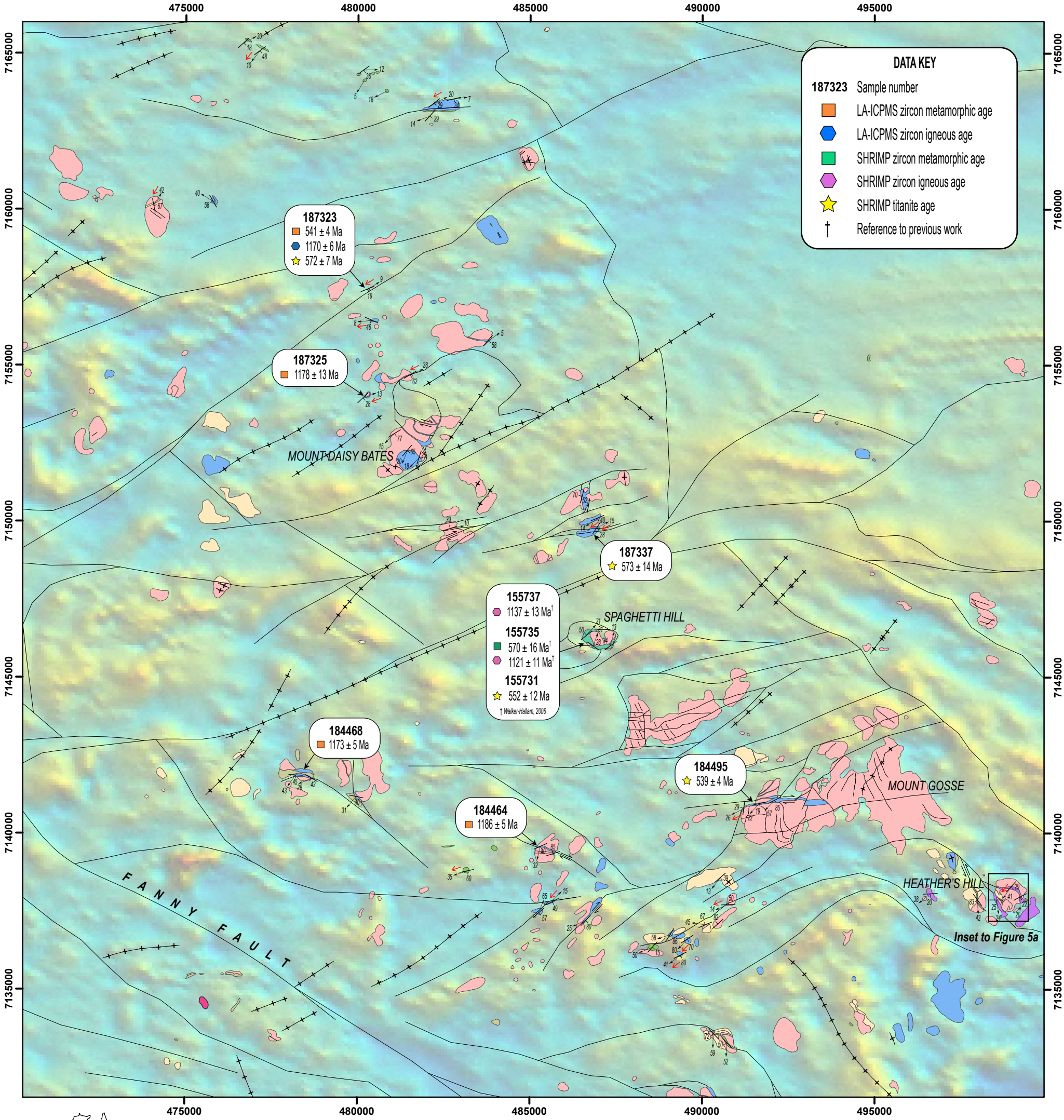

REFERENCE

GEOLOGICAL UNITS

MESOPROTEROZOIC

- Warakuna Supersuite (1050-1078 Ma): predominantly mafic intrusives and gabbros
- Felsic mylonite and blastomylonite; unassigned; typically garnet bearing
- Pitjantjatjara Supersuite (1171-1215 Ma): predominantly metamorphosed seriate to porphyritic granitic rock
- Mylonitic and blastomylonitic seriate to porphyritic granitic rock
- Mylonitic pyroxene granodiorite to quartz monzodiorite
- Mylonitic seriate to porphyritic pyroxene-biotite-hornblende monzogranite
- Mylonitic pyroxene-biotite-hornblende monzogranite with K-feldspar augen relict textures (rapakivi-granite)
- Unassigned group (<1390-1580 Ma): pre-Musgravian Orogeny rocks, including the Birksgate Metamorphics and undifferentiated felsic granulties and granitic gneisses, locally migmatitic and mylonitic
- Mylonitic granitic gneiss; typically augen bearing

SYMBOLS

- Geological boundary
- Fault or shear
- Strike-slip fault, showing relative sinistral horizontal displacement
- Strike-slip fault, showing relative dextral horizontal displacement
- Dyke intrusion, predominantly metadolerite and dolerite of various ages
- 23 Metamorphic foliation, showing strike and dip
- 52 Mineral stretching lineation, showing trend and plunge
- Tectonic transport indicator, showing tectonic transport direction of upper plate

Map compilation: Modified after Howard et al., 2006
Superimposed pseudocolour aeromagnetics image (TMI): Geological Survey of Western Australia, 2006
Structural data compiled by Tom Raimondo & Rodney King (University of Adelaide) and Hugh Smithies & Paul Evins (GSWA)

Figure 14

SAMPLE 187323

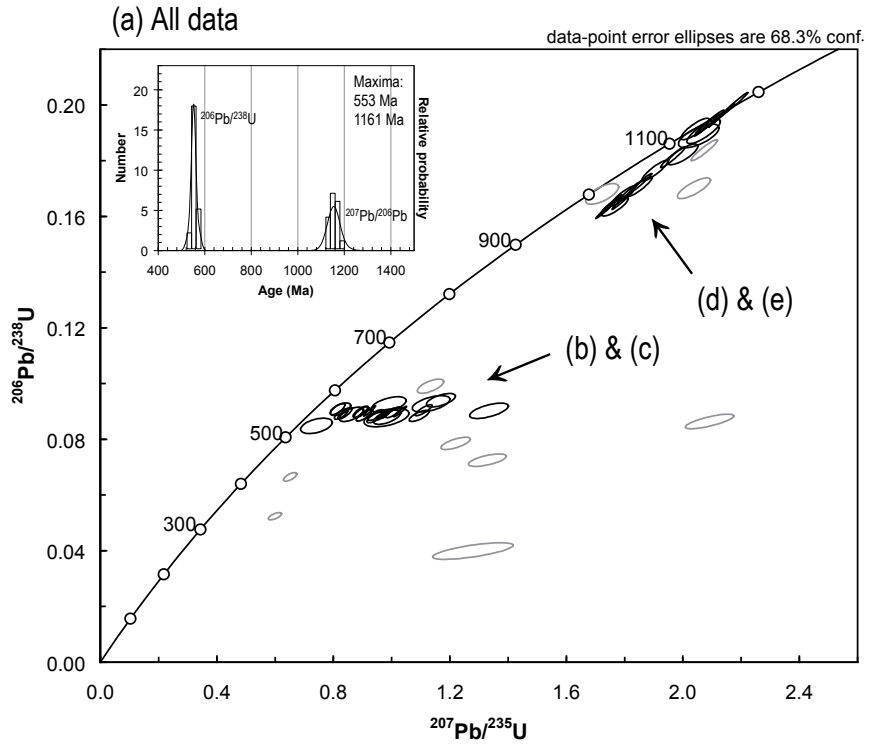

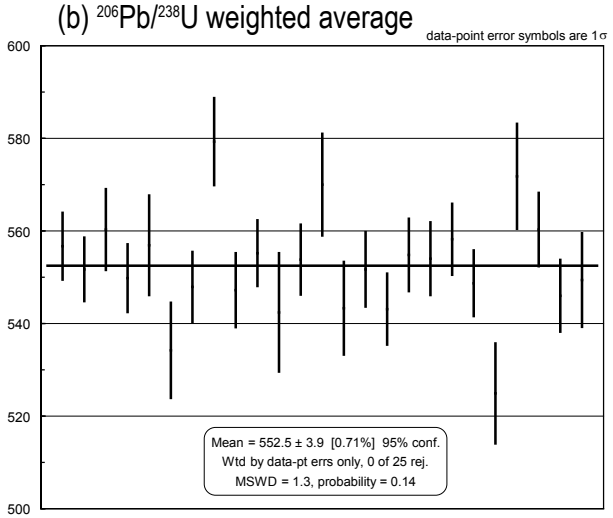

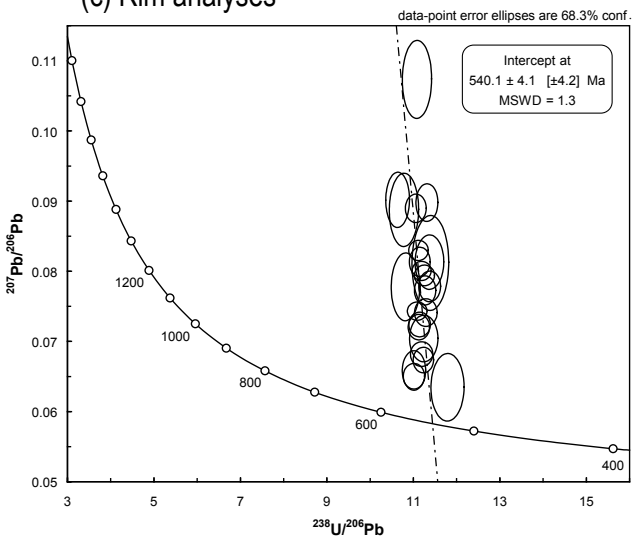

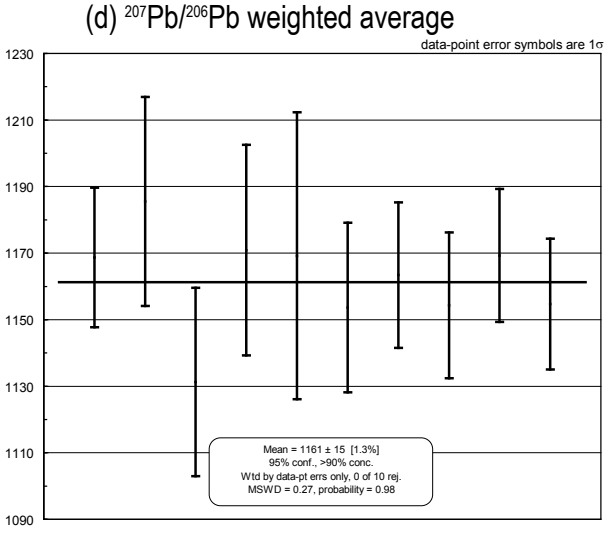

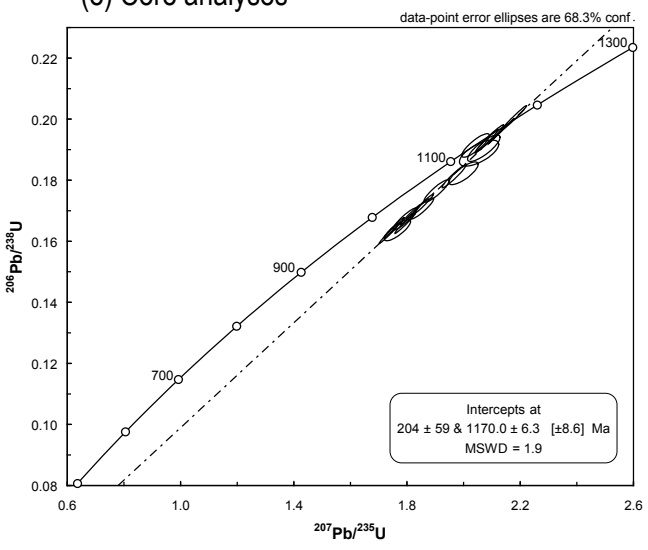

Figure 15

SAMPLE 187325

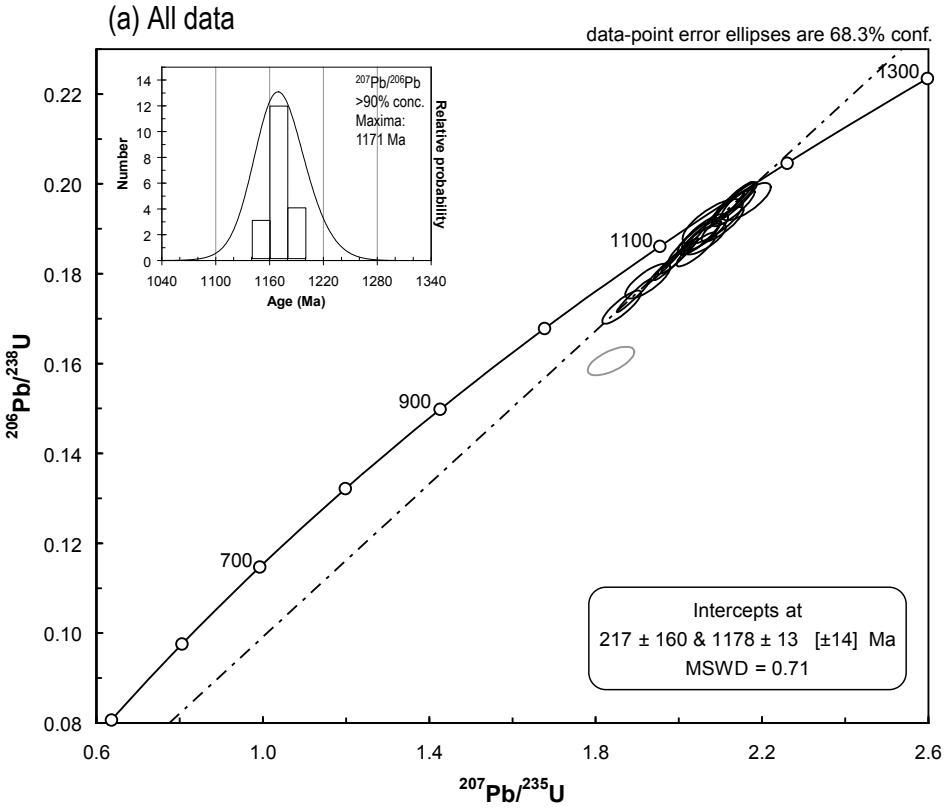

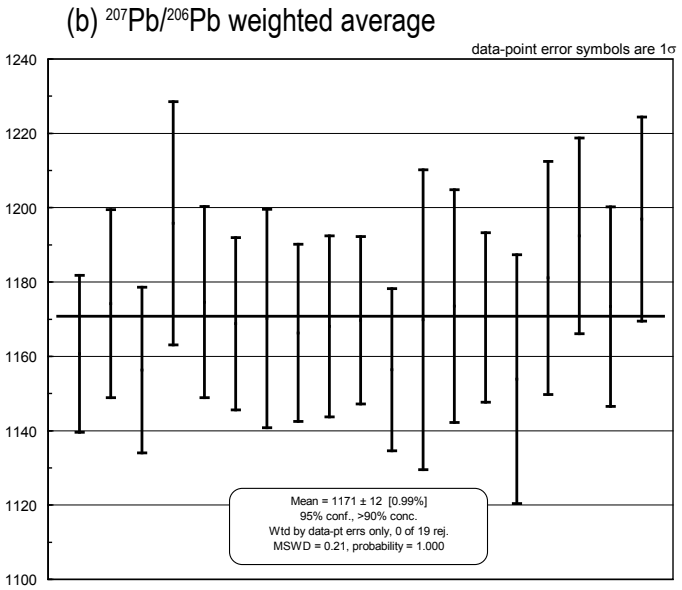

Figure 16

SAMPLE 184464

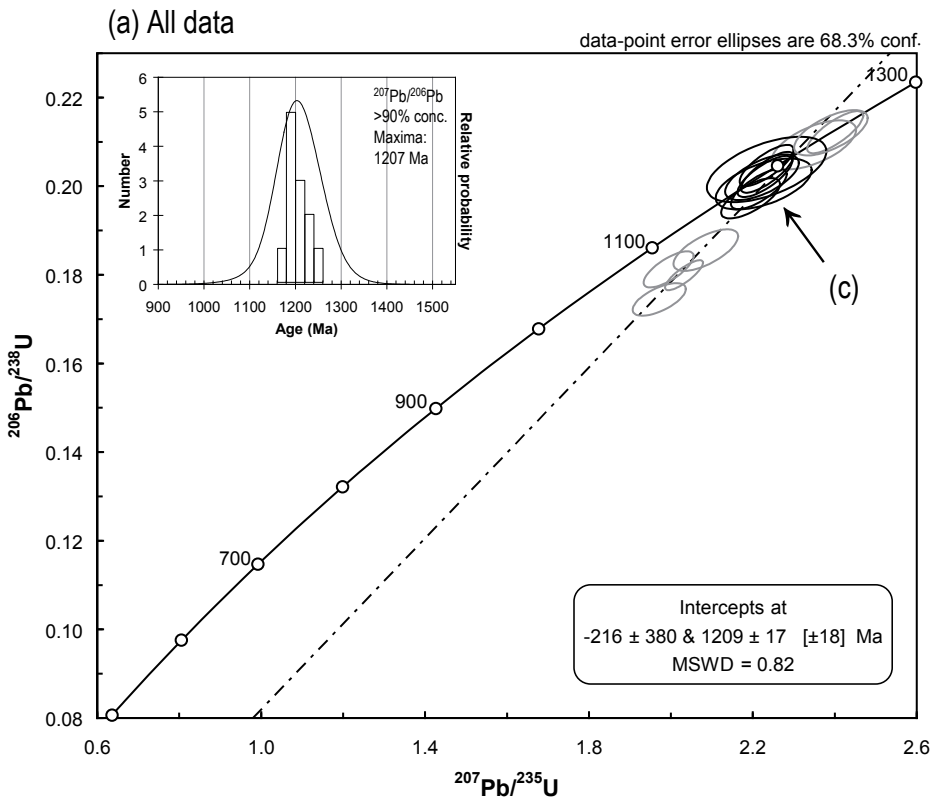

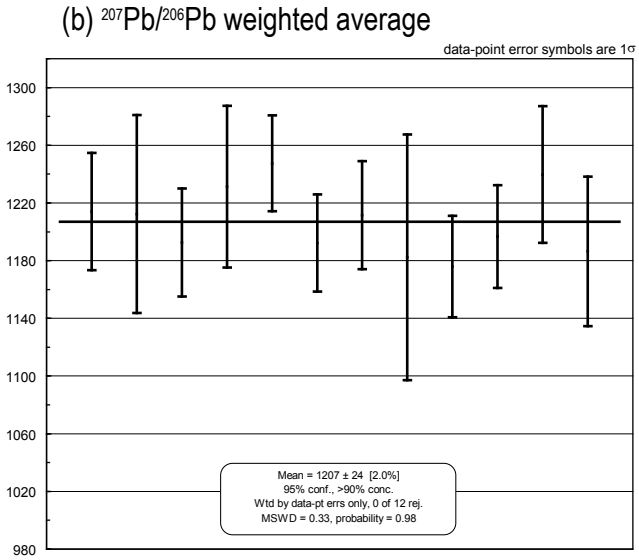

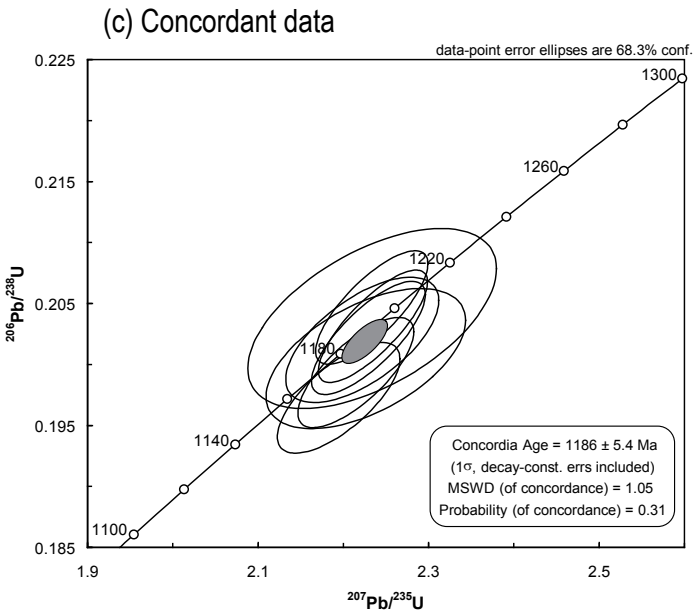

Figure 17

SAMPLE 184468

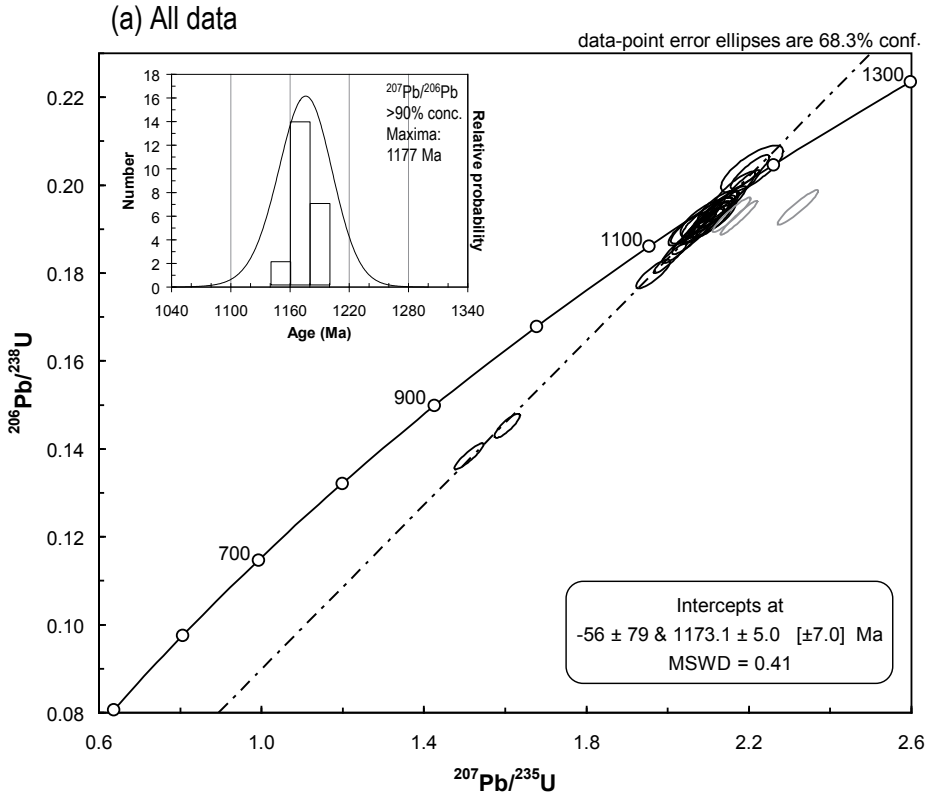

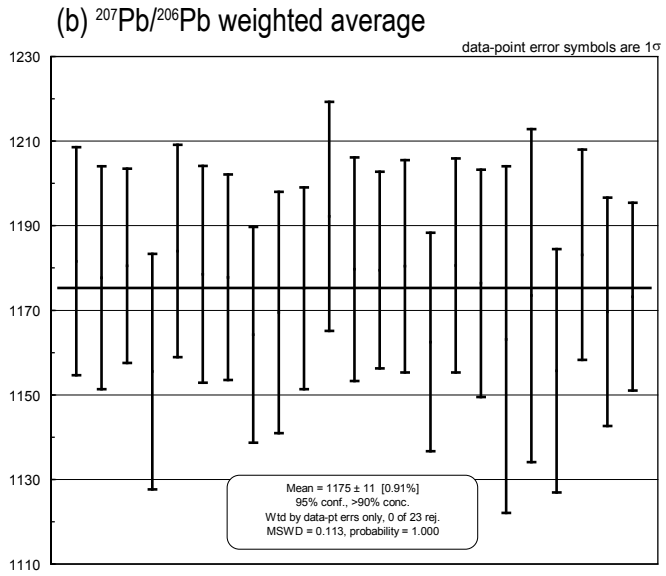

Figure 18

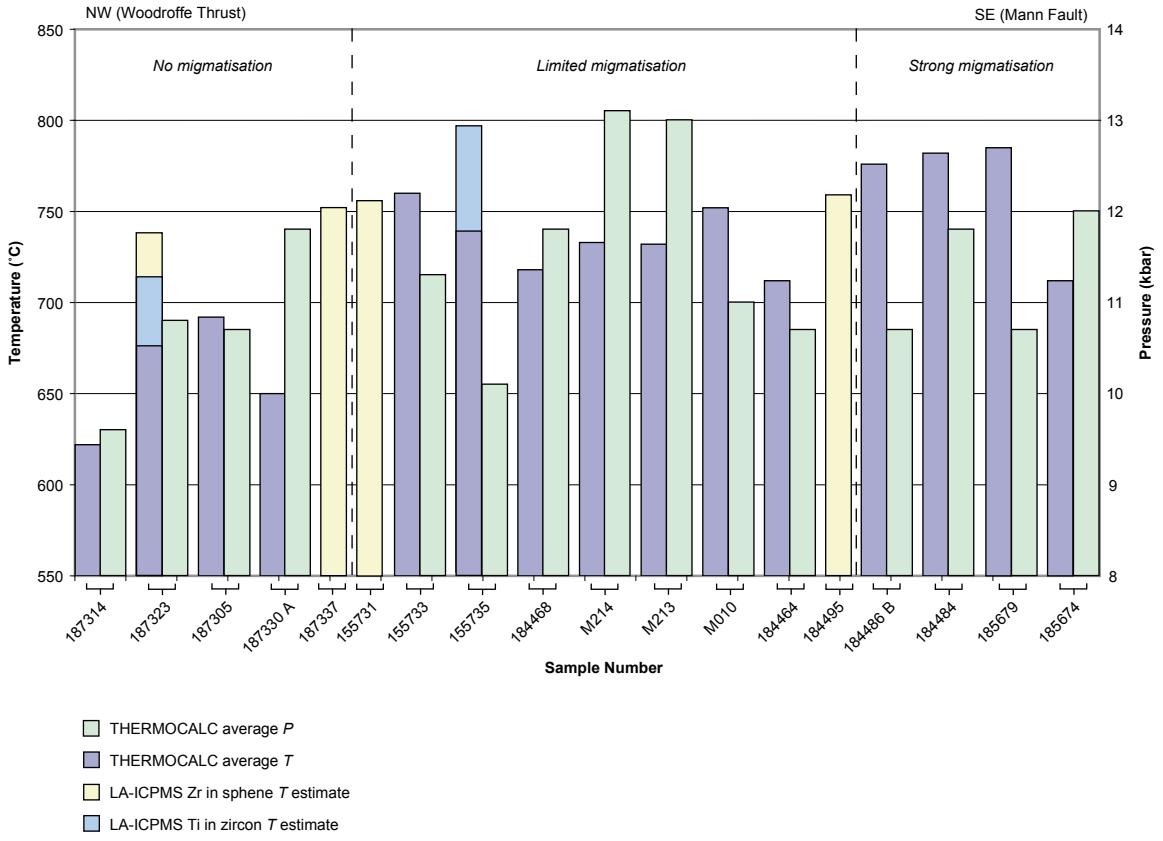
NW (Woodroffe Thrust)
SE (Mann Fault)
No migmatisation
Limited migmatisation
Strong migmatisation
Temperature (˚C)
Pressure (kbar)
850
800
750
700
650
600
550
14
13
12
11
10
9
8
187314
187323
187305
187330 A
187337
155731
155733
155735
184468
M214
M213
M010
184464
184495
184486 B
184484
185679
185674
Sample Number
THERMOCALC average P
THERMOCALC average T
LA-ICPMS Zr in sphene T estimate
LA-ICPMS Ti in zircon T estimate

Figure 19

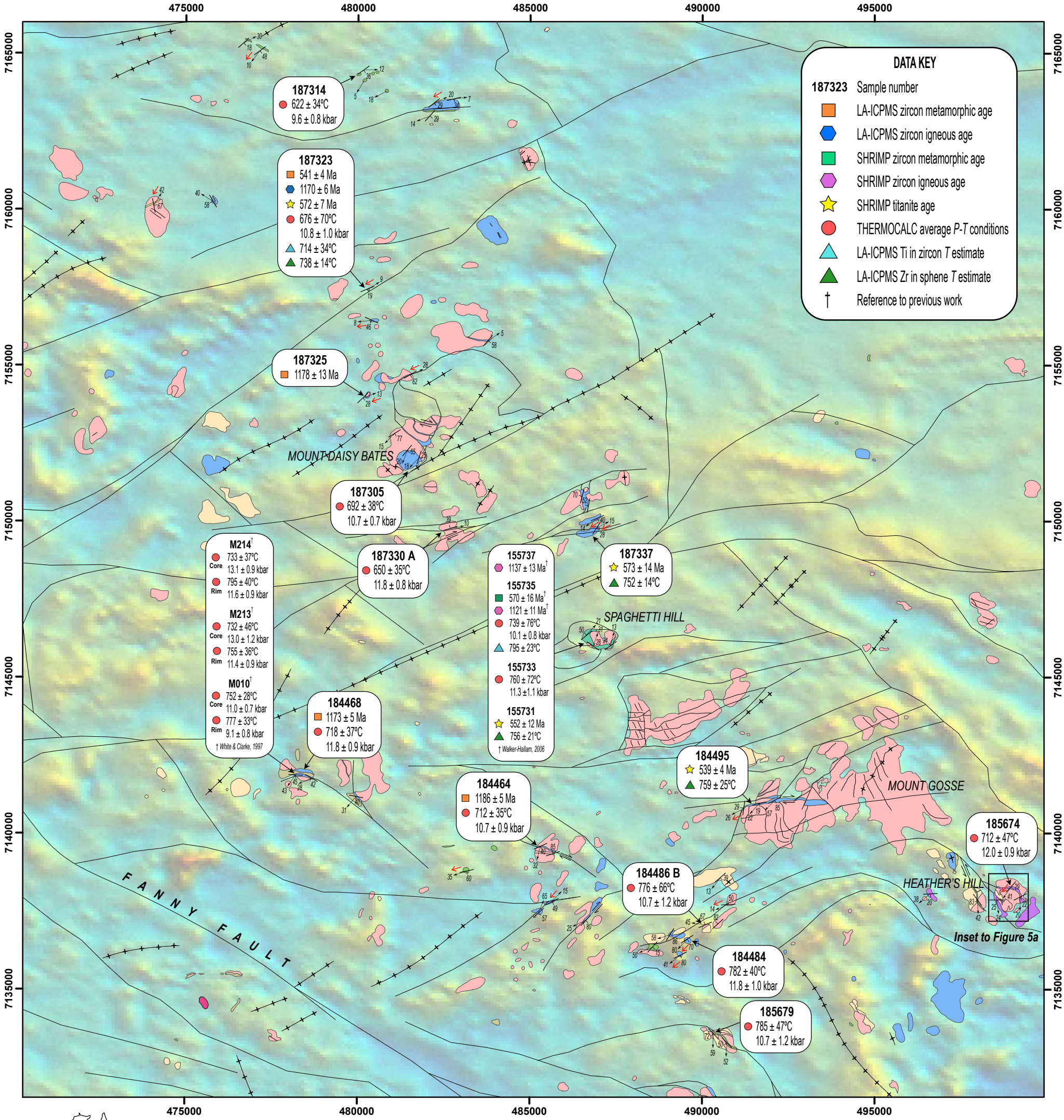

REFERENCE

GEOLOGICAL UNITS

MESOPROTEROZOIC

- Warakuna Supersuite (1050-1078 Ma): predominantly mafic intrusives and gabbros
- Felsic mylonite and blastomylonite; unassigned; typically garnet bearing
- Pitjantjatjara Supersuite (1171-1215 Ma): predominantly metamorphosed seriate to porphyritic granitic rock
- Mylonitic and blastomylonitic seriate to porphyritic granitic rock
- Mylonitic pyroxene granodiorite to quartz monzodiorite
- Mylonitic seriate to porphyritic pyroxene-biotite-hornblende monzogranite
- Mylonitic pyroxene-biotite-hornblende monzogranite with K-feldspar augen relict textures (rapakivi-granite)
- Unassigned group (<1390-1580 Ma): pre-Musgravian Orogeny rocks, including the Birksgate Metamorphics and undifferentiated felsic granulties and granitic gneisses, locally migmatitic and mylonitic
- Mylonitic granitic gneiss; typically augen bearing

SYMBOLS

- Geological boundary
- Fault or shear
- Strike-slip fault, showing relative sinistral horizontal displacement
- Strike-slip fault, showing relative dextral horizontal displacement
- Dyke intrusion, predominantly metadolerite and dolerite of various ages
- 23 Metamorphic foliation, showing strike and dip
- 52 Mineral stretching lineation, showing trend and plunge
- Tectonic transport indicator, showing tectonic transport direction of upper plate

Map compilation: Modified after Howard et al., 2006
Superimposed pseudocolour aeromagnetics image (TMI): Geological Survey of Western Australia, 2006
Structural data compiled by Tom Raimondo & Rodney King (University of Adelaide) and Hugh Smithies & Paul Evins (GSWA)

Figure 20

Titanite REE patterns (chondrite normalised)

(a) Sample 155731

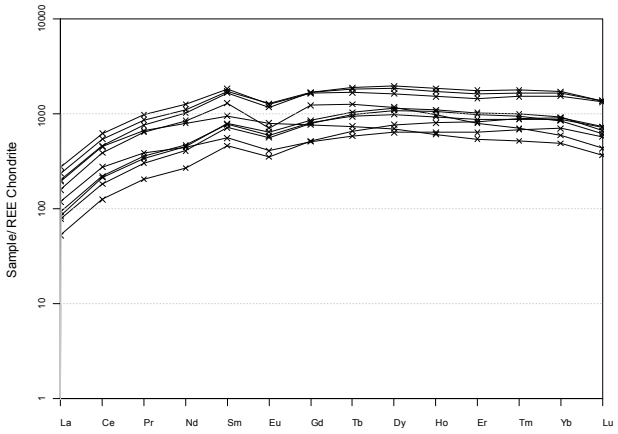

(b) Sample 187323

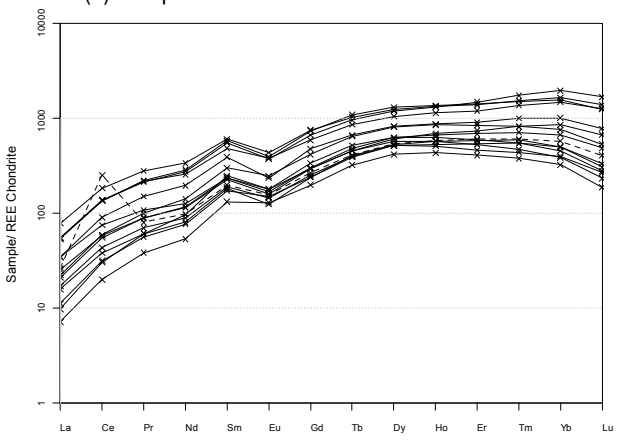

(c) Sample 187337

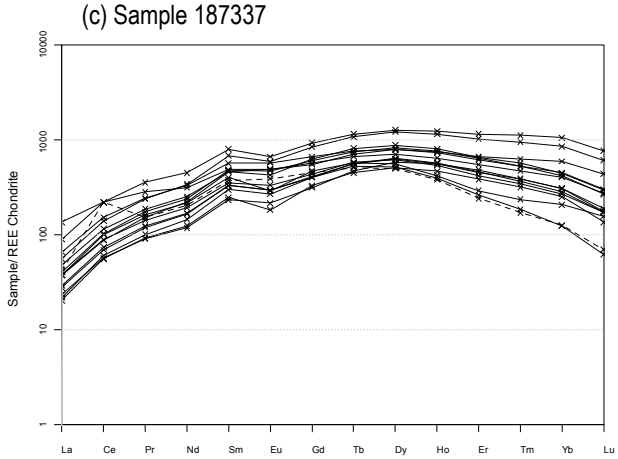

(d) Sample 184495

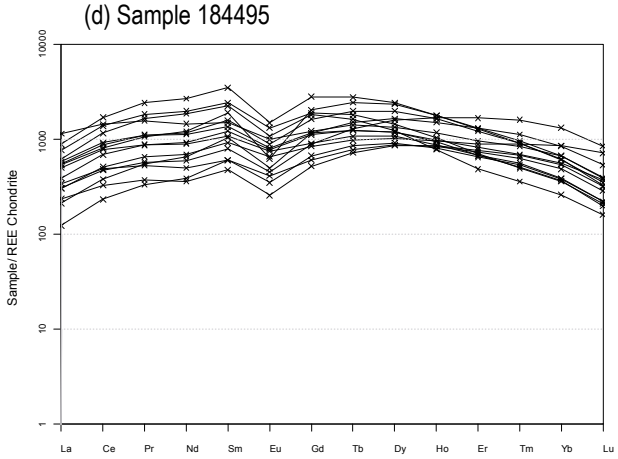

Zircon REE patterns (chondrite normalised)

(e) Sample 187323

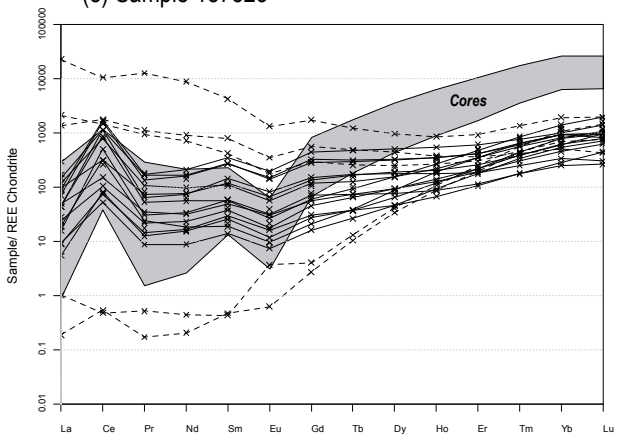

(f) Sample 155735

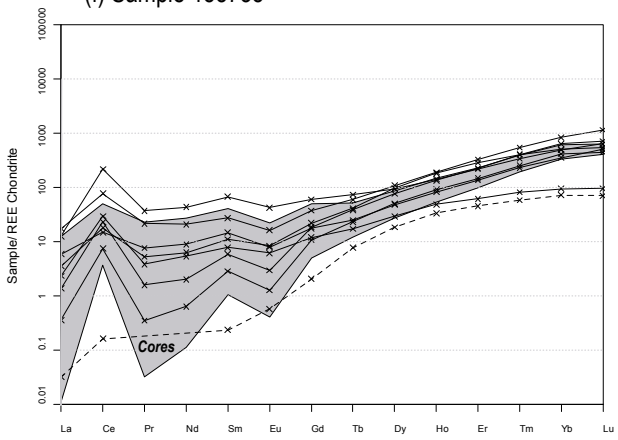

Figure 21

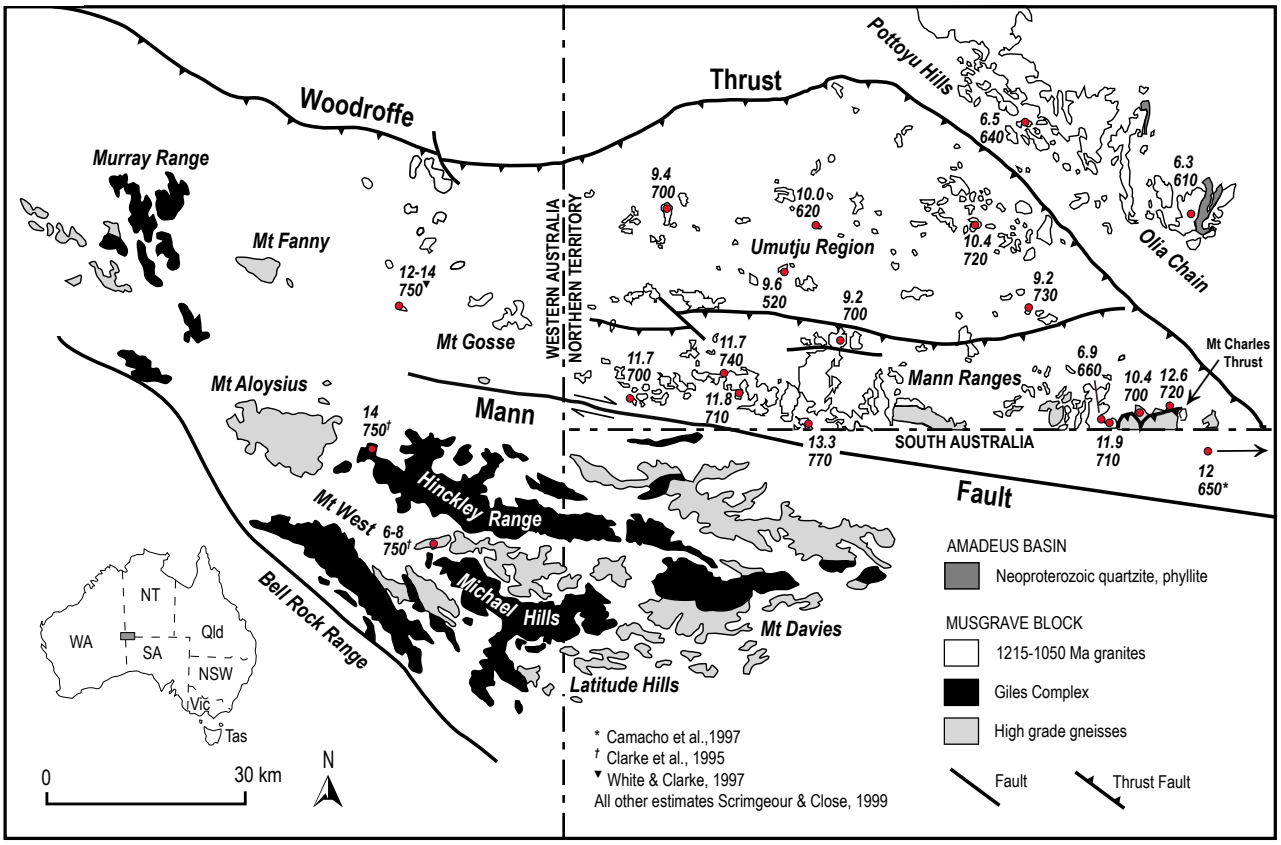
Woodroffe
Thrust
Pottoyu Hills
Murray Range
Mt Fanny
12-14
750▼
Mt Gosse
WESTERN AUSTRALIA
NORTHERN TERRITORY
9.4
700
10.0
620
Umutju Region
6.5
640
6.3
610
Olia Chain
10.4
720
9.6
520
9.2
700
9.2
730
Mt Charles
Thrust
11.7
700
11.7
740
Mann Ranges
6.9
660
10.4
700
12.6
720
Mt Aloysius
Mann
11.8
710
14
750†
13.3
770
SOUTH AUSTRALIA
11.9
710
12
650*
Fault
Hinckley Range
Mt West
6-8
750†
Michael Hills
Mt Davies
Bell Rock Range
Latitude Hills
NT
WA
SA
Qld
NSW
Vic
Tas
0
30 km
N
* Camacho et al.,1997
† Clarke et al., 1995
▼ White & Clarke, 1997
All other estimates Scrimgeour & Close, 1999
AMADEUS BASIN
Neoproterozoic quartzite, phyllite
MUSGRAVE BLOCK
1215-1050 Ma granites
Giles Complex
High grade gneisses
Fault
Thrust Fault

Figure 22

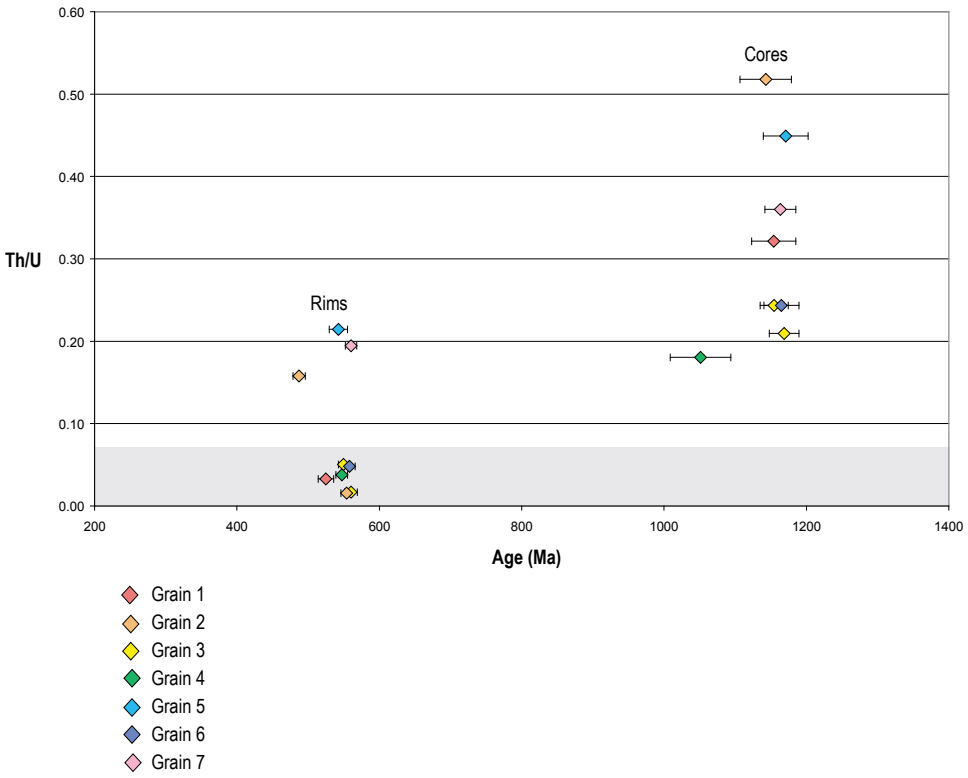
0.60
0.50
0.40
0.30
0.20
0.10
0.00
Th/U
Cores
Rims
200
400
600
800
1000
1200
1400
Age (Ma)
Grain 1
Grain 2
Grain 3
Grain 4
Grain 5
Grain 6
Grain 7

Figure 23

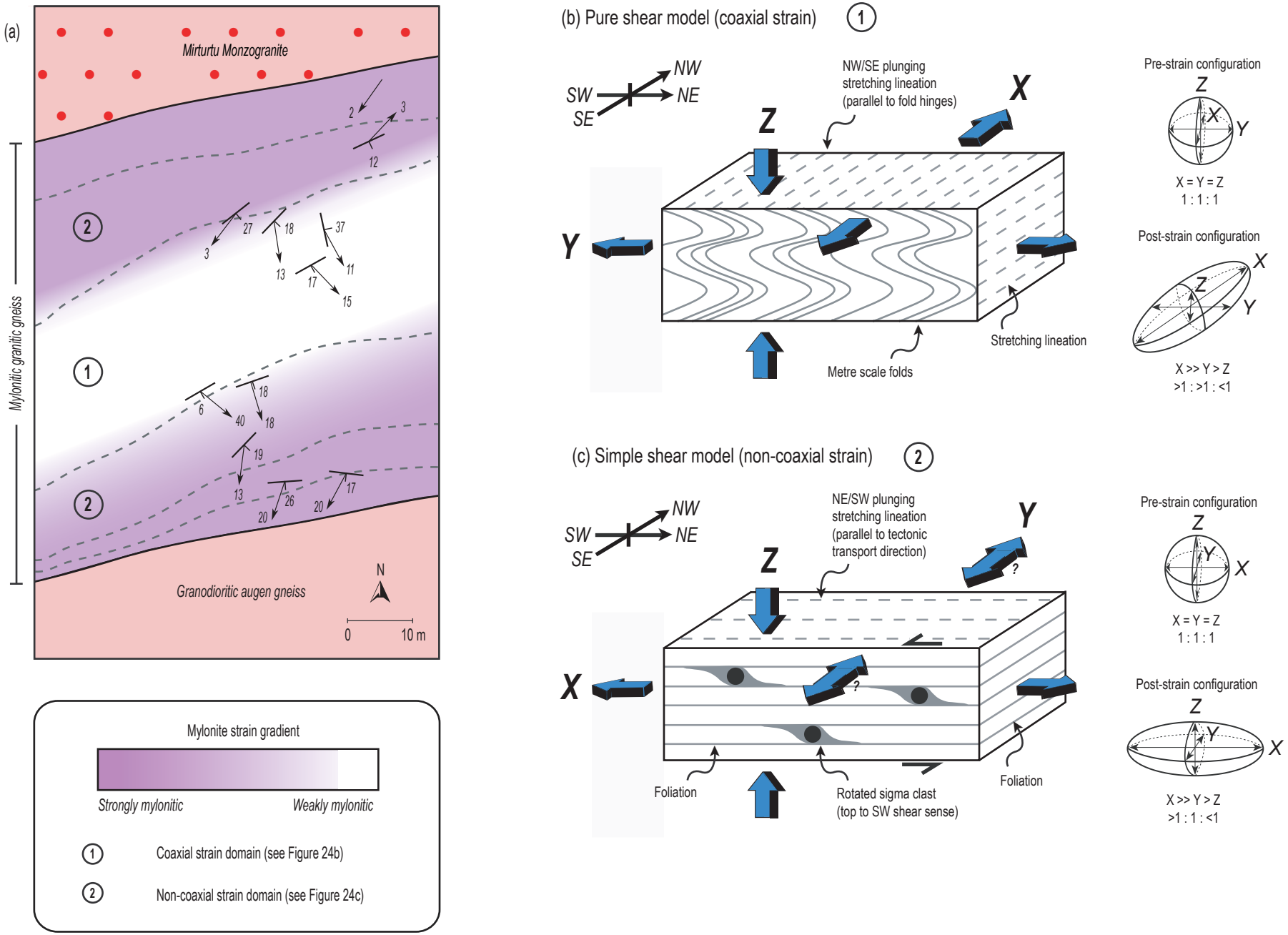
(a)
Mirturtu Monzogranite
Mylonitic granitic gneiss
Granodioritic augen gneiss
N
0
10 m
(b) Pure shear model (coaxial strain)
1
NW
SW
SE
NE
Z
X
Y
NW/SE plunging
stretching lineation
(parallel to fold hinges)
Stretching lineation
Metre scale folds
Pre-strain configuration
X = Y = Z
1 : 1 : 1
Post-strain configuration
X >> Y > Z
>1 : >1 : <1
(c) Simple shear model (non-coaxial strain)
2
NE/SW plunging
stretching lineation
(parallel to tectonic
transport direction)
Foliation
Rotated sigma clast
(top to SW shear sense)
Mylonite strain gradient
Strongly mylonitic
Weakly mylonitic
Coaxial strain domain (see Figure 24b)
Non-coaxial strain domain (see Figure 24c)

Figure 24

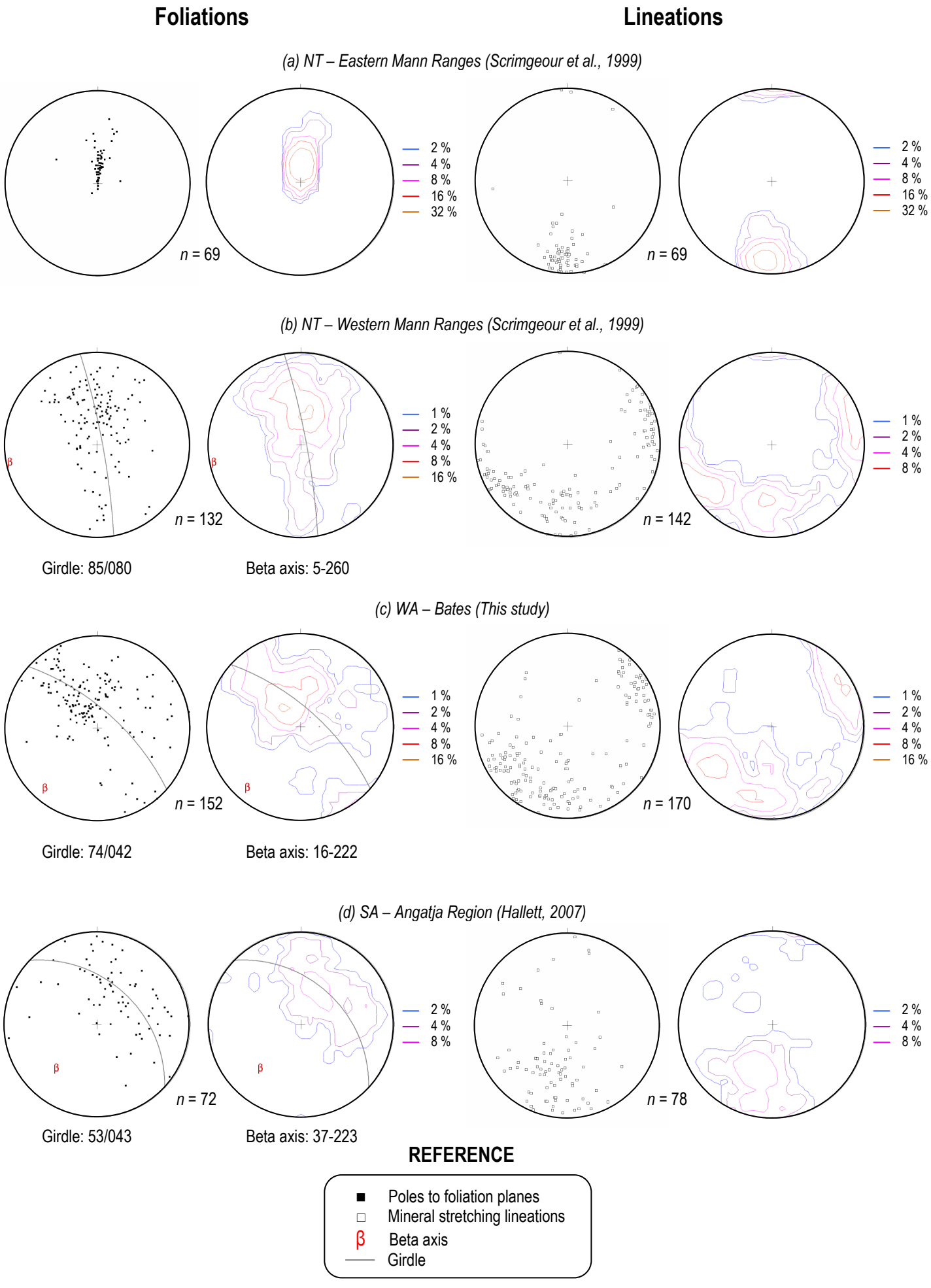
Foliations
Lineations
(a) NT – Eastern Mann Ranges (Scrimgeour et al., 1999)
2 %
4 %
8 %
16 %
32 %
n = 69
n = 69
(b) NT – Western Mann Ranges (Scrimgeour et al., 1999)
1 %
2 %
4 %
8 %
16 %
β
n = 132
n = 142
Girdle: 85/080
Beta axis: 5-260
(c) WA – Bates (This study)
n = 152
n = 170
Girdle: 74/042
Beta axis: 16-222
(d) SA – Angatja Region (Hallett, 2007)
n = 72
n = 78
Girdle: 53/043
Beta axis: 37-223
REFERENCE
Poles to foliation planes
Mineral stretching lineations
Beta axis
Girdle

Figure 25

RECORD 2009/12

A KINEMATIC, METAMORPHIC, GEOCHEMICAL AND GEOCHRONOLOGICAL FRAMEWORK FOR INTRACRATONIC REWORKING IN THE WESTERN MUSGRAVE BLOCK, CENTRAL AUSTRALIA

RAIMONDO

This Record is published in digital format (PDF) and is available online at: www.dmp.wa.gov.au/GSWApublications.
Laser-printed copies can be ordered from the Information Centre for the cost of printing and binding.

Further details of geological publications and maps produced by the Geological Survey of Western Australia can be obtained by contacting:

Information Centre
Department of Mines and Petroleum
100 Plain Street
EAST PERTH, WESTERN AUSTRALIA 6004
Phone: (08) 9222 3459 Fax: (08) 9222 3444
www.dmp.wa.gov.au/GSWApublications